Electroless nickel-boron deposits:

Synthesis, formation and characterization;
Effect of heat treatments;
Analytical modeling of the structural state.

Véronique VITRY

Thèse de Doctorat présentée en vue de l'obtention du titre de Docteur en Sciences de l'Ingénieur.

Jury members

Chair	Prof. M-G. Olivier	UMONS
Secretary	Prof. E. Filippi	UMONS
Members	Prof. F. Delaunois	UMONS (promoter)
	Prof. J. Lecomte-Beckers	ULG
	Prof. S. Godet	ULB
	Dr. J. Alexis	ENIT-Tarbes
	Dr. Y. Riddle	UCT Coatings

DEDICATION.

In memoriam

Professor Christian Dumortier
16/02/1950 - 23/10/2008

Professor Philippe Liénard
02/01/1952 - 11/10/2004

THANKS.

After five years working on this project, there are many people I'd like to thank.

I'd like first of all to thank Professor Fabienne Delaunois who has accompanied me during this whole project, first as an advisor and then as head of department and who has become far more than a boss to me. Her input in my scientific work, but also in my personal approach to work in general, has been invaluable to me.

I am also infinitely grateful to professors J. Lecomte-Beckers from Service de Métallurgie et Science des Matériaux at ULG, M. Olivier from Service de Science des Matériaux at UMONS and E. Filippi from Service de Génie Mécanique at UMONS who have been part of my thesis committee and whose council has always been helpful and insightful.

Many thanks also to Dr Y. Riddle from UCT Coatings who followed the last two years of the work with great interest and has accepted to be part of the jury, and to the other members of the jury, Professor S. Godet from ULB, Dr J. Alexis from ENIT-Tarbes.

I would like to express my gratitude to Dr Abdoul-Fatah Kanta who has worked alongside with me on the nickel-boron project for the last 18 months for its help with the experimental work and the interpretation of the results.

Research is not only done by the scientists: we are useless without our technical staff. I'd like to thank the technical staff of the Metallurgy Department, and specifically Sébastien Colmant, for their fantastic work.

A great part of the experimental work was carried out in various labs and research centers and I'd like to thank all the people who have welcomed me and helped me with those experiments: Jacques Dutrieux from INISMA whose expertise with the SEM is matchless, Dr Jean Dille from ULB without whom the nanoindenation and TEM experiments would

To those I may have omitted in here, please don't feel affronted: what my mind may have forgotten, my heart has not.

ABSTRACT

Electroless nickel-boron coatings are obtained by a chemical aqueous process that possesses most of the advantages of electrolysis but is exempt of its major inconveniences. This process allows the deposition of continuous coatings with a constant thickness on a very large range of substrates including non-metallic materials. The coatings have a wide range of interesting properties that make them suitable for application in various industries.

The properties of the coatings are really interesting and overall well known, but the fundamental knowledge about the formation mechanisms and the structural state of the coatings is not extensive. This work aims to increase this knowledge.

In the present work, the formation of the coating was studied by various techniques which lead to several findings:

- the rate limiting step of the plating process was identified,

- a routine for semi-predetermined replenishment was implemented,

- the initiation of the coating was investigated and the effects of roughness and substrate nature on this were observed,

- the formation of the coating was observed and a link between the local lead content and the morphology was established.

The structural state of as-deposited electroless nickel-boron coatings was also extensively studied and their nanocrystalline nature was identified. The mechanical properties, wear and corrosion resistances of the deposits were also observed, as well as the influence of heat treatments on the coatings.

Finally, modeling of the structural state of as-deposited coatings and of the influence of heat treatments on electroless nickel-boron was undertaken. A model of the grain size of the material was obtained, and the basis for the predetermination of the crystallization temperature of nickel-boron were set.

RÉSUMÉ

Les dépôts chimiques de nickel sont obtenus par la réduction de sels de nickel en phase aqueuse par un réactif chimique. Le procédé est similaire sur certains aspects à l'électrolyse, mais il est exempt de la plupart des inconvénients de cette dernière. Les dépôts obtenus sont continus, d'épaisseur constante et peuvent être appliqués sur une large gamme de substrats, y compris non-métalliques. Ils possèdent des propriétés très intéressantes pour un grand nombre d'applications industrielles.

Bien que les propriétés des dépôts sont généralement bien connues, la connaissance des mécanismes de formation et de la structure de ceux-ci n'est pas très approfondie. L'objectif de ce travail est d'apporter de nouvelles informations à ce sujet.

La formation des dépôts a été étudiée par diverses techniques et les résultats suivants ont été obtenus:

- le procédé est limité par la diffusion du réducteur dans la solution,

- une procédure semi-prédéterminée de régénération des bains a été mise au point,

- l'initiation du dépôt et l'influence qu'ont sur celle-ci la rugosité et la nature du substrat ont été observées,

- un lien a pu être établi entre la teneur locale en plomb des dépôts et leur morphologie.

La structure des dépôts de nickel-bore a été étudiée et il a été possible d'observer leur état nanocrystallin et de déterminer la taille des grains. Les propriétés mécaniques, les résistances à l'usure et à la corrosion des couches ont également été évaluées, de même que les effets des traitements thermiques.

Enfin la modélisation de la structure des dépôts en sortie de bain et l'influence des traitements thermiques sur celle-ci a été entamée. Un modèle analytique de la taille des grains a pu être établi et validé, tandis que les bases d'un modèle de prédétermination de la température de crystallisation des dépôts ont été posées.

CONTENTS

GENERAL INTRODUCTION.

GENERAL INTRODUCTION.

Electroless nickel-boron coatings are obtained by a chemical aqueous process that possesses most of the advantages of electrolysis but is exempt of its major inconveniences. This process allows the deposition of continuous coatings with a constant thickness on a very large range of substrates including non-metallic materials. Electroless coatings have a wide range of interesting properties that make them suitable for application in various industries: their electrical and magnetic properties are useful in electronic applications, their corrosion resistance is used in the chemical and food industries, their hardness and wear resistance allow them to be used in mechanical applications, such as aeronautic and automobile parts, molds, cutting tools (for examples saws) and firearms.

The properties of the deposits are overall well known. This is attested by the numerous studies focused on this subject and their various industrial applications. However, the same cannot be said about the mechanisms inducing those coatings and their more fundamental aspects, in particular for electroless nickel-boron: most fundamental studies dedicated to those deposits are entirely focused on the observation of the effect of bath composition and parameters and/or heat treatments on the coatings' properties and very few of them examine the causes and mechanisms that bring about those effects.

The fundamental knowledge about electroless deposition is really paradoxical: there is a very extended comprehension of the electrochemical aspect of the deposition process (everything that leads to the reduction of nickel) but the understanding of why and how the reduced metal adheres to the substrates and then forms the coatings is not well developed. The lack of knowledge is even worse for electroless nickel-boron than for nickel-phosphorous as most of time the behavior of the first is simply considered to be the same that (or similar to) those observed on the NiP.

This is unfortunate because knowledge of those aspects could be really useful for the electroless nickel-boron industry: they could allow improvement of the in-use properties and optimization of the products and processes involved for their synthesis simply by eliminating problems during the synthesis and heat treating of the coatings.

The present work aims mainly to explore some of the overlooked aspects of electroless nickel-boron coatings: their formation, their structural state and the way heat-treatments influence their structure, not only in a descriptive point of view but also from a mechanistic approach. The ultimate goal is to get a better understanding of the coatings' comportment. This will be carried out through several more defined objectives. The first is to observe the initiation and formation of the coating, which have a great influence on their structure and properties. Observation of the effect that several parameters, such as

the substrate roughness, have on the creation of the coating will provide useful pointers for their industrial uses.

A second aim of this work is to gain the best possible knowledge of the coatings that we synthesize, with an important focus on the structure of the deposits: materials science has evolved tremendously in the last couple of decades and most of the investigation work about the structural state of electroless nickel-boron was carried out in the eighties or early nineties. It thus predates, for example, the discovery of nanocrystalline materials and structures. As such, there is a lot of information that can be obtained from a careful investigation of the coating using the more modern techniques and the latest evolutions of materials science.

Another of our objectives is the understanding of the structural state of the coatings and how it is influenced by heat treatments. For this, analytical modeling including thermodynamic and kinetic aspects of the material was used to obtain, on one hand, the size of the crystallites inside an as-deposited film and, on the other hand, the crystallization temperature of electroless nickel-boron coatings.

One last, secondary, objective of our work arose from our intent to decrease our wastes and to increase the synthesizing capacity of our equipment. For this, an extended study of the consumption of reactive during the deposition process is needed. This study will then be used to implement a replenishment process that will bring the desired savings.

The present work will be divided in three main parts, each one being dedicated to a single aspect of the project. In the first part, the theoretical background of electroless plating will first be presented. Then, practical aspects of nickel-boron coatings and the state of the art knowledge about their properties will be described. Their applications will also be briefly discussed.

The second section will be focused on the experimental work carried out for this study and on its exploitation. In that, the experimental set up and conditions for the synthesis of electroless nickel-boron coatings will be described. Then, the study of the reactive consumption and the bath replenishment will be discussed. This will be followed by the observation of the initiation and formation of the deposit, including the influence of various substrate parameters, such as roughness and chemical composition. After that, two chapters will be dedicated to the characterization of the coatings and to the investigation of the influence of heat treatments on their properties. In the two last chapters, the structural study of the material will be emphasized as this aspect of the coatings' characteristics is often overlooked in recent research.

The last part of this text contains the modeling work. In that part, the theoretical background for the determination of the grain size and crystallization temperature of the coating will be presented. After this, the modeling assumptions and equations will be presented.

Part I

LITERATURE REVIEW OF THE MAKING AND PROPERTIES OF NICKEL-BORON DEPOSITS AND EFFECT OF HEAT TREATMENT ON THEM.

INTRODUCTION.

Electroless deposition was accidentally discovered in the 19th century by Wurtz [1, 2]. However, it was at the time considered as a lab curiosity because of the unpredictable nature of the reaction: the reduced metal was precipitated in powder form at the bottom of the vessel. Other 19th century researchers managed to obtain coatings but they appeared indiscriminately on all surfaces in the reaction cell. This early electroless process did not lead to any practical application and was soon forgotten.

This process was incidentally rediscovered in 1946 by Brenner an Riddel [3] while developing an electroplating process for coating the inside of steel tubes with nickel alloys [2, 4]. They observed, while trying to avoid oxidation of some reactive, that the current efficiency was higher than 100% when hypophosphite was added to the plating bath and that the outer face of the tube was also coated. Their work led to the development of the 'kanigen' process (catalytic nickel generation) by the General American Transportation Corp (G.A.T.C.) which lauched a pilot line in 1955 [2]. Since then, the industrial uses of the electroless deposition process have increased manifold.

The first electroless deposition bath was based on a solution of nickel salts to which sodium hypophosphite was added as a reducing agent. It was later discovered that other agents could be used to the same results, which allowed the deposition of other alloys like pure nickel and nickel-boron alloys [2]. The first borohydride reduced bath was proposed in 1954 and the technology was developed in 1957-1958, less than 20 years after the first synthesis of sodium borohydride [5].

While nickel-phosphorous remains to this day the most used electroless plating process, nickel-boron, which is the subject of this work comes second and is preferred, despite its higher cost [2], for a lot of high technology applications.

This part of the work will be dedicated to a comprehensive study of nickel-boron plating and of the resulting deposits. This study will begin by a description of theoretical aspects of the electroless deposition process. After this, practical bath compositions and procedures for nickel-boron deposition, then the known properties of nickel-boron coatings, will be examined.

1. SYNTHESIS OF NICKEL-BORON DEPOSITS.

In this chapter, each aspect of electroless nickel-boron deposition will be discussed. First, the theory of aqueous redox deposition processes and, among those, of electroless deposition will be presented. As this process is controlled by two sets of conditions, the first related to the thermodynamic possibility of the electroless reaction, and the second to the kinetic aspects of the process, both being strongly linked to the choice of the reducing agent, they will be described in the general case and specifically for nickel deposition.

After this, the composition and control of industrial electroless nickel deposition baths will also be discussed, beginning from a theoretical point of view and then in view of their practical application to nickel-boron deposition.

1.1   Aqueous redox deposition processes.

Aqueous redox deposition processes are based on the reduction of metal salts, in aqueous solution, following equation 1.1.

$$Me^{z+} + ze^{-} \overset{reduction}{\rightarrow} Me \tag{1.1}$$

Deposition processes can be separated in three main classes according to the electron giving source[2, 6]:

1. The electrons needed for reduction are given by the dissolution of a less noble metal (mostly the substrate). This process is called displacement coating and follows equation 1.2. The displacement coating ends as soon as the substrate is entirely covered by the nobler metal, generating extremely thin coatings.

$$Me_2 \overset{oxidation}{\rightarrow} Me_2^{z+} + ze^{-} \tag{1.2}$$

2. If the electrons are given by an external current source, the deposition process is called electrolysis and the principal chemical reaction that takes place is the reduction of the dissolved metal as in equation 1.1.

3. If the electrons are brought by reduction of a chemical agent instead of a less noble metal, the process is called chemical or electroless deposition. This process follows equation 1.3

$$Reducing\ agent \overset{oxidation}{\rightarrow} oxidised\ reducing\ agent^{z+} + ze^{-} \tag{1.3}$$

1.2   Theory of electroless deposition.

1.2.1   Introduction.

Electroless deposition is based on the spontaneous reduction of metals salts, in aqueous solution, by a reducing agent. To allow this process, two sets of conditions must be respected. First of all, the oxydoreduction potentials of the metal and the reducing agent must be chosen in a way that the spontaneous reaction is thermodynamically possible. This is described by the thermodynamic condition.

Secondly, the deposition must be controlled to obtain quick coating buildup on the substrate and no deposition on other surfaces nor reduction of the metal salts inside the solution. This can only be obtained by a catalytic phenomenon. This catalytic aspect is the reason why electroless deposits are often called autocatalytic. It constitutes the kinetic and catalytic condition for deposit formation.

The choice of reagents for electroless deposition must be made according to both sets of conditions. It will be discussed in the general case and for nickel deposition.

1.2.2   Thermodynamic condition.[7–10]

The thermodynamic condition can be easily deduced from the global electroless nickel deposition reaction (as written in equation 1.4).

$$Ni^{2+} + reducing\ agent \rightarrow Ni_{coating} + oxidized\ form\ of\ the\ reducing\ agent \qquad (1.4)$$
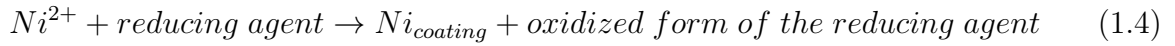
This reaction can be expressed as a combination of two partial reactions, both taking place at the substrate:

- metal salts reduction: $Me^{z+} + ze^- \rightarrow Me$

- reducing agent oxidization: $reducing\ agent \rightarrow oxidized\ reducing\ agent^{z+} + ze^-$

It is possible to obtain the oxydoreduction potential of the redox couple for each partial reaction following Nernst's law. Those potentials are expressed as functions of solute concentration and pH.

$$U_{Ni/Ni^{2+}} = U^0_{Ni/Ni^{2+}} + \frac{2.3 * RT}{2 * F} log\left[Ni^{2+}\right] \qquad (1.5)$$

$$U_{Réd/Ox} = U^0_{Réd/Ox} + \frac{2.3 * RT}{n * F} log\frac{[Ox]}{[Réd]} \qquad (1.6)$$

The knowledge of the equilibrium potential of each couple leads to an analytical expression of the thermodynamic condition: as the reaction must be spontaneous, its free energy variation ΔG must be negative (or it's affinity ($A = (-\Delta G)$) must be positive). It can be written as a function of electrochemical potential:

$$A = (-\Delta G) = n \ F \ \Delta U_{eq} \tag{1.7}$$

With

- $\Delta U_{eq} = U_{Ni/Ni^{2+}} - U_{reducing\ agent/oxidised\ reducing\ agent}$;

- $n =$ number of exchanged electrons;

- $F =$ Faraday's constant, representing the electrical energy needed for the reduction of a mole of electrons.

A spontaneous reaction can thus take place only if A is positive, meaning $U_{Ni/Ni^{2+}} > U_{reducing\ agent/oxidized\ reducing\ agent}$. Moreover, the more positive the affinity the better, so the reducing agent will be chosen to maximize the potential difference, while keeping in mind that a too big difference will lead to bath destabilization by spontaneous oxidization of the reducing agent.

1.2.3   Kinetic and catalytic condition.[7, 9–16]

The need for preferential deposition on the substrate implies that a catalytic phenomenon must take place: in its absence, there would be no guarantee that the reducing agent's oxidization would not happen spontaneously in the bulk of the solution, causing the formation of small nickel particles that can then deposit anarchically on every surface in contact with the solution.

To avoid this kind of destabilization, the solution must be (meta)stable in the absence of a suitable substrate and reaction can only be happening on the substrate's surface and after that on the previously deposited substrate. This condition is only respected if the substrate **and** the deposited metal are catalysts of for the oxidization of the reducing agent, which is the reason why this process is sometimes called 'autocatalytic'.

Those conditions can be expressed in terms of potential: when two redox couples are put together, they reach their kinetic equilibrium by a progressive equalization of their potentials. This equilibrium potential is called Mixed Potential (U_m) and can be calculated from the partial polarization curves. Those curves are obtained from electroless nickel baths without reducing agent for the cathodic polarization curve of the metal (i=f(U_{cath}/ECS)) and without metallic ions for the anodic polarization curve of the reducing agent, any other parameters and concentrations kept constant. The drawing of both curves on a single diagram allows determination of the mixed potential, where oxidization et reduction currents are equal, as is shown on figure 1.1.

If we consider that the deposition current is the current at the mixed potential, an intuitive expression of the catalytic condition is: the deposition current must be important

on the substrate and the deposited metal and must be approximatively nil everywhere else. This current is dependent on the equilibrium potential of both couples but also on the overpotential, as shown on figure 1.2. An important overpotential will displace the mixed potential towards less negative values and will generate a less important deposition current meaning smaller deposition rate while a small one will ensure a very negative mixed potential and a important deposition current.
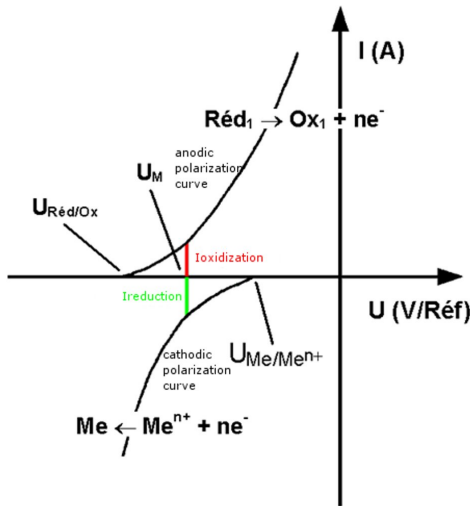
Fig. 1.1: Mixed potential determination. [7]
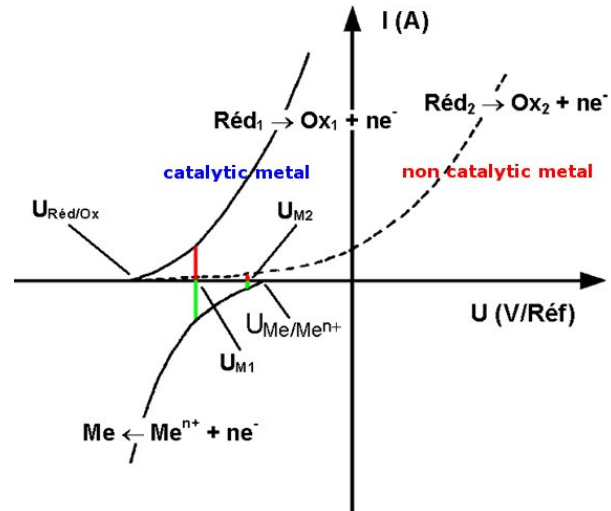
Fig. 1.2: Effect of the catalytic activity of the metal on the deposition current. [7]

1.2.3.1 Determination of the deposition rate.

The drawing of polarization curves is informative about the mixed potential but not really reliable to calculate the deposition rate. The deposition rate can nevertheless be evaluated from the polarization resistance (R_p), $R_p = \left(\frac{d\eta}{di}\right)_{\eta \to 0}$, which is the slope of the global polarization curve at the proximity of the mixed potential, as shown on figure 1.3. The polarization resistance has the dimensions of an electrical resistance and is inversely proportional to the deposition current and by this to the deposition rate by $I = \frac{K}{R_p}$. This last expression allows to assess, by the use of R_p, the variations of the deposition rate because K is constant for a given bath.

While evaluating the deposition rate by way of the polarization resistance, prudence is required because the two reactions occurring in the bath (reduction of metallic ions and oxidization of the reducing agent) are interdependent and are also influenced by local pH. Extrapolation of partial results for the determination of the deposition rate is thus not very reliable and the measurement of the polarization resistance in an operating bath is thus recommended.
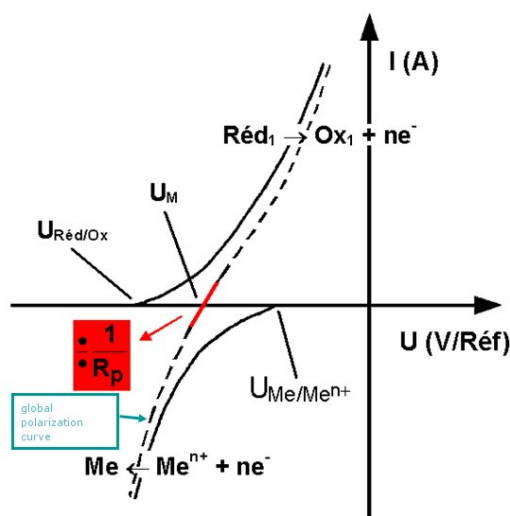
Fig. 1.3: Polarization resistance. [7]

The other way to obtain the deposition rate of an electroless process is by measurement of the deposition current. The relation between deposition rate and current is:

$$r = \frac{M * I}{96500 * n} \tag{1.8}$$

with

- r, deposition rate (g/s.cm^2)

- M, atomic mass of deposited metal (g)

- i, current density (A/cm^2)

- n, number of electrons exchanged during the reaction

1.2.4   Summary of the conditions for electroless deposition.

The two conditions for electroless deposition can be written as:

1. the global reaction must be possible and spontaneous ($U_{Ni/Ni^{2+}} > U_{Réd/Ox}$),

2. the reaction rate must be high on the substrate and nil at any other point in the bath (in solution and on any other surface put in contact with the bath).

1.2.5   Importance of the metal - reducing agent association.

The kinetic condition for electroless deposition shows how important the choice of the couple (reducing agent - metal) is: the catalytic activity of the substrate and of the deposited metal is required for the formation of a deposit. Of course, this activity is not the

same for all reducing agents, as was documented by Ohno et al. [10] for the oxidization of several reducers on various metals. This classification of metals by their catalytic activity was obtained by galvanostatic tests: the potential of each metal placed in a solution of the reducing agent under an anodic current of 10^{-4} A/cm^2 was measured. The results of this classification are shown on figure 1.4.
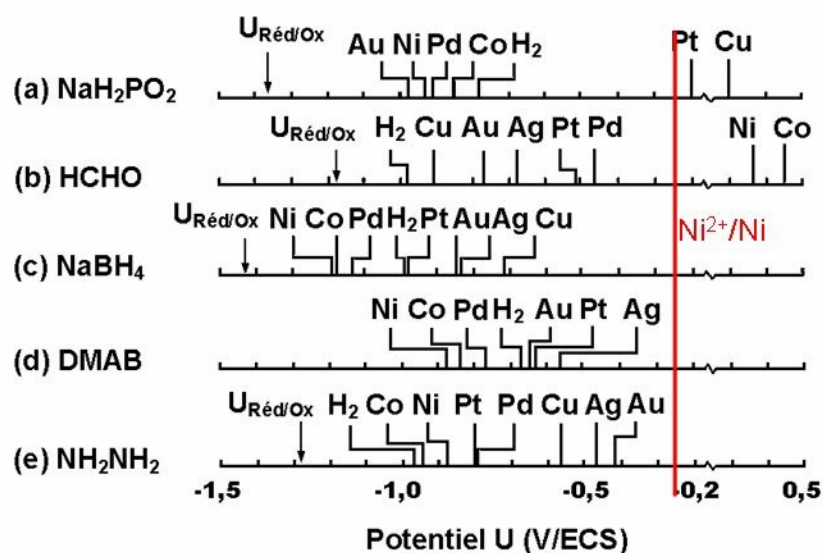
Fig. 1.4: Catalytic activity of various metals at 25℃, under an anodic current of 10^{-4} A/cm^2, for diverse reducing agents. [10]

A metal is considered as having a catalytic activity against a given reducing agent if the potential taken by this metal in the solution of reducing agent is more negative than the equilibrium potential of the metal couple ($U_{Me/Me^{n+}}$). Otherwise, the establishment of a mixed potential is impossible. For example, in the case of nickel (whose equilibrium potential is drawn in red on figure 1.4), electroless deposition is only possible using the reducing agents that have a potential on nickel drawn at the left side of the equilibrium potential of nickel, meaning all the possible agents, except formaldehyde.

This last part is only usable in the steady state, after the initiation of the deposit. For the initial reaction, the substrate is not yet covered by nickel and the nickel redox couple Ni/Ni^{2+} must be compared with the oxidization potential of the reducing agent on the substrate. This means, in the case of nickel, that it is not possible to plate copper using sodium hypophosphite without previous preparation because copper is not catalytic for the oxidization of this reducing agent. It is however possible to avoid the need for a catalytic substrate by various methods: the deposition can be initiated by putting the substrate in contact with a less noble metal, by displacement (if the substrate is less noble than nickel) or, in extreme cases, by immersing the substrate in a catalytic solution (containing for example PdCl$_2$) [2, 17–19] or by functionnalizing the surface [20].

1.2.6   Reducing agents for electroless nickel deposition.

The thermodynamical (paragraph 1.2.2) and catalytic (paragraph 1.2.3) conditions allow the determination of the reducing agent that can be used for electroless nickel deposition.

1. Sodium hypophosphite can be used to obtain a nickel-phosphorous alloy. This reducing agent is stable in a large range of pH and is used in both acid and alkaline media.

2. Hydrazine can be used to produce quasi pure nickel.

3. Two families of reducing agents can be used to obtain nickel-boron alloys:

   - Dimethylamineborane (DMAB) is stable in acid and alkaline media.
   - Sodium borohydride can only be used in strong alkaline media because it hydrolyses spontaneously in acid and neutral solutions [21, 22].

1.3   Electroless nickel baths.

Now that the theoretical principles of electroless deposition have been introduced, it is useful to take our interest to more practical aspects of the deposition process: the composition and control parameters of the electroless baths. Their study is indispensable for a good understanding and application of those processes. Without knowledge of this, the bath can be seen as a 'black box' process and the problems encountered during its use are often unsolvable, leading to important quality problems in the deposit. Moreover, when experimenting with processes like electroless deposition, which can often be tricky, a very thorough understanding of the phenomena and of the importance of each bath constituent is required to allow for process flexibility.

For this, the role of the bath components, the bath formulations and the influence of the many process parameters will be extensively presented in this section.

1.3.1   Chemistry of electroless nickel baths.

Electroless deposition baths are constituted of several chemical agents, each of whose have a critical role in the working of the bath. Firstly (in paragraph 1.3.1.1), the role of each component will be examined in a general way, without reference to any particular bath composition. The composition of the baths used for nickel-boron deposition will be examined later (in paragraph 1.3.1.2).

1.3.1.1   Role of the components of electroless nickel baths.[2, 7, 22–28]

There are lots of formulations for electroless nickel deposition baths. However, each and every of those are similar as far as the general set up is concerned: the number of reagents and their functions are similar, whatever the formulation and the baths differ only by the actual reagent used for a particular use.

In this paragraph, we will only examine the roles of the components of the bath, explain the way those components work in the bath and, when needed, give examples of reagents that can be used.

Electroless nickel deposition, in its most basic expression, can be obtained when a well-chosen reducing agent and metallic ions are mixed in liquid solution. While it is not impossible that such a composition would work, electroless baths contain other components whose role is not directly linked to the principal reaction but is nevertheless crucial for the good functionment of the deposition process.

A typical electroless deposition bath is thus composed of at least 5 components:

1. A metallic salt which is the source of the metallic ions that will be reduced to form the deposit.

2. A reducing agent which, during its oxidization, produces the electrons needed to reduce the metallic ions. The choice of a reducing agent must be made very carefully, following the principles exposed in paragraph 1.2, in order to ensure that the substrate and the metal deposited are both catalytically active for the reducing agent's oxidization.

3. A complexing agent, whose tasks in the electroless bath are multiple:

   • The complexing agent regulates the free metallic ions concentration and increases the solubility of those ions in the solution.

   • In alkaline media, the precipitation of insoluble hydroxides is avoided by the formation of stable complex with the metallic ions. The absence of any hydroxide precipitates is very important for the good operation of a bath because they can serve as heterogeneous germs for metal deposition, leading to destabilization of the bath. The use of complexants is thus unavoidable when the reducing agent imposes to work in alkaline conditions (for example: sodium borohydride, which is not stable in neutral and acid solutions).

   • The complexing agent modifies the equilibrium potential: the more stable the complex, the more negative the equilibrium potential.

   • The complexing agent has got a buffering effect on the bath.

   The effect of of the complexant in the particular case of strongly alkaline baths will be explained in paragraph 1.3.1.2.

4. The stabilizer limits the risk of uncontrolled reactions: the main reaction in electroless baths is catalytic and spontaneous reduction must be avoided **in the solution** and **on the surfaces** of the cell, precipitates and eventual impurities. Spontaneous reduction in the solution is often accompanied by the formation of a powdery deposit at the bottom of the deposition cell and is called 'plate out'.

The risk of plate out is diminished by a precise control of the bath kinetic, by blocking of a part of the catalytically active sites. This is generally obtained by the adsorption of primary stabilizers on the reactive surface and consecutive limitation of the number of active sites for the reaction. The most popular stabilizers are organic molecules (mainly sulfur-based, like thiourea) and heavy metals salts.

The use of stabilizers can have some negative side effects:

- increase of internal stress,

- increase of deposit porosity,

- decrease of corrosion resistance,

- decrease of plating rate,

- increase of deposit brightness.

To limit those side effects, the amount of stabilizer in the bath must be the smallest possible.

Deposition on surfaces and impurities is avoided by secondary stabilizers that are poisons of the homogeneous catalysis of the deposit.

5. pH regulators (and buffers) are used to maintain the bath in the optimal working conditions.

Electroless nickel bath can also contain, but not systematically, other components such as accelerating agents that prevent to some extent the decrease of plating rate caused by the complexing agents and stabilizers. In use, the baths accumulate reaction byproducts (orthophosphite HPO_3^{2-}, borate BO_2^-, ions H$^+$,...) which must be eliminated periodically in the case of replenished baths (which are the norm for industrial deposition facilities).

1.3.1.2 Bath formulations and reactions for electroless nickel-boron deposition.[2, 7, 8, 22, 24]

As we said earlier (in paragraph 1.2.6), two categories of reducing agents can be used to synthesize electroless nickel-boron deposits: borohydride compounds such as NaBH$_4$ or KBH$_4$ and amineborane compounds such as dimethylamineborane (usually cited as DMAB). According to the reducer that is used and the plating conditions, it is possible to obtain deposits containing from 1 to 8% boron. In this section, we will describe only borohydride-based bath as it the class of bath that was used in this study.

In the following sections, the reactions that take place inside the nickel-boron deposition baths are first described, then the problem of the very restrictive pH conditions needed for the good operation of those baths is discussed and finally some typical bath compositions are presented.

1.3.1.2.1 Deposition reaction in borohydride-reduced electroless nickel-boron baths.

There are two principal reactions involved in the deposition of electroless nickel-boron. The first one is the reduction of metal by the borohydride ion and the second one is the formation of metallic boron that is then codeposited. The reduction reaction is not very dependent on the metal that is reduced and is thus used to describe the deposition of nickel but also of other metals such as those used as stabilizing agents.

The reduction of nickel by sodium borohydride follows equation 1.9 [7]:

$$2Ni^{2+} + NaBH_4 + 4OH^- \rightarrow 2Ni + NaBO_2 + 2H_2O + 2H_2 \uparrow \qquad (1.9)$$

This reaction leads to the formation of a boron-based by-product, $NaBO_2$, that can accumulate in the bath during operation and may need to be removed in industrial (replenished) baths. The build up of this sodium borate can lead to several problems concerning bath operations and deposit quality that will be discussed later. The previous reaction is of course accompanied by the 'autogeneration' of metallic boron following equation 1.10:

$$2BH_4^- + 2H_2O \rightarrow 2B + 2OH^- + 5H_2 \uparrow \qquad (1.10)$$
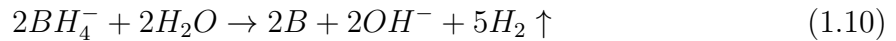
Both reactions are accompanied by hydrogen evolution that can induce hydrogen trapping in the coating if the growth rate is high. When this phenomenon is observed, a heat treatment at low temperature to facilitate hydrogen release can be beneficial for the coating's properties.

Non negligible amounts of other metals can also be deposited together with the nickel and boron due to the use of heavy metal salts as stabilizing agents in electroless baths. Those metallic ions can be reduced by boron according to equation 1.11.

$$xMe^{y+} + NaBH_4 + 4OH^- \rightarrow xMe + NaBO_2 + 2H_2O \qquad (1.11)$$
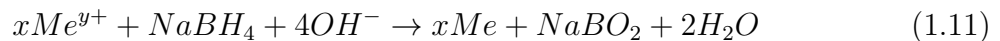
As was said before, the reaction that describes the codeposition of other metals with nickel is very similar to nickel deposition.

The spontaneous formation of nickel boride Ni_2B is also possible, as in equation 1.12

$$8BH_4^- + 4Ni^{2+} + 18H_2O \rightarrow 2Ni_2B + 6H_3BO_3 + 25H_2 \uparrow \qquad (1.12)$$
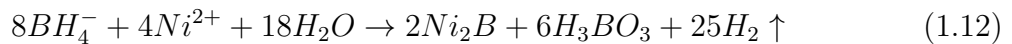
The 4 reactions that were just described are the desired reactions in electroless nickel-boron baths. However, other reactions can also take place in those baths and some of them can be very detrimental to bath operation, as shown in section 1.3.1.2.2.

1.3.1.2.2 Stability and unwanted reactions of the borohydride ion.[2, 7]

Sodium borohydride is a very unstable compound. It hydrolyzes in slightly alkaline, neutral and acidic media. This implies that borohydride-reduced baths must always operates at a very high pH (> 12). The hydrolysis reactions in various pH conditions are

described hereunder. Those reactions are very detrimental to bath operation because they use an important part of the reactive and deplete the bath. They can lead to very low (and even possibly null) reaction rate.

In slightly alkaline solution, the hydrolyze of borohydride follows equation 1.13.

$$BH_4^- + 2H_2O \rightarrow BO_2^- + 4H_2 \uparrow \qquad (1.13)$$
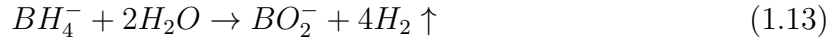
This reaction can be very detrimental to electroless deposition because the deposition reactions induce a constant reducing of the pH value, as shown in equations 1.9 and 1.11. When the pH value reaches 12, equation 1.13 becomes possible and the borohydride ceases to be active for the reduction of nickel. To avoid this, borohydride baths formulation must contain a strong alkaline compound (such as concentrated NaOH) and eventually a buffering agent. A regular or, if possible, continuous pH verification is also indispensable and alkali additions may be needed.

If the pH is lowered further, the following equations can take place in neutral (equation 1.14) and acid (equation 1.15) solutions. However, if the bath is managed carefully, the pH conditions needed for those parasitic reactions is never reached.

$$BH_4^- + 4H_2O \rightarrow B(OH)_4^- + 4H_2 \uparrow \qquad (1.14)$$

$$BH_4^- + H_3O^+ + 2H_2O \rightarrow H_3BO_3 + 4H_2O \qquad (1.15)$$
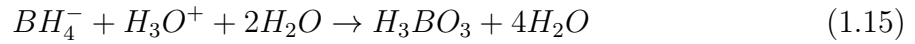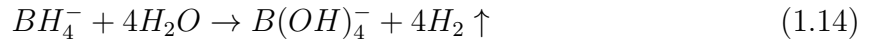
1.3.1.2.3   *Importance of the complexing agent in borohydride-based baths.[2, 7]*

As borohydride-reduced electroless deposition baths work in strongly alcaline conditions, preventive steps must be taken to avoid nickel hydroxide precipitation. This precipitation follows equation 1.16 and the solubility (K_s) of nickel hydroxide at 25℃ is $K_s = [Ni^{2+}] \times [OH^-]^2 = 10^{-16}$. As the electroless baths operate in strongly alkaline conditions (pH = 14), it is possible to simplify the K_s expression because $[OH^-]=1$.

$$Ni^{2+} + 2OH^- \rightarrow Ni(OH)_2 \qquad (1.16)$$

If a complexing agent is used, the equilibrium reaction between the free and complexed forms of the nickel ions is:

$$Me^{n+} + \text{Z Complexing agent} \leftrightarrow Me(\text{complexing agent})_z^{n+} \qquad (1.17)$$
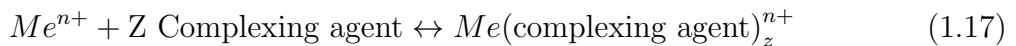
The stability of the complex increases together with the value of the complexing constant (K_c), that is expressed by equation 1.18.

$$K_{C_{\text{Ni-Complexing agent}}} = \frac{[\text{Complex}]}{[\text{Complexing agent}]^z \times [Ni^{2+}]} \qquad (1.18)$$

When a complexing agent is used, the concentration of free Ni^{2+} ions is greatly decreased and the importance of the decrease is proportional with the stability of the complex. This allows to reach free nickel ions concentrations that are lower than the threshold

for $Ni(OH)_2$ precipitation, thus avoiding the presence of particles in the bath that can serve as germs for the destabilization of the solution. Moreover, the decrease of the free ions concentration influences strongly the value of the mixed potential: as was shown in equation 1.5, the equilibrium redox potential of the Ni/Ni^{2+} couple becomes more and more negative when the free Ni^{2+} decreases, meaning a more negative mixed potential can be established.

$$U_{Ni/Ni^{2+}} = U^0_{Ni/Ni^{2+}} + \frac{2.3 * RT}{2 * F} log \left[Ni^{2+} \right] = -0.25 + \frac{0.059}{2} log \left[Ni^{2+} \right] \qquad (1.5)$$

The use of a complexing agent decreases the affinity of the reaction because it decreases the gap between the equilibrium potentials of the Ni/Ni^{2+} and the 'oxidized agent/reducing agent' couples. This is a great opportunity for bath control because a wise choice of complexing agent allows to finetune the value of the mixed potential and consequently to regulate the plating rate. However, the composition and plating operation must be optimized for each complexing agent separately.

1.3.1.2.4   Typical formulations and operating conditions for borohydride-reduced electroless nickel-boron baths.   [2, 6, 7, 22, 29]

Borohydride is the most powerfull of the reducing agents suitable for electroless nickel deposition. As we already said, sodium borohydride is not stable in neutral and acid media, so plating must be carried out at pH over 12. It is possible to reduce approximatively one mole of nickel using one mole of borohydride (0.6kg of $NaBH_4$ for 1kg of Ni). Strong complexing agents (such as ethylene diamine) are needed to avoid the precipitation of nickel hydroxide. Typical electroless nickel-boron deposition bath compositions are shown on tables 1.1, 1.2 and 1.3.

Constituents - parameters	baths			
	Bath 1	**Bath 2**	**Bath 3**	**Bath 4**
Nickel chloride, g/l	20	30	24	36
Sodium hydroxide, g/l	40	40		
Ammonia (28 % NH_3), g/l			120	132
pH	12-14	12-14	10-12	10-12
Sodium borohydride, g/l	0.67	0.6	0.4	2.2
Ethylene diamine, g/l	44	50		
Thallium sulfate, g/l		0.07		
Temperature, ℃	97	90	60	40
Plating rate, $\mu m/h$	8.8	12.5	1.3	0.7

Tab. 1.1: Typical compositions for electroless deposition baths.[30]

Constituent or condition	Aminoborane		Borohydride	
	Bath 7	Bath 8	Bath 9	Bath 10
Composition				
Nickel chloride, g/l	30	24-48		20
Nickel sulfate, g/l			50	
DMAB, g/l		3-4.8	3	
DEAB, g/l	3			
Isopropoanol, mL	50			
Sodium citrate, g/l	10			
Sodium succinate, g/l	20			
Potassium acetate, g/l		18-37		
Sodium pyrophosphate, g/l			100	
Sodium borohydride, g/l				0.4
Sodium hydroxide, g/l				90
Ethylene diamine, g/l				90
Thallium sulfate, g/l				0.4
Operating conditions				
pH	5-7	5.5	10	14
Temperature, ℃	65	70	25	95
Plating rate, $\mu m/h$	7-12	7-12		15-20

Tab. 1.2: Typical compositions for electroless deposition baths.[22]

Nickel chloride, g/l	31
Sodium hydroxide, g/l	42
Ethylene diamine (98%), g/l	52
Sodium borohydride, g/l	1.2
Thallium nitrate, g/l	0.022
pH	>13
Temperature, ℃	93-95

Tab. 1.3: Typical composition for a borohydride-reduced electroless nickel deposition bath.[29]

In most electroless nickel-boron baths, nickel is provided as chloride or sulfate and is complexed by ethylene diamine. The amount of reducing agent is generally in the range 0.4-1.2g/l but some baths operate with concentration up to 2.2g/l. The pH of all baths is over 10 and is adjusted using either sodium hydroxide or ammoniac. The operating temperature is generally high (around 95℃) but the baths with higher $NaBH_4$ concentrations are used at lower temperature (40-60℃), for very specific application were heating is prohibited and deposition rate is not the main goal (their deposition rate is close to $1\mu m/h$ instead of $10\mu m/h$ or more for high temperature baths).

The choice of stabilizing agent is what differentiates most nickel-boron baths: while thallium, in its nitrate or acetate form, is probably the most effective agent and is widely used [2, 6, 7, 22, 29, 31], its toxicity has lead to research for alternatives. Recently developed baths operate with lead compounds such as $PbWO_4$ [7, 8, 32] or $PbNO_3$ [33, 34]. In all cases, the amount of stabilizer is never higher than 0.5g/l.

1.3.2 Bath control parameters.[2, 7, 15, 22, 25, 27, 33, 35–38]

The chemistry of electroless nickel baths is far more complex than that of electrolytic baths, particularly because many precautions must be taken to avoid destabilization and uncontrolled deposition on the walls of the deposition cell.

Bath operation can be operated with good quality, stability and reproducibility only if a great number of parameters are fine tuned coordinately. The deposit growth rate is a function of those parameters and can be written as [2, 7]:

$$\text{deposition rate} = f\left(T, pH, C_{Ni^{2+}}, C_{Red}, C_{ORed}, \frac{S}{V}, K, B, n_1, n_2, \ldots\right)(\mu m/h) \quad (1.19)$$

In this expression,

- T represents the bath temperature,

- pH is of course the pH of the solution,

- $C_{Ni^{2+}}$ is the free nickel ions concentration,

- C_{Red} is the reducing agent concentration,

- C_{ORed} is the consumed reducing agent concentration. This amount is linked to the formation of byproducts,

- $\frac{S}{V}$ is the ratio between the surface of the sample and the volume of solution (i.e. bath charge),

- K is the complexing agent concentration,

- B represents the influence of accelerating agents,

- $n_1, n_2, \ldots$ represent other factors such as agitation, contamination, age of the bath, ...

We will now discuss shortly the influence of those parameters on the deposition rate and the deposit quality. This section does not intend to be an exhaustive review of the influence of the many variable parameters on bath operation but rather to be a short reminder of the most important parameters. Further information on bath operation can be found in the abundant literature dedicated to the deposition of electroless nickel-boron [7, 8, 36, 39–43] and nickel-phosphorous [2, 25–27, 35, 44–47] coatings.

1. Influence of bath temperature.

   Temperature is one of the more important control parameters for electroless baths because the heat is the only energy source for the deposition process. Moreover, the kinetics of the reactions taking place in the bath are very strongly influenced by the temperature. Consequently, there are few electroless nickel-boron baths that operate at low temperature because reaction rates are too small below 40℃ for the formation of deposits. On the other hand, most baths operate under 95℃ because the very high reaction rates obtained over this temperature induce a loss of bath stability. The effect of temperature on the reaction rate is similar whatever the bath chemistry and the reducing agent.
   This effect implies that the operating temperature is chosen wisely to provide the best possible compromise between fast deposition and stability. It also indicates that this parameter must be closely monitored and that the presence of any hot spots in the deposition unit must be avoided because even a very localized overheating can engender a plate out (destabilization) of the bath. This leads to very strict operating instructions as far as temperature control is concerned.
   The choice of the heating method for the solution must be made to avoid the formation of hot spots. An external heating such as water (or oil) bath can be a wise choice for a small unit but the use of resistive heaters is often preferred for bigger deposition tanks.

2. Influence of pH.

   As was said earlier in diverse sections, the pH of the solution is very important. When nickel ions are reduced, the pH of the solution decreases continuously (equation 1.9) and this causes generally an increase of the equilibrium potential of the reducing agent's couple, thus leading to a diminution of the potential gap between the equilibrium couples of the metal and the reducing agent, all this resulting in a reduction of the deposition rate. To avoid this, buffers are usually added to deposition baths and the bath pH is monitored and adjusted if needed.

3. Effect of the reducing agent's concentration.

   The amount of reducing agent in the bath is of course an important parameter for the deposition rate. However, the ratio between the reducing agent and the nickel ions concentration is the important parameter as there is an optimum value of this ratio for quick deposition.

4. Influence of the nickel ions and complexing agent concentrations.

   As most of the electroless processes use complexing agent, the concentration of nickel ions has a very small influence on the deposition rate: the free ions concentration is lowered by several orders of size by the addition of the complexing agent and it

stays nearly constant over the deposition process as long as the total nickel ions concentration is sufficient. As nickel is put in an important excess in electroless baths, the effects of nickel depletion are not observed because it is preceded by the depletion of the reducing agent.

The effect of the complexing agent concentration is more marked: the deposition rate usually increases when a small amount of complexing agent is added and decreases for high concentrations.

5. Influence of stabilizer concentration.

   As the stabilizer blocks a lot of the catalytically active sites, it has a tremendous influence on the deposition rate. Any other conditions kept constant, the deposition rate will decrease with an increase in the amount of stabilizer. However, if no stabilizer is used, the bath may be unstable and thus be unsuitable for deposition. This is the reason why most stabilizers are used only in minute quantities.

6. Influence of the bath charge and agitation.

   Those two parameters influence the deposition rate but their influence must be studied for each bath chemistry.

7. Influence of the bath aging.

   Bath life of electroless nickel solutions is limited, even in the case of continuous filtration and replenishment. The bath life is calculated from the number of times the nickel content of the initial bath has been consumed (MTO : Metal Turn Over). The extension of bath life is a constant preoccupation of the people that use electroless plating in industry [48]. The deposition rate of aged baths decreases strongly.

As we have seen, the parameters that influence the deposition of electroless nickel are numerous. For this reason, a very strict monitoring of the process is always needed.

1.3.3   Bath replenishment.

We have seen in the previous section that nickel is put in excess in the bath and that an industrial bath can be used for several MTO, meaning its nickel content can be replaced many times. To implement this prolongation of the bath life, a regeneration or replenishing process is needed and can take several forms, from the simple periodic addition of new reactives in the bath to a continuous bath analysis accompanied by filtration and additions.

It is not the object of the present work to study the regeneration of electroless nickel-boron deposition baths but, as we work with a bath that was developed in our department by Dr Delaunois [7, 8], we had to take some interest in the regeneration process in order to implement it for our bath.

Replenishment is indispensable for an economic (and hopefully ecologic) use of electroless deposition: the electroless deposition bath contains compounds that do not react during operation, such as the complexing agent, or that are in strong excess, such as nickel salts. The use of non-regenerated baths implies that every unreacted substance is disposed of after one use of the bath. This brings an important cost in waste treatment and in reactive replacement. Moreover, as some of the reactive present a non-negligible toxicity, bath regeneration decreases strongly the risk of toxic matter release in the environment. For those reasons, we decided to implement a very basic regeneration process for our bath, that will be described in the experimental section.

However, as regeneration is mainly an industrial concern, we won't describe it any further in the theoretical part. Pertinent information can be found in the following references [2, 45, 48–53].

2. PROPERTIES OF NICKEL-BORON DEPOSITS.

The theory and practical aspects of electroless deposition have been introduced in the previous chapter. This one is dedicated to another important aspect of those deposits: their properties.

The attributes of electroless nickel-boron deposits are of great interest in regard to their industrial applications. They are very often compared to the characteristics of nickel-phosphorous coatings as those are more widespread. As nickel-phosphorous coatings are not the object of this work, we won't include a section on their properties.

2.1 *General properties, composition and morphology of nickel-boron deposits.[2, 7, 54]*

The denomination 'electroless' puts into evidence one of the most important properties of this kind of deposits: they are synthesized without the use of an external current source. This is very important for potential applications because it means that

- they can be deposited on non-conducting substrate (the substrate doesn't have to channel the electrical power needed for their formation);

- they are exempt of edge current effects. This means that the deposit thickness is not contingent on the current repartition in the part and is thus constant on the whole substrate, even in the case of complex shapes, as is shown on figure 2.1.
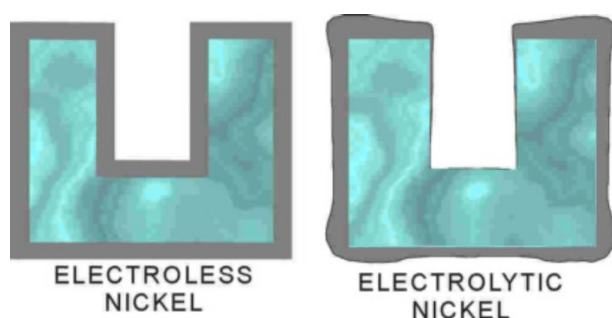
Fig. 2.1: comparison of thickness homogeneity of electroless and electrolytic deposits.

Fig. 2.2: brightness of an electroless nickel-boron deposit.

One other general characteristic of electroless nickel deposits is their bright aspect, that is shown in figure 2.2.

Those two properties are common to all electroless deposits, contrary to those that are described in this section and the next ones for electroless nickel-boron deposits.

The boron content of electroless nickel-boron deposits varies between 0,5 and 10% boron. This content depends on the bath chemistry and operating conditions.

The morphology of electroless nickel-boron deposits is very distinctive: cross-section observation reveals a columnar structure due to the deposit growth (see figure 2.3) and their surface presents a typical 'cauliflower-like' aspect that is the consequence of the growth mechanism of the coating (see figure 2.4). The morphology of the coating seems strongly related to its growth mechanism.
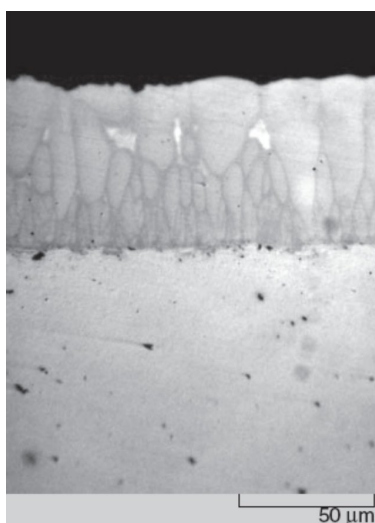
Fig. 2.3: Cross-section of a nickel-boron deposit showing the columnar structure.[55]
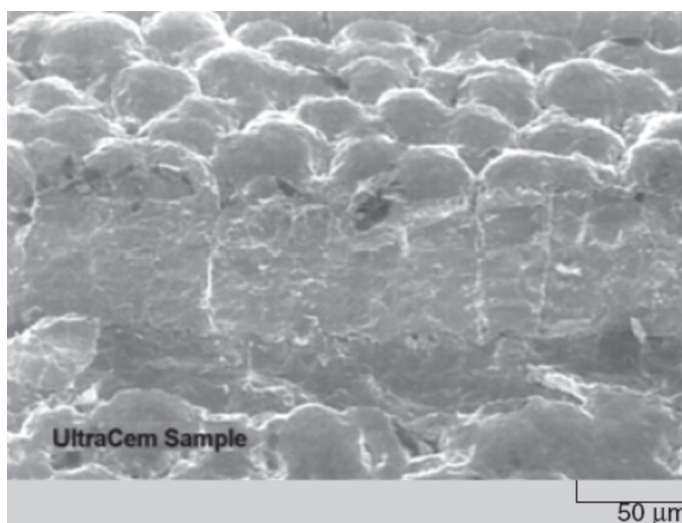
Fig. 2.4: Surface of a columnar nickel-boron deposit showing the typical 'cauliflower-like' surface texture.[55]

They are not many works dedicated to the study of the morphology and growth of electroless nickel-boron coatings but the few existing works offer many useful information.

In 1986, Clerc [54], described the structure of electroless nickel-boron coatings as constituted of several layers of columns. She observed that the number of columns in each stratum decreased with increasing distance form the substrate. This phenomenon is attributed to an important germination of the columns in the early phase of deposition that enters in concurrence with column growth in the later growth of the deposit. 3 main classes of columns were thus identified: the smaller ones, that are the first to be blocked, are never bigger than $2,5\mu m$; the second layer is constituted of columns with an average size of 5 to $6\mu m$; the third layer constitutes the rest of the deposit. She did not describe her operating conditions but the drawings of her experimental set up suggest an non agitated and non replenished bath.

Rao et al. [56] have observed the formation of electroless nickel-boron deposits in a non-replenished and non-agitated bath. While their results could not be extrapolated

to industrial baths (which operate under agitation and nearly always constant replenishment), they are pertinent in view of an experimental bath. They observed, in the first stages of their experiment, the typical columnar morphology of electroless nickel-boron deposits but this was then replaced by a nodular growth later in the experiment. According to them, this morphology is due to the formation of a thick diffusion layer near the deposits when the bath depletes in reactive species (as shown in figure 2.5). This diffusion layer would then slow the growth of the columns and induce a new germination phase leading to the nodular layer.
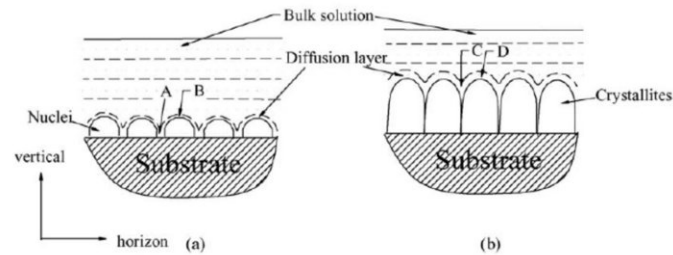
Fig. 2.5: Diffusion layer on top of nickel-boron deposit during deposition [56].

As there is so few information about the formation of the coatings and its influence on their morphology, a section of our experimental work will be dedicated to those subjects.

2.2   Structure of as-deposited nickel-boron deposits.

The structure of as-deposited nickel-boron coatings is of a very great importance for their in use properties. This structure is greatly modified by any kind of heat treatment that is applied to the nickel-boron after the deposit synthesis.
As one of the aims of this work is to describe and model the structural modifications occurring during heat treatments, an in depth knowledge of the initial state is needed. This is the reason why we will describe the structure of as-deposited coatings as in depth as possible from the knowledge of the literature.

2.2.1   The nickel-boron phase diagram and the equilibrium structure of nickel-boron alloys.

The solubility of boron in solid nickel is very low and boron and nickel can form several line compounds such as Ni_3B, Ni_2B, Ni_4B_3 and NiB [57]. As such, the nickel-boron phase diagram (shown on figure 2.6) predicts a mixture of c.f.c nickel and orthorhombic Ni_3B (with a structure similar to cementite Fe_3C) for alloys with a boron content lower than 5.8 wt.% (or 25 at.%). Between 5.8 and 8.5 wt.% of boron, the equilibrium structure is composed of Ni_3B and Ni_2B phases.

2.2.2   Structure observed by X-ray diffraction in nickel-boron deposits [2, 7, 22, 31, 33, 54–56, 58–60].

As boron has a very low solubility in solid nickel and diffusion is very difficult in the range of temperature used for electroless deposition, it is not surprising that the structure
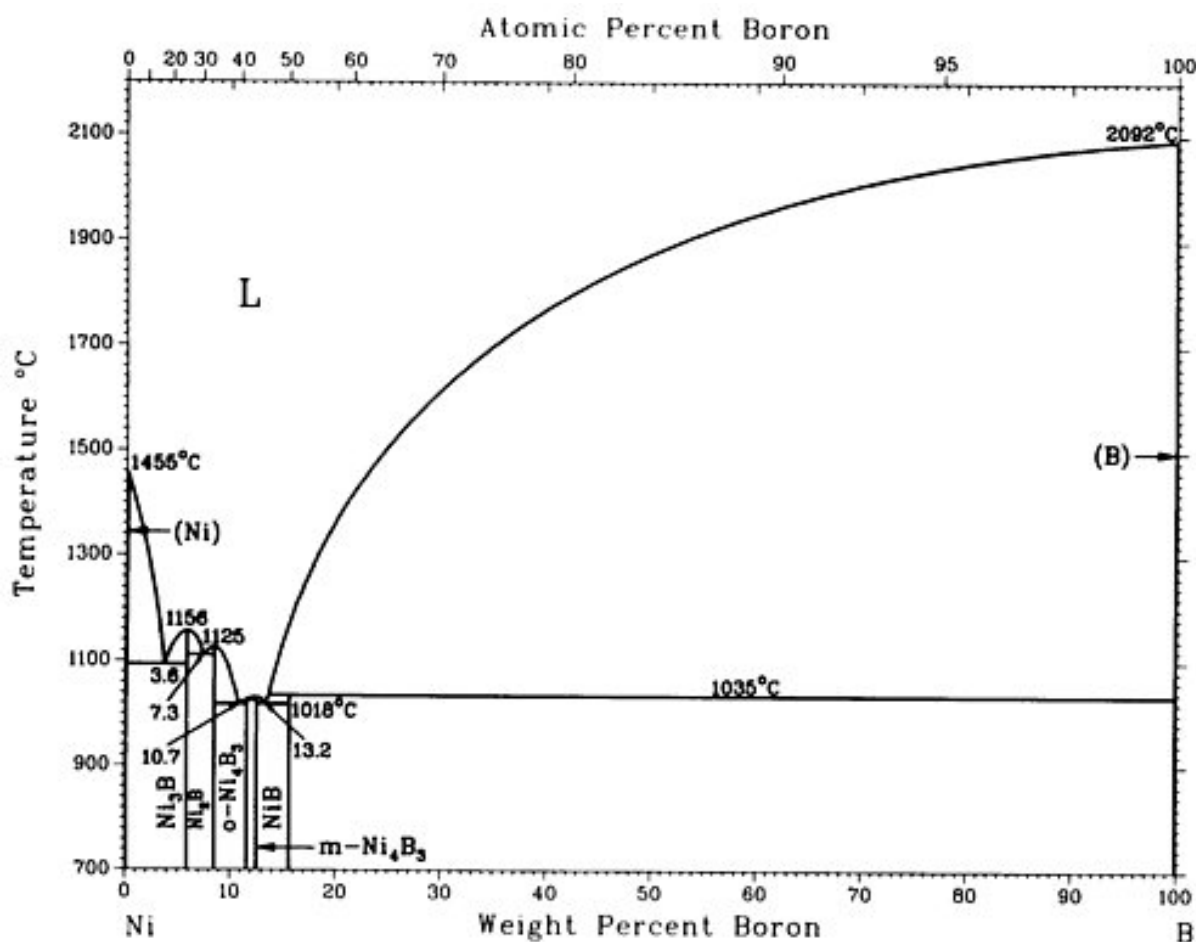
Fig. 2.6: Nickel-boron phase diagram. [57]

of nickel-boron deposits, as observed by X-ray diffraction, is different from the expected equilibrium structure.

In a macroscopic point of view, nickel-boron deposits are supersaturated solid solutions of boron in nickel. Most authors consider that the structure of the deposit is microcrystalline for the lowest boron contents and becomes progressively amorphous when the boron content increases, reaching a completely amorphous character for 5 to 6 wt% of boron. This is supported by X-ray diffraction data, as shown in figure 2.7, which present a typical X-ray diffraction pattern for an 'amorphous' electroless nickel-boron deposit.

Some researcher have discriminated the amorphous and crystalline phases in nickel-boron deposits by X-ray diffraction pattern deconvolution [60]. They have followed the amount of crystalline and amorphous phases in electroless nickel-boron deposits with variable boron content.

It is generally accepted that electroless deposits with 4 to 6 wt.% are fully amorphous. However, the amorphous character of nickel-boron deposits has been described as early as

1970 [61] and has never been questionned since in the literature. In regard of the recent discovery (in the late 1980's [62, 63]) of nanostructured (or nanocrystalline) materials, it is a real possibility that the gerenally accepted structure is not the most revelant. We will, in the next section, discuss some generalities on nanocrystalline materials and examine if it is possible to consider electroless nickel-boron coatings as materials of this type.
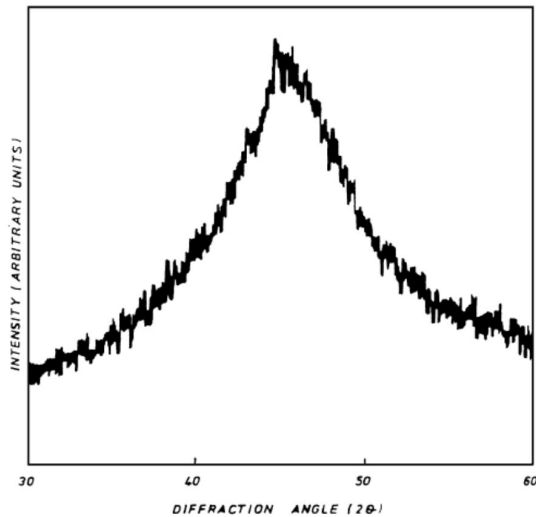
Fig. 2.7: Typical X-ray diffraction pattern for an electroless nickel-boron coating.[58]
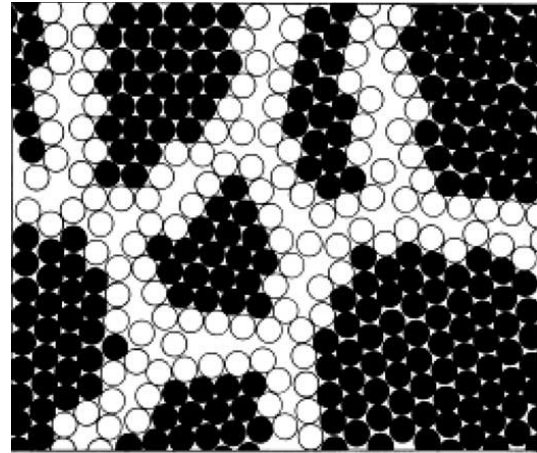
Fig. 2.8: Disposition of atoms in nanocrystalline material (black circles = atoms in crystal; open circles = atoms in boundaries) [63]

2.2.3 Notions of nanocrystalline structure and application to electroless nickel-boron deposits.[63, 64]

The concept of 'nano'-materials was introduced by gleiter [62], in the late 1980's. Nanocrystalline materials are polycrystals with grain size in the nanometer range (less than 100nm in at least one dimension). They are characterized by a large volume fraction of grain boundaries (or interfaces), which can alter their properties compared to those of 'macrocrystalline' coarse-grained materials. Assuming that grains are spherical (or cubic), it is easy to estimate the volume fraction of boundaries in the material as $3\frac{\Delta}{d}$ (where Δ is the average grain boundary (or interface) thickness and d is the average grain diameter). This volume fraction is of the order of 50% for 5nm grains, while it is only 3% for 100nm grains [64].

Nanocrystalline materials are often considered as formed of dispersed nanocrystals (with a structure similar to coarse-grained crystals) and of a continous boundary phase [65–67] that is considered as a 'frozen gas' [62] by some authors and as 'cement-like' [68] by others. The cement-like theory is derived from early (1910s) theories about grain boundary structure in coarse grained materials. Phillpot et al. think that the most important feature of grain boundaries in nanocrystalline materials is not their detailed atomic structure but the existence of heavily disordered structural inhomogeneities of more or less uniform width which act as a 'cement-like' phase holding the grains together but

they cannot affirm that this grain-boundary phase is actually amorphous[68]. A 'dilated crystal' model was also proposed [65]. The grain boundary phase has always a lower density than the crystallized phase in nanocrystalline materials. A schematic representation of the grains and grain-boundaries in nanocrystalline materials is shown on figure 2.8. Properties of nano-grain-boundaries, especially their thermodynamic properties will be discussed in more details in the model development (part III)

Keeping in mind this definition of nanocrystalline materials, one must now try to see if it can be applied to electroless nickel deposits and in particular to electroless nickel-boron, based on the published data available on those coatings.

- As early as 1983, Watanabe [59] published an extensive study of the structural properties of DMAB-reduced nickel-boron coatings, for a wide range of boron content (up to 17.1 at.%). As of today, this work stays the more extensive study of this kind. The thin sections were obtained by dissolution of the substrate. The TEM observation was thus carried out parallel to the growth direction of the coating. They concluded that films containing 5.5 at.% B were composed of

> ... the aggregation of Ni microcrystals about 10nm in size.

As their paper predates the concept of nanocrystalline materials by some years, the nanocrystalline nature of this particular nickel-boron alloy cannot be questioned.

In the same paper, they describe coatings with a boron content of 7.9 at.% B as

> ... an aggregation of many microcrystals about 3nm in size and has high elastic strain. The formation of the lattice strain implies an increase in internal strain together with a decrease in the size of Ni microcrystals. This structure shows a transitional state from the crystalline to the amorphous phase.

This description matches what one would expect of a nanocrystalline material. However, as those materials had not yet been described, the authors used the concepts in use in their time and suggested an amorphous character of the coating.

The same can be told about coatings with 17.1 at.%B (3.6 wt.%B) which are described as

> ... almost homogeneous amorphous structure. However, ... , some lattice fringes are observed. The spacing of these fringes... agrees with that of Ni 111. Hence the above results suggest that this film has area where score of atoms arranged orderly in the amorphous matrix are dispersed. However, the structure ... may mean that this plated film consists of aggregation of microcrystals with a size about 1 nm in diameter. For observations of lattice image by transmission electron microscopy only the lattice plane which is parallel or very nearly parallel to the incident beam gives lattice fringes in the photograph, but there is a possibility that the microcrystals also exist in the area from which the lattice fringes are not observed. ... it should be considered that the lattice fringes ... result from the real existence of ordered regions of atoms. For this reason the Ni-B film has a heterogeneous structure with very fine crystals about 1 nm in diameter, distributed in an amorpous structure. This heterogeneous structure was termed 'amorphous-like' ....

If one looks at this description using the newer knowledge of nanocrystalline materials, it is obvious that the material is described as nanostructured, the so-called amorphous matrix being the grain-boundaries, which constitute the greater part of the material for grain sizes under 5nm.

Most of the works on nickel-boron coatings still use nowadays the 'amorphous-like' concept introduced by Watanabe et al.

- Kumar and Nair [60], also carried out an extensive structural study of electroless nickel-boron coatings in 1984 (thus before the first paper on nanomaterials). Their work was mainly focused on the deconvolution of the X-ray diffraction profiles of nickel-boron coatings to calculate the relative intensities of the crystallized and 'amorphous' phases. When read with the knowledge of nanocrystalline materials, their work can indicate that the coatings, which they consider as amorphous, is in fact nanocrystalline.

- Recent work done on the structural characterization of electroless nickel-phosphorous by APFIM (Atom probe field-ion microscopy) and TAP (Tomographic atom probe) lead to several conclusions that are of great interest in our case. Cerezo et al.[69] measured, by atom probe techniques, the grains size and segregation of phosphorous in electroless nickel with varying phosphorous content. Table 2.1 presents the results they obtained. They obtain an unquestionable nanocrystalline structure for coatings with P content as high as 22 at.%.

The structure of electrodeposited Ni-B is slightly different but not unlike that of electroless Ni-B. It can thus be reasonably assumed that electroless Ni-B coatings

with roughly the same composition can be considered as nanocrystalline and not as amorphous as they are usually described [2, 22]. It can be useful to note that Riedel emitted doubts about the structural characterization of electroless coatings on pages 68 to 71 of his book ' Electroless nickel plating' [2].

Material	Grain size (nm)
Large grained Ni	$\succ 100$
Ni	18.3 ± 0.7
Ni-9 at.%P	13.0 ± 0.4
Ni-22 at.%P	7.3 ± 0.1

Tab. 2.1: Grain size in electrodeposited Nickel-Phosphorous alloys measured by atom probe techniques [69].

- As there is few extensive work on structural characterization of electroless NiB, we took a look at what was done in the case of electrodeposited Ni-B alloys [70, 71]. The work of Gaevskaya et al. [71] is really interesting in this regard. They recorded X-ray diffraction patterns for coatings containing up to 30 at.% B. Their results are very similar to results obtained for electroless deposits of comparable composition. They also determined the average grain size from their X-ray diffraction data. They obtained a grain size of 3.5 nm for a coating with 6 at.%B.

All the works described above indicate a strong possibility that the structure of electroless nickel boron coatings has been to some extent wrongly described as amorphous while it is in fact nanocrystalline.

The strong tendency to segregation that is common to both phosphorous and boron in traditional metallurgy [72–79] is also observed in the case of electroless or electrodeposited coatings when modern methods of investigation are used [69, 80, 81]. As this tendency to segregation is known to impede grain coarsening [82], it is not unexpected that an increase in boron or phosphorous content in the alloy should be accompanied by a sensible reduction in grain size, that can, for very high solute content, reach sizes so small that the materials are nearly amorphous.

To support this, figures 2.9 and 2.10 present X-ray diffraction patterns obtained on nanocrystalline TiO_2 and NiP. Both sets of diffraction curves are very similar and they resemble strongly the typical X-ray pattern of NiB coatings (see figure 2.7). The similarity of those X-ray diffraction data can be verified by the examen of other works focused on structural characterization of nanostructured materials [83–85].
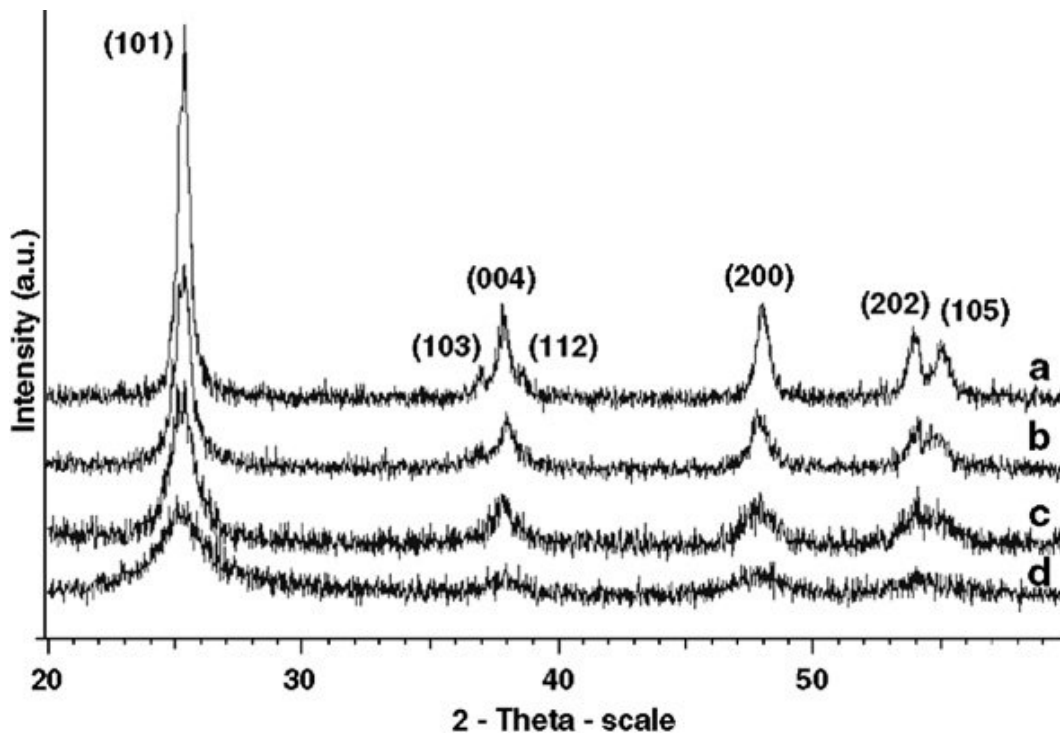
Fig. 2.9: X-ray diffraction patterns of nanocrystalline TiO_2 with an average grain size of a - 21.6 nm, b - 14.8 nm, c - 9.2 nm, d - 4.6 nm.[85]
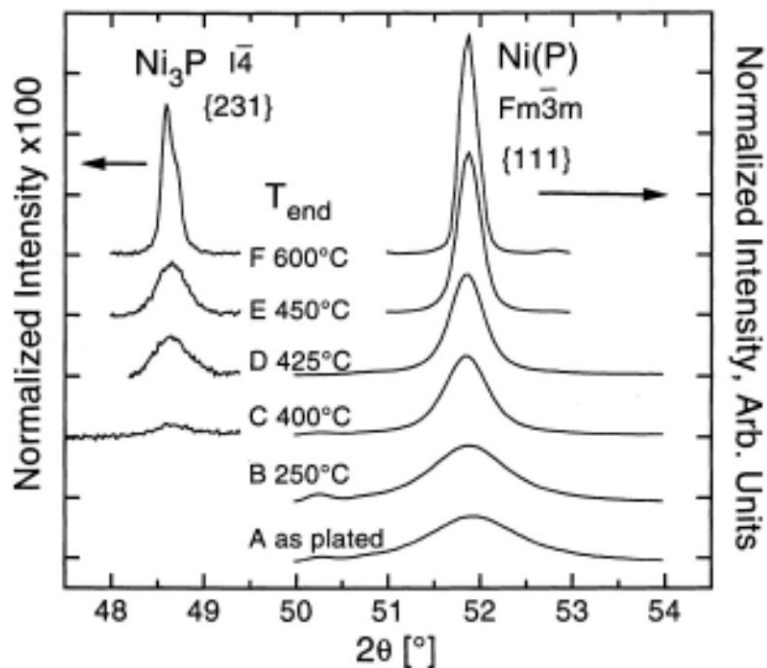
Fig. 2.10: X-ray diffraction patterns of nanocrystalline NiP (3.6%atP) with average grain size of a: 9nm, b: 11nm, c: 22nm, d: 33nm, e: 78nm.[80]

It is not possible to draw a definitive conclusion on the structural characteristics of electroless NiB coatings using only published data. For this reason, we will dedicate a section of our experimental work to the experimental observation of the structure of our coatings by transmission electron microscopy. It can be however interesting to note that even authors that consider electroless nickel coatings as amorphous state that they contain ordered nuclei (see figure 2.11) [86].
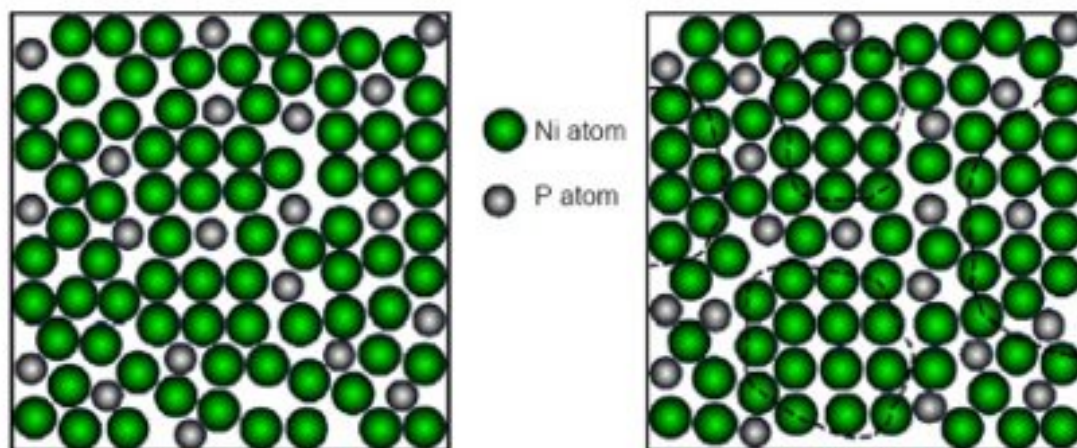
Fig. 2.11: schematic illustration of nuclei growth of NiP alloy in 2D (20 at.% P) [86].
        (left) Ordered clusters of as-deposited coating.
        (right) Crystalline nuclei in the alloy after P segregation.

2.3   Physical properties of nickel-boron deposits.

The physical properties of nickel-boron coatings, just as many of their other properties, vary with the amount of boron contained in the coating. The present section is not dedicated to a complete description of theses properties, but rather to an overview of the main tendencies in these properties.

2.3.1   Density [2, 7, 22].

The density of electroless nickel-boron deposits is always lower than the density of pure bulk nickel (8.91) and decreases when the boron content increases. It is generally accepted that deposits with 5 wt.% B have a density of 8.25.

2.3.2   Porosity [2, 55].

Electroless nickel-boron coatings can be used as protection against corrosion. As their protection is of a cathodic (barrier) type, their (lack of) porosity is very important for this kind of applications. It is possible to assess the porosity of an electroless coating by accelerated corrosion tests.

In the case of a porous coating, the substrate is not perfectly isolated from the corrosive environment by the coating and can suffer some damage due to corrosion. It is thus very important to avoid at all cost the presence of defects (and especially of transversal porosity) in electroless coatings when they are destined to corrosion applications.

While the first generations of electroless nickel-boron baths did not allow to prepare coatings with sufficient compactness, recent developments have lead to coatings that are at least as compact as electroless nickel-phosphorous coatings and present a very low pore density [55].

2.3.3 Melting point [2, 7, 24].

The melting point of electroless nickel-boron coatings follows the prediction of the Ni-B alloy phase diagram (fig 2.6). It varies between the melting temperature of pure nickel (1455℃) and the temperature of the eutectic solidification of Ni/Ni$_3$B (1093℃), meaning that the melting temperature, just like the density, decreases with an increase of boron content.

2.3.4 Electrical and magnetic properties [2, 7, 40, 87].

The presence of boron leads to an increase of resistivity of the deposits, as compared to pure nickel, which goes from $8\mu\Omega \times cm$ for pure nickel up to $90\mu\Omega \times cm$ for a deposit with 5 wt.% boron. Deposits with 1 wt. % boron have a lower resistivity (around 10 to $20\mu\Omega \times cm$) and deposits with 7 wt. % boron can reach values as high as $190\mu\Omega \times cm$.

As-deposited nickel-boron coatings are slightly ferromagnetic. Baskaran et al.[27] measured the magnetic hysteresis loop of deposits with varying boron content (fig 2.12). They observed a decrease of the saturation field with an increase of boron content of the deposits. As a matter of fact, the magnetic properties of electroless nickel-boron coatings evolve similarly to their grain size or crystallinity.
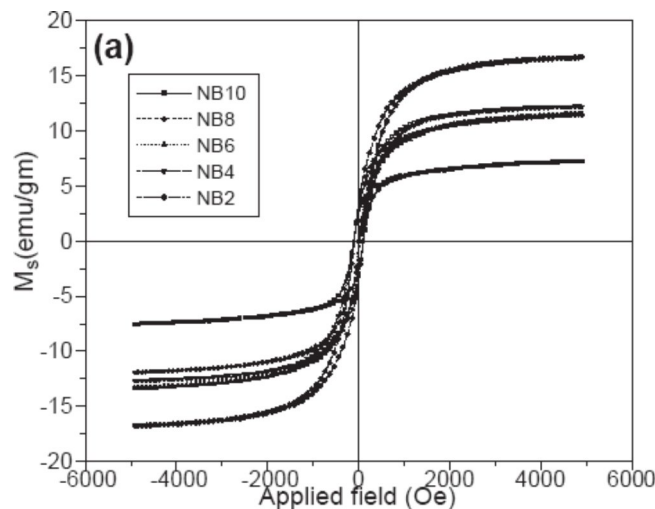
Fig. 2.12: Magnetic properties of electroless nickel-boron deposits.[40]

2.3.5 Thermal properties [2, 7, 22].

The thermal conductivity of electroless nickel-boron is influenced by their boron content and thermal history. There are few, if any, published numeric data for this property and one is limited to qualitative assessments.

The thermal expansion coefficient of Ni-5wt.% B coatings has been measured as $12.6 \mu m/m \times$ ℃, compared to $13.3 \mu m/m \times$ ℃ for pure nickel. It can be further modified by an heat treatment to reach $10.8 \ \mu m/m \times$℃.

2.3.6 Solderability [2, 7].

Electroless nickel is often used in microelectronics because of its good solderability [45, 88–92]. The solderability of electroless NiP coatings has been studied much more extensively than NiB but NiB is easily solderable and is used as a barrier against diffusion in flip chips if the boron content of the coating is low [87, 93, 94].

2.3.7 Adhesion of NiB coating on the substrate [2, 7, 22, 24, 32, 55].

The adhesion of electroless nickel-boron coatings is good on metallic substrates. It is difficult to obtain precise quantitative information on this kind of properties because of the high sensitivity of the measure to the experimental method. However, here are some results that can be used to back this affirmation: pulling out tests carried out with epoxy glue have shown that the adhesion of the electroless nickel-boron coating to the substrate was greater than the cohesive resistance of the glue (68.9 MPa).

Dr Delaunois carried out scratch tests on nickel-boron coated aluminium [7, 32] and has shown the good adhesion of those coatings.

2.4 Mechanical and tribological properties of nickel-boron deposits.

The mechanical properties of nickel-boron deposits have been of great interest for a lot of industrial applications because they are, even in the as-deposited state, quite remarkable. As a section of our experimental work is dedicated to the mechanical and tribological characterization of electroless nickel-boron coatings, we will try the describe them as clearly as possible in order to provide the reader with a comparison point for our results.

2.4.1 Internal stress[2, 7, 22].

The internal stress level of electroless nickel-boron deposits is usually very high (and higher than the stress level in electroless nickel-phosphorous deposits). Typical values for borohydride reduced coatings are 110 to 200 MPa and the internal stress level can reach 480MPa for coatings with 0.6 wt.% boron. The internal tensile stress level seems to be decreased by an increase of boron content of the coating but stays high in every case.

It has to be noted that the internal stress level is strongly dependent on the coating's thickness and is higher in thicker deposits. Other factors such as bath temperature and composition have also a significant influence on this parameter.

Hydrogen entrapment, which was an important problem of early nickel-boron deposition technologies, can also increase the internal stress level. However, recent technological development have allowed an important reduction of this phenomenon.

A too high internal stress level can lead to several problems during the use of the coating, such as premature breakdown of the part by fatigue of the substrate, loss of deposit adherence and cracks formation in the coating.

2.4.2   Hardness[2, 7, 8, 22, 24, 31, 32, 39, 42, 55, 58, 95].

The hardness of electroless nickel-boron coatings is remarkable because it reaches, in their as-deposited state, 650 to 750 hv_{100}, instead of 500 to 700 hv_{100} for electroless NiP deposits. Moreover, as we will see in section 3, well chosen heat treatments can be used to increase it to higher values still.

It is often difficult to compare hardness values obtained by different research groups because they do not use the same additives and operating conditions, and thus the effect of boron on the deposit properties is difficult to isolate. However, a recent paper by Anyk et al. [39] has studied the hardness of electroless nickel-boron coatings with variable boron content. As the results were obtained by a sole group, we can use them to describe the effect of boron on the properties. The hardness of electroless nickel-boron deposits increases from 500 hv_{100} for 5wt.% boron to nearly 800 hv_{100} for 8wt.% boron, as shown on figure 2.13.
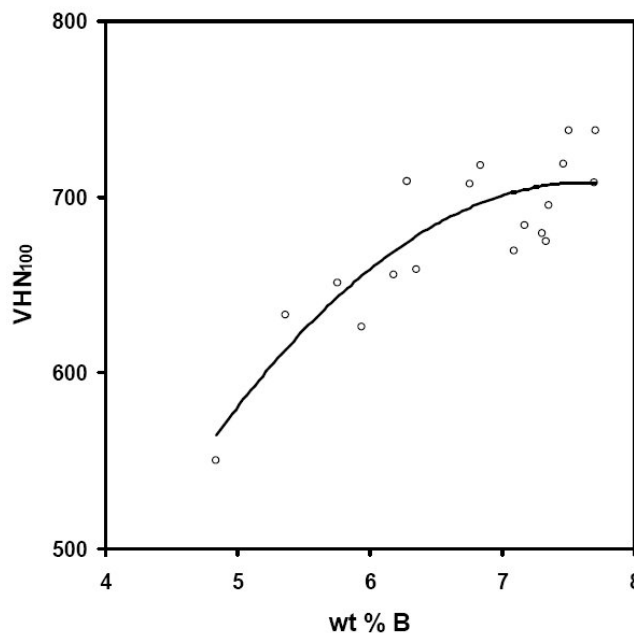
Fig. 2.13: Effect of boron content on hardness of as-deposited electroless nickel-boron.[39]

2.4.3   Young's modulus, ductility, yield strength.[2, 7, 24]

Nickel-boron coatings have a relatively low ductility and tensile strength (Rm). A deposit with 5 wt.% boron has an elongation of 0.2% and a yield strength of roughly 110MPa. The modulus of elasticity of those coatings is close to 120GPa and their final elongation is close to 0.25%.

2.4.4   Roughness [54].

The roughness of nickel-boron coatings has not been studied very much. However, in the early days of this technology, Clerc did an extensive research on this subsject [54]. The roughness of electroless nickel-boron deposits is dependent on the substrate roughness. This is due to the growth mechanism of the coating that forms columns locally perpendicular to the surface. If the substrate is smooth, the columns will be parallel and the coating will be even smoother than the substrate. However, if the substrate is rough, the columns will be arranged in a 'fan'-like disposition and the coating will be rougher than the substrate.

2.4.5   Wear resistance and friction coefficient [2, 7, 22, 24, 54, 55, 58, 95–97].

Electroless nickel-boron deposits have a low friction coefficient (fig. 2.14) when compared to other materials such as hard chrome or electroless nickel-phosphorous. The value of the friction coefficient is 0.12 in lubricated condition and 0.43 in dry sliding. This coefficient is nearly constant during the testing, as shown on figure 2.15.
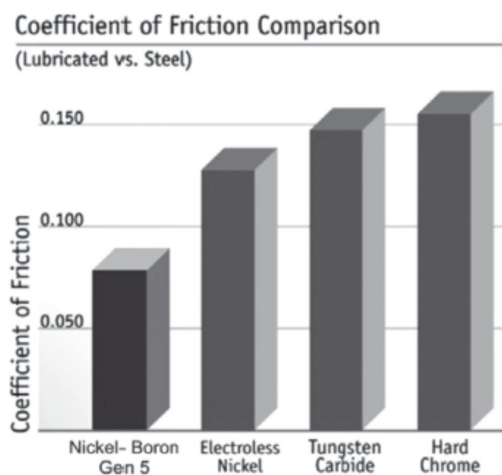
Fig. 2.14: Friction coefficient of electroless nickel-boron against steel, in lubricated conditions; comparison with other materials. [55]
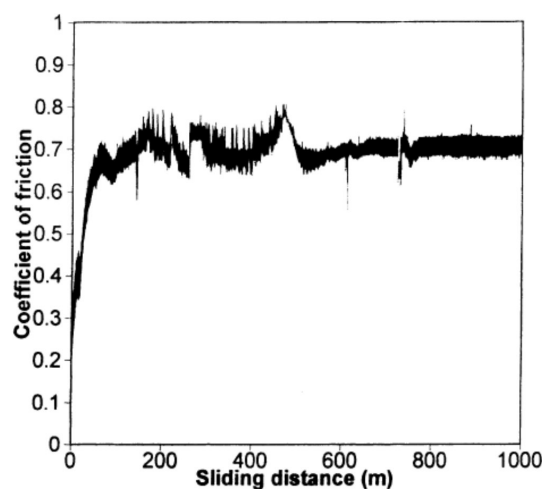
Fig. 2.15: Evolution of the friction coefficient of nickel-boron deposits during testing.[58]

Wear resistance of electroless nickel-boron coatings is better than nickel-phosphorous coatings. Wear tests carried out by Sankara et al. [96] led to wear losses of $2.45 \times 10^{-10} kg/(N \times m)$ for NiB and $4.6 \times 10^{-10} kg/(N \times m)$ for NiP. As can be seen on figure 2.16, the wear resistance of electroless nickel-boron is better than hard chromium, which is often considered as the reference coating for tribological applications. Typical value of Taber Wear Index for as-deposited electroless nickel-boron (with CS-10 wheels) is 9.
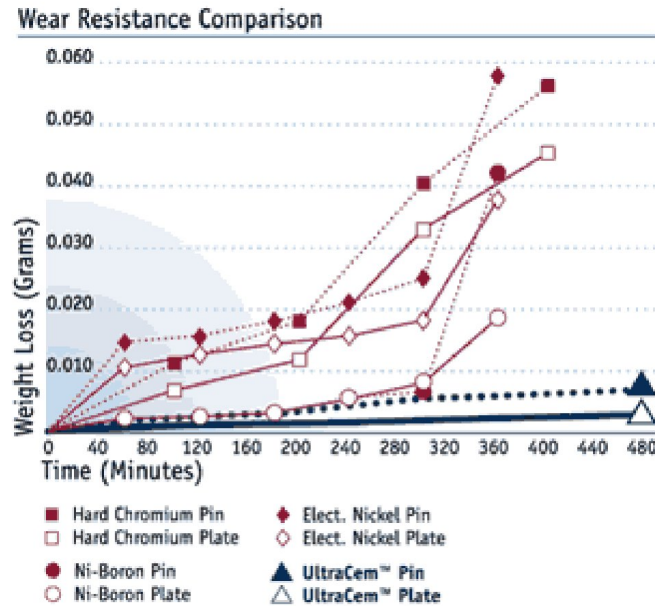
Fig. 2.16: Wear loss of electroless nickel-boron and comparison with other materials.[55]

Electroless nickel-boron deposits have good wear properties because, firstly, the boron in the deposits can act as a solid lubricant and decrease adhesive, fretting and abrasive wear, secondly, the typical 'cauliflower-like' surface texture reduces the contact area up to 70% and decreases as a result the friction between the parts, and finally, the 'cauliflower-like' texture is favourable to the retention of lubricants.

2.4.6 Fatigue resistance [22]

As electroless nickel-boron coatings have a tendency to cracking under cyclic load, they can lead to a significant decrease of the fatigue resistance of the substrate by 10 to 50%. The importance of this effect is influenced by various factors such as deposit composition, thermal history and the initial fatigue resistance of the substrate. The fatigue resistance of the susbtrate is also dependent on the deposit thickness: the thicker the deposit, the higher the decrease of the fatigue limit (fig: 2.17).
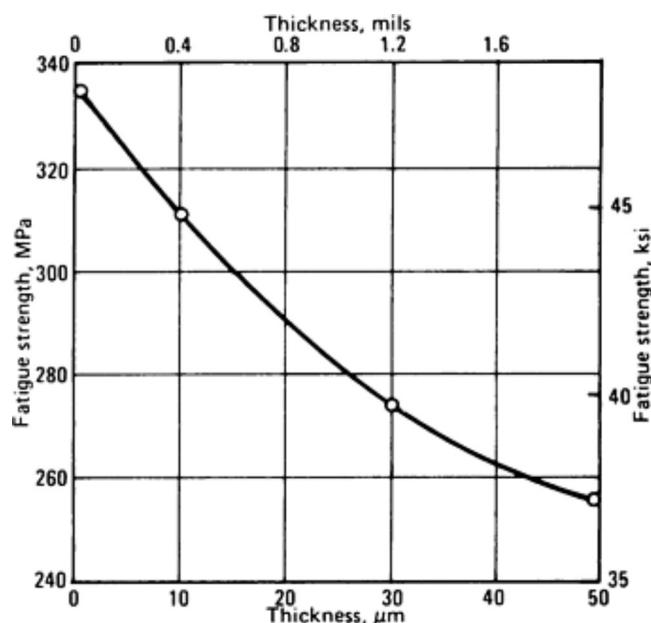
Fig. 2.17: Effect of NiB deposit thickness on the fatigue resistance of the substrate.[22]

2.5 Corrosion resistance of nickel-boron deposits.[2, 7, 22, 31, 55, 98, 99]

The corrosion resistance of electroless nickel-boron, while reputed to be less good than electroless nickel-phosphorous deposits in some media, is better than the resistance of electrolytic nickel coatings. Electroless nickel-boron coatings are used as cathodic protection, and as such, a great part of their action is linked to their ability to completely isolate the substrate from the corrosive medium.

Electroless nickel-boron coatings have an interesting resistance to non-oxidizing mineral acids, hydrofluoric acid and heavy metals. Data about the relative corrosion resistance of nickel-boron in various media can be found in Riedel's 'Electroless Nickel Plating' [2].

Tests carried out by Riddle et al. [99] proved that electroless nickel-boron coatings provided a protection against corrosion for 380 hours, and even for 1000 hours, using the ASTM B117-02 standard. The coating is left undamaged after this test, as shown on figure 2.18.

Other research groups [31, 39, 98] have recently studied the corrosion resistance of electroless nickel-boron coatings by electrochemical methods, and mainly Electrochemical Impedance Spectroscopy (EIS). They obtained single semi-circles for as-deposited coatings and a good corrosion resistance (event if it is not as good as the best electroless nickel-phorphorous coatings), as shown on figure 2.19
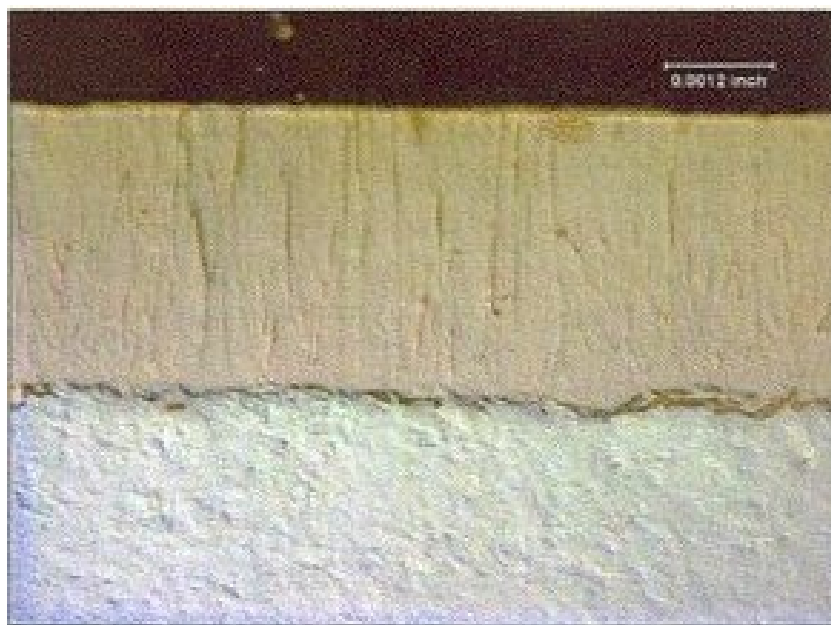
Fig. 2.18: Electroless nickel-boron coating after a 380 hours long corrosion test.[99]
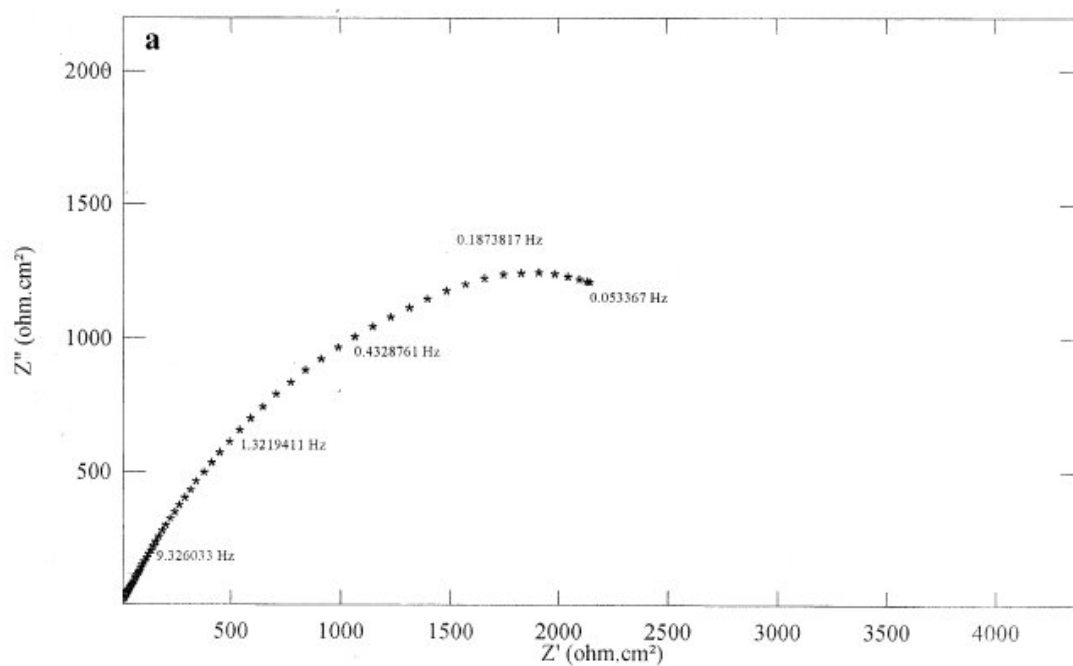
Fig. 2.19: EIS results on an as-deposited electroless nickel-boron coating.[31]

2.6   catalytic properties.

The catalytic properties of electroless deposits, and particularly of electroless nickel-boron, have been studied with great interest in recent years [100–110], mainly as a catalyst for the hydrogenation of various chemicals, such as soy bean oil, sulfolene and

p-chloronitrobenzene. It is well known that nickel possesses catalytic properties, and Raney's nickel is a very widespread catalyst. The advantages of electroless deposits for this kind of application is that they can be deposited on any support, once the surface has been sensitized to deposition. Moreover, the thickness of the coating can be easily adapted to the need of the user.

3. INFLUENCE OF HEAT TREATMENT ON THE PROPERTIES OF NICKEL-BORON DEPOSITS.

Heat treatment is often applied to electroless nickel-boron coatings because it allows the enhancement of several properties in ways that will be described hereunder. Typically, heat treatments are carried out in neutral atmosphere (argon-based) or in air, between 150 and 450 ℃, and for relatively short times (up to 10 hours).

Heat treating electroless nickel-boron deposits induces important modifications of nearly every properties of electroless nickel-boron coatings. For this reason, we will examine each group of properties and how they are modified by those treatments. The properties linked to the microscopic state of the deposits are subject to very important changes while the macroscopic properties are less influenced.

3.1 Morphology, composition and general properties of heat treated nickel-boron deposits.
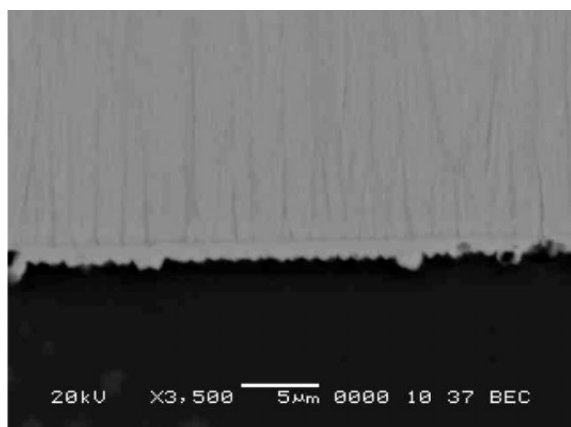
Fig. 3.1: cross section of an eletroless nickel-boron deposit after heat treatment at 180℃. [32]
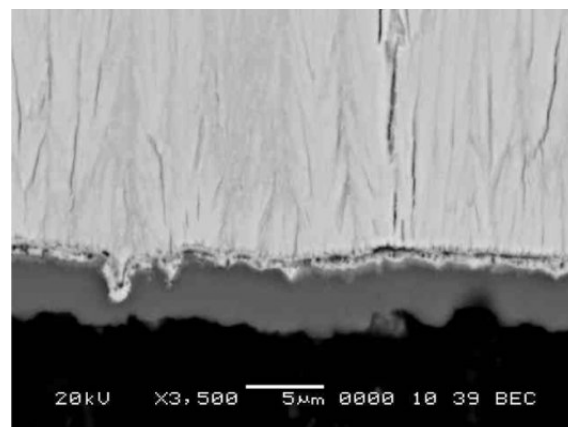
Fig. 3.2: cross section of an eletroless nickel-boron deposit after heat treatment at 450℃. [32]

The composition and general properties of electroless nickel-boron deposits are 'macroscopic' properties. As such they are not really influenced by heat treatments. The morphology of the coating stays mainly unmodified after conventional heat treatments [2, 7, 32, 34, 96] and retains its columnar aspect (fig. 3.1 and 3.2) and 'cauliflower-like' surface texture. It is nevertheless possible to modify the visible morphology by treatment

at high temperature [111]. Moreover, even in cases where the morphology was not visibly modified, important diffusion phenomena have been reported on some substrates, such as aluminium alloys [7, 32].

3.2   Structure of heat treated nickel-boron deposits[2, 7, 22, 31–33, 39, 59, 60, 98, 112–114].

Electroless nickel-boron coatings possess, in their as-deposited state, a non-equilibrium structure: the Ni-B phase diagram predicts a mixture of crystallized Ni and Ni_xB_y phases and the observed structures can be considered as either nanocrystalline monophase nickel or an amorphous phase. Consequently, any heat treatment applied to those coatings will induce important modifications and structural reorganization in the coating. Those modifications can be studied either by X-ray diffraction (post treatment or in situ) or by Differential Scanning Calorimetry (DSC).

The modification appears, on X-ray diffraction data, as either the crystallization of a previously amorphous phase or the growth of previously very small grains, according to the chosen description for the as-deposited coating. In any case, heat treated coatings appear, after a sufficient heat treatment, to be fully crystalline and their grain size, which can be obtained from the breadth of the X-ray peaks, increases with increasing treatment length and temperature.

The structural modifications become noticeable when the treatment temperature exceeds 250℃ and the use of calorimetry allows to determine the crystallization temperature of the various Ni_xB_y phases (such as Ni, Ni_2B, Ni_3B and Ni_4B_3). The phases that are observed and the temperature at which they are formed depends strongly on the boron content of the deposits: deposits with a very small boron content (less than 1 wt.%) are fully crystallized (with large nanocrystallites or even microcrystals) even in their as-deposited state because such small amounts of boron do not constitute an obstacle to the crystallization of nickel during the deposition process. Consequently, those deposits do not present any detectable structural modification during heat treament. Deposits containing 1 to 4.5 wt.% boron are not fully crystallized after deposition and the nanocrystals they contain are modified during heat treatment. In this range of composition, only the crystallization of Ni_3B is observed by DSC, between 300 and 350℃. Between, 4.5 ant 7 wt.% boron, the crystallization of Ni_3B is followed by another DSC peek, slightly over 400℃ that corresponds to the formation of Ni_2B. This is shown on figure 3.3 for an electroless deposit with 6.4wt% boron. Deposits with more than 7wt.% boron will only present the Ni_2B peak in DSC. However, some authors have detected another peak around 350℃, that is attributed to Ni_4B_3, as shown on figure 3.4.
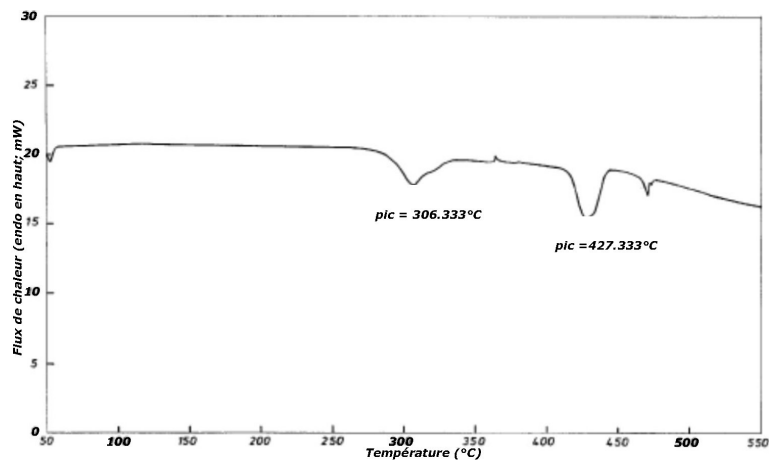
Fig. 3.3: DSC profile of an electroless nickel-boron deposit with 6.4wt.% boron [31]
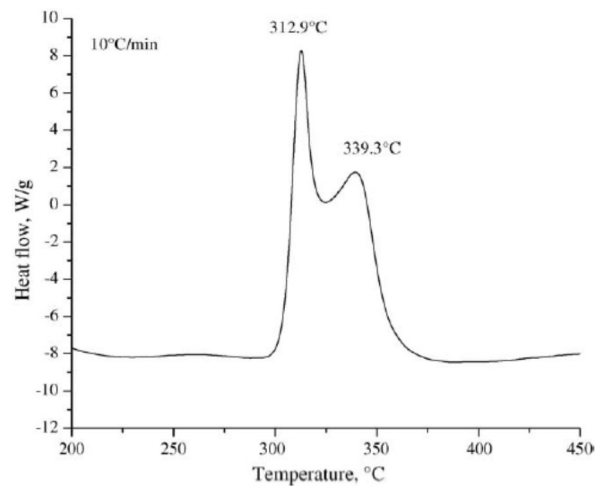
Fig. 3.4: DSC profile of an electroless nickel-boron deposit showing crystallization of the Ni_4B_3 phase.[98]
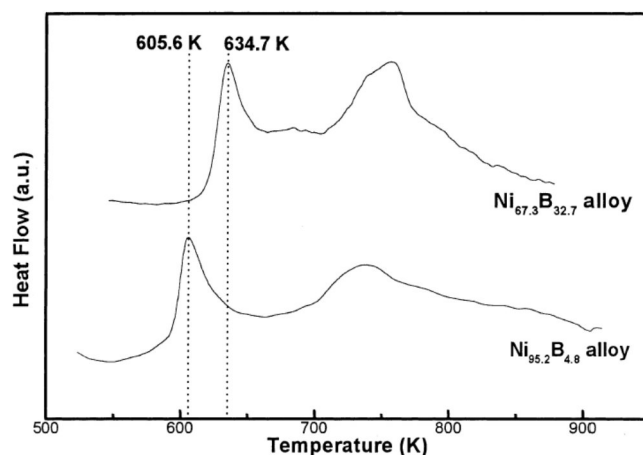
Fig. 3.5: DSC profile of an electroless nickel-boron deposit showing the change of crystallization temperature with the boron content (0.9 to 8.2 wt.%) .[112]

The crystallization temperature of the different phases is influenced by the boron content of the deposit, as is shown on figure 3.5. Moreover, the boron content influences strongly the kinetics of the nickel borides formation which is retarded in presence of a low boron content because boron must first be concentrated by diffusion[113].

After heat treatment, several phases can be found in nickel-boron coatings, depending on their boron content and thermal history, among which Ni, Ni_2B, Ni_3B and Ni_4B_3. The crystallography of the Ni_3B phase has only recently been described [115].

It is usually accepted that the crystallinity of electroless nickel-boron deposits increases with length and temperature of the heat treatment, as shown on figures 3.6 and 3.7.
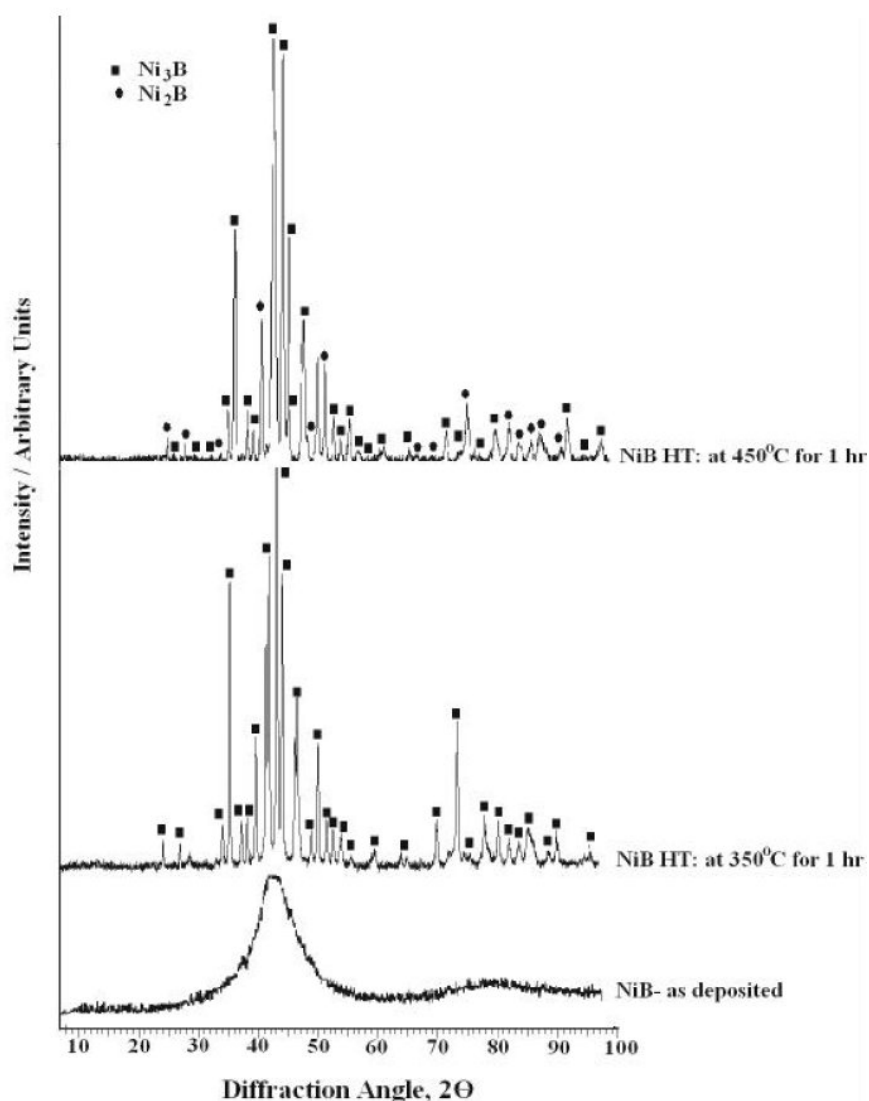
Fig. 3.6: Structural evolution of electroless nickel-boron deposits during heat treatment.[39]
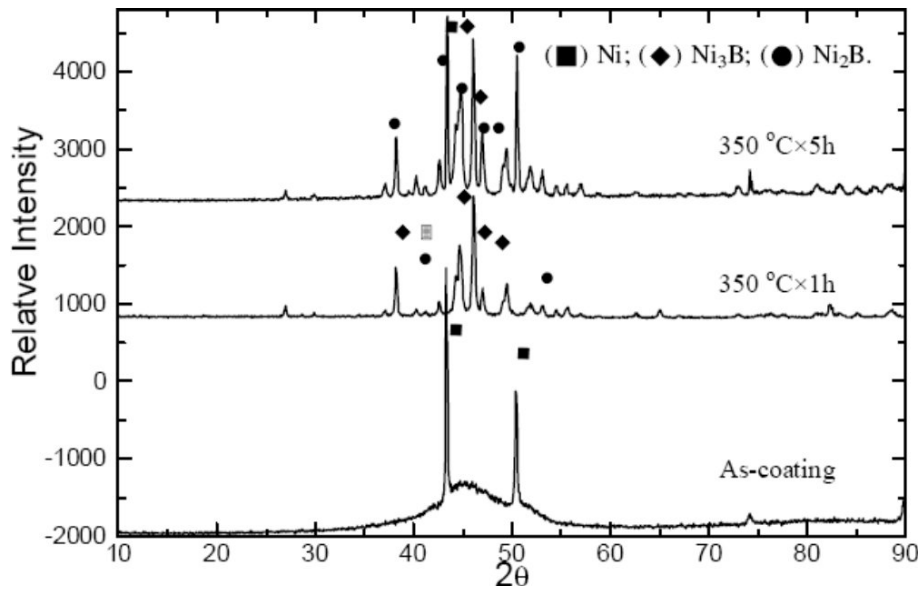
Fig. 3.7: Structural evolution of electroless nickel-boron deposits during heat treatment.[33]

3.3 Mechanical and wear properties of heat treated nickel-boron[2, 7, 22, 31–33, 39, 42, 114].

The important structural reorganization induced by heat treatment is accompanied by a modification of the mechanical properties of the coatings. Those modifications are of course strongly influenced by the temperature and length of the heat treatment: the hardness of the deposits is first improved by heat treatment up to an optimum. However for treatments longer or hotter than the optimum, a degradation of the mechanical properties is observed due to grain growth and decrease of grain-boundaries density (according to the Hall-Petch effect).
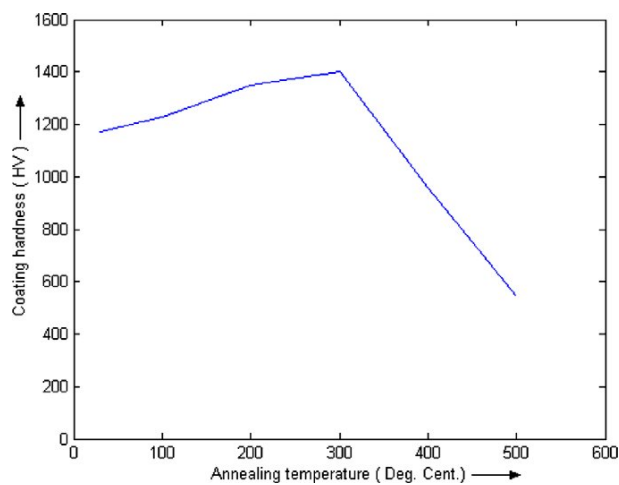
Fig. 3.8: Effect of treatment temperature on hardness of electroless nickel-boron coatings. Heat treatment length: 1 hour [42].

Several studies have been made about the optimal heat treatment for electroless nickel-boron [7, 31–33] and it is now widely accepted that a treatment of one hour at 400°C, or equivalent, allows to obtain the best mechanical properties for electroless nickel-boron, as shown on figures 3.8 and 3.9. The hardness of those deposits can reach 1200 hv_{100}.
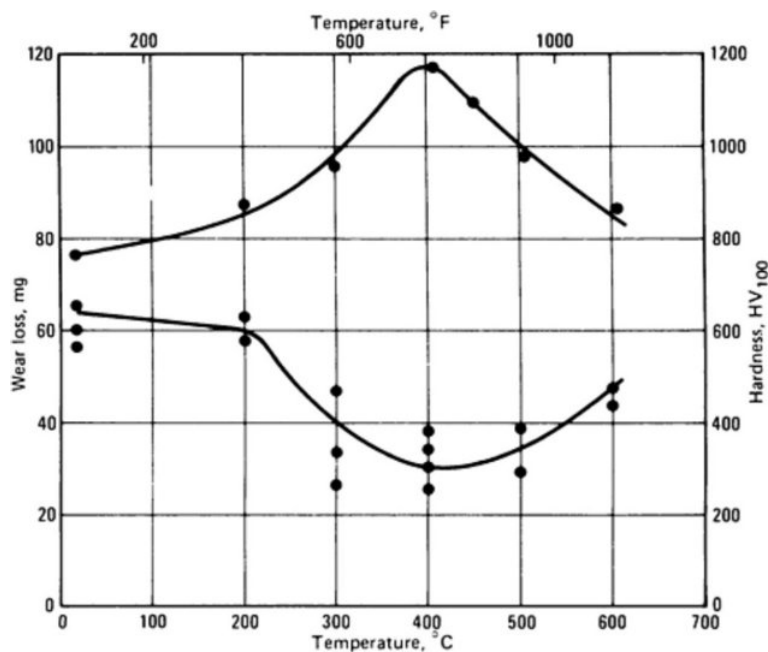
Fig. 3.9: Effect of treatment temperature on hardness and wear resistance of electroless nickel-boron coatings. Heat treatment length: 1 hour [22].

Hardness is not the only mechanical property of electroless nickel-boron coatings that is favorably influenced by heat treatment: the wear resistance of the coatings is also improved by crystallization, as shown on figure 3.9. As a matter of fact, the heat treatment conditions that give the best hardness are also those who maximize the wear resistance of the coating.

However, heat treatment is not always beneficial for electroless nickel-boron as they can lead to an increase of internal stress in the coating. As such, they are thus detrimental for the fatigue resistance of the substrate material. The evolution of the fatigue resistance of steel coated with a 5wt.% B electroless nickel coating is shown in table 3.1 during heat treatment. While they induce a loss of hardness, heat treatments at higher temperature (600 to 800 °C) suppress the fatigue sensitization of the substrate by formation of a diffusion layer at the substrate-coating interface.

Heat treatment conditions	Fatigue limit (MPa)
Nude steel	350
As-deposited coating	270
250℃, 1h	260
350℃, 1h	245
400℃, 1h	270

Tab. 3.1: Evolution of the fatigue limit of steel (0.42%C) coated with electroless nickel-5 wt.% boron during heat treatment. [22]

3.4 Corrosion resistance of heat treated nickel-boron deposits[2, 7, 22, 31, 39, 98].

The corrosion resistance of electroless nickel-boron coating is lower after a crystallization heat treatment than in the as-deposited condition, as shown on figures 3.10, 3.11 and 3.12. Most authors attribute this comportment to the structural modification of the coating: the crystallization that occurs during the heat treatment is said to be accompanied by the formation of defects and grain boundaries that are of lesser importance in as-plated coatings [31, 39, 98]. Moreover, as the heat treatment can induce cracking in some coatings, its detrimental effect on the corrosion properties is undiscussed.
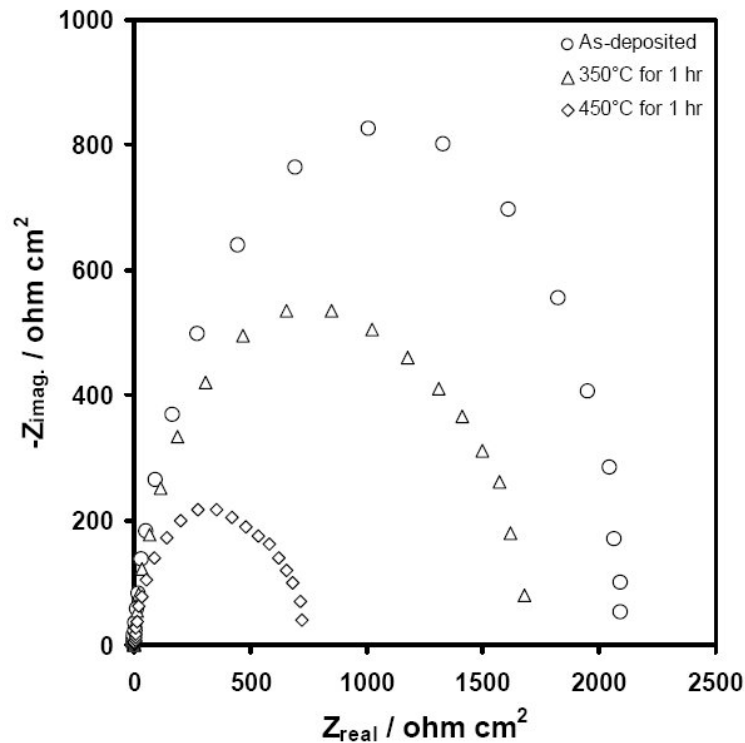
Fig. 3.10: Effect of heat treatment temperature on the EIS comportment of electroless nickel-boron coatings.[39]
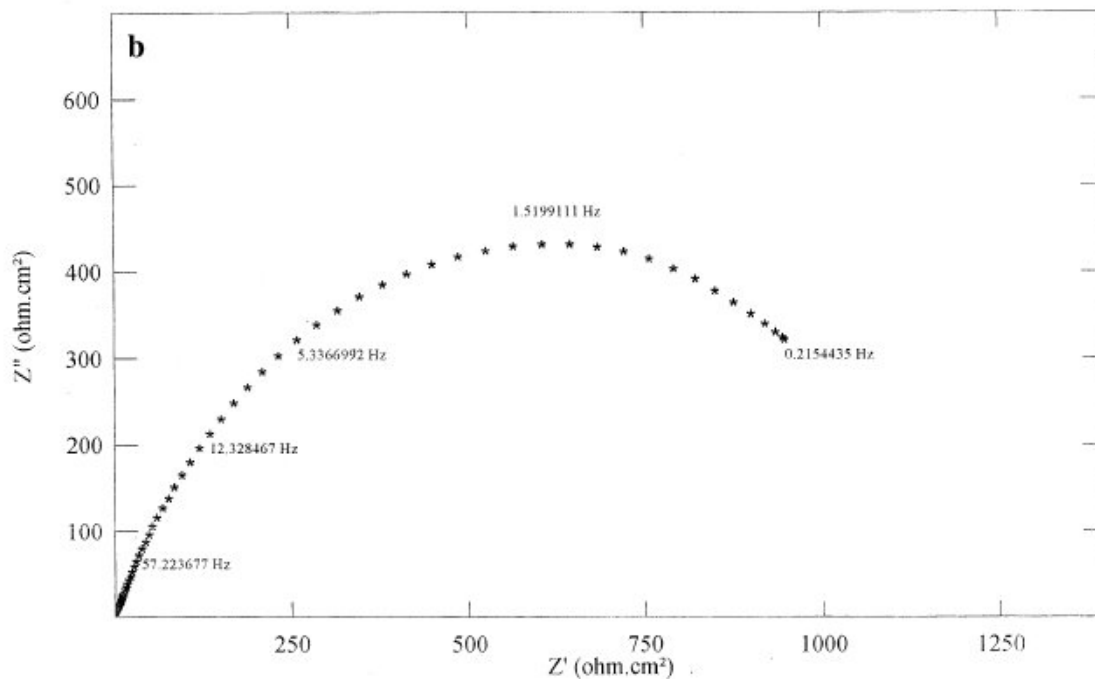
Fig. 3.11: EIS results on heat treated electroless nickel-boron coating [31]
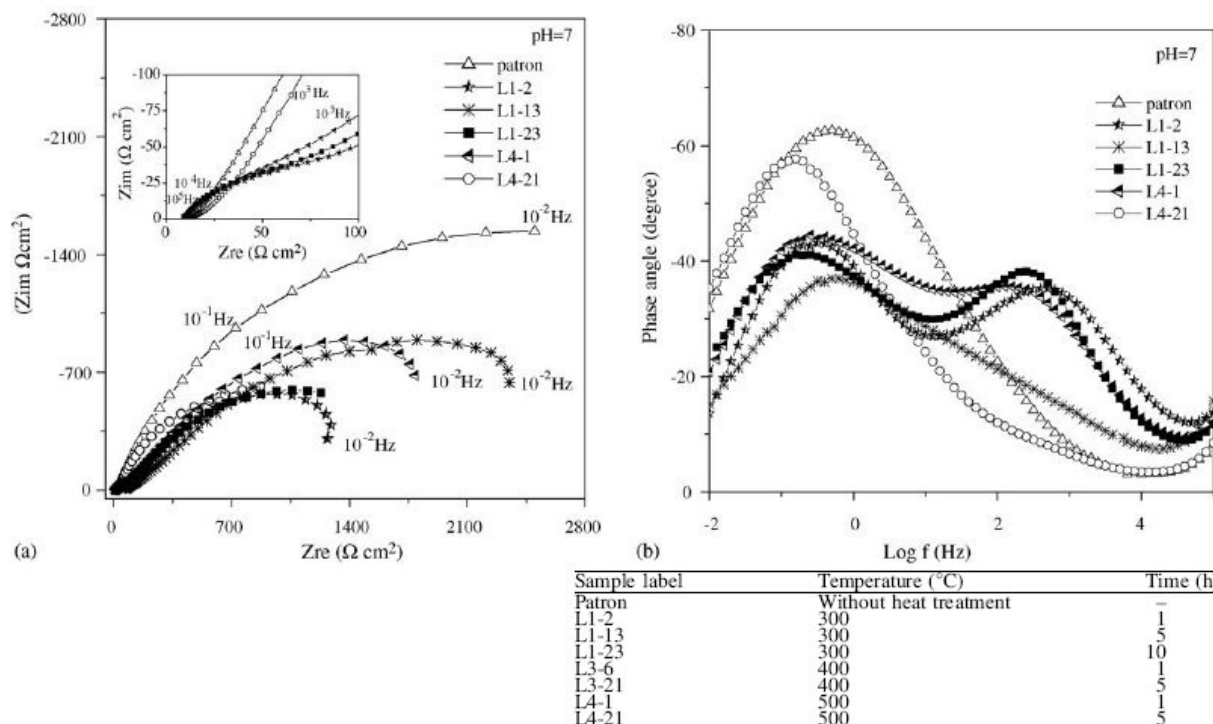
Fig. 3.12: Effect of heat treatment length and temperature on the EIS comportment of electroless nickel-boron coatings.[98].

4. APPLICATIONS OF ELECTROLESS COATINGS.

It is not our objective to provide an exhaustive review of the numerous applications of electroless nickel coatings, as they are extensive works presenting those [2, 22, 116, 117]. However, we feel that any work carried out on those coatings would be incomplete without a section, whatever short, on their practical uses as they dictate the research for better and better properties of the deposits.

In the very beginning, electroless nickel-coatings were developed as a protective coating for the transport of molten sodium hydroxide. Their good corrosion resistance ensures that they are still very much used in the chemical industry, for applications as various as compressors and valves (see figure 4.1) in the chlorine industry, transport and handling of chemicals, distillation apparatus and coolers. Electroless-nickel coatings allows the replacement of costly alloys by cheaper ones that can reach the same corrosion resistance with the coating. They are often cheaper, and just as effective as other alternative for the chemical industry such as glass or PTFE-coated steel [116].

The food industry uses also electroless nickel for various applications such as packing apparatus and molds (see figure 4.2). The meat transforming (mainly the minced meat production) and bread making industries make a great use of electroless nickel coatings to reduce the corrosion of their equipment due to exposition to sodium chloride [22, 116, 117].

Fig. 4.1: Electroless nickel coated control valve.[117]
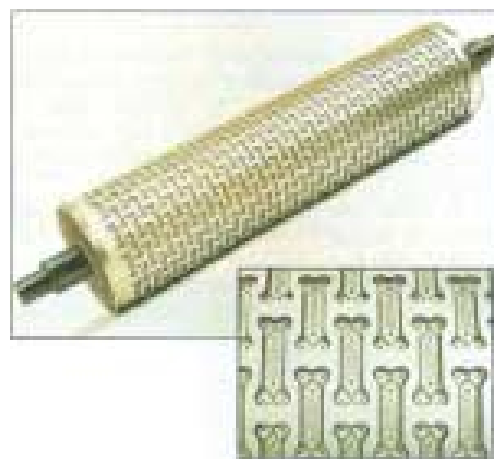
Fig. 4.2: Electroless nickel coated mold for agri-food industry.[117].

The petroleum and gas industry is also a great user of electroless nickel, which is used to coat pumps, valves and pipes because it has a good comportment to abrasion, corrosion and heat, and also to erosion corrosion [22, 46, 116]. In this industry, electroless nickel is used in all types of operation, either on surface, downhole or off shore. Ball valves (figure 4.3) and downhole drill motor rotors (figure 4.4) are usually coated with eletroless nickel .
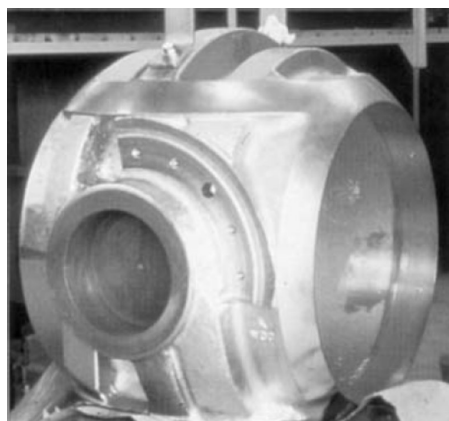
Fig. 4.3: Electroless nickel coated 105 cm ball valve plug.[116]

Fig. 4.4: Electroless nickel coated downhole drill motor rotors.[116]

In the automotive industry, the applications of electroless nickel are numerous: it is often used to enhance the performances of steel and aluminum components such as heat sinks, pistons, engine bearings, pinion gear shafts (figure 4.5), synchronizer rings, hose couplings,carburetor parts and exhaust systems [22, 99, 116–118]. Recently, the successful application of electroless to plastic portable fuel containers (figure 4.6) has been reported [119].

Fig. 4.5: Electroless nickel coated pinion gear shaft.[99]

Fig. 4.6: Electroless nickel coated portable fuel container.[119]

In the aerospace industry, electroless nickel plating is used in the refurbishing of motor parts [116, 117, 120] but also to enhance the durability of various elements such as landing gear, flap and actuators components, navigational systems (see figure 4.7), metallic optics. The defense aerospace industry uses electroless nickel for catapult covers and caps and missile guidance systems (see figure 4.8). In defense applications, electroless is used to coat firearms parts and allows the construction of lubrication-free armaments [121].
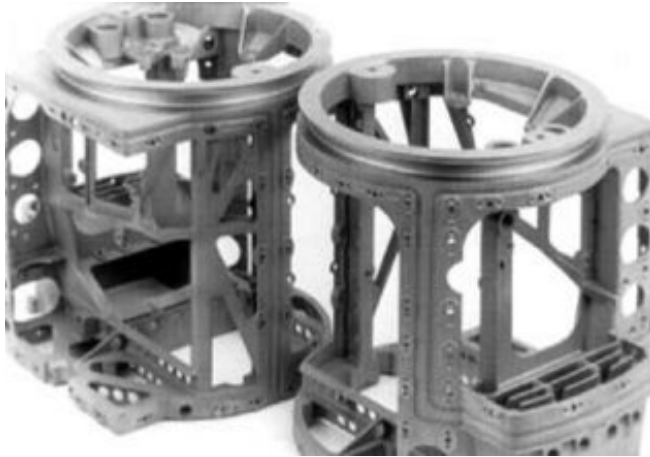
Fig. 4.7: Electroless nickel coated navigational system.[116]

Fig. 4.8: Electroless nickel coated missile directional canister.[117]

The electronics industry is also a great user of electroless nickel coatings. The most well known application in this field is hard drive manufacturing (see figure 4.9), for which electroless nickel has become a standard barrier coating to avoid interferences between opposite sides of the disk [22, 116, 117]. Printed circuit boards do also make an important use of electroless nickel [45, 87, 122] because it is solderable and constitute a good diffusion barrier. The electroless-nickel/immersion gold (ENIG) finish is a standard procedure in the electronic industry. An important part of the research about electroless nickel nowadays concerns its use in printed board applications and its comportment to soldering and reheating.

Electroless nickel is also used in sand foundry to coat the parts used to shape molds because it has a good resistance to abrasion and the resins used do not adhere to this material. In various industries using molding as a shaping process, such as the glass, ceramic and plastic industries (see figure 4.10), electroless nickel is used to protect the mold against abrasion and corrosion. In the printing industry, electroless nickel is used for the coating of printing rolls, while it is also used in the textile industry to decrease the wear of parts that are in direct contact with the textile fibers. A lot of industrial machinery, such as saw blades and chain saws are also regularly coated with electroless nickel to reduce their wear and corrosion.
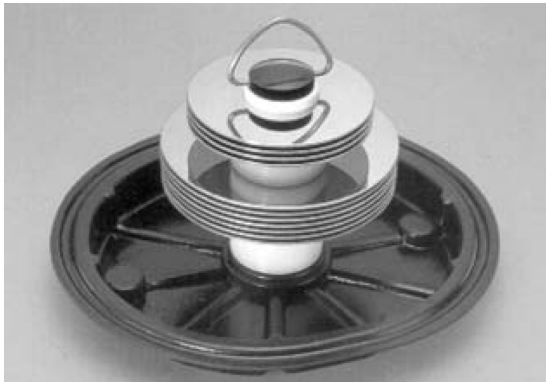
Fig. 4.9: Electroless nickel coated memory discs.[116]
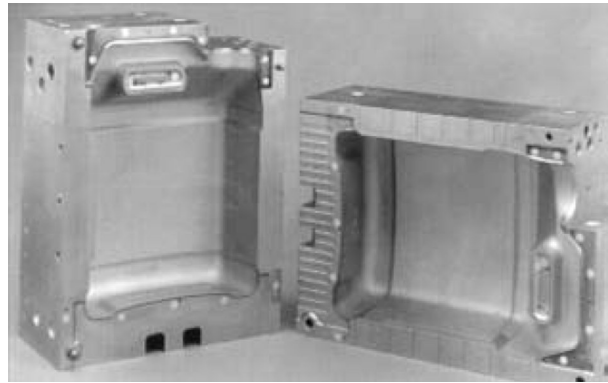
Fig. 4.10: Electroless nickel coated molds.[116]

Finally there are other, less current, applications for those coatings, such as ultra-high precision molding dies [123], ultra-high solar absorbers for optical instruments (after an appropriate blackening treatment) [124] and the reduction of friction in orthodontic wire [125]. Recent research on the catalytic activity of electroless coatings indicates future applications in catalysis and in particular for the hydrogenation reaction [100–110].

Part II

SYNTHESIS AND CHARACTERIZATION OF
NICKEL-BORON COATINGS, IMPLEMENTATION AND
EFFECT OF HEAT TREATMENTS.

INTRODUCTION.

The present part of this work is dedicated to experimental set-ups and results. It is divided in several chapters and sections, each one emphasizing one particular point of the project.

The first chapter of this part will be dedicated to the description of the experimental procedures that were used for the production of electroless nickel-boron. This chapter will be constituted of 3 main parts, corresponding respectively to the bath composition and operating conditions, the sample preparation procedures and the deposition cells. In each part, the evolutions and improvements of the set-ups and procedure will be described.

The second chapter will be alloted to the experimental work carried out to develop a semi-predictive, batch, bath replenishment. This section may look out of place in a work that uses a pre-established bath but it is not devoid of interest. First of all, because the implementation of bath regeneration, whatever rudimentary, allows the saving of important amounts of reactive and decreases the cost of waste treatment, and finally because working on bath composition and its evolution gave very useful indication about some mechanisms of the deposition process.

The third chapter will focus on a more fundamental aspect of our work, which is the description and understanding of the formation of the deposits. Surprisingly, there is very little work in the electroless nickel-boron community dedicated to the formation of the coatings and its influence on the properties. Most of the work focuses either on the development and improvement of bath chemistry and operation or on the characterization of the coatings. What happens during the immersion is nearly never discussed in the literature. However, as the deposition itself conditions all the properties of the coatings, we thought it was useful to try and see how this was happening.

The fourth and fifth chapters of this part are dedicated to more classical work about the characterization of electroless nickel-boron deposits, in their as-deposited state and after heat treatments. The aim of those chapters is to describe in the most complete way possible the coatings that we synthesized in order to compare them with other products.

5. EXPERIMENTAL SET UP AND PROCESS, BATH COMPOSITION AND OPERATION.

The experimental part of this work is completely based on a bath (and the corresponding operating conditions) that was developed by Dr Fabienne Delaunois during her PhD project [7]. However, a lot of the procedures were developed specially for this work and the experimental setting was greatly modified. The objective of this chapter is thus to describe the procedures as they were first developed by Dr Delaunois and the successive modifications we implemented to improve the quality of the samples or increase their size.

5.1 *Bath composition and operating conditions.*

The bath we use is a borohydride-based bath. As such, there are a few conditions that have to be respected for smooth operations. First of all, as we said in section 1.3.1.2.2, the borohydride ion is not stable in acidic, neutral and slightly alkaline media. This means that the pH of the bath must be very high in all circumstances to avoid destabilization. For this reason, it will contain an important amount of sodium hydroxide. The second condition is a direct consequence of the pH: to avoid the precipitation of insoluble nickel hydroxide, the nickel will be complexed in this bath.

The electroless nickel-boron deposition solution formulated by Dr Delaunois has the following composition [7]:

- 24g/l nickel chloride hexahydrate ($NiCl_2.6H_2O$)

- 39g/l sodium hydroxide (NaOH)

- 59g/l (60ml) ethylene diamine (NH_2–CH_2–CH_2–NH_2)

- 0.021g/l lead tungstate ($PbWO_4$)

- 0.482g/l sodium borohydride ($NaBH_4$)

This bath operates at 95℃, under continuous agitation. The average immersion length is 1 hour and the resulting coating is roughly $15 - 20\mu m$ thick.

As the complete formulation is quite unstable, even before being heated, the bath is constituted of 3 solutions. The first one contains the nickel chloride, sodium hydroxide, ethylene diamine and distilled water and is called the basis solution. The second one is a

solution of the stabilizer (lead tungstate) in concentrated sodium hydroxide. The last one is the reducing agent, dissolved in concentrated sodium hydroxide. The break up of the bath in 3 solutions not only allows to avoid destabilization before the use of the bath but is also really useful for the replenishment as it is possible to add the main components in a non-dependent manner.

Before deposition, the basis solution is heated up to 95℃. The stabilizer and reducing agent are then added, successively, just before the sample is immersed. Great care is taken during the addition of those reactive because their faulty dispersion could lead to serious operation problems. They are thus added under strong agitation, near the center of the cell.

The stability window of this bath is not very large: the solution is definitively destabilized when heated over 97℃ and when its pH is lowered. For this reason a very fine control of the parameters must be carried out and the temperature must always be kept within 1℃ of the consign. Hot points in the plating installation must also be avoided at all cost.

5.2   Substrate preparation procedures.

Surface preparation of the substrate is a crucial step of the electroless plating process because of its catalytic nature: if the sample is not entirely clean and free of pollution, the formation of the deposit will be difficult and can even be impossible in extreme cases. To obtain a clean, catalytically active surface, the preparation procedure must adapted to the nature of the substrate. In this section, we will discuss the procedure we applied to aluminum alloys and steel (stainless and mild).

Before any preparation, the pieces that are to be coated must be cut accordingly to the tests they will be submitted to. If necessary, holes are drilled in the parts to allow mounting on the sample-holding system.

Whatever the nature of the substrate, the surface condition is of tremendous importance for the process. All the parts are thus mechanically polished up to 4000 mesh. Depending on the shape of the part, a metallographic polisher or a hand polisher can be used. After the polishing, the chemical part of the surface preparation process is carried out. It differs for every kind of substrate.

Most of our experimental work was carried out on mild steel, as this substrate is cheap, easily machinable, can be submitted to various heat treatments without losing its mechanical properties and requires only a very simple surface preparation process. However, as this project is a follow up of Dr Delaunois' work on nickel-boron coating of aluminum alloys, some of our experiments were carried out on aluminum. For this reason, the preparation process for this kind of alloys, while fastidious, will be described hereunder along with the process we developed to prepare steel.

5.2.1   *Chemical preparation steel samples.*

The chemical preparation of steel is very straightforward, even in the case of stainless steel. We were able to develop a single procedure that allowed us to plate monophased steel alloys : extra mild steel (ST 37 grade) and austenitic stainless steel (AISI 304).

After polishing, the samples are degreased in acetone or isopropanol. They are then submitted to an activation etching in 30 vol.% hydrochoric acid, for 5 minutes, rinced in distilled water and directly immersed into the deposition bath.

In the case of stainless steel, while the procedure is perfectly identical with mild steel, the less important surface reactivity of the samples requires that the hydrochloric acid is renewed far more often. In rare cases, principally just before the acid is changed, the etching was not sufficient to activate the surface of some stainless steel samples. The deposition was thus initiated by putting the sample in contact with a less noble metal (zinc) in the solution.

5.2.2   *Chemical preparation of aluminum-based samples.*

The chemical preparation of aluminum samples is far more complicated than the preparation of steel, for diverse reasons.

First, aluminum is a very reactive metal and a protective oxide layer is spontaneously formed on this metal when exposed to air. This layer is very stable from a chemical point of view and is not at all catalytic.

Secondly, aluminum is amphoteric and dissolves in strongly alkaline media. This means that a continuous protective coating must be deposited on the sample before its immersion in the electroless nickel-boron bath. We have chosen to coat the sample with a thin coating of electroless nickel-phosphorous, using an acid bath.

After polishing, the aluminum parts are first degreased in acetone or isopropanol. They are then desoxidized with a commercial acid solution (Ridoline 124N, Henkel®). After this, they are rinsed in distilled water before being submitted to the double zincate process.

The aim of the zincate process is to replace the unreactive Al_2O_3 surface layer by a zinc-based layer that is dissolved during the deposition of the protecting layer and allows the initiation of the acid nickel-phosphorous deposition by displacement of nickel [2, 7, 126, 127]. The process is the following:

- Immersion for one minute in a commercial zincate solution (ARP 303 ZN, Mac Dermid).

- Distilled water rinse.

- Immersion for 30 seconds in 50 vol.% nitric acid.

- Distilled water rinse.

- Immersion for 30 seconds in a commercial zincate solution (ARP 303 ZN, Mac Dermid).

- Distilled water rinse.

- Immediate immersion in the electroless nickel-phosphorous bath.

All operations are carried out at room temperature.

This particular treatment is called 'double zincate' process because it involve 2 immersions in the zincate bath. It allows the growth of a continuous, extremely thin and fine grained zinc layer on the aluminum surface : the first immersion leads to the growth of an irregular layer with overlapping grains, that leads to an incomplete coverage. The dissolution of this layer by nitric acid leaves only very small residues on zinc on the surface that later serve as germ for the growth of the final zinc layer during the second immersion in the zincate bath [7]. The zincate process and its influence on the roughness and surface topography have been extensively studied by Alexis [126].

As we already said, the double zincate process does not allow the immediate immersion of the part in the alkaline nickel-boron bath. The part is thus first immersed in an acid commercial nickel-phosphorous bath (Niklad 767, Mac Dermid) for 5 minutes. This leads to the formation of a roughly $5\mu m$ thick mid-phosphorous NiP protective layer on the substrate. After this, the sample can be conserved some time before the actual electroless nickel-boron deposition.

5.3   Experimental setting.
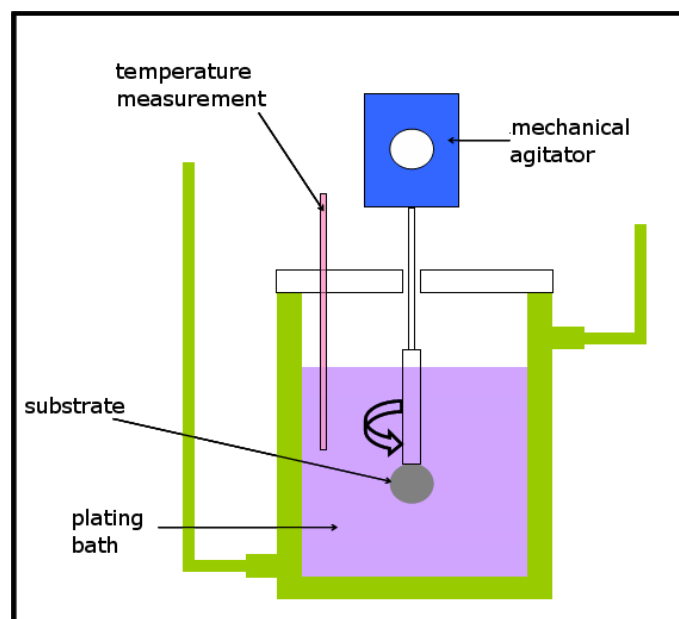
Fig. 5.1: Schematic representation of the early deposition cell [7].

The experimental setting has been greatly modified in the progress of this work, for various reasons. Our early setting was a double-walled cell, thermostatted by oil circulation. The agitation was carried out by the rotation of the sample that was mounted on a home-made mechanical agitator, as shown on figure 5.1. The capacity of this cell was 0.8 liters.

The first reason that lead to the successive modifications of the experimental set-up was the aspect of the samples: the agitation mean used on the early cell was not at all optimal and the samples presented flame-like surface effects (see figure 5.2) that were caused by inhomogeneities in the coating's structure. Those inhomogeneities, while acceptable for the development of a bath, were very detrimental to the fine characterization of the coating.

Fig. 5.2: Flame-like surface defects on electroless nickel-boron deposits synthesized in the early deposition cell.
Sample 6: best results obtained on early deposition cell.
Sample 11: results currently obtained.

Another, and very important, driving force for the changes implemented to the deposition cell, was the size of the early cell. The maximal sample size that was risk-free coated in this cell was a cylinder with a diameter of 25 mm and a thickness of roughly 10 mm. While this kind of sample is useful, it is impossible to use them for some tests, such as Taber abrasion tests or electrochemical corrosion tests, due to their small size. A bigger cell was thus needed if those characterization were to be implemented.

The third reason for the cell modification is the regeneration of the bath: in the early configuration, the implementation of bath regeneration is nearly impossible because the amount of reactive is very small which leads to important errors. In this configuration, it is necessary to use a new bath for every sample and this leads to wastage of an important amount of reactive. However, the use of greater quantities of solution reduces the importance of the measuring errors and will allow the implementation of a basic bath regeneration.

The modifications were carried out in 2 phases. The first phase began at the very beginning of the project and concerned only the agitation mechanism. The second phase, more radical, consisted of a complete replacement of the early cell by a newer, bigger one. As a long time elapsed before the final cell was operational, a very important part of the project was carried out using the old cell. As such, we think it is important to describe all set up adaptations. They will be separated in 2 sections: the agitation modification will be discussed first, then the new cell.

5.3.1 Modification of the agitation system.

In order to improve the surface state of the deposit, the agitation system was greatly modified. A 4 blades mechanical agitator was placed on the vertical axis of the deposition cell in the position used earlier for the sample holder. This blade agitator is propelled by a electrical motor with varying speed. The sample is maintained in the bath by the mean of a threaded rod fixed to the cell roof, at a distance of the cell center equal to a half of the cell radius, as shown on figure 5.3.
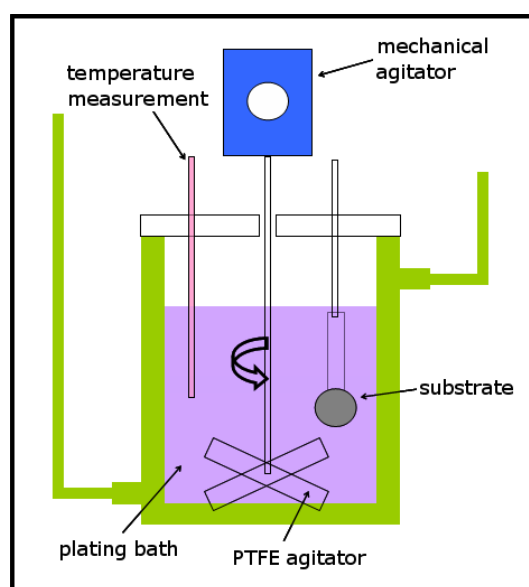
Fig. 5.3: Modified installation with new agitation mean.

The material chosen for the agitator, was PTFE. Stainless steel was used for an early test but electroless nickel deposited on the surface after 2-3 uses, which rendered the system unusable. However, this problem was less important for the PTFE agitator: the deposits that form on the surface after 5-6 uses are easy to dissolve in concentrated nitric acid without degradation of the PTFE. This allows almost infinite use of the agitator if the cleaning is done carefully after each deposit and the agitator is soaked in nitric acid every night during the deposition campaign.

The choice of the agitation mean is not the only parameter that allowed the improvement of the surface of the samples; the agitation speed and sample position were also optimized for the small cell by a trial and error method. The results of this optimization were that the agitation speed should be as low as possible (40 rpm in this case), that the sample should be positioned at an angle of 75° with the radius of the cell (see figure 5.4) and that the samples should not be left static during the experiment but should be rotated by 180° every quarter of an hour. This allowed to obtain an improved, nearly homogeneous, surface texture that is shown on figure 5.5.
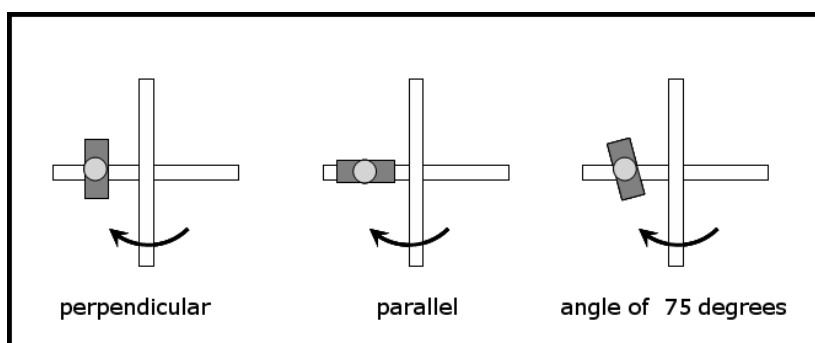
Fig. 5.4: Positions of the samples in the cell, in the new configuration.
          left: perpendicular to the radius;
          center: parallel;
          right: 75°.

Fig. 5.5: Improved surface texture of a sample synthesized in the new configuration.

5.3.2 Design and implementation of the new deposition cell.

Even with the improved agitation system, the small early cell was not able to answer all our needs for the synthesis of electroless nickel-boron samples: while the surface of our samples was far better than with the early system, their size was still limited by the small dimensions of the deposition cell. A new, bigger, one was thus put into use during the project. This cell is constituted of a PTFE-lined thermostable bath with a nominal capacity of 11 liters (see figure 5.6) and presents a lot of advantages compared to the older one:

- it is auto-regulated (the temperature regulation of the early heater was based on the measure of the temperature of the oil that circulated in the double-lined vessel),

- it warms quicker (the solution needed to be pre-heated in an external vessel in the early configuration),

- the temperature of the bath is more homogeneous,

- the PTFE lining is less susceptible to electroless nickel deposition than the surface of the old glass vessel,

- the increased volume allows to place more control means (thermometers, ...) in the bath.
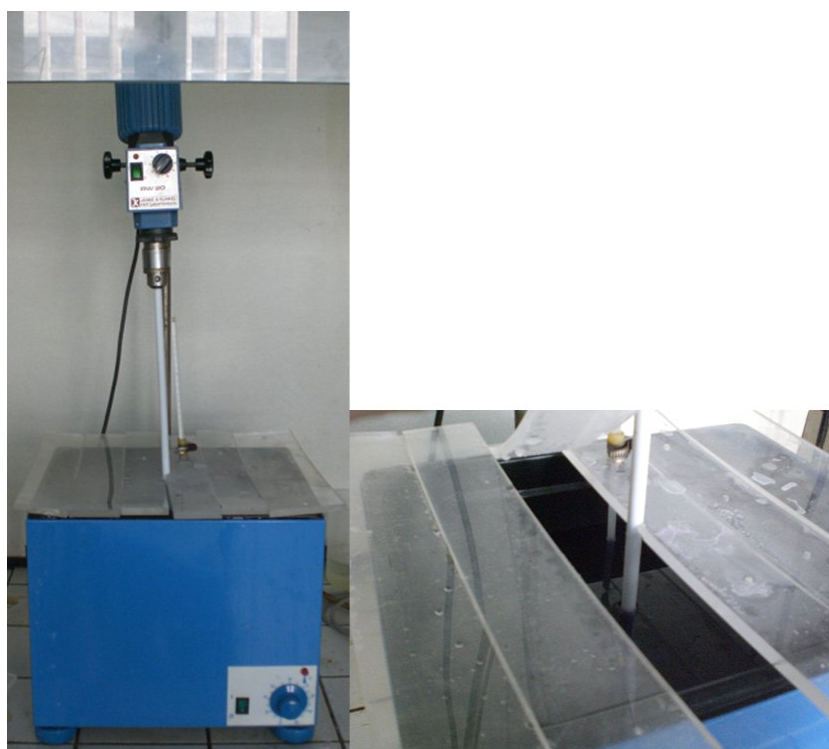
Fig. 5.6: New installation, with agitator and modular cover.

The cell was initially coverless. However, as the work temperature is very high, the loss of solution by evaporation was detrimental to the good working of the deposition. The cover designed for this cell is a modular Plexiglas cover. It is constituted of 6 sections; two of them are designed to hold the agitator and control thermometers, the others are designed to hold 1 sample each and can be replaced by unperforated sections during the heating and cooling phases.

As the agitation developed for the small cell was satisfactory, it was kept mostly unmodified: the PTFE agitator was placed in the center of the cell, but the agitation speed was slightly modified and was fixed at 60 rpm after optimization trials. The new cell being exempt of cylindrical symmetry, the flow is very different from the older one and it has been needed to adjust the orientation and movement of the samples. The samples placement is as follow: one or two samples are hanged from the cover on each side of the agitator. The samples are parallel to the small side of the cell and are not displaced during the coating experiment (see figure 5.7). The surface state obtained in this configuration is as good as with the optimized small system.
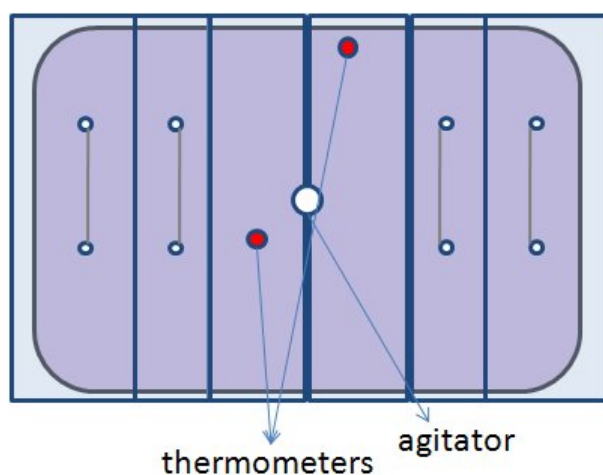
Fig. 5.7: Disposition of the samples in the new installation.

6. REACTIVE CONSUMPTION DURING BATH OPERATION AND BATH REPLENISHMENT.

As we said before, bath replenishment, while out of the main focus of this work, is a much needed step for any work on electroless nickel, because it allows to cut the cost and loss of reactive and to speed the synthesis by avoiding the heating of a new bath before each deposition process. It is impossible to implement a replenishment process, whatever primitive, without adequate knowledge of the evolution of reactive consumption during plating. For this reason, an important part of the present chapter will be dedicated to the study of reactive consumption.

This study was lead in 4 phases. The first, preliminary phase, was carried out with the small deposition cell and aimed to select adequate methods to follow the concentration of reactive. A second preliminary phase, carried simultaneously with the first one, allowed to observe the major trends of the evolution of reactive concentration. The third step consisted of a more detailed study of the reactive consumption, carried out on the bigger cell and aimed to get a more precise idea of the reactive consumption. The fourth and last step was the actual implementation of the replenishment.

6.1 Selection of the analytical methods for the measure of reactive concentration in the bath.

Several analytical techniques were tested to study the concentration of reactive of the bath, depending on the element to be analyzed. First, some simple methods were used to measure the concentration of reactive in a new bath and their efficiency was evaluated. In a second phase, other ones were implemented to supplement the inaccuracies of some of the first ones.

6.1.1 Analysis of nickel concentration.

Three different methods were used for the titration of nickel in the solution: atomic absorption spectroscopy (AAS), ICP-AES (inductively coupled plasma - atomic emission spectrometry) and a gravimetric method based on the formation of an insoluble complex of nickel with dimethylglyoxime (see section **??** for a detailed description of this method.).

All three of those methods present various advantages and disadvantages:

- Atomic absorption is a rapid and flexible method. However, it is usually used for very diluted solutions (1 to 100 ppm), which is not the case for the titration of nickel in the electroless nickel-boron bath. The solution must thus be diluted a great number of times before being analyzed and those dilutions bring errors into the measures.

- ICP-AES, while it usually allows to measure the concentration of several elements in one run and thus to shorten the analysis time, could not be used in this way in our case because of the great difference in the reactive concentrations. Moreover, the ICP-AES apparatus is less flexible than the AAS and its operating cost is higher.

- The gravimetric method is time consuming because of the numerous steps and cooling times it needs. Moreover, for this method to be really precise, the dexterity of the operator is critical as there is a lot of sampling and dilution implied.

At first, the gravimetric method appeared to be the most effective because it can be used on an undiluted solution. However, the length and complexity of the manipulation were a obstacle to the implementation of a rapid regeneration process. For this reason, a great effort was made for the dilutions needed before AAS and this method was chosen for the measure of the nickel content of the bath.

The results obtained for the analysis of a new bath by this method are :

- Nominal concentration : 5.93 g of nickel by liter,

- Mean concentration : 5.843 g of nickel by liter,

- Confidence interval (95%) $5.76 g/l < [Ni^{2+}] < 5.94 g/l$.

Those results are well into the accepted range, knowing the nickel solution is synthesized in a 5l beaker, which implies a non negligible error on the solution volume and thus on the concentration.

6.1.2   Analysis of borohydride concentration.

ICP-AES (inductively coupled plasma - atomic emission spectrometry) was first used for the measure of the boron concentration in the electroless bath, together with a colorimetric method (see section ??). However, those techniques are not really adapted to this testing because they measure the concentration of elemental boron which is not necessarily the same as the borohydride concentration. Indeed, during the deposition process some of the borohydride is oxydized in $NaBO_2$ and other compounds that accumulate in the bath and elemental analysis techniques cannot differentiate those compounds from borohydride. The results obtained with those 2 techniques are thus not really reliable for used baths.

There is however an analysis method that allows to measure only the boron in its borohydride form: the iodometric titration described in section **??** is based on the reaction of borohydride with iodine (equation 6.1), which is selective with the oxidation state of boron.

$$4\,I_2 \; + \; NaBH_4 \; + 10\,OH^- \; \rightarrow \; 8\,I^- \; + BO_3^{3-} \; + \; 7\,H_2O \; + \; Na^+ \qquad (6.1)$$
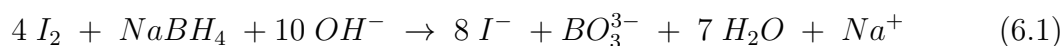
This method, while not as quick as AAS, takes less than half an hour of manipulation and the results that are obtained are quite good: analysis of a new bath leads to a borohydride concentration of 0.568 g/l against a nominal concentration of 0.602 g/l, which means an error of around 5%. This iodometric method is thus chosen for the systematic investigation of the borohydride concentration in used baths.

6.1.3   Analysis of lead concentration.

The range of analytical techniques applicable for the measure of the lead concentration is less wide than for the other elements because of the far lower concentration of lead in the bath (the lead concentration is in the ppm range). AAS and ICA-AES are the only techniques fit for this range of concentration. As in the case of nickel, AAS is preferred because it is more flexible.

Measures carried out on a new bath lead to calculated concentrations ranging from 8.86 up to 10.48 mg/l instead of 9.56 mg/l, meaning an error of less than 10%.

6.1.4   Analysis of carbon concentration.

The carbon concentration of the bath was not included in the first stages of the consumption study. However, in the course of the experiment, some questions were raised about the comportment of ethylenediamine during the deposition process: did this component decompose due to the heat and thus did it need to be replaced regularly? Or was it left unmodified during the deposition process thus building up every time some was added?

Ethylenediamine being the only carbon-based component of the bath, the measure of the total carbon concentration of the bath was used to study its comportment in the bath. This method is based on the calcination of a known amount of solution and measure of the quantity of emitted CO_2 and is usually used in water and effluent analysis.

6.1.5   Evolution of bath pH.

The pH of the bath was evaluated using indicator papers, as this method is by far the simpler to implement and is reliable.

6.2   Preliminary study of reactive consumption in the small cell (volume : 800 ml).

The aim of this preliminary study was to evaluate the evolution of the concentration of the various reactive in the bath during the synthesis of a deposit. The objective was not to obtain precise data but to observe the main trends of the reactive consumption, and thus to be able to plan the experiment in the best way possible for the study in the 8 liters cell. In this preliminary study, only the concentration of the 3 most important reactive (nickel, borohydride and lead) were studied.

This study was carried out on baths that were used for the coating of a sample with a surface close to 20 cm^2, which means that the bath load is in the order of 25 cm^2 per liter. For this preliminary study, the samples were immersed in the bath for a predetermined time, then the bath was left to cool down before sampling. This methodology was used because the amount of solution needed for the bath analysis (50 ml) represents more than 6% of the total bath volume and its withdrawal modifies sensibly the bath which then becomes unusable for further analysis.

6.2.1   Nickel consumption.

The preliminary study of nickel consumption was carried out mainly by ICP-AES and AAS. The results that were obtained before and after the use of the bath where unreproducible and some anomalies were detected, such as an apparent increase of nickel concentration. Those problems were studied in detail and several conclusions were drawn from them:

- A sensible part of the anomalies can be explained by dilution errors. A greater emphasis was put on experimental precision and the results obtained after this were better.

- An observation of the solution level in the cell showed that the evaporation was important. Moreover, this effect varies from sample to sample and brings thus a non-reproducible factor in the experiment.

- The apparent increase in nickel concentration observed in certain cases is directly linked to the solution evaporation. This evaporation happens mostly during the pre-heating of the solution and the placement of the sample (when the cover is not placed on the cell) but there is also a non negligible evaporation through holes of the cover (around the sample, thermometer and agitator).

- The analysis of nickel consumption realized on the 800 ml cell cannot be used in either a quantitative or qualitative way and the other results obtained on this cell must be used with the utmost prudence.

While those results could not be used, the experiment was not wasted because it put an emphasis on some important points for the implementation of the study on the bigger cell:

- The evaporation of the solution must be compensated (by a liquid addition) before the analysis of the bath to obtain reproducible results.

- In order to study and compensate the bath evaporation, a mean must be implemented to measure the bath volume or to mark the nominal volume of the bath.

- In order to limit the evaporation phenomena, the cell cover must be as air-tight as possible. This means that the sections of the cover must be adapted as closely as possible; the cover must be fastened and kept together by a closing system; the holes destined to receive agitators, sample holders, thermometers and other appliances must be the smallest possible and in the smallest number possible and unperforated sections must be used whenever possible, mainly during heating and cooling phases.

- Another action that can be easily implemented to avoid excessive evaporation is to pre-heat the solution in the cell (which was not practicable with the smaller cell) and to shorten the periods when the cell is uncovered (placement and pick-up of samples).

- The AAS results must be checked against another technique (in our case, the gravimetric method) in the early stages of the study to ensure that the experimental errors are kept as low as possible.

6.2.2 Borohydride consumption.

The boron concentration was followed by colorimetry, ICP-AES and iodometry. However, only the iodometric method gave usable results, even on new baths. Results obtained on 5 successive baths are listed in table 6.1. The values measured on new baths are very close to the nominal value and the results of reproduced experiments are in very good accord (the standard deviation for new bath and after a deposition of 60 minutes is less than 4 mg/l).

Bath number	Deposition time (min)	$NaBH_4$ concentration (mg/l)
	nominal value	137
1	0	141
5	0	135
4	15	111
3	30	107
1	60	104
2	60	95
5	60	98

Tab. 6.1: Measure of borohydride concentration in electroless nickel-boron bath after deposition (iodometric method).

Contrary to the measure of nickel concentration, the experiment carried out with borohydride seems reproducible and the results follow the expectations. The most of the borohydride consumption seems to happen during the first 15 minutes of deposition, as shown on figure 6.1. The study on the bigger cell will thus focus as much as possible on the beginning of the deposition process to confirm this observation. However, as the evaporation was not taken into account, it is possible that the apparent lower use of borohydride during the last stages of the process is not so pronounced.
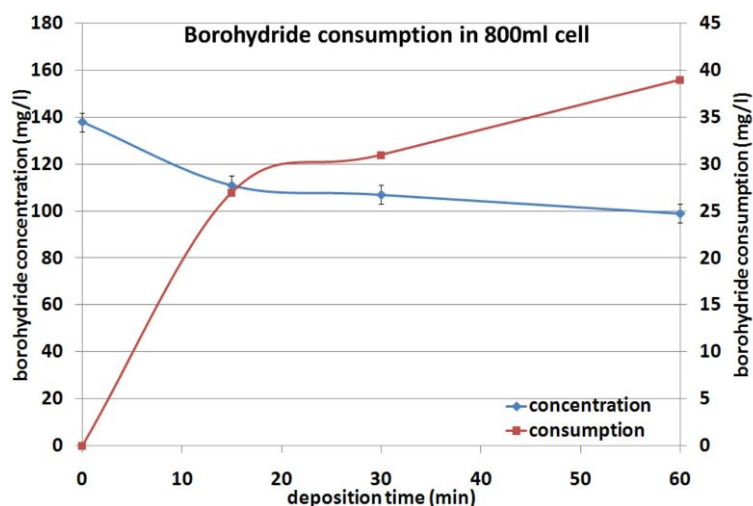
Fig. 6.1: Borohydride consumption, measured by an iodometric method, in the 800ml cell.

6.2.3 Lead consumption.

The lead concentration was measured by AAS and ICP-AES. The ICP results proved to be less consistent than the AAS so only the latter were used for the study. Results obtained on the same 5 baths as previously are listed in table 6.2. It is clearly visible that the measures are less reproducible than in the case of boron (the standard deviation is close to 1 mg/l, which amounts to nearly 10% of the measure). The results don't look anomalous and the lead use appears to be slightly more important in the beginning of the deposition process, as shown on figure 6.2. However, these results must be confirmed by testing on the bigger cell.

Bath number	Deposition time (min)	PbWO$_4$ concentration (mg/l)
	nominal value	9,56
1	0	10.48
3	0	8.86
5	0	9.968
4	15	8.506
3	30	7.73
1	60	7.46
5	60	5.487

Tab. 6.2: Measure of lead tungstate concentration in Ni-B plating bath after deposition (AAS).
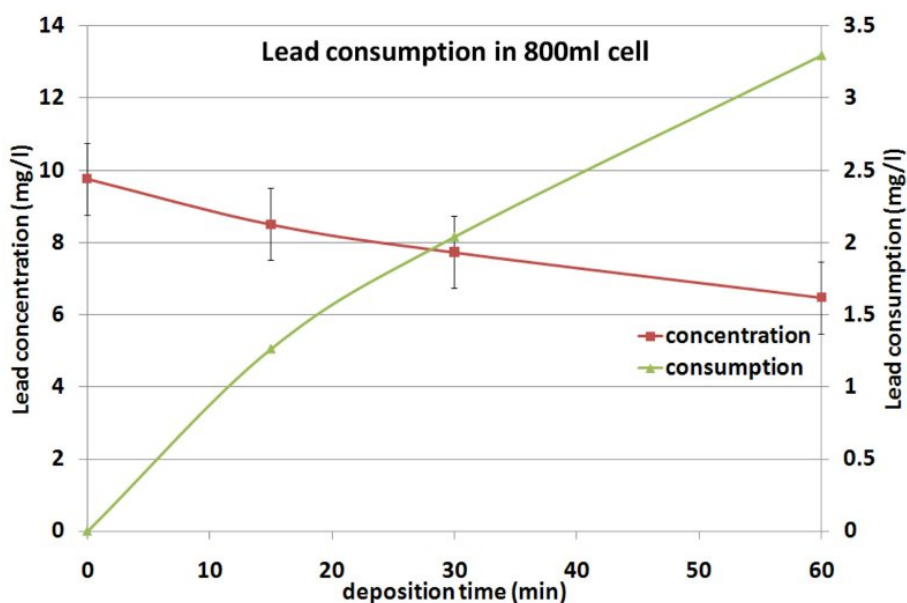
Fig. 6.2: Lead tungstate consumption in the 800ml cell.

6.2.4 Summary of the observations and actions to implement in the further study.

The observations made during this preliminary study will be transcribed into actions that will be implemented during the reactive consumption study on the 8 liters cell. Here is a summary of the most important ones:

- The evaporation of the solution induces irreproducibility in the concentration study. Several actions must be taken to remedy this fact: the cell cover must be designed to limit the size and number of openings; the plating procedure must be studied to avoid opening of the cell cover; the cell must be equipped with a mean of measuring the solution volume and the evaporation loss must be compensated before the chemical analysis are carried out.

- Most of the reactive consumption seems to happen during the first 30 minutes of the plating. This period must thus be investigated very thoroughly. However, as the effect of evaporation may mask some phenomena later in the process, the later part of the deposition will be studied as well.

- The measure of nickel concentration by AAS is the most adapted method but it must be used very carefully (to avoid dilution errors) and it must be checked against another method regularly.

- Iodometry is the best method for the measure of borohydride concentration.

- Lead tungstate must be measured by AAS if possible but great care must be taken because of the important error observed on the measures.

6.3   Study of reactive consumption in the 8 liters cell.

After getting a rough idea of the reactive consumption by the way of tests made with the 800ml cell, a better knowledge of it was needed. Tests were thus carried out on the 8 liters cell to determine the concentration profile of the various reactive.

For the implementation of those tests, simple 10 * 10 cm square sheets of extra-mild steel were used. The bath load was modified by varying the number of samples placed in the bath (0.5, 1 and 2 samples respectively). To follow the composition changes as precisely as possible while modifying the bath load in the least possible extent, we chose to withdraw approximatively 25 ml from the bath for each test. The sampling was carried out firstly after the lead tungstate addition (and, in some cases but not all, after the sodium borohydride addition) and then after 5, 10, 15, 20, 30, 45 and 60 minutes of deposition.

6.3.1   Initial concentration of reactive in the bath.

Before any study of reactive consumption, it is indispensable to have a precise idea of the initial amount of each chemical present in the bath. This is the object of the present section.

The sampling of solution before the beginning of the deposition allowed us to measure the exact lead tungstate (and, when possible, sodium borohydride) content in the bath before operation. Those values were in most of case different from the nominal concentration, as shown in table 6.3. The nickel content was measured only for the very first trial run because the results obtained for this reactive were unreliable, as will be shown in section 6.3.3.1, and is thus not discussed in this section.

Bath reference	$PbWO_4$ content (g)	$NaBH_4$ content (g)
nominal value	0.167	4.816
1 sample	0.224	
1 sample (2nd run)	0.165	5.696
1 sample (3rd run)	0.166	4.917
2 samples	0.205	
2 samples (2nd run)	0.218	4.109
2 samples (3rd run)	0.186	4.425
1/2 sample	0.182	
1/2 sample (2nd run)		5.534
1/2 sample (3rd run)	0.207	5.732
1/2 sample (4th run)	0.218	6.127
Average	0.177	4.567
Standard deviation	0.022	0.749

Tab. 6.3: Measure of initial reactive concentration in the bath.

As can be seen in table 6.3, only one sample (shown in red) is very close to the nominal value for both the lead tungstate and sodium borohydride concentration. The initial concentrations are always higher or equal to the nominal value for the lead tungstate but there are a few occurrences of lower values for the sodium borohydride. The origins of the dispersion of the values are multiple:

- The basis solution (containing the nickel, ethylene diamine and sodium hydroxide) is prepared in a 5 liters beaker, which can already induce a slight error on the volume and concentration. As 8 liters are needed, a whole beaker is used plus 3 liters drawn out of another one. The measure of the 3 liters is another source of error. Moreover it is not unusual that some liquid is lost during the transfer into the cell. It is thus possible that the volume of solution present in the cell before the experiment is sensibly smaller than 8 liters.

- The bath is heated before the lead tungstate and sodium borohydride are added. While all precautions are taken to avoid evaporation, it is impossible to fully circumvent this phenomenon. As such, a further decrease of the cell volume can be expected.

- The amount of lead tungstate solution that must be added is very small (less than 20 ml) and it is drawn from a larger volume prepared in advance (because that solution is very stable). As such, the amount of lead tunsgtate added to the bath is usually reliable. This is not the case however for the sodium borohydride: this solution is very unstable and the 40 ml needed for a bath are prepared just before they are used. As sodium borohydride cannot be put in contact with water, it is difficult to rinse the container after emptying it in the bath. Moreover, the concentrated sodium hydroxide solution in which this compound is dissolved is quite viscous and it is difficult to avoid that a small amount of solution remains in the container. The amount of sodium borohydride put in the bath can thus be, in some cases that we try to avoid, slightly smaller than the nominal amount.

- The experimental technique used to measure the borohydride content of the solution is an iodometric titration. It is thus very much influenced by the dexterity and experience of the operator and this technique can induce non negligible experimental errors, even when the experiment is carried out with the utmost care.

As the initial reactive concentration varies slightly from bath to bath, we decided to use a normalization of the values in order to compare different baths. This was carried out by calculation of the initial divergence (difference between the measured and nominal value) which was then subtracted from the measured data.

6.3.2   Evaluation of the consistency of the experiment.

Now that steps were taken to ensure that the initial state of all baths is controlled and corrected, there is a need for a way to discriminate eventual abnormal runs of the experiment: as the electroless nickel-boron bath may be quite unstable, it was necessary to ensure that the experiment was carried out in adequate conditions. To do this, the samples were weighed before and after the deposition process to determine the amount of nickel deposited on their surface. This allowed us to reject experiment during which the amount of nickel deposited was abnormally low or high. Table 6.4 presents the amount of deposit weighed on the samples during the regeneration experiment. The weights deposited with a similar load (the load is the ratio of the sample surface and bath volume) are close. It is expected that different amounts of nickel are deposited when different bath loads are tested.

Sample	bath load (cm^2/l)	deposit weight (g)
1 sample (2nd run)	25	3.46
1 sample (3rd run)	25	3.12
2 samples (2nd run)	50	4.34
2 samples (3rd run)	50	4.79
1/2 sample (2nd run)	12.5	1.59
1/2 sample (3rd run)	12.5	1.39
1/2 sample (4th run)	12.5	1.52

Tab. 6.4: Amount of nickel-boron deposited on the samples after one hour, as a function of the bath load.

6.3.3   Evolution of the concentration of reactive during deposition.

In this section, the actual results of the experiment will be discussed.

The evolution of the concentration of the various reactive in the bath was studied as follow: samples were drawn just before the substrate is immersed in the bath, then after 5, 10, 15, 20, 30, 45 and 60 minutes. This was carried out without replenishment of the bath, with a constant substrate nature (St 37 steel), position and size (10 * 10 cm). Most samples were weighed before and after the deposition process to ascertain that the deposit growth was unimpeded.

The samples of solution were analyzed as soon as possible after the experiment and never later than 48 hours after their making. The techniques used were AAS for the following of nickel and lead concentration and iodometric titration for the sodium borohydride content.

6.3.3.1 Evolution of nickel chloride concentration

As was already said in section 6.2.1, the study of nickel concentration in the bath is not very easy: the AAS technique is quick but it needs important dilutions of the solution and is not very reliable. The gravimetric technique is far too time-consuming to be implemented for a systematic study of the concentrations (it takes at least 1 hour per sample excluding the heating, cooling and settling times). Given the important number of samples that had to be analyzed, we chose to use the AAS method. Partial results obtained on the first run of the experiment are found in table 6.5. As can be seen, the measured values fluctuate due to experimental error in a range of roughly 10% of the value. However, the nickel excess is such that the nickel content stays within the range of the experimental error. It is thus impossible to use those results to assess the consumption of nickel.

Sample	Nickel content (g)
Nominal value	192
Initial value	178.20
After 5 minutes	193.49
After 15 minutes	181.18

Tab. 6.5: Evolution of nickel chloride concentration during plating.

The study of the kinetics of nickel consumption in the bath was not carried out further because of the very important nickel excess in the bath: the maximal amount deposited during this experiment was weighed in the case of 2 samples plated simultaneously and was 4.8g. If we consider that only nickel is deposited on the sample, we can obtain the amount of nickel chloride needed to make this deposit: 19.4 g. That represents only 10% of the initial amount of nickel present in the bath.

This very low relative consumption of nickel explains partially the difficulties encountered while following the evolution of its concentration. Moreover, as very few of the initial nickel is used after one hour of deposition, there is no need for nickel replenishment during the deposition, even when thicker samples are needed: the nickel concentration will never become the rate limiting parameter of the process, except if extremely thick coatings were envisaged, which is not the case.

6.3.3.2 Evolution of lead tungstate and sodium borohydride concentrations.

The evolution of lead tungstate and sodium borohydride concentrations were studied simultaneously, in order to evaluate if both reactive were used in the same manner or not. First, the consumption in a bath with the typical load (one sample: $25cm^2/l$) was studied, then the effect of bath load on the amplitude and kinetics of reactive consumption was investigated.

6.3.3.2.1   Evolution of the concentrations under the 'normal' load of the bath.

Figure 6.3 presents the evolution of normalized reactive concentration during deposition with a bath load of $25 cm^2/l$. Several observations can be made from this figure.
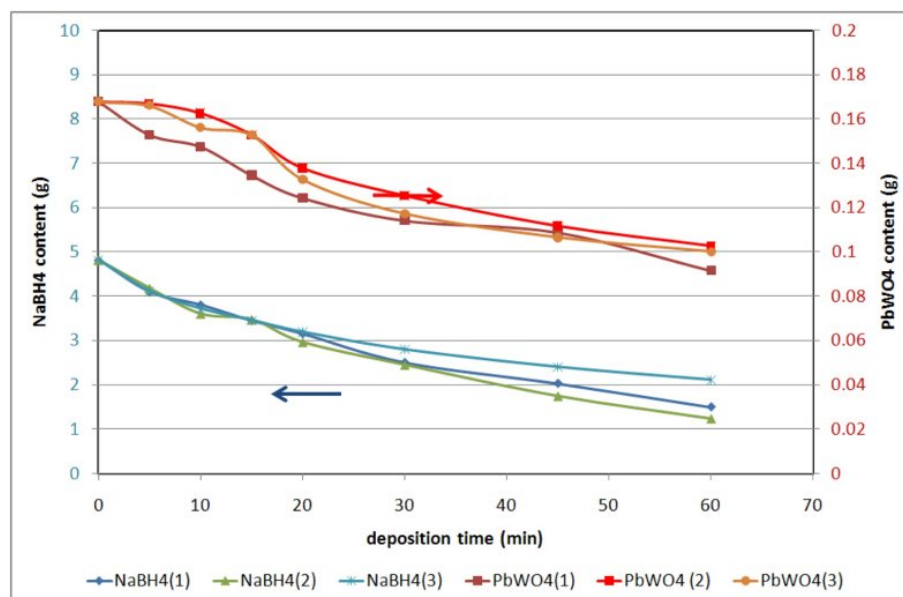
Fig. 6.3: Evolution of reactive concentration in the 8 liter cell with a load of 25 cm^2/l.

- First, the experiment appears to be reproducible: 3 runs were carried out and the curves for those follow the same trend. The borohydride concentration appears to evolve in a very similar way for all samples, while the evolution of lead concentration is somewhat different for each sample, however, in both cases, the end value is similar.

- The low residual borohydride concentration indicates that the bath is nearly depleted after one hour and that continuing the experiment after one hour without replenishment is thus not useful to obtain thicker coatings.

- The evolution of the reactive consumption is similar to what was observed in the 800 ml cell with a load close to $25 cm^2/l$ (see figures 6.1, page 72 and 6.2, page 73). The concentration decreases in a non-linear way, with an higher use of reactive at the beginning of the process. The half of the sodium borohydride present in the bath is consumed during the first 30 minutes and 70% of this reactive are used at the end of the experiment (after one hour). The consumption of lead tungstate is less important: only 40% of the reactive are used at the end of the experiment, of which only 25-30% during the first 30 minutes. The choice of 30 minutes for the timing of bath replenishment appears thus to be a good compromise between deposition rate (the consumption rate is proportional to this rate) and practical aspects (regeneration is carried out manually, so must not be too frequent to allow preparation of the reactive).

- The sodium borohydride seems to be consumed more regularly than the lead tungstate, that appears to be used by steps. However, as the steps of lead tunsgtate consumption are not the same on three runs and its concentration is very low, it is possible that this comportment is an artefact of the analysis.

- A comparison of the initial sodium borohydride concentrations (table 6.3) and the amount of nickel deposited (table 6.4) with the normalized concentration curve shows that an higher initial concentrations (observed for the second run) induces a more important nickel deposit and a more important consumption of reactive. However, the real concentration of borohydride in the bath after the experiment is similar in both cases (2.11g for run 2 and 2.21g for run 3 in real concentration against 1.23g (run 2) and 2.11g (run 3) as normalized concentration). For the lead on the opposite, the initial value seems not to have any influence on the amount of reactive used during the experiment: the initial value for run 1 was higher than for run 2 and 3. However, the normalized residual values are similar: 0.091, 0.102 and 0.100g respectively while the real values keep the initial difference (0.148, 0.100 and 0.099g respectively), and the amounts of lead tungstate consumed are respectively 0.076, 0.065 and 0.067g.

6.3.3.2.2 Influence of bath load on reactive consumption.

Now that the evolution of reactive concentration was investigated with one sample in the bath, the influence of the bath load on this evolution will be examined by doubling and halving the load.

6.3.3.2.2.1 Reproducibility.
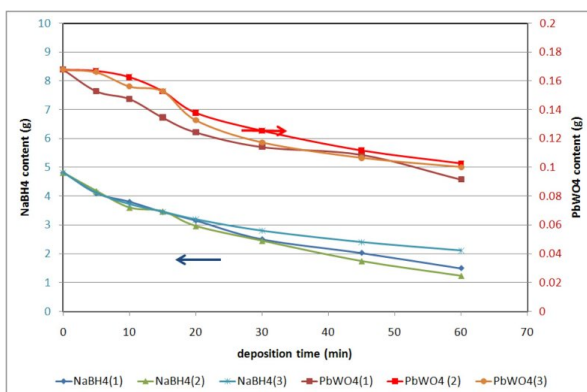
Fig. 6.4: Evolution of reactive concentration in the 8 liter cell with a load of 50 cm^2/l.
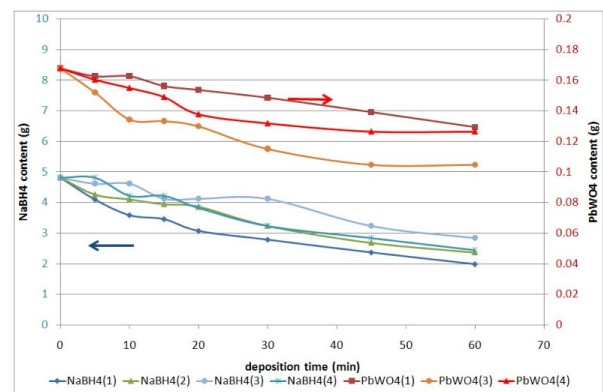
Fig. 6.5: Evolution of reactive concentration in the 8 liter cell with a load of 12.5 cm^2/l.

First, the reproducibility of both experiments was investigated by comparing normalized concentrations for at least 3 runs. Those results are presented in figures 6.4 and 6.5.

The reproducibility of the results obtained for borohydride consumption with a load of $50\text{cm}^2/\text{l}$ (2 samples) is very good. It is not as good for the other measures but it stays acceptable: the trends are the same for every sample and the residual concentrations are in the same range. The differences can be explained, in the case of lead tungstate, by the very low concentration of this reactive in the bath that induces important relative errors and, for borohydride in the case of a very low load (1/2 sample), by the very low reactive surface (a load of $25\text{cm}^2/\text{l}$ is already considered low for industrial baths).

6.3.3.2.2.2   Use of sodium borohydride.
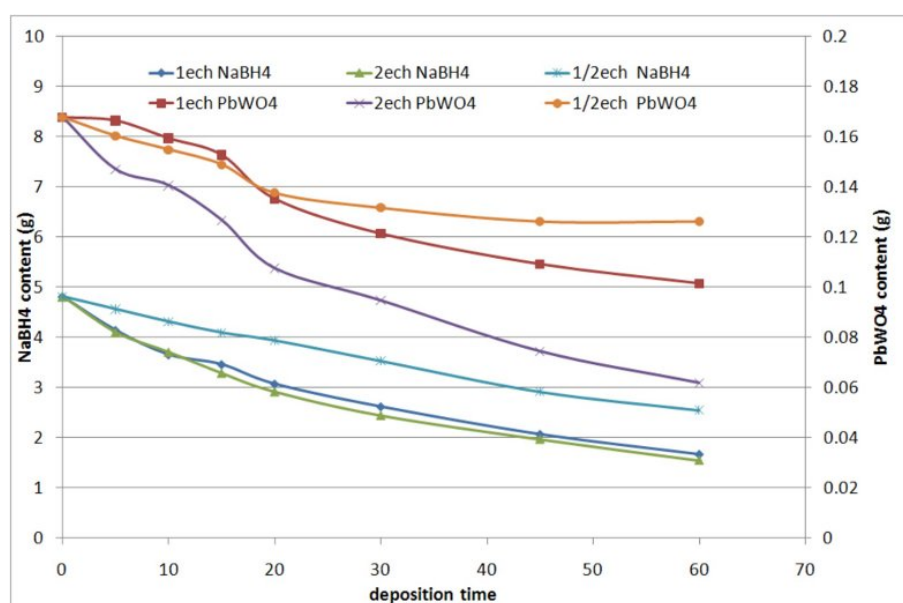
Fig. 6.6: Evolution of reactive concentration in the 8 liter cell as a function of bath load.

To compare the evolution of composition for baths used with different loads, the average normalized composition for the different loads were plotted altogether in figure 6.6. The normalized consumption of sodium borohydride is nearly identical for loads of 25 and 50 cm^2/l (the residual concentration with the higher load being only slightly lower). It could mean that the maximal amount of sodium borohydride consumed is reached in both cases, which is not very realistic. Examination of the real sodium borohydride concentrations brings a more pertinent explanation: after one hour of deposition, the residual sodium borohydride content is on average (see table 6.6 for complete data) 3.45g for a load of 12.5 cm^2/l, 2.03g for a load of 25 cm^2/l and 1.08g for a load of 50 cm^2/l. The same concentration level is reached after one hour, for baths with a similar load, even if the initial reactive concentration is different, as shown in table 6.7. This means that the amount of nickel deposited is less linked to the bath load than the final concentration of reactive.

Sample	final NaBH$_4$ content (g)	final PbWO$_4$ content (g)	NaBH$_4$ used (g)	PbWO$_4$ used (g)
1 sample (1st run)	1.77	0.148		0.076
1 sample (2nd run)	2.11	0.100	3.58	0.065
1 sample (3rd run)	2.21	0.099	2.7	0.067
2 sample (1st run)	1.23	0.106		0.099
2 samples (2nd run)	0.95	0.109	3.16	0.109
2 samples (3rd run)	1.05	0.084	3.37	0.102
1/2 sample (1st run)	3.20	0.143		0.039
1/2 sample (2nd run)	3.08		2.54	
1/2 sample (3rd run)	3.755	0.144	1.98	0.063
1/2 sample (4th run)	3.755	0.177	2.37	0.041

Tab. 6.6: Consumption and final concentration of NaBH$_4$ and PbWO$_4$ as a function of the bath load.

Run	Initial content (g)	Final content (g)	Consumption (g)
2	5.696	2.112	3.58
3	4.917	2.212	2.75

Tab. 6.7: Initial and final sodium borohydride content, for a bath load of 25 cm^2/l.

The clear correlation between the bath load and those concentrations, and the lesser correlation between the load and the amount of borohydride consumed (and thus with the amount of material deposited), indicates that the rate limiting step in for the use of borohydride is diffusion and that the reaction of borohydride at the surface is instantaneous. This confirms the findings of Rao [56] for an unagitated bath but this adds new information: the diffusion is the rate limiting step even when the bath is agitated. The differences in residual concentration between baths with different loads shows that there still is a correlation between the bath load and the sodium borohydride consumption.

6.3.3.2.2.3 *Use of lead tungstate.*

The comportment of lead, however, is very different from borohydride: while the lead tungstate content is different in every bath after one hour of plating (see table 6.6), the amount of lead consumed during the experiment is nearly constant for every load: 0.105g in average for 50 cm^2/l, 0.066 for 25 cm^2/l and 0.041 for 12.5 cm^2/l. This means that diffusion is not the rate limiting step for the use of lead in the bath and that the amount of lead used is correlated with the surface of the sample. Knowing the role of the lead salts in the electroless bath, it is not surprising: the lead salts play a regulating role in the

plating process by blocking a part of the active catalytic sites. The correlation between the surface of the sample and the lead ions consumption cannot be established directly because lead serves also to block other catalytic sites in the cell (surface of the vessel, particles in suspension, ...). However, as the amount of lead tungstate needed to block those sites is not dependent on the bath load and should thus be constant, it is possible to calculate it: it is approximatively 0.022 g. If this amount is subtracted from the lead salt used during plating, the consumption is 0.0831 g in average for 50 cm^2/l, 0.0441 for 25 cm^2/l and 0.0195 for 12.5 cm^2/l. The correlation is thus established (see table 6.8).

Bath load (cm^2/l)	bath load ratio	consumption (g)	variable part of the consumption (g)	consumption ratio
50	2	0.105	0.0831	1.88
25	1	0.066	0.0441	1
12.5	0.5	0.041	0.0195	0.44

Tab. 6.8: Influence of bath load on lead consumption.

6.3.3.2.2.4   *Correlation between the bath load, the consumption of reactive, the amount of material deposited and the deposit composition.*

The bath load has a great influence on the reactive consumption and weight deposited. However, when comparing results for both those parameters, it appears that the amount of boron used is similar for 25 and 50 cm^2/l while the amount of material deposited is consequently higher in the case of the higher bath load (4.57 g instead of 3.29 g), as shown on table 6.9. This suggest that the composition of the deposit could be influenced by the bath load.

Bath load	12.5 cm^2/l	25 cm^2/l	50 cm^2/l
$NaBH_4$ used (g)	2.26	3.14	3.27
$PbWO_4$ used (g)	0.0414	0.0663	0.1058
Weight deposited (g)	1.5	3.29	4.57
Wt % Ni	94.01	94.31	93.15
Wt % B	4.78	4.64	5.45
Wt % Pb	1.20	1.05	1.40

Tab. 6.9: Influence of bath load on reactive consumption, amount of material deposited and composition of the deposit.

To verify this, samples synthesized with varying bath loads were analyzed by ICP to obtain their average composition. Those results are also shown in table 6.9. The lead content of the samples appears to be quite stable, whatever the bath load. The boron content, while similar for 12.5 and 25 cm^2/l, is higher for the highest bath load. This is

unexpected because the deposition of an higher weight of material with a similar amount of boron suggest that more of the borohydride is used for the reduction of nickel and less for the auto-deposition of boron, which would lead to a lower boron concentration in the deposited material.

There is another possible explanation for the difference in weight and composition of the deposition in the case of an higher load: the borohydride ion is unstable and tends to be oxidized or hydrolyzed spontaneously. Moreover, it has been shown in section 6.3.3.2.2.2 that the diffusion of the borohydride ion towards the surface is the rate limiting step of the deposition process. Consequently, it is probable that the use of an higher bath load, which increases the deposition kinetics, will favor the use of the reducing agent for the actual deposition against its decomposition. The higher amount of material deposited, and the higher boron concentration in the deposit, could thus be linked to a better efficiency of the reaction in the case of higher loads. However it has not been possible at the present time to prove that hypothesis.

6.3.4 Conclusions and preparation of the bath replenishment.

The study of the initial concentration of reactive in the bath and of the evolution of the bath content was very informative. First, it was shown that the experimental error stays very important even with a more important volume of solution and that part of the discrepancies between successive experiments can be attributed to the making and use of the bath. However, the main trends have been proved reproducible, which allow conclusions to be drawn from the data.

Secondly, the monitoring of the nickel content of the bath has been as non-conclusive as when studied on the smaller cell. It is possible that the evaporation loss, which could not be taken into account during this study (because all the volume measuring devices are calibrated at 25℃), is important enough to mask the evolution of the nickel concentration. Nevertheless, other means than bath analysis will probably have to be used to provide data for nickel replenishment.

Thirdly, the lead tungstate and sodium borohydride are mostly consumed during the first 30 minutes of the deposition process. The replenishment of in-use baths to obtain thicker deposits will thus have to be carried out at that time at the latest. The deposition time before addition of reactive could be shortened but would have to stay long enough to allow preparation of the solutions to be added, as the whole procedure will be designed to be implemented entirely by one operator.

Fourthly, the final concentration of sodium borohydride is more influenced by the bath load than the amount of this reactive that is used during the experiment. However, as far as lead tungstate is concerned, it is the consumed amount that is directly linked to the bath load. The reason for this divergence resides in the very different way both reactive are consumed: sodium borohydride reacts as soon as it reaches the reactive surface (the diffusion being the rate-limiting step) while lead tunsgtate adsorbs much slower on the surfaces.

This information will be taken into account during the implementation of a replenishment procedure, to decide of the best time for the addition of reactive but also to keep in mind that the measure of nickel content of the bath is not very reliable and that a known amount of lead tungstate is used by adsorption on the various walls of the cell.

6.4   Bath replenishment.

The aim of the study of bath replenishment, as we have carried it out is not to obtain a replenishment algorithm or a predictive model of reactive consumption but to gain a sufficient knowledge of the bath to be able to synthesize a maximal number of successive samples without having to throw away the bath and to add reactive during the plating of a sample to obtain a thicker coating.

The study and implementation of bath replenishment was carried out in a number of phases. First, the used baths were left to cool before sampling, analysis and replenishment to the initial composition. This first phase of the study allowed to detect a series of problems that had to be solved and to get a database of values in prevision of the next phases. The second phase of the implementation was the use of the collected data to replenish the bath after each coating without the need to measure the concentrations systematically. Finally, the data were used to evaluate the amount of reactive to add in the bath in order to obtain samples with a predetermined thickness.

6.4.1   Replenishment of spent, cold baths; Problems encountered during replenishment and their solutions.

This first step towards replenishment, which is by far the most important, was carried out during a sample-making campaign. After each sample was coated, the bath heating was switched off, the cover was sealed (to avoid evaporation during the cooling) and the bath was left to cool, typically for a whole night. Then, after complete cooling, a 50ml sample of the spent solution was taken and its boron, lead and nickel content were analyzed to calculate the amount of reactive used. Finally, the bath was replenished (just before the next sample is immersed) using three different solutions for the nickel, the stabilizer and the reducing agent.

During the implementation of this procedure, simple and straightforward as it appears, several problems were encountered and had to be examined.

6.4.1.1   Compensation of the evaporation loss.

The compensation of the volume loss by evaporation was the first issue to be studied because without this, there is no possibility to obtain reproducible data for the measure of reactive concentration in the bath. The first step towards the compensation of evaporation loss is the knowledge of the solution volume in the bath. As the thermostable

bath was not equipped with level or volume measurement, we had to implement our own measuring device. To this effect we used a simple graduated rule and we calibrated this device by adding known amount of water in the bath. We obtained a calibration curve that is shown on figure 6.7.
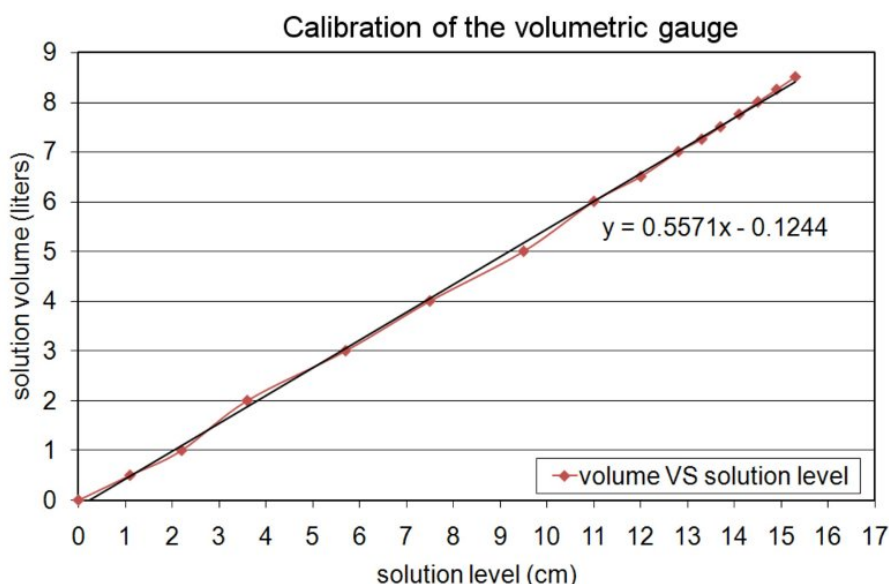
Fig. 6.7: Calibration of the volume measurement.

Once the volume calibration obtained, it was easy to measure the volume of the bath and to determine the amount of fluid needed to compensate the evaporation loss. The choice of fluid to compensate the missing solution was the next step to implement. Several choices were available for this: distilled water, the basis solution of the bath (nickel chloride, ethylene diamine and sodium hydroxyde) or a solution of nickel chloride in distilled water. Each of these possibilities possesses advantages and disadvantages for this application so we decided to use alternatively distilled water and the basis solution for the following reasons:

- The boiling point of ethylene diamine is slightly higher than that of water (116℃), thus the loss of this compound by evaporation should be less than water. Systematic replenishment by the basis solution would indubitably lead to ethylene diamine build up.

- Sodium hydroxide is not lost by evaporation of the solution. Consequently this compounds does not require systematic compensation. However, the pH increase due to the deposition reaction must be taken into account and may require the addition of alkaline reagents. Using the basis solution regularly for the evaporation compensation would guarantee sufficient alkalinity of the solution.

6.4.1.2   Measurement precision and reliability.

The problems linked to the precision, reliability and reproducibility of the measurements are really important in view of the bath replenishment. The amount of $NaBH_4$, $PbWO_4$ and $NiCl_2.6H_2O$ to add in the solution after use and analysis are presented in table 6.10 for 21 experiments, together with the coating thickness and the weight of nickel deposited. Those results are relative to samples with a total surface of 150 or 200 cm^2 that were left in the bath for 1 hour.

Bath number	sample thick-ness (μm)	Ni (g)	$NiCl_2.6H_2O$ add. (g) from analysis	$NiCl_2.6H_2O$ add. (g) from Ni deposited	$NaBH_4$ addition (g)	$PbWO_4$ addition (mg)
1			22.79		3.69	107.91
2					4.71	
3	12.16	2.17	-15.47	8.78	2.73	102.39
4	9.00	1.61	-16.94	6.50	3.41	71.54
5 (New)	18.28	2.44	28.87	9.86	3.17	68.22
6	8.65	1.20	-4.51	4.85		38.79
7	9.89	1.37	-9.74	5.55	3.34	57.62
8 (New)	16.91	2.34	-18.41	9.48	2.60	64.83
9	16.95	2.39	-6.31	9.69	2.59	69.97
10	13.85	1.86	-7.78	7.54	2.79	72.03
11	18.93	2.67		10.81	2.17	92.61
12	12.31	1.71		6.90	2.40	63.80
13	14.17	1.96	-11.06	7.94	1.97	
14	13.91	1.93		7.80	2.68	61.74
15	12.32	2.20	-20.51	8.90	3.24	43.19
16	8.65	1.54	-3.14	6.25	4.54	33.79
17	6.44	1.15	3.77	4.65	4.77	22.26
18	15.33	2.73	4.83	11.07	4.55	22.26
19	9.58	1.71	6.31	6.92	3.44	58.47
20	8.85	1.58	17.80	6.39	3.37	67.89
21	6.95	1.24		5.02	3.85	92.69
min	6.44	1.15	-20.51	4.65	1.97	22.26
max	18.93	2.73	28.87	11.07	4.77	107.91
mean			-2.63	7.56	3.23	58.92
median			-5.41	7.54	3.29	64.83
std deviation			13.43	1.97	0.81	20.20
variation (%)				26.04	24.95	34.28

Tab. 6.10: Composition analysis for bath regeneration: sample size 10*10 cm, deposition lenght: 1h, solution volume : 8l.

Bath number	sample surface(cm^2)	sample thickness (μm)	nickel deposited (mg)
Bigger cell			
1	156.31	18.28	2440
2	156.31	16.91	2340
3	156.31	16.29	2090
4	242.00	17.46	3460
5	242.00	15.73	3120
smaller cell			
6	19.57	15.90	256.40
7	19.24	14.05	221.80
8	19.32	14.20	225.60
9	19.39	12.29	195.50
10	17.38	15.60	223.70
11	17.45	14.40	206.90
12	17.39	15.10	216.40
13	17.44	15.60	224.10
14	16.84	16.04	221.60
15	17.38	14.80	211.90
16	17.84	14.80	216.80
17	17.61	16.20	234.10
18	17.34	16.75	238.30
19	18.97	16.87	262.60
20	18.74	16.76	257.70
21	19.08	15.77	247.00
22	19.17	16.22	255.00
23	19.14	17.21	270.30
24	17.78	16.65	242.90
25	19.20	17.19	270.80
26	19.12	14.30	224.40
27	19.85	13.01	202.30
28	17.59	12.48	180.00
29	18.73	12.18	187.10
30	19.02	12.42	193.70
30	19.18	14.18	233.10
32	20.07	14.45	237.90
33	16.96	15.97	222.30
mean (small - whole)		15.05 - 15.34	227.86
std dev. (small - whole)		1.52 - 1.59	23.97
median (small - whole)		15.35 - 15.73	224.25

Tab. 6.11: Weight of nickel deposited and thickness for various samples. Substrate: steel, plating duration: 1h.

The weight of nickel deposited on the sample varies from 1.15 to 2.73 grams. This is due to (sometimes very slight) variations in the experimental conditions such as sample size, bath volume and temperature but also in an important way to the inherent error induced on the bath composition by the replenishment. As a proof of this, the thickness and weight of nickel deposited are listed in table 6.11 for samples made using each time a new bath (to have a more important database, samples synthesized using both the small (0.8l) and the bigger (8l) cells are listed in this table). The range of thickness and deposited weight is far smaller in the case of samples synthesized with a new bath than for an used bath, even without taking into account the sample surface variations, which were important in the small cell due to the geometry of the samples. However, the reproducibility of the deposition process is not perfect, even when a new bath is used and the slight differences between samples are accentuated by the errors induced by the replenishment process.

The calculation of nickel consumption (and of the subsequent additions) from the measure of the bath concentration caused some problems: the reliability and precision of the nickel analysis (either by AAS or gravimetric method) is not good, even when great care is taken during the experiment. The amount of nickel chloride to be added to the bath varies from -20.51g (!) which is entirely impossible to 28.87g which is far too high. We thus decided no to give too much credit to those values and to use the amount of deposited nickel (obtained by weighing the samples before and after plating) to calculate the nickel chloride additions. Those values vary between 4.65 and 11.07g. Their dispersion is less important than the dispersion of the analysis results but the standard deviation still amounts to 26% of the average value, due to the lack of reproducibility of the deposition when the bath is replenished.

The variations obtained for sodium borohydride and lead tungstate consumption are of the same order as the variations of the weight of deposited nickel (with standard deviations of respectively 25 and 34 % of the average value). This means that the precision of the analysis is good, because it doesn't increase the dispersion of the values compared to the fluctuations of the process (measured by the amount of nickel deposited on a sample of fixed surface area during a given time).

By surveying the results of the analysis of cold, spent baths, we were able to show that:

- As was expected from the study of bath composition, the analysis of the nickel content by AAS or by a gravimetric method is not a reliable tool to determine the amount of nickel chloride to add for the replenishment of the bath.

- The analysis of the boron and lead content of the bath can be used to calculate the amount of the corresponding reactive (sodium borohydride and lead tunsgtate) to add in the bath.

- The amount of nickel to add in the bath can be evaluated quite satisfactorily by the weight of nickel deposited on the sample.

6.4.1.3 Nickel additions and ethylenediamine build up.

Replenishing the bath in nickel chloride is a problem for other reasons than just the unreliability of the analytical methods for this reactive: the nature of the medium used for this addition is also the source of some difficulties.

Nickel chloride is readily soluble in water but forms insoluble hydroxide in alkaline media if it does not form stable complexes with an agent such as ethylene diamine. It is thus possible to use either a neutral solution of nickel chloride in water or an alkaline complexed solution for the nickel chloride replenishment.

For the first tests, the replenishment was carried out with a solution of nickel chloride in 100 g/l sodium hydroxide and 140 g/l ethylene diamine. The amount of nickel chloride varied according to the replenishment needed. The volume of solution used for the replenishment was kept constant, at 100ml. The use of this combination, heavily concentrated in sodium hydroxide and ethylene diamine, together with the use of the basis solution (also containing sodium hydroxide and ethylene diamine) for the compensation of evaporation was however rapidly questioned as we thought it would lead to a build up of ethylene diamine which does not react during the deposition process.

To investigate the possible build up of ethylene diamine, the total carbon content of the sample was measured (the apparatus and analytical method are described in section **??**). The measure of the carbon content of the bath allowed us to obtain the ethylene diamine concentration because it is the only carbon containing compound of the bath. Table 6.12 presents the results of the analysis of new and replenished baths. It is clear that the use of a solution containing ethylene diamine for the replenishment of the bath causes an increase of the concentration of this reactive: the measured concentration varies from 20.5 g/l for a new bath (which is quite close to the nominal value) up to 31g/l after only 6 replenishments, and up to 33g/l after 7 replenishments. To avoid potential problems linked with this build up, the replenishment procedure was modified and the nickel chloride was dissolved in distilled water. We thus assume that the eventual loss of ethylene diamine will be compensated by the regular use of the basis solution for the compensation of evaporation.

Bath	EN content (g/l)	Carbon content measured g/l
Nominal concentration	53.940	21.576
New bath	44.652	20.540
After 6 replenishments	68.000	31.280
After 7 replenishments	71.696	32.980

Tab. 6.12: Evolution of the ethylene diamine content of the bath after replenishment.

6.4.1.4   Lead target concentration.

In section 6.3.3.2.2.3, the comsuption of lead tungstate during the deposition process was studied and it was found that a non negligible amount of this reactive is used whatever the bath load, because it adsorbs on the walls of the deposition cell. When the lead concentration of the bath is measured, this amount (22 mg) is not detected but is not needed anymore if the cell has not been emptied and rinsed (if the lead can stay adsorbed on the cell walls). This means that replenishment made using the measured value of lead tungstate consumption will produce a bath with an higher lead concentration that what is needed.

The consequences of this lead tungstate increase can be observed intuitively in table 6.10 (page 86): samples made with a new bath (no over-concentration of lead tungstate) appear thicker than most of the other ones. It was thus envisaged to lower the amount of lead tungstate addition by the adsorbed amount. However as the volume of solution it represents is very low (only 1 ml to be added in 8l of plating bath) and clearly does not exceed the standard deviation of the measures, we preferred to use the calculated value for the lead tungstate addition. This increases the risk of slightly lowering the deposition rate but allows us to avoid destabilization and plate out that could be induced by a bath with an under-concentration of lead tungstate.

Moreover, as it is not known if lead continues to adsorb on the cell walls after one hour (the consumption study was not carried out for times longer than that), it is possible that some of the added lead will be used at this effect after replenishment. Lowering the lead tungstate additions to take into account the adsorbed fraction could thus greatly increase the risk of plate out.

Observation of table 6.10 (page 86) also shows that the lowest measured consumption of lead tungstate corresponds to the calculated value of the adsorption on the walls.

6.4.2   Towards replenishment of hot, in use bath.

As shown in the previous section on the replenishment of cold, spent, baths, the regeneration process is not very reliable nor easy to implement at the lab scale. Two options are however open to us for our approach of this problem in the case of hot baths (in order to coat several samples without cooling the bath).

The first option is to withdraw liquid from the bath systematically between two plating sessions (after the evaporation compensation), to cool it in the fastest possible way and to proceed to an immediate analysis of the bath composition. This option was used by Dr Delaunois when she worked with a Thallium stabilized bath [7]. It is time consuming and requires attention and precision from the operator to obtain usable results.

The other option is to evaluate the reactive consumption from a database of previous experiments and to use the average value to replenish the bath. To avoid important de-

viation of the bath composition, the bath is analyzed once a day (in the morning, during the heating phase).

The second option was implemented for this study because the first option, while it is usable for the bath replenishment between samples, is very difficult to implement during the deposition process (it is impossible to run the complete analysis in less than 15 minutes, cooling time excluded). This means that the amount of reactive to add during the process in order to extend the plating time has to be predetermined. It is thus more coherent to use the predetermination for the whole process.

In order to choose the values as wisely as possible, we compared the average and median values for the various additions (see table 6.10 for the complete data). In the case of nickel chloride and sodium borohydride, both values are very close (average : 7.56 g for $NiCl_2.6\,H_2O$ and 3.23 g for $NaBH_4$; median 7.54 g for $NiCl_2.6\,H_2O$ and 3.29 g for $NaBH_4$). The difference seems higher for lead tunsgtate (average : 58.92 mg; median : 64.83 mg) but it is merely due to the very small amount of this reactive that is needed. The values chosen for bath replenishment were : 7.5 g $NiCl_2.6\,H_2O$, 3.3 g $NaBH_4$ and 60 mg $PbWO_4$.

This procedure proved useful and reliable as it rendered possible to plate 11 successive samples in the bath without plate out or any other problem while the previous procedure (using the analysis of cold baths) allowed a maximum of 7 replenishments. Our goal of reducing waste and the cost of reactive was thus reached.

6.4.3 Replenishment during the deposition process.

The problem of replenishment during the plating of one (or more) sample is intimately linked to the problem of the regeneration of hot baths. This process is used mostly to obtain thicker samples (the thickness is in the 10 - 15 μm range after one hour without replenishment) but can also be used when more than one sample must be plated simultaneously.

As the thickness goal for thicker samples is around 20-30μm (instead of 10-15 μm), the choice was made to consider the replenishment during the deposition process as needing as much reactive as the replenishment between two following samples. This replenishment was carried out 30 minutes into the deposition process and the sample was left in the bath for another hour. When very thick samples were needed, two replenishments were carried out after 60 and 90 minutes of plating (the first replenishment is delayed to avoid any over-concentration of reactive during the second replenishment). This allowed us to obtain samples as thick as 36 μm (plating time 2.5 h, with replenishment after 60 and 90 minutes).

6.5   Conclusion.

The study of reactive use during the deposition process and of bath replenishment was very informative. Firstly, it allowed us to obtain data about the amount of reactive really consumed by the plating process and to measure what was lost when a bath was thrown away after only one plating.

Secondly, the kinetics of the various reactions taking place into the bath could be determined: the oxidation of sodium borohydride is immediate as the reactive arrives at the reactive surface, the rate limiting step being the diffusion of reactive towards the reaction site. The consumption of lead tungstate however, is not limited by diffusion and the adsorption must be the rate limiting step. It also possible to determine the amount of lead tungstate that is consumed by the cell walls independently of the samples during one hour.

Thirdly, the study of the influence of the bath load on the concentration of reactive has shown that the composition of the deposit is not an intrinsic property of the deposition bath as it is influenced by the ratio of the bath volume to the sample surface.

Fourthly, the problem of evaporation loss was identified and solutions were implemented to limit its impact on the deposition process. Other problems, like the progressive build up of nickel and ethylene diamine, were also detected and resolved during the study of cold bath replenishment.

The implementation of a semi-predetermined replenishment system (in which the concentrations are controlled once a day and the additions during the day are predetermined) allowed us to plate up to 11 successive samples in a same bath, which represents a very important economy of reactive (mainly nickel, sodium hydroxide and ethylene diamine) and a non negligible decrease of the waste treatment costs. Moreover, it is now possible to synthesize thicker coatings (up to near 40 μm) if they are required for a particular test.

In short, this study has brought a better working understanding of the deposition bath and has increased our control over its comportment. As a direct consequence of this, the occurrence of unexplainable plate-outs has decreased very much after this study was carried out: most of the remaining plate-outs have been easily linked to experimental problems like overheating or aged reactive.

7. INITIATION AND GROWTH OF NICKEL-BORON DEPOSITS.

The initiation and growth of electroless deposits, while it is assumed to have an influence on the coating's properties, is not very extensively studied. Many reasons can be proposed to explain this: the chemistry of the baths is very complex and results found with a particular composition could not be easily transposed to other baths; most studies on electroless deposition are carried out on experimental unreplenished baths while industrial applications use continuously replenished ones; the experimental means for an in-situ study of initiation and growth are very limited. Moreover, there is a lot of interest on the achievement of better properties for electroless nickel but not on the understanding of how and why those properties are obtained.

In the present chapter, we will try to gain a better understanding of the initiation and growth mechanisms of electroless nickel-boron deposits and to link it with the properties of the coating. First, a review of previously published studies on deposit growth will be presented, then the initiation of the deposit will be observed, as well as the influence of substrate roughness and nature on the phenomenon. Finally, the growth of the coating will be studied in a un-replenished bath.

7.1   Review of previous research about electroless nickel deposits initiation and formation.

The study of the initiation and formation of electroless deposits has not been the object of many works but some of the existing papers are of great interest. In this section, the findings of those papers will be summarized and their application to the present study will be discussed. The papers and sources describing the growth of electroless nickel-boron will be presented first, then the research about the initiation and formation of other electroless coatings (Nickel-Phosphorous and ternary alloys) will be described.

7.1.1   Work carried out on electroless nickel-boron deposit formation.

There are two main works describing the formation of electroless nickel-boron coatings, as was already said in section 2.1. Dr Clerc's thesis, written in 1986 [54] is the most extensive but Rao's work that was published in 2005 [56] is also of great interest.

Clerc worked with a borohydride reduced bath (of a slightly different composition that the one developed by Dr Delaunois) that uses nickel chloride, ethylene diamine (as a complexing agent), sodium hydroxide, lead chloride (instead of lead tunsgtate in our case)

and mercapto-2 benzothiazol (as a brightening agent, that is not used in Dr Delaunois'
bath). The bath temperature was maintained at 95 ± 1 ℃, with a pH of 14 and a bath
load of 1 dm^2/l. The bath was not agitated by any means other than natural convection.

The samples used for Clerc's study of deposit growth were made of ARMCO iron.
They were plated for times varying from 5 to 60 minutes (by 5 minutes intervals). The
influence of different parameters such as grain size, substrate roughness and bath temper-
ature was observed.

She observed a columnar growth of the deposit that could be divided in 3 phases,
each one corresponding to one stratum of the deposit. During the first phase, which in-
cludes the first 2.5 μm of the deposit, the thickness of the columns is close to 0.1 μm and
is clearly observed on the sample surface. During the second phase, wider columns are
growing and the surface texture has been qualified by Clerc as 'walled'. This phase begins
after the deposition of approximatively 2.5 μm and ends after 5-6 μm. The last phase of
the deposition, including the topmost part of the deposit, is constituted of columns with a
diameter close to 0.5 μm. The deposition rate differs during the process: it is the highest
during the third step and the lowest during the second one.

This three-layered deposit morphology is not modified by the experimental parame-
ters but the arrangement of the columns is modified by the roughness of the substrate:
rough substrates induce a fan-like arrangement of columns that induces an increase of the
part's roughness after deposition while the columns formed on smooth substrates are par-
allel and lead to a slight decrease of the part's roughness by a leveling effect of the deposit.

Rao also used a borohydride reduced bath, with nickel chloride complexed with ethy-
lene diamine and lead ions. However he used potassium borohydride and does not state
which lead salt was used. The pH of the bath was fixed at 13 and the temperature at 85
$\pm$ 1℃. The bath was not agitated nor replenished. The substrate was mild steel.

By a combination of low penetration X-ray diffraction and etching (by sputtering),
Rao et al. observed an increase in deposit crystallinity from the surface to the substrate.
They attribute this to an influence of the substrate structure on the structure of the de-
posit that decreases when the deposit gets thicker.

They also studied the morphology of cross sections of the coatings at different stages of
the deposition process and observed firstly the typical columnar morphology of electroless
nickel-boron deposits. However, later in the deposition, the columnar growth gave place
to a nodular one. They attributed this phenomenon to a diffusion layer, formed on the
top of the deposit when the bath is depleting, that slowed the growth of the columns (as
shown on figure 2.5 (page 27)) and induced the germination of a nodular layer on areas
where the diffusion films is broken by bubbling of evolved hydrogen.

7.1.2 Work carried out on the initiation of other electroless deposits.

The morphology of electroless nickel-boron deposits is not very similar to nickel-phosphorous (which usually present a layered morphology with a very smooth surface) or other electroless nickel deposits [2]. As such, work carried out on the formation of those deposits would not be useful in the present context. However, a review of the studies done on deposit initiation is relevant because such work is quasi non existent in the case of nickel-boron.

First of all, it should be noted that a lot of studies are dedicated to the trial of various activators and catalysts that allow deposition of electroless nickel on all kinds of surfaces [128–131] but they are mostly centered on the resulting coating and few of them focus on the catalyst's effect on the first steps of deposition. Examination of the first steps of the deposition process without the application of a catalyst is nearly unheard of.

The most popular catalyst seems to be palladium which is the subject of a number of studies. Li et al.[132] used an acidic $PdCl_2$ solution to sensitize the surface of SiC_p/Al composites for the deposition of NiP. They observed that the palladium was adsorbed on the surface partly as clusters of $PdCl_2$ and partly as Pd(0). After immersion in the bath, the Pd(2+) species are reduced into Pd(0) by the hypophosphite. This allows the nucleation of the nickel deposit which appears first as hemispheric grains that grow simultaneously vertically and laterally until the whole surface of the sample is covered.
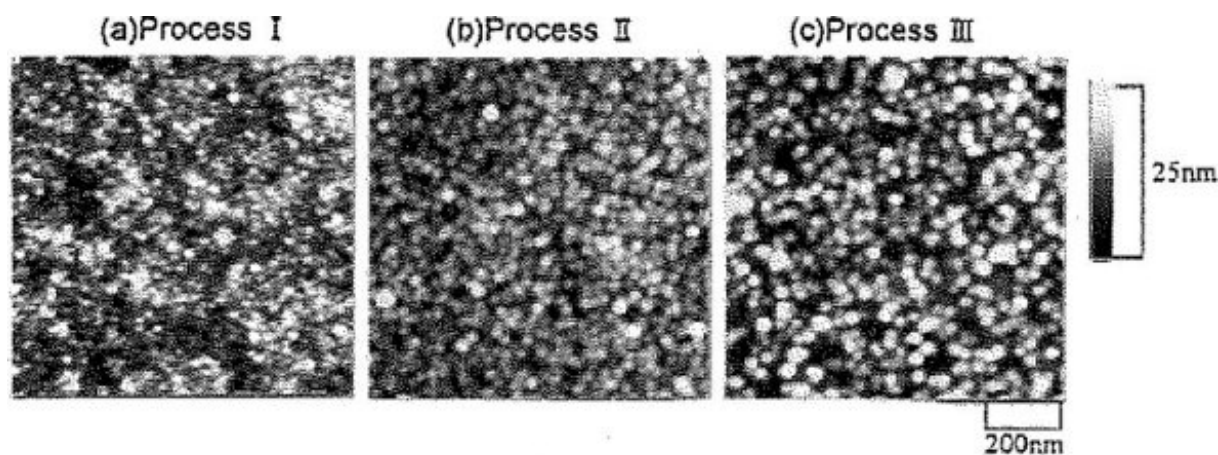
Fig. 7.1: TMAFM image of electroless NiP films on polyimide at the initial stage of deposition with various activation methods [133].

Homma et al. [133] used several variations on the $PdCl_2$ activation process to sensitize a polyimide substrate. They then observed the formation of the deposit by tapping mode atomic force microscopy (TMAFM). They observed the nuclei formed at the very first stages of deposition (see figure 7.1) and compared the nucleation density obtained after the different activation processes. They observed that all the films were constituted of aggregated 'particles' with a size from a few to 10 nm and that the films differed only in the aggregation state of the 'particles' (observable by the size of the aggregates, see

figure 7.2). However when the thickness of the film reaches 2000 nm, the differences due to the initial germination density are completely leveled. They also affirm that the film formation takes places by germination and growth of successive very small 'particles'.
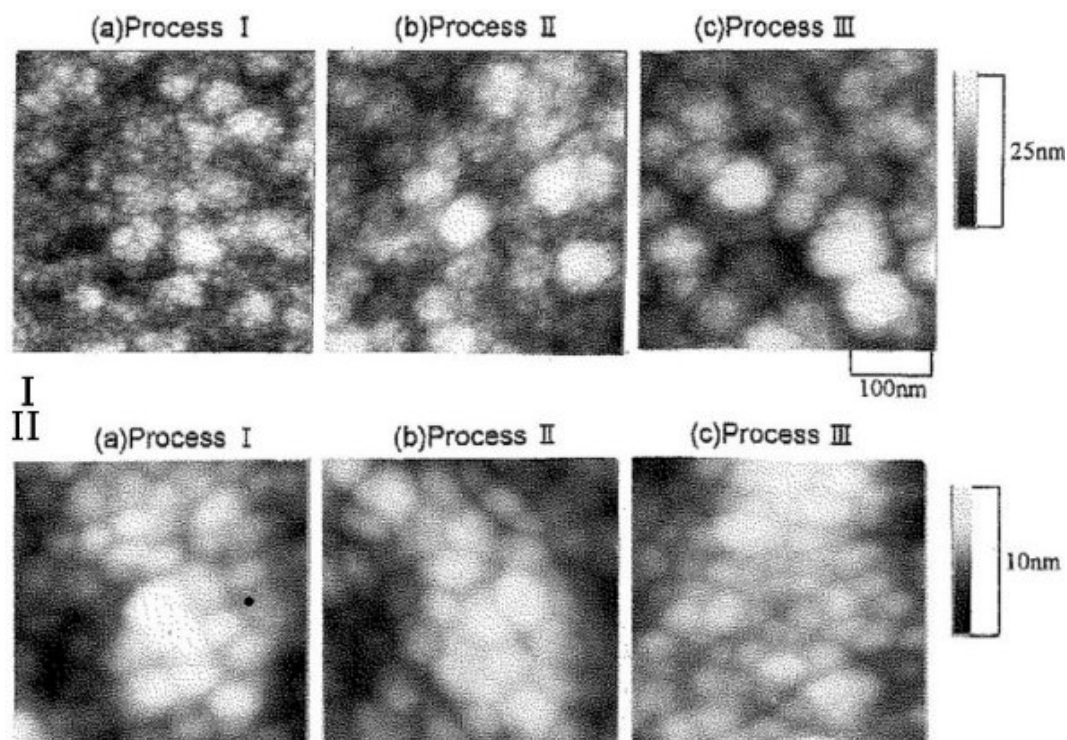
Fig. 7.2: TMAFM image of electroless NiP films on polyimide morphology of the grains [133].
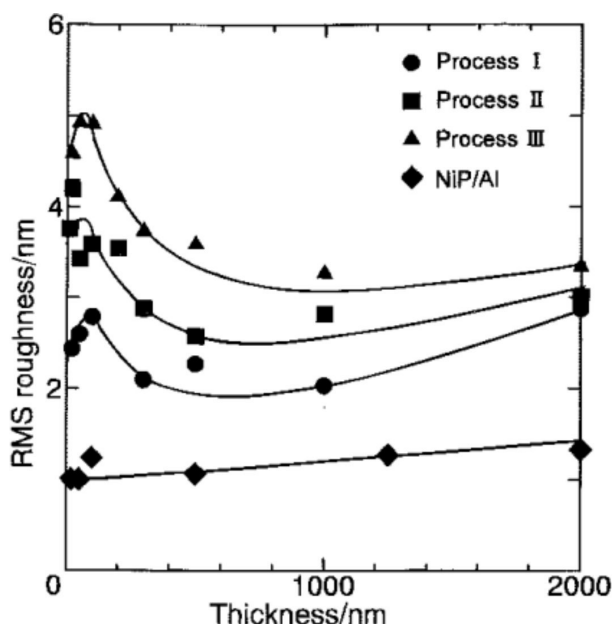
Fig. 7.3: Roughness evolution of NiP films during their formation [133].

They also observed nucleation on an NiP/Al surface and noticed a similar comportment but with an higher nucleation density, the size of the 'particles' or grains that form on that surface being the same as on sensitized polyimide.

Furthermore, they measured the roughness of the growing films and observed an initial increase of roughness followed by a leveling for the unconductive substrate while they observed a monotonous increase of roughness on the NiP/Al substrate (which was originally smoother), but at a lower level, as shown on figure 7.3.

Matsubara et al. [18, 19] carried out an in situ study of the formation of electroless NiP films with a quartz micro-balance, completed by TEM observation of peeled off films. The substrate used for this study (polyimide and quartz micro-balance sensor) were catalyzed with palladium prior to the experiment. They observed, in the very first stages of deposition, an induction period of approximately 20 seconds before the nucleation of the deposit, then a period of fast growth, followed by a decrease of deposition rate down to a stabilized level (see figure 7.4).
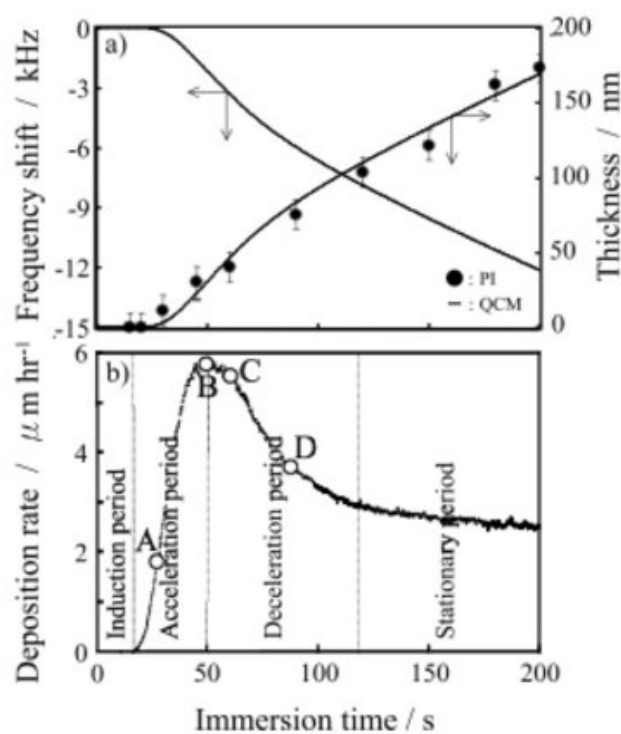
Fig. 7.4: Deposition rate and thickness evolution observed by QCM method [18].

Their observation of the first stages of deposition by TEM showed that the process began on some of the catalyst particles to form islands that then grow up to the formation of a continuous film (obtained for a thickness close to 40 nm, at the beginning of the deposit rate deceleration). A cauliflower-like texture is very quickly formed, as shown on figure 7.5.
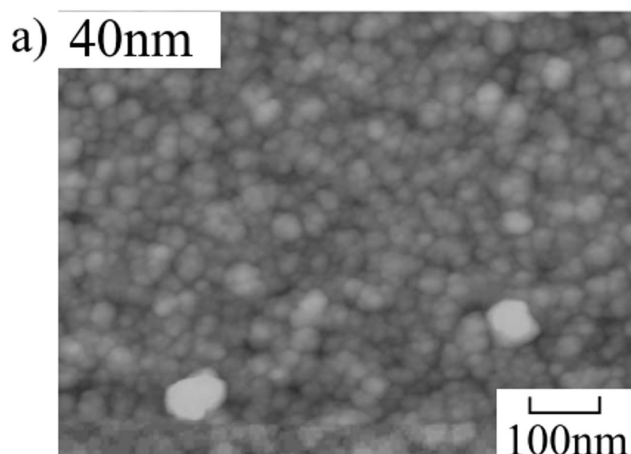
Fig. 7.5: Surface morphology of an electroless NiP coating with a thickness of 40 nm measured by AFM [18].
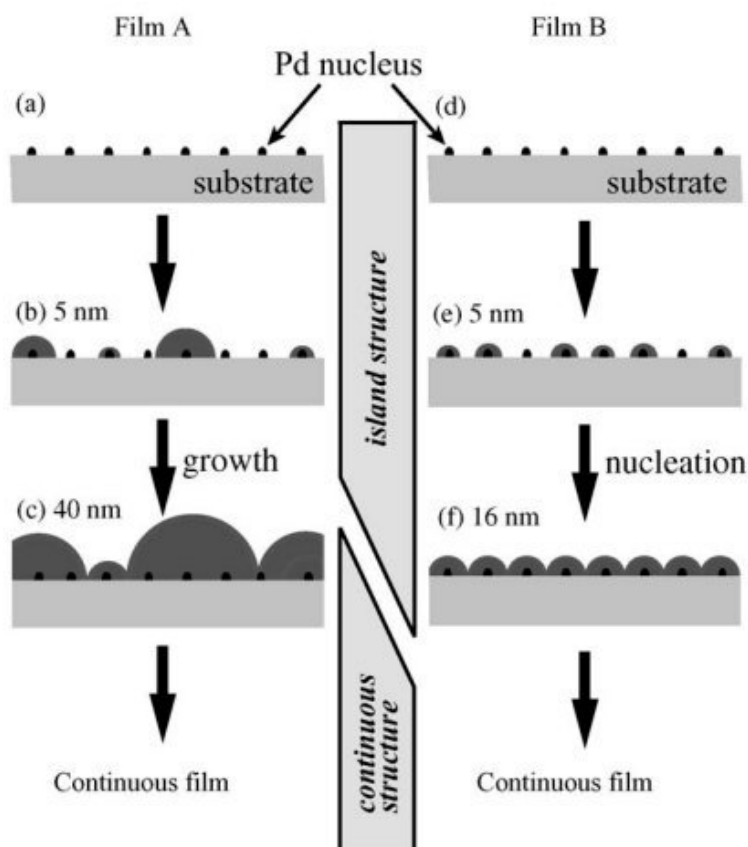
Fig. 7.6: Model of initial deposition of NiP on Pd-catalyzed surface [19].

Matsubara et al. also observed a grain size in the nanometer range in their NiP films. This grain size decreased from 34 down to 10 nm when the nucleation density increased. However, it was not linked to the density of palladium nuclei adsorbed on the surface but to the bath chemistry and deposit composition. Those authors established a schematic

model in which they describe the initial deposition of NiP (presented on figure 7.6): the deposition is in all cases initiated at the palladium nuclei (which have a similar density) but the density of grains is higher in case B (which has a slower growth rate) than in case A in which the grain growth is the most important phenomenon and where unused Pd nuclei are covered by growing grains instead of being used as germs for the formation of new ones. This growth-based process leads to bigger grains and to an increase of the transition thickness between the island and continuous structures. On the other hand, in case B, where growth is slower, the more important mechanism is germination and an higher density of smaller grains is obtained, meaning the thickness required to obtain a continuous deposit is smaller. The main factor influencing the growth morphology seems thus to be the autocatalytic activity of the deposit itself: the lower this activity, the thinner the continuous deposit.

The initiation of electroless deposition on magnesium alloys, mainly after fluoride activation, has been studied by several authors in recent years [134–138]. Liu [135], Ambat[136] and Anik[137] have observed the initiation of electroless nickel-phosphorous deposit on AZ91 magnesium alloys after fluoride activation. They observed that the deposit nucleates primarily on the grain boundaries of the β phase then spread progressively to the whole surface, as shown on figure 7.7. Ambat et al attributed this to a galvanic coupling effect between the more cathodic β phase and the α phase in the magnesium alloy. They also observed that the deposit grows slower, is discontinuous and has a more important defect density on the β phase.
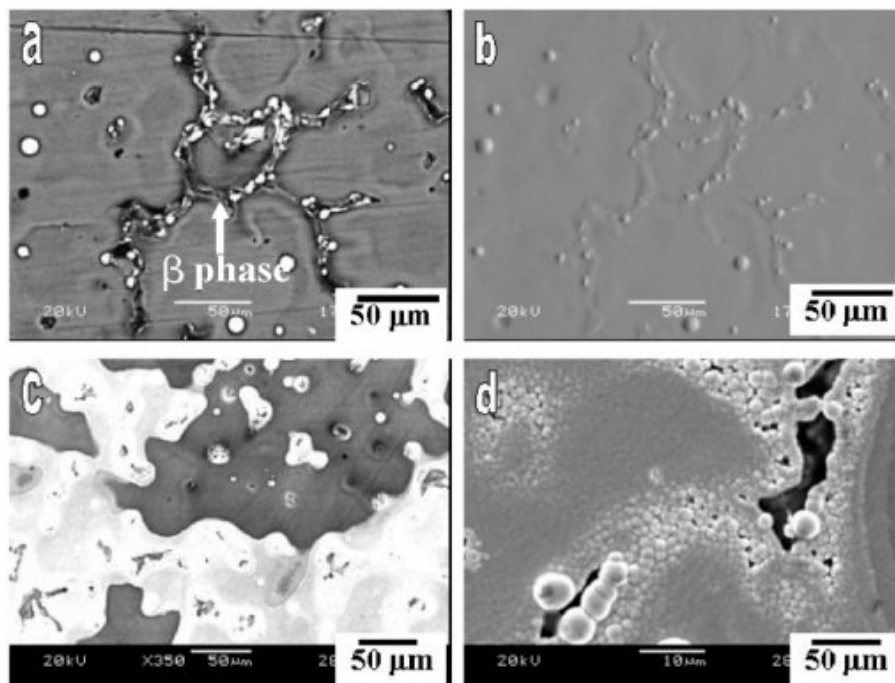
Fig. 7.7: Initiation of electroless deposition on the β phase of AZ91 Magnesium alloy. [136]
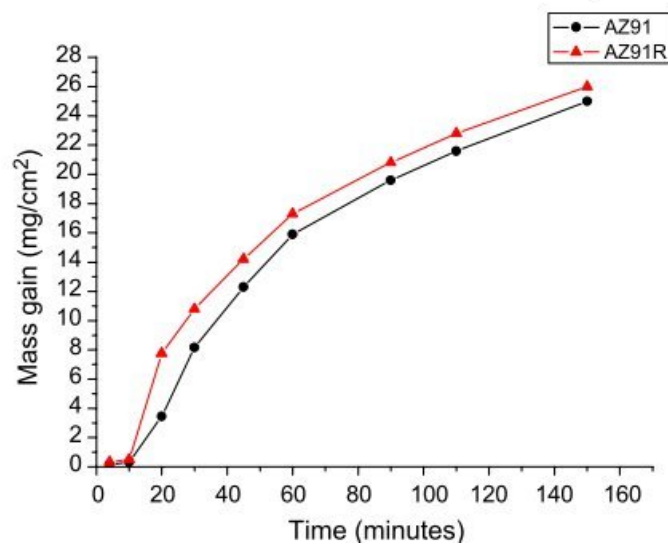
Fig. 7.8: Kinetics of deposit growth on smooth and rough AZ91 Mg alloy. [135]

Liu [135] observed the deposition rate on AZ91 magnesium alloy (see figure 7.8) and noticed a rather long incubation period at the beginning of the process. The deposition rate was also shown to be higher on the rough substrate than on the smooth AZ91 alloy notably because the first nuclei are bigger and more numerous on the rough surface, as shown on figure 7.9. In another paper, they also showed that the deposition rate is higher, and the induction period shorter on magnesium alloys than on pure magnesium [134], because the galvanic coupling that allows the primary nucleation is not present on the pure metal.
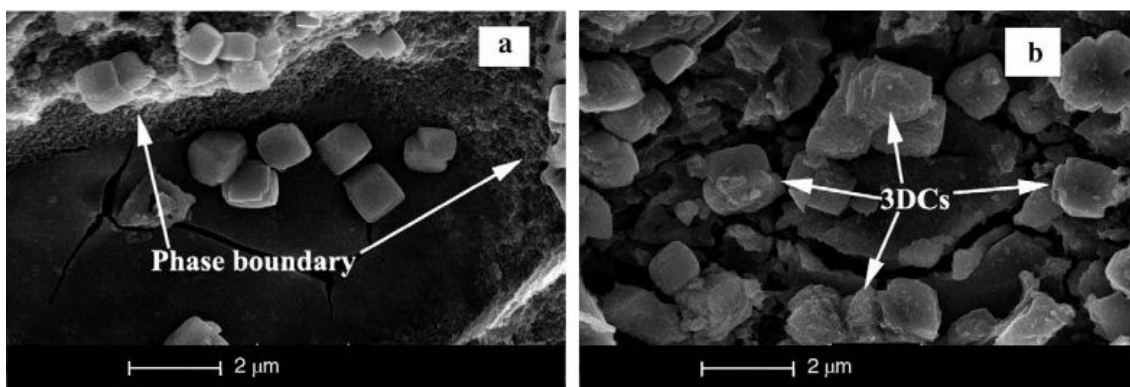
Fig. 7.9: Influence of substrate roughness on germination:
            a) smooth surface; b) rough surface. [135]

Sun et al [138] used a very different method of activation: they coated their magnesium alloy with a composite of an organic adhesive and TiB_2 particles that have a catalytic activity for the deposition of electroless nickel. As the surface of the alloy is completely coated by the adhesive, the initiation of the coating is very different than what was observed by the other groups.

Finally, Khan et al [139] studied the initiation of electroless deposition on the surface of zincated aluminum alloys. In this case, the deposition process is initiated by the anodic dissolution of the zinc layer, the nickel coating is thus deposited on an oxide-free aluminum surface, as shown on figure 7.10.
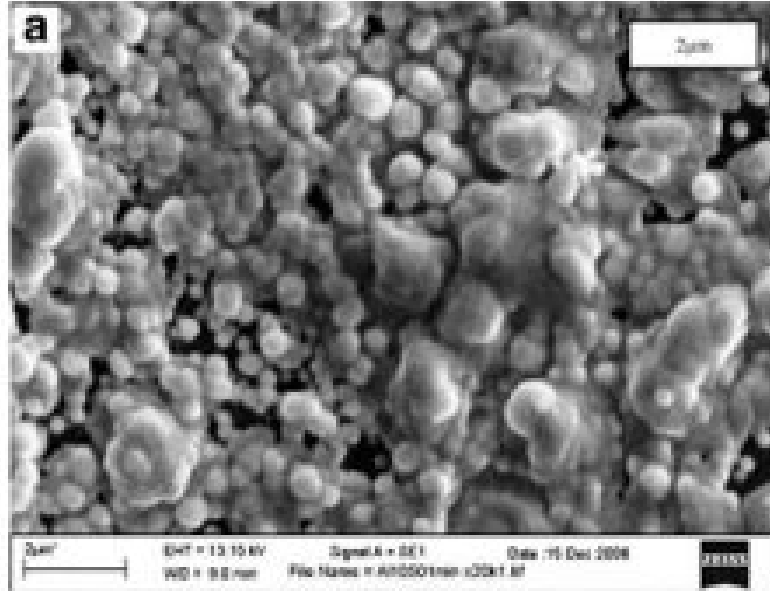
Fig. 7.10: Initiation of electroless nickel deposit on zincated aluminum surface. [139]

7.1.3 Conclusion.

In the literature review presented hereover (in sections 7.1.1 and 7.1.2), most of the research is dedicated to either the initiation of electroless nickel-phosphorous coatings on a determined substrate after a catalysis process (as in the case of non-conductive substrate, aluminum or magnesium) or the growth of the deposit in un-agitated conditions. As we are working with a non-catalyzed (the activation phase consists only of an etching of the oxide layer formed on the steel sample) and agitated system, the data we found in this review cannot be a priori applied in our case. The system used in this study will thus have to be characterized for the initiation and germination of the deposit, but also for the growth phase, as it is possible the comportment of an agitated system is different from an unagitated one. The results obtained will then be compared to the literature to get a more complete understanding of the phenomena.

The influence of roughness and substrate nature (monophased, polyphased and composition) on the initiation will also be examined.

7.2   Study of the initiation of electroless nickel-boron deposits.

7.2.1   Introduction.

The study of deposit initiation will be carried out in 3 phases. The first phase will be dedicated to the observation of electroless nickel deposition on the substrates that are usually used for this study (hand polished mild steel sheets), which will constitute the reference state. After this, two parameters will be examined separately and compared to the reference state: the roughness of the substrate that will be modified by varying the grade of the last grinding paper and the nature of the substrate.

7.2.2   Study of deposit initiation on polished mild steel.

This study was carried out on mild steel (St 37) coupons that were submitted to the usual surface preparation process for this kind of alloy (see section 5.2 for details). The samples were immersed in the plating solution from 5 second up to 4 minutes, as shown in table 7.1.

Sample number	1	2	3	4	5	6
Deposition time	5s	15s	30s	60s	90s	4min (240s)

Tab. 7.1: Deposition time for the observation of the initiation of electroless deposits.

To assess the germination sites and the initiation mechanism, the progressive colonization of the surface, and other parameters linked to the first stages of the deposition process, the surface was investigated by several analytical techniques, such as SEM, EDX and XPS analysis and roughness measurement.

7.2.2.1   Surface and cross section observations.

The surface morphology of the samples will be examined first. Immersion in the bath up to 15 seconds brought no evidence of nickel deposition detectable by SEM observation. This period can be considered, as far as the microscopic observation is concerned, as an induction period. The first nodules of electroless deposit are observed after an immersion of 30 seconds and are preferentially concentrated on the scratches and defects of the surface. As can be seen on figure 7.11a, they do not form a continuous layer yet and their size is in the range of 0.1-0.2 μm. The shortness of this induction period is in good agreement with the fact that the rate-limiting step of the process is sodium borohydride diffusion towards the active surface (see section 6.3.3.2.2.2).

60 seconds after the immersion, the whole surface has been colonized by the aggregates but the layer formed is not yet continuous (see figure 7.11b). Observation at higher magnification (figure 7.11c) shows that, on some part of the samples, the deposit is already constituted of several layers of nodules. At this stage, the size of the nodules is close to 0.5 μm.
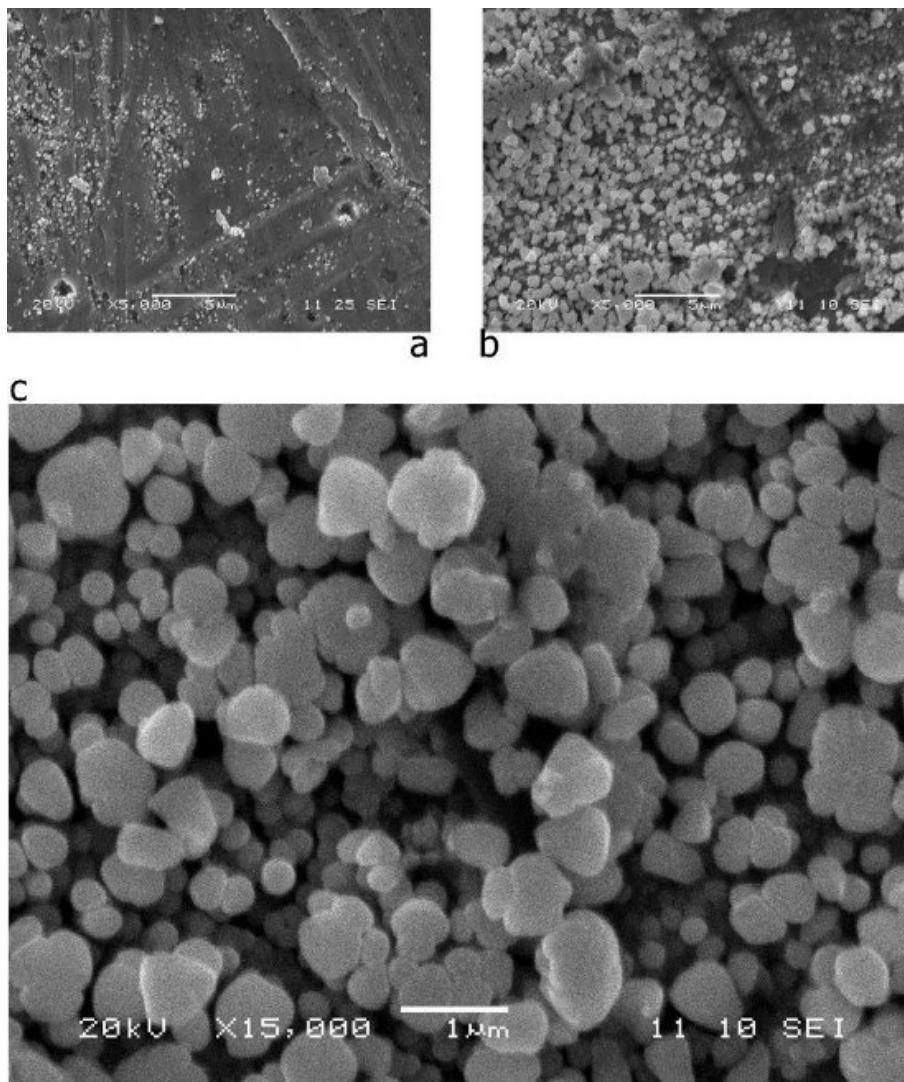
Fig. 7.11: SEM image of the surface of a steel sample after immersion in the electroless nickel-boron bath for 30s (a) and 60s (b and c)

After 90s and 4 minutes (240s) of plating, the size of the nodules is bigger and the surface appears to be more leveled, as can be seen on figure 7.12. This will of course have to be confirmed by roughness measurements on the samples.

On cross section observations, a very thin and continuous layer of nickel can be seen near the interface after an immersion of 90s (see figure 7.13a). Over this layer, nodules of various size can be seen growing. The presence of this continuous layer under a low-compacity arrangement of nodules suggests that some nickel must be deposited before the formation of the nodules (probably during the very first seconds of immersion), in such a way as not to modify the topography of the surface and thus not to be observable on the SEM micrographs. After an immersion time of 4 minutes (240s), the whole surface is colonized and the nodules have begun to coalesce (see figure 7.13b). The coating thickness reaches then nearly $1\mu m$ and the porosities are beginning to close.
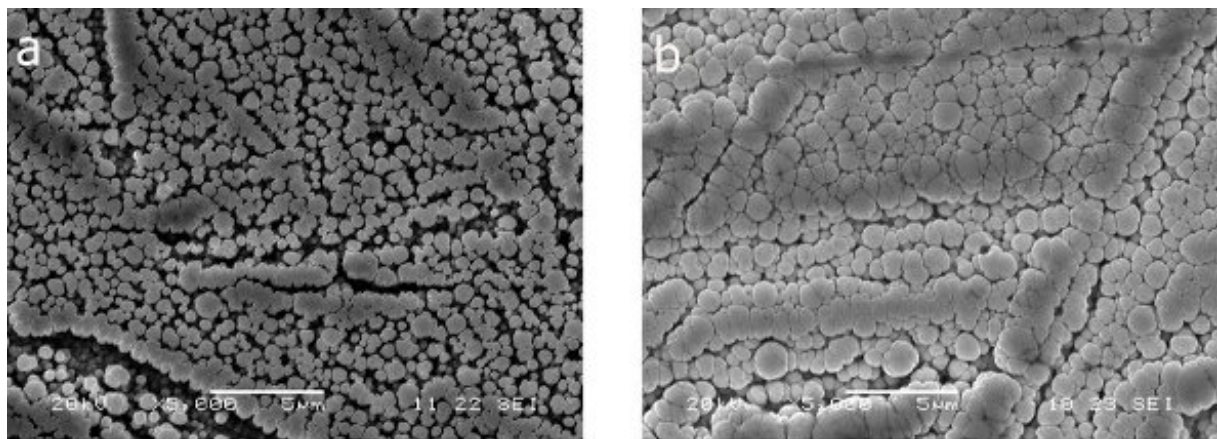
Fig. 7.12: SEM image of the surface of a steel sample after immersion in the electroless nickel-boron bath for 90s (a) and 240s (b)
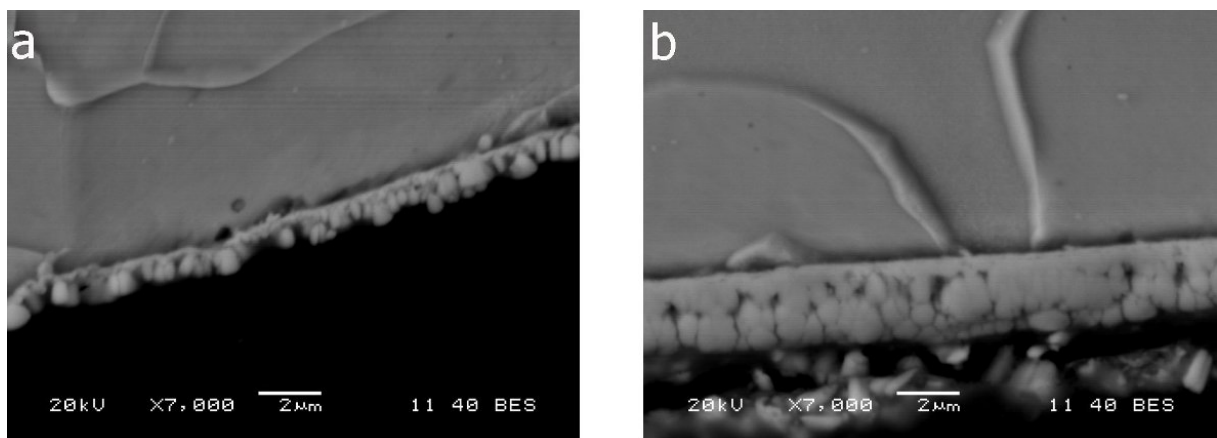
Fig. 7.13: SEM cross section of a steel sample after immersion in the electroless nickel-boron bath for 90s (a) and 240s (b).

7.2.2.2   Roughness.

Figure 7.14 presents the evolution of roughness during the plating process. This confirms the observations made during the previous experiments: the roughness of the sample increases during the beginning of the process because of the formation of isolated nodules (islands). It then decreases up to a plating time of 4 minutes because a continuous layer is progressively formed. The depths of valleys (R_v) increases more than the height of peaks (R_p) which is not surprising, knowing the morphology of the deposit at this stage of growth: the deposit is formed of nodules that grow close together but there are some spaces left between them (the valleys). Other than that, all parameters evolve in a similar way. The evolution of roughness during the first stages of plating is in accord with the results of Homma et al. [133], that were shown on figure 7.3 on page 96.
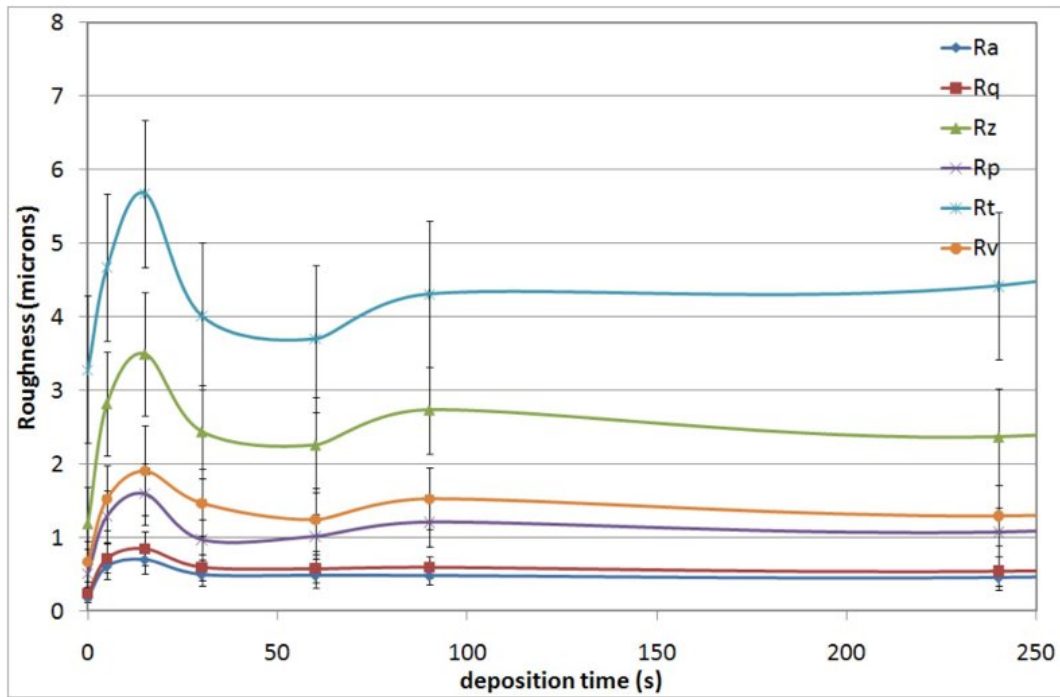
Fig. 7.14: Roughness evolution of electroless nickel-boron coated steel during the plating process.

7.2.2.3 EDX analysis.

EDX analysis was used to determine a 'nickel coverage ratio' of the coating. To obtain consistent results, a surface of 1 square millimeter (1 mm^2) was analyzed at a magnification of 100 times, during 60 seconds. The results of this analysis represent the composition measured on the surface of the sample. However, this does not represent the uppermost surface because, contrary to XPS analysis that only interact with the first 60 nm of the coating, the penetration depth of the EDX analysis is of the order of $1\mu m$. Moreover, as boron is not detected by this technique, the nickel/iron ratio cannot be used as a quantitative tool. Nevertheless, this analysis allows to detect the complete absence of nickel on the surface and gives qualitative indications about the formation of a continuous coating.

As can be seen in table 7.2, while no nickel is detected after 5 seconds of immersion, a non negligible amount is already measured after 15 second, while no nodules are observed. The induction period is thus shorter than 15 seconds as far as chemical analysis is concerned.

Deposition time	5s	15s	30s	60s	90s	4min (240s)
Fe (%)	100	94.3	81	42	26	7
Ni (%)	0	5.7	19	58	74	93

Tab. 7.2: Evolution of the surface composition (by EDX analysis) during the first stages of deposition.

As the nickel deposited after 15 seconds cannot be observed by SEM, it is highly probable that either a very thin continuous layer is formed on the whole surface or the nickel is present on the surface as nuclei too small to be observed. A mapping of the surface indicated that the nickel is homogeneously distributed on the surface, thus reinforcing the idea of a continuous layer, such as the one observed on cross sections of the samples immersed for 90s.

After a plating time of only 30s, the amount of nickel detected is already close to 20%. The nodules that are observed on the surface cover a quite smaller fraction of the sample. This suggest that a non-negligible amount of nickel is detected outside of the nodules. After 60s, the nickel content reaches 60%, which confirms that a nearly continuous layer is formed. The continuity is attained after 4 minutes, as indicated by the SEM observations.

7.2.2.4   X-ray Photoelectron Spectroscopy (XPS) analysis.

As EDX analysis does not give information about the surface of the sample but about the sub-surface (roughly the top $1\mu m$), X-ray Photoelectron Spectroscopy (XPS) analysis were carried out in order to obtain information about the composition of the last deposited material (the instantaneous composition of the deposit). The aim of this experiment was to detect the time of the complete disappearance of the iron signal, and thus of the formation of a continuous film.

Deposition time (s)	15	30	60	90	240	600	3600
Fe (at.%)	31.22	28.58	23.86	26.39	18.67	16.04	24.28

Tab. 7.3: Evolution of the iron content at the surface of the sample (by XPS analysis) during the first stages of deposition.

The first noteworthy result obtained by XPS analysis is that, contrary to our expectations, it cannot be used to determine when a continuous coating is formed: an important amount of iron is detected on the surface of the sample even after one hour of plating, as can be seen in table 7.3. We were able to ensure that the iron that is detected does not come from the bulk of the coating by GD-OES analysis (the results of this analysis are presented and discussed in section 7.3.1.3). However, a non-negligible amount of iron was also detected at the very beginning of the GD-OES analysis (even before any nickel is detected). It is thus quite sure that the detected iron comes from a superficial contamination of the samples. It was impossible to identify the origin of this pollution but it is possible that the iron come from the bath or the bath surface (the samples are only rinsed once between the etching and plating and some iron could be dissolved in the plating solution), from any other ulterior manipulation (the samples are weighted on a metallic scale, cut to size with metallic shears, ...) or even from exposition to iron dust in the lab (in some places of the lab, iron and steel samples are cut, polished and manipulated every day, which produces iron dust that can then deposit on the samples left nearby).

While the XPS results are not exploitable to determine the formation of a continuous coating, they confirm the information gained from the EDX analysis that there is already

a non-negligible amount of nickel deposited on the surface of the sample after 15s. In this case, even boron and lead are already detected at the following levels (including the iron substrate and possible iron pollution): Ni: 57.15 at.%; B: 11.35 at.%; Pb: 0.29 at.%; Fe: 31.22 at.%.

Other interesting information, like the evolution of the composition of the last formed deposit was obtained from the XPS results. It will be discussed in section 7.3.1.5.

7.2.2.5   Initiation mechanism.

The SEM observation and EDX analysis do not allow to identify the mechanism that induces the initiation of the deposit formation: a non-negligible amount of nickel has been detected on the surface after a very short time but this nickel does not appear to form the typical nodules of electroless nickel-boron deposits. The presence of this nickel can be attributed to 2 phenomena:

1. The formation of an ultra thin layer of nickel by displacement (redox reaction between nickel ions and the substrate, accompanied by dissolution of the substrate material, without intervention of the reducing agent).

2. Deposition of a very thin nickel layer by the electroless process (catalytic oxidation of sodium borohydride and reduction of nickel salts) on which the growth is then impeded by lead adsorption.
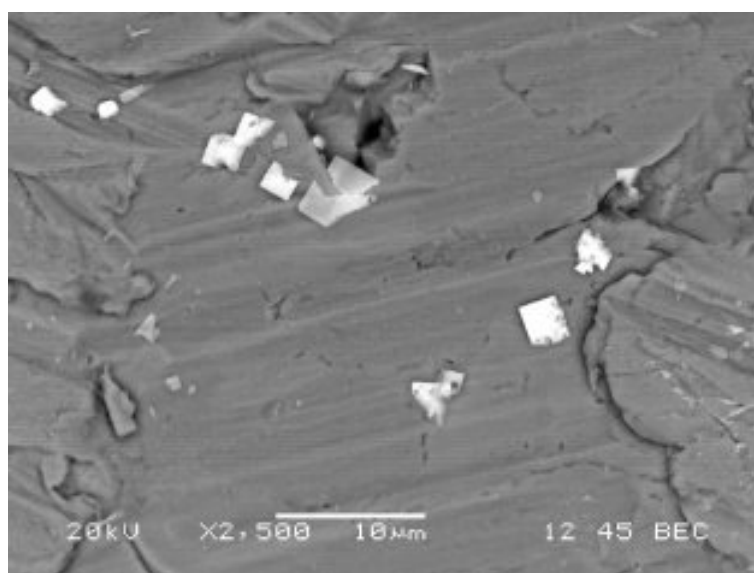
Fig. 7.15: SEM observation of the surface of a sample immersed in a bath exempt of reducing agent for 240s.

To identify the mechanism taking place in our bath, an experiment was carried out in a bath exempt of the reducing agent, every other parameter kept constant. The samples were immersed in this bath for the same lengths of time as for the previous experiment

(see table 7.1) and were then observed by SEM. No nickel was detected on any of the samples, even after an immersion of 4 minutes. However, lead has been detected on the surface by EDX and forms small cubic crystals that are concentrated on the surface defects (polishing scratches, ..), as shown on figure 7.15. This observation allows to exclude that the deposit is initiated by displacement, as this reaction would have happened without the reducing agent were it the case. The formation of lead crystals is however attributed to a displacement reaction between iron and lead, which is not really surprising because the redox potential of lead is higher than nickel and iron (-0.47 V for Fe^{2+}/Fe ; -0.27 V for Ni^{2+}/Ni ; -0.13 V for Pb^{2+}/Pb).

7.2.3   Influence of substrate roughness.

It is well known by the electroless platers that the state of the substrate has a great influence on the plating process, but also on the coating's properties. Among research about of this kind, lets emphasize two: first, the work of Liu [135] about the influence of the roughness of a magnesium-based alloy; secondly a study that was carried out by Lee [140] about the influence of substrate roughness on the corrosion resistance of electroless Ni-P.

The substrate roughness is a parameter that is sometimes difficult to control in an industrial process: the parts are often supplied by the client without particular surface preparation, and most of them have complicated geometries (because the plating of this kind of parts is a major application of electroless plating), which makes mechanical preparation (such as grinding) difficult to implement. As such, it is of great interest for the final application of the process to gain the most extensive knowledge of the influence of the substrate surface condition on the initiation. This will allow to judge more effectively when and which preparation process is needed.

To study the influence of this parameter on the initiation, we will follow three main properties of the coating: the morphology of the coating, the coverage (as measured by EDX analysis), and the roughness. This will be carried out on substrate having been submitted to 5 different mechanical preparation processes, as described in table 7.4, before the chemical step of the surface preparation. The samples where then left in the plating bath for the same lengths of time as previously (see table 7.1).

The parameters chosen to represent the roughness in this study are R_a (arithmetic average of the height of every point of the surface) and R_p (maximum peak height). R_a was chosen because it is the most in use roughness parameter. However, as the electroless process takes place in solution, we feel that the peaks will have a more important contribution to the deposit initiation and growth than the valleys, thus we chose to use R_p conjointly with R_a.

Table 7.4 shows that grinding with grade 220 SiC abrasive paper (P1) induces a slight decrease of R_a with a non negligible increase of R_p. Here follow the results of ordering the samples from the rougher to the smoother according to R_a : NP, P1, P3, P2, Complete;

	Process description	$R_a(\mu m)$	$R_p(\mu m)$
NP	unpolished substrate (as received)	0.674±0.111	1.896±0.502
P1	polished with grade 220 SiC paper	0.559±0.144	2.122±0.467
P2	polished with grade 1200 SiC paper	0.294±0.084	1.103±0.515
P3	polished with grade 4000 SiC paper	0.476±0.120	1.759±0.596
Complete	polished with grade 1200 and 4000 SiC paper (usual preparation process)	0.184±0.0640	0.510±0.329

Tab. 7.4: Mechanical preparation processes for substrate roughness influence on deposit initiation.

and according to R_p: P1, NP, P3, P2, Complete.

The P3 sample, which has been ground with 4000 grade paper only is rougher than the sample ground with grade 1200 paper (P2) because this paper, when used without pre-grinding, provides a less effective surface preparation. The P1 sample has an higher R_p roughness than the NP sample but this difference is not statistically significant because the standard deviation for both values (close to 0.5) is higher than the difference between them.

7.2.3.1 Influence of the substrate roughness on the coating morphology during the first stages of deposition.

After a plating time of 5 seconds, the increase of substrate roughness favors the deposit initiation, as shown on figure 7.16: the sample with the complete surface preparation treatment is exempt of nodules and their density increases on the other samples with increasing roughness. Moreover, the size of the nodules present on the surface appears smaller when the roughness is higher, with a nodule size of the order of 50nm on the unpolished surface. This shows that the germination of the nickel nodules on the substrate is easier when the substrate is rougher. The higher density of nodules on the rougher substrate is in accordance with the findings of Liu et al [135] but we don't observe the formation of bigger nodules on the rougher substrate as they do. However the NiP does not form nodules on the Mg alloy substrate but small cubic crystals, which denotes a different initiation mechanism. Moreover, low magnification micrographs on our samples give the impression of bigger deposits on the rougher substrate because aggregates are already formed in this case.

After an immersion of 15 seconds in the plating bath, the density of nickel nodules is still decreasing with decreasing roughness (see figure 7.17) but the size of the nodules appears homogeneous on all the samples and is close to 50 nm. On the smoother sample, the deposition process is not yet initiated.
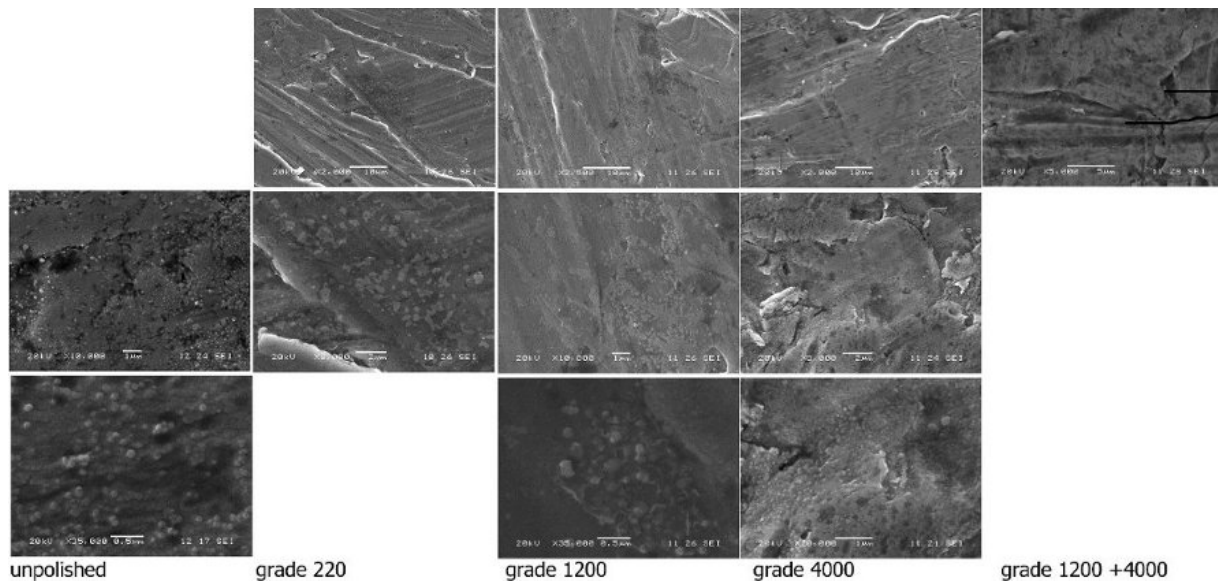
Fig. 7.16: SEM observation of the surface of samples with varying roughness immersed in the plating bath for 5s.
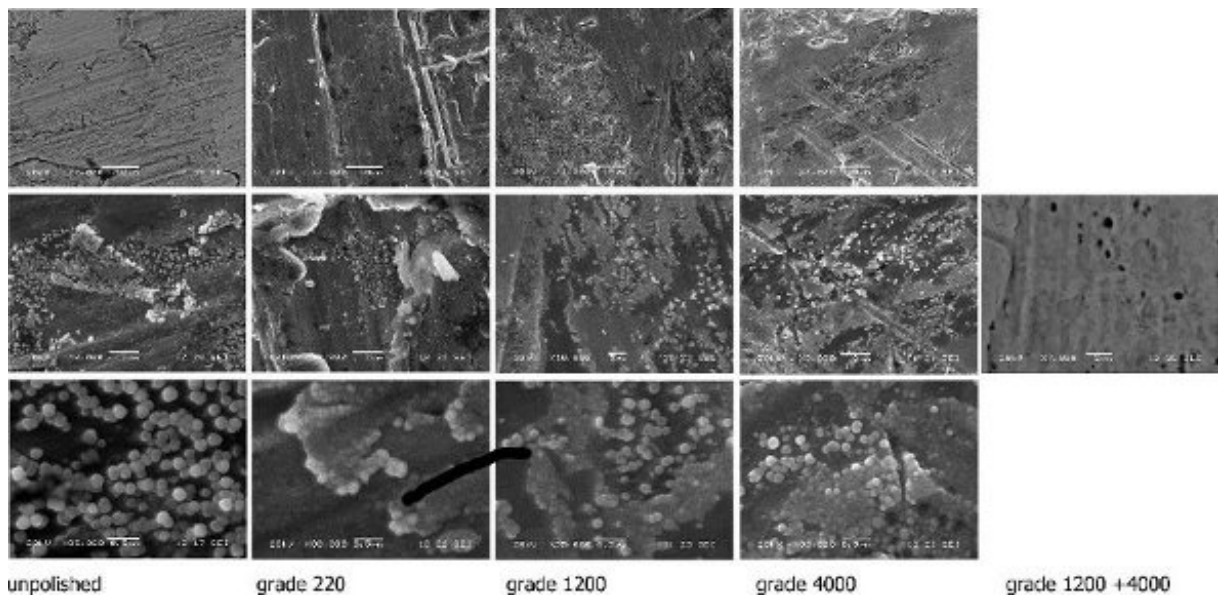
Fig. 7.17: SEM observation of the surface of samples with varying roughness immersed in the plating bath for 15s.

After 30 seconds in the plating bath, the first nodules are observed on the sample submitted to the 'complete' grinding process while the surface of the other samples is nearly completely colonized by the nickel deposit (see figure 7.18). The size of the nodules is still similar for all the samples.

After one minute, all the samples are completely colonized (see figure 7.19). However, the deposit appears more homogeneous on the sample that was submitted to the 'P1' surface treatment (which has the higher R_p), but this will have to be verified by roughness measurements. Longer immersions in the plating bath lead to homogeneization and
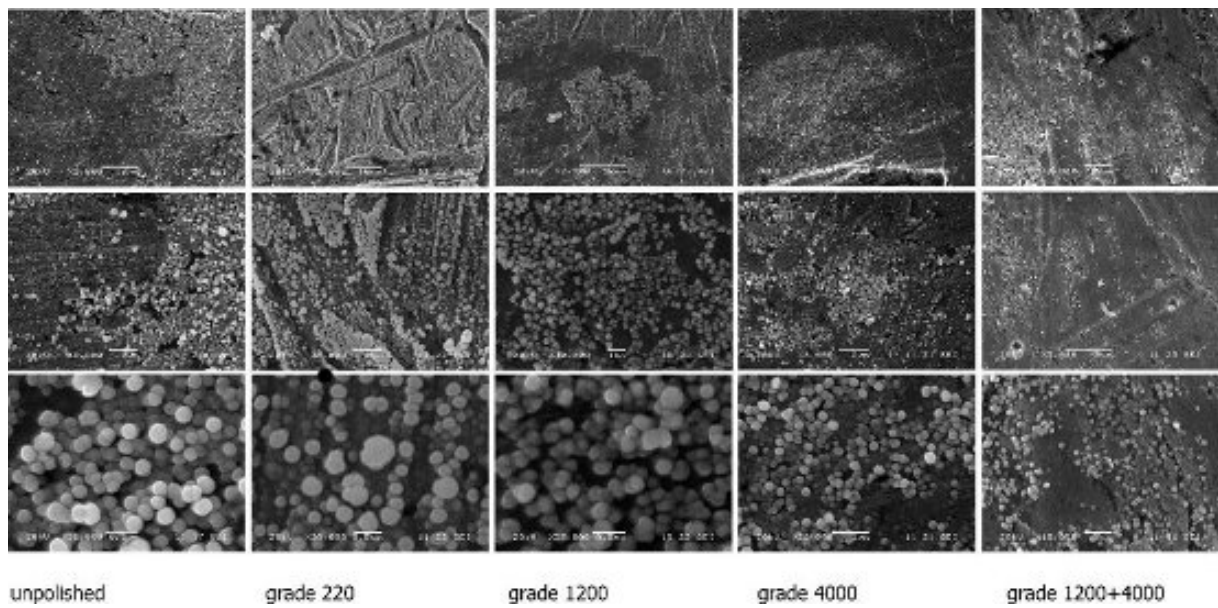
Fig. 7.18: SEM observation of the surface of samples with varying roughness immersed in the plating bath for 30s.
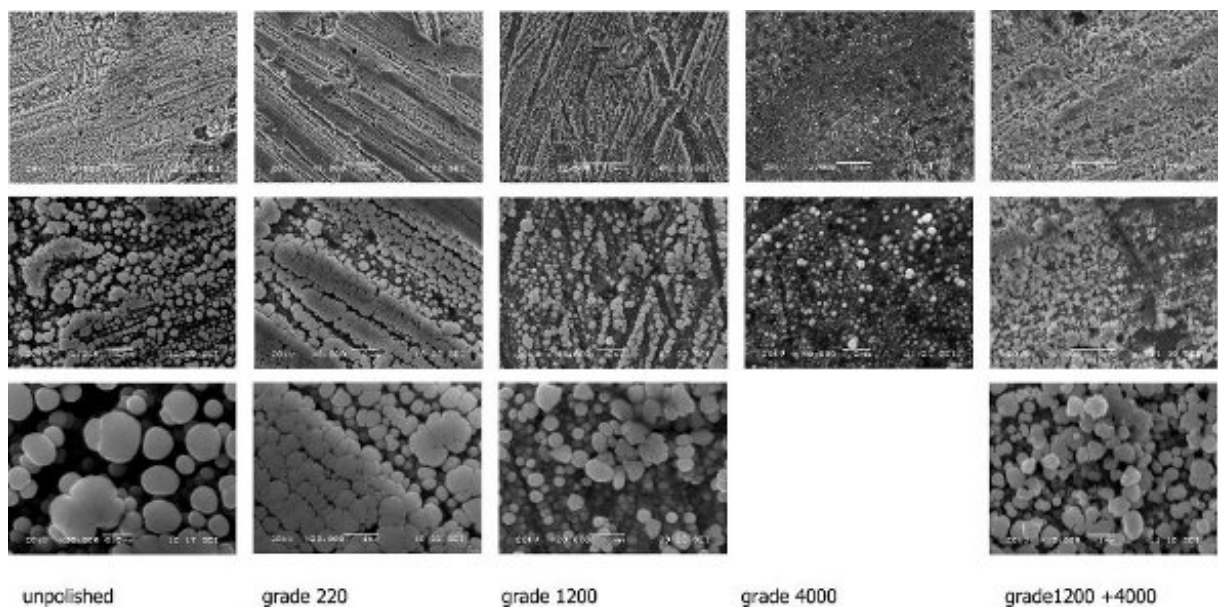
Fig. 7.19: SEM observation of the surface of samples with varying roughness immersed in the plating bath for 60s.

densification of the coating, as shown on figure 7.20. The size of the nodules is still in the same range as in the previous cases but they tend to form aggregates, that are clearly distinguishable on low magnification images while the nodules are only observables at high magnification. Cross section examination reveals that, while the coating appears homogeneous from the surface, it is not yet the case (see figure 7.21). Between 90 and 240 seconds of plating, a transition occurs between three dimensional (equiaxial) nodules and columns growing perpendicular to the substrate. However, the coating is not yet fully

densified.
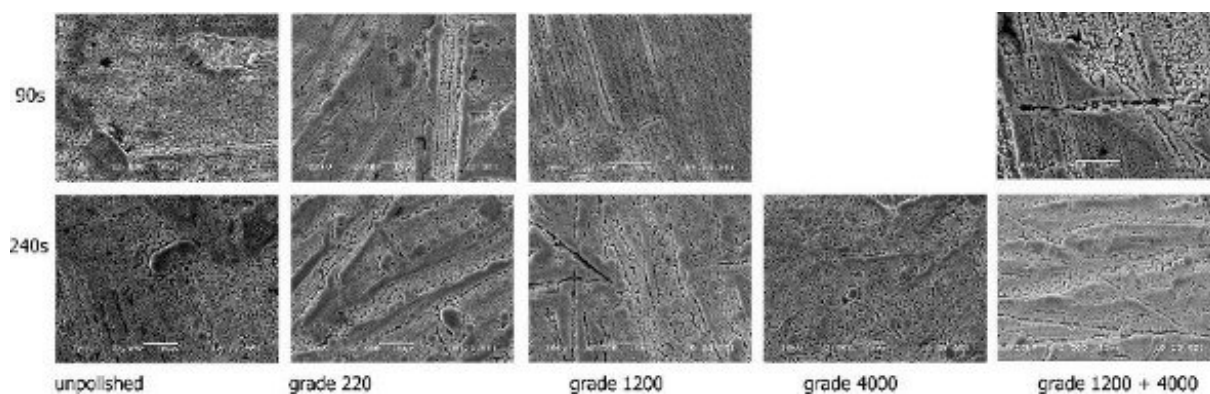
Fig. 7.20: SEM observation of the surface of samples with varying roughness immersed in the plating bath for 90 and 240s.
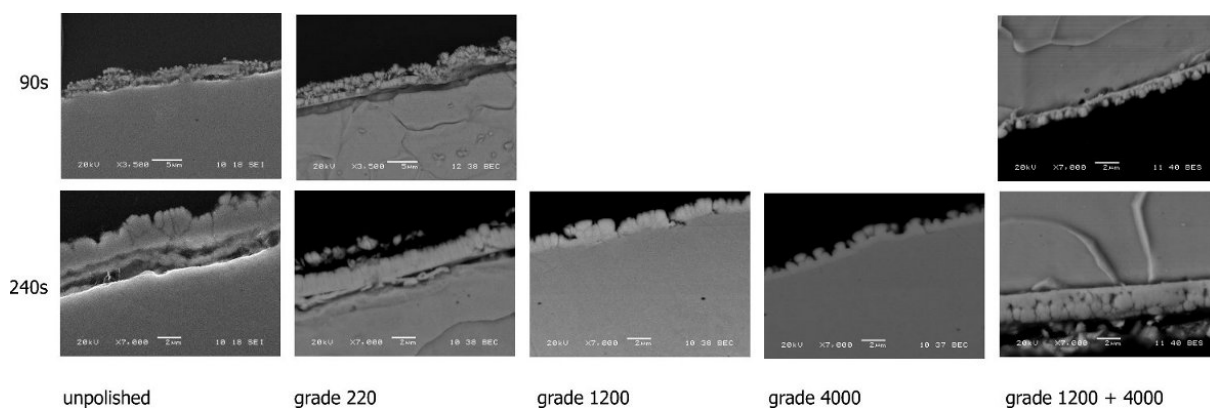
Fig. 7.21: SEM observation of the cross section of samples with varying roughness immersed in the plating bath for 90 and 240 s.

7.2.3.2   Influence of the substrate roughness on the deposition rate.

It is difficult to measure accurately the deposition rate (by weighting or thickness measurement) of electroless nickel-boron in the first stages of the plating process, and thus to compare the deposition rate on substrates with different roughnesses. However, EDX analysis can be used as a qualitative tool to compare the deposition rate coatings of a similar composition: the thicker the deposit, the more nickel is detected on the surface. This technique can be used as long as the coating thickness has not reached the maximal penetration depth of the EDX analysis.

The results of the EDX analysis carried out on substrates with varying roughness are presented in table 7.5 and figure 7.22. After 5 seconds, a similar amount of nickel is detected on the samples with NP, P1 and P2 preparation while the nickel is slightly lower on the P3 sample and completely absent on the 'Complete' sample. This is in agreement with the SEM observation that roughness favors deposit initiation. After 15 seconds, the P3 sample has reached the same level as the NP, P1 and P2 samples and only the 'Complete' sample has a lower nickel content on the surface.

Surface state		Deposition time					
		5s	15s	30s	60s	90s	4min (240s)
Unpolished	Fe(%)	95.18	88.8	69.62	40.56	25.75	6.47
	Ni (%)	4.82	11.2	30.38	59.44	74.25	93.53
Grade 220 paper	Fe(%)	95.6	87.48	63.68	26.22	13.96	6.9
	Ni(%)	4.34	12.52	36.32	73.78	86.04	93.10
Grade 1200 paper	Fe(%)	95.17	88.99	75.36	51.9	21.72	6.54
	Ni(%)	4.83	11.01	24.64	48.10	78.28	93.55
Grade 4000 paper	Fe(%)	97.5	89.34	77.38	51.13		7.75
	Ni(%)	2.5	10.66	22.62	48.87		92.25
Complete	Fe (%)	100	94.3	81	42	26	7
	Ni (%)	0	5.7	19	58	74	93

Tab. 7.5: Evolution of the surface composition (by EDX analysis) during the first stages of deposition, as a function of the substrate preparation.
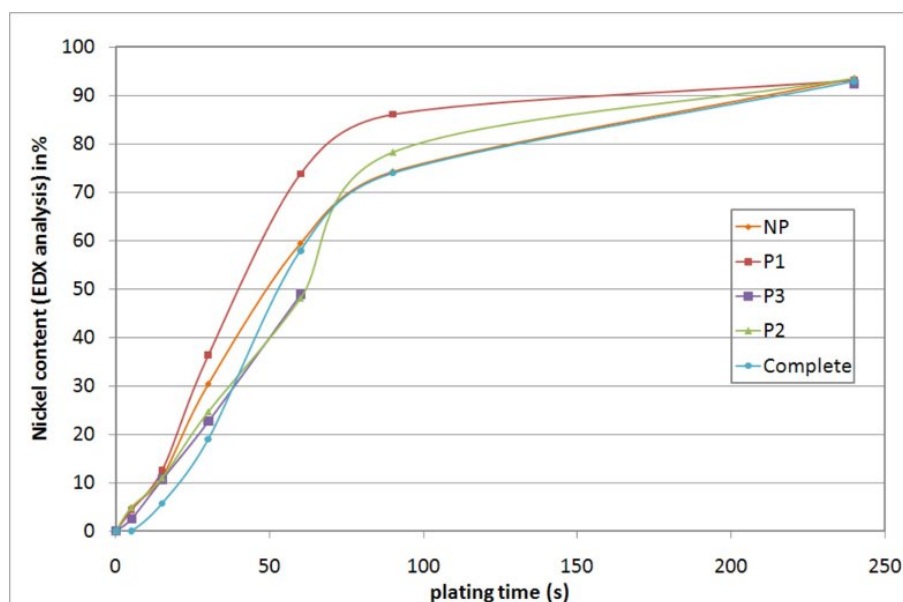
Fig. 7.22: EDX analysis carried out on samples with varying substrate roughness, during the first stages of the plating process.

At later stages, is it clear that the P1 samples has an higher deposition rate (its nickel content is already close to 90% after 90 seconds) than all the other samples. The 'Complete' sample has a longer induction period but grows quicker once the deposit is initiated. The NP sample on the other hand has a faster initiation but grows slower and reaches similar valuer to the 'Complete' sample after 60 to 90 seconds.

From those results, it seems that the P1 surface treatment produces the best results as far as deposit initation is concerned, which confirms the results of section 7.2.3.1. This is not surprising because the sample submitted to the P1 treatment has the higher R_p roughness. This sample has thus higher peaks that are preferred nucleation sites. The NP sample shows a good comportment at the very first stages but the deposit grows slower on this sample, probably because its higher roughness is due to valleys (the R_v roughness, that measures the depth of valleys, is 1.98±0.4 for the NP sample and 1.75±0.6 for the P1 sample) in which the deposition is slowed by the diffusion of reactive needed to attain them. A similar phenomena explains why the sample submitted to the 'Complete' treatment grows quicker than the others after the initiation took place on it: while there are less peaks that provide favorable sites for the deposit nucleation, there are also far less valleys that need diffusion to be coated.

7.2.3.3   Influence of the substrate roughness on the roughness of the coating during the first stages of deposition.

It would be very difficult to present a review of all interesting parameters for the samples concerned. As the R_p parameters appears to play an important role in the initiation of the deposit and all parameters have previously (see section 7.2.2.2) shown a similar comportment, only the evolution of this parameter was examined.

The roughness increase observed during the very first steps of the deposition process on the sample submitted to the complete surface preparation treatment is still observable on the other samples (see figure 7.23). However, this effect appears to be amplified by the initial roughness of the sample, which is in agreement with the results of Homma [133]. The very important roughness increase on the P2 sample however cannot be explained this way but a careful observation of the SEM images can lead to an explanation: on this sample, the nodules appear to grow on top of the others before the previous layer of nodules is complete. The reason behind the apparition of this phenomenon, however, remains unknown.

After a deposition time of 4 minutes, the roughness of the deposits evolves in the same manner than the average roughness (R_a) of the substrates: (in decreasing order) NP, P1, P3 and nearly ex-aequo P2 and 'Complete'. The values after 4 minutes are however generally slightly higher than the initial roughness of the substrate.
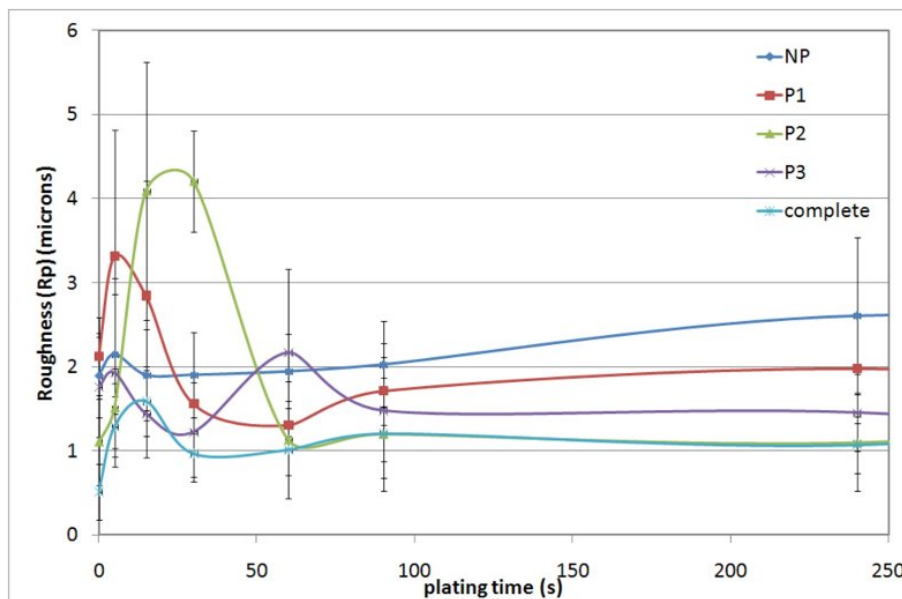
Fig. 7.23: Evolution of the coating roughness, as a function of time and initial roughness of the substrate.

7.2.4   Influence of the nature of the substrate.

The nature of the substrate influences the initiation process as much, if not more, than its roughness. In section 7.1.2, published results obtained on different magnesium alloys were examined and it appeared that the initiation of the deposition process was favored on polyphased alloys (probably due to galvanic coupling) and took place principally on phase boundaries [134–136].

Studying the influence of the substrate's nature is very difficult because it is close to impossible to compare effectively substrate of very different natures: the surface preparation needed to allow deposition on aluminum, for example, is very different than for steel. Moreover, the initiation mechanism is very influenced by the redox comportment of the substrate. We thus decided to limit this study to ferrous alloys that can be plated using a single surface preparation process.

The alloys that were used for this study are :

- St 37 low carbon steel. This alloy is the ferritic steel that was used for the previous initiation study.

- AISI 304 austenitic stainless steel. This alloy was chosen because it is widely used for lots of applications and it is monophased.

- 2205 Duplex stainless steel. This polyphased (austeno-ferritic) alloy was chosen to determine if the galvanic coupling effects described by Liu et al. for magnesium alloys are also observable on steel alloys.

The composition of the alloys used are shown in table 7.6. They were similarly prepared by grinding up to 4000 grade SiC paper, degreasing and etching in 30 volume % chlorhidric acid. The only parameters changed were the duration of the etching (1 minute for st 37 steel; 5 minutes for stainless steels) and the frequency of the renewal of the etching bath that was higher for the stainless steels.

	C	Cr	Ni	Mo	N	Mn	Si	P	S	Fe
St 37	0.17				0.009	0.20-0.50	0.30	0.05	0.05	bal.
AISI 304	<0.08	17.5-20	8-11			<2	<1	<0.045	<0.03	bal.
2205 duplex steel (Ur 45N)	<0.03	21-23	4.5-6.5	2.5-3.5	0.8-2	<2	<1	<0.03	<0.02	bal.

Tab. 7.6: Composition of the ferrous alloys used to investigate the influence of the substrate nature on the initiation of the deposit (wt %).

The initiation of the deposition process on the three different substrates was studied by the observation of their morphology and of the coverage ration determined by EDX.

7.2.4.1 Influence of the substrate nature on the coating morphology during the first stages of deposition.

The initiation on St 37 steel was already described in section 7.2.2. As shown on figure 7.24, the first nodules observed on the surface appear after an immersion time of 30 seconds and the surface is wholly colonized after only 60 seconds.
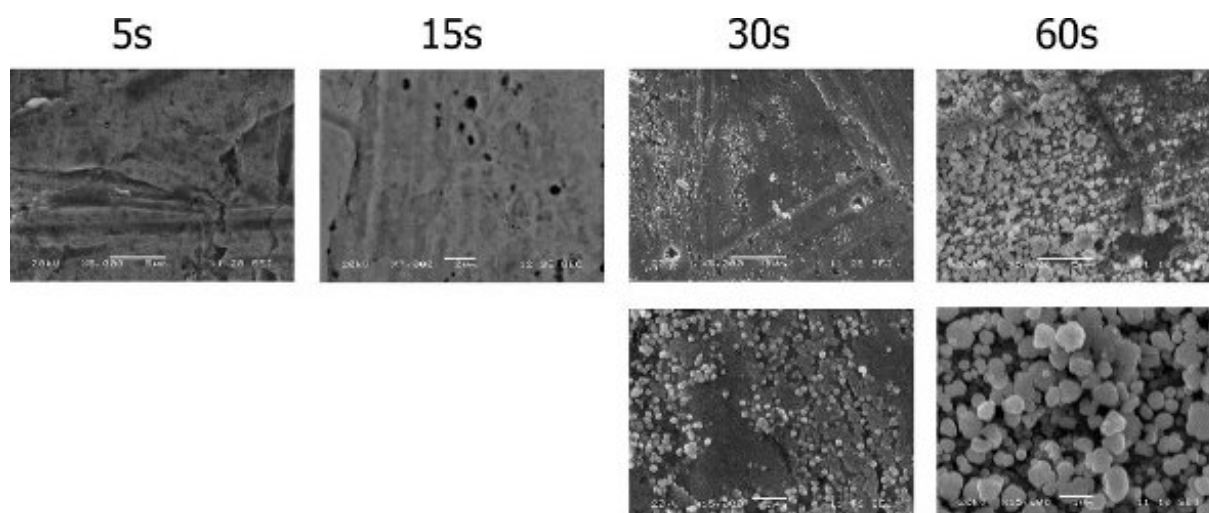
Fig. 7.24: Morphology of the deposit in the beginning of the deposition process on St37 steel.

On AISI 304 stainless steel, the very first nodules of nickel are observed after only 15 seconds (figure 7.25) but their density after 30 s and 60 s is far lower than on the low carbon steel. It appears thus that, while the initiation is quicker on stainless steel than on mild steel, the propagation of the deposit on the surface is then far slower. The quicker initiation could be caused by a displacement reaction between nickel and some component of the alloy (probably Cr which has a very low redox potential). This hypothesis is reinforced by the slower propagation of the deposit on the surface: the presence of dissolved metal salts in the solution could reinforce the catalytic blocking of sites caused by the lead salts.
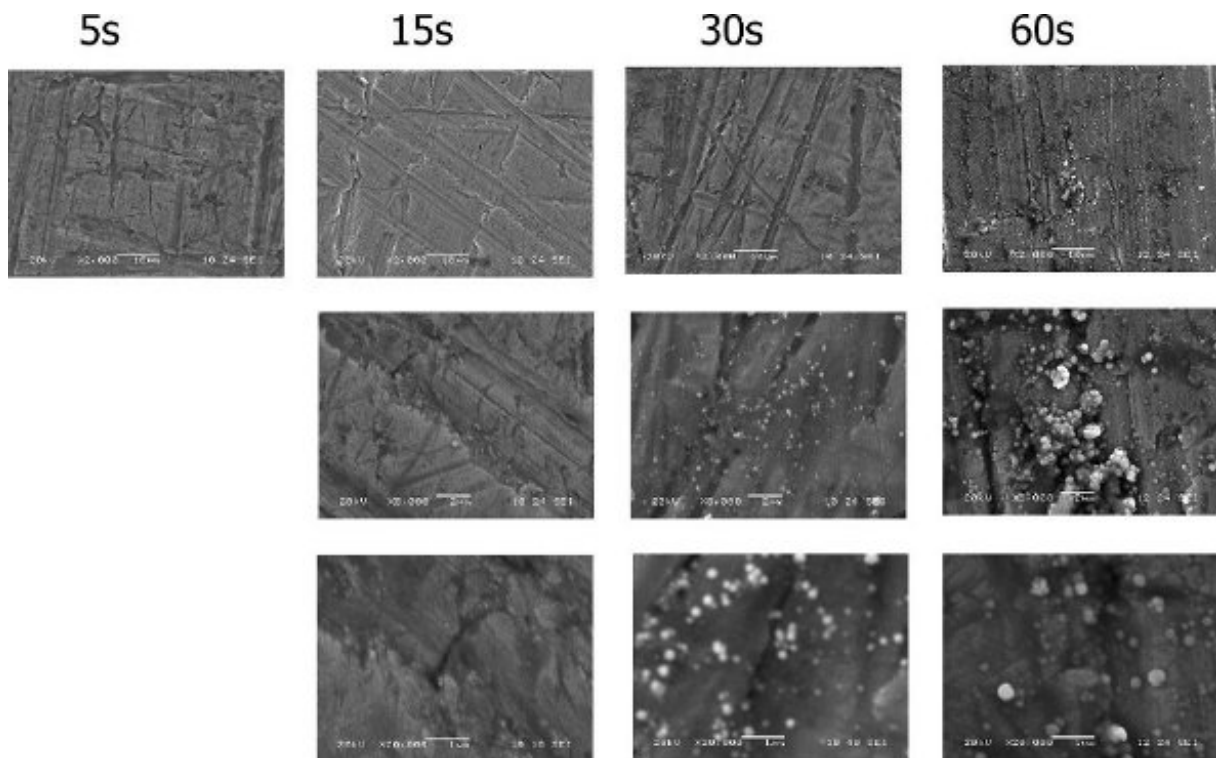
Fig. 7.25: Morphology of the deposit in the beginning of the deposition process on AISI 304 stainless steel.

On 2205 duplex steel, the initiation of the deposition takes place even sooner than on AISI 304 as the first evidence of nickel nodules formation can be observed after only 5 seconds of plating (figure 7.26). However, the progression of the deposit on the surface does not appear to be quicker than on the other stainless steel.

The diminution of the apparent induction time on stainless could be imputed to several factors:

- A first factor that applies to both stainless alloys: the lower redox potential of the alloy (stainless steels are not corrosion resistant because they are noble but because they have the ability to form a dense protective oxide coating on their surface) that can lead to a very quick displacement reaction inside the solution.
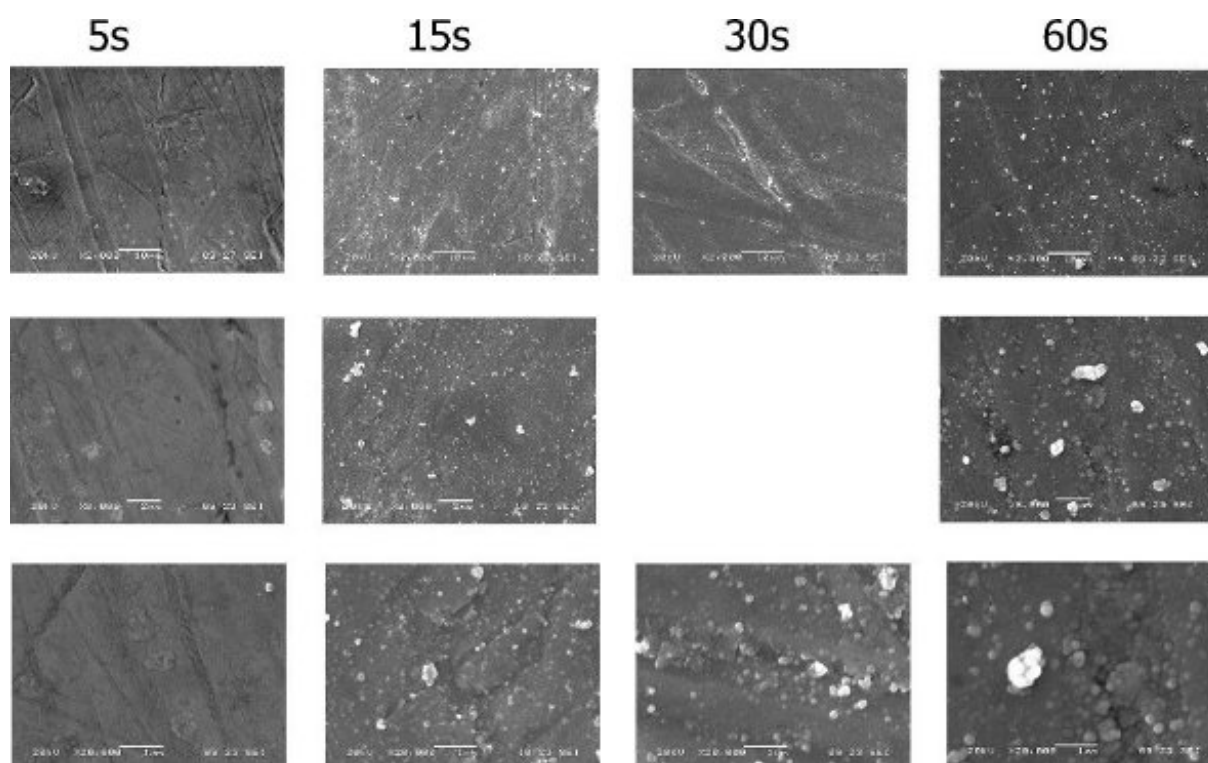
Fig. 7.26: Morphology of the deposit in the beginning of the deposition process on 2205 duplex stainless steel.

- A second factor that also applies to both alloys: the presence of nickel (which is catalytic for the oxidation of sodium borohydride) in the substrate. However, the low concentration of nickel in the alloys (8-11 wt.% for AISI 304 and 4.5-6.5 wt.% for 2205 duplex stainless steel) does suggest that this factor is not the principal one.

- A last one that only applies to the duplex steel: galvanic coupling between the austenitic and ferritic phases of the alloy.

It is evident that the lowering of the redox potential on stainless steel plays an important role in deposit initiation. Moreover, comparison of the comportment on Duplex and Austenitic stainless steel shows that the initiation is quicker on the Duplex steel, which has an higher nickel and chromium content and is polyphased. This suggests that galvanic coupling may influence the initiation.

The observation of samples immersed in the solution for longer times shows that the substrate is already completely covered by the deposit after 60 s on the St 37 sample but the coating stays porous until a plating time of 4 minutes is reached (figure 7.27). On the AISI 304 (figure 7.28), the surface appears to be completely colonized only after 7 minutes of plating but the coating looks dense as soon as it is continuous. On the duplex steel (figure 7.29), the substrate is completely covered by a densified coating after 4 minutes in the bath. Those results confirm that the propagation of the deposit on the sample surface is slower on stainless steel than on low carbon steel.
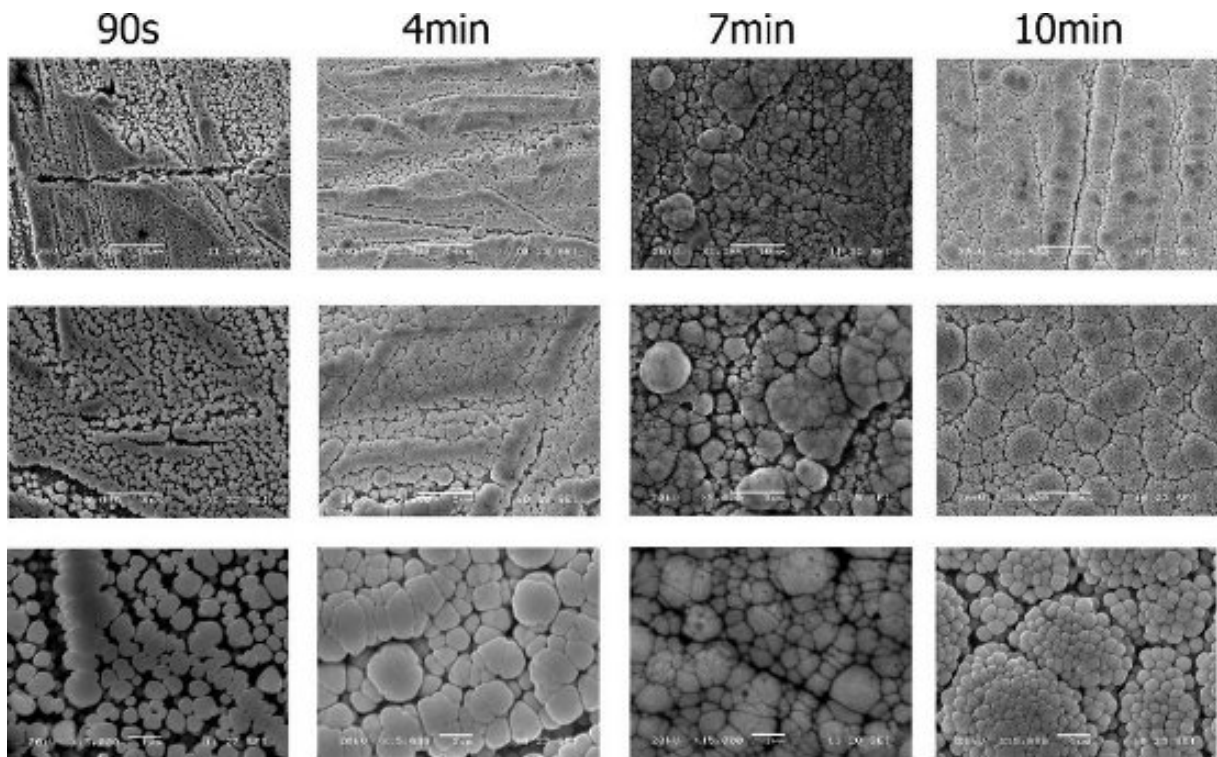
Fig. 7.27: Morphology of the deposit after 90s to 10 minutes of the deposition process on st37 steel.
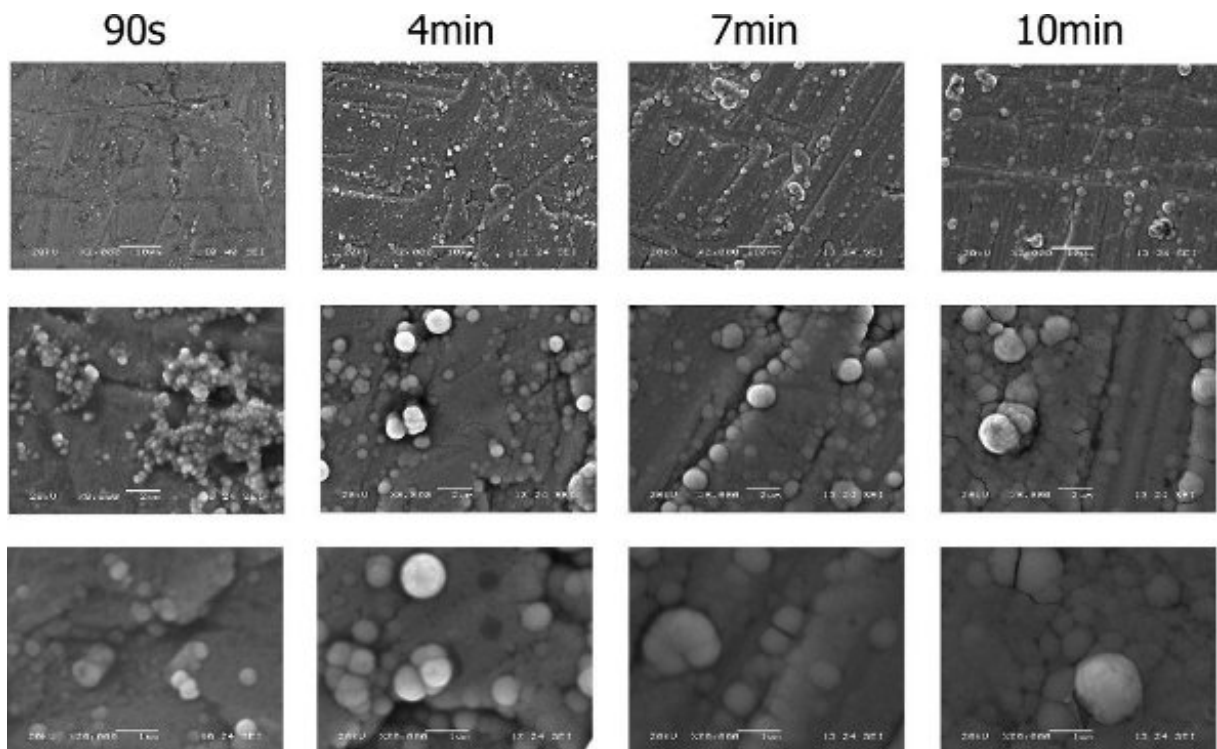
Fig. 7.28: Morphology of the deposit after 90s to 10 minutes of the deposition process on AISI 304 stainless steel.
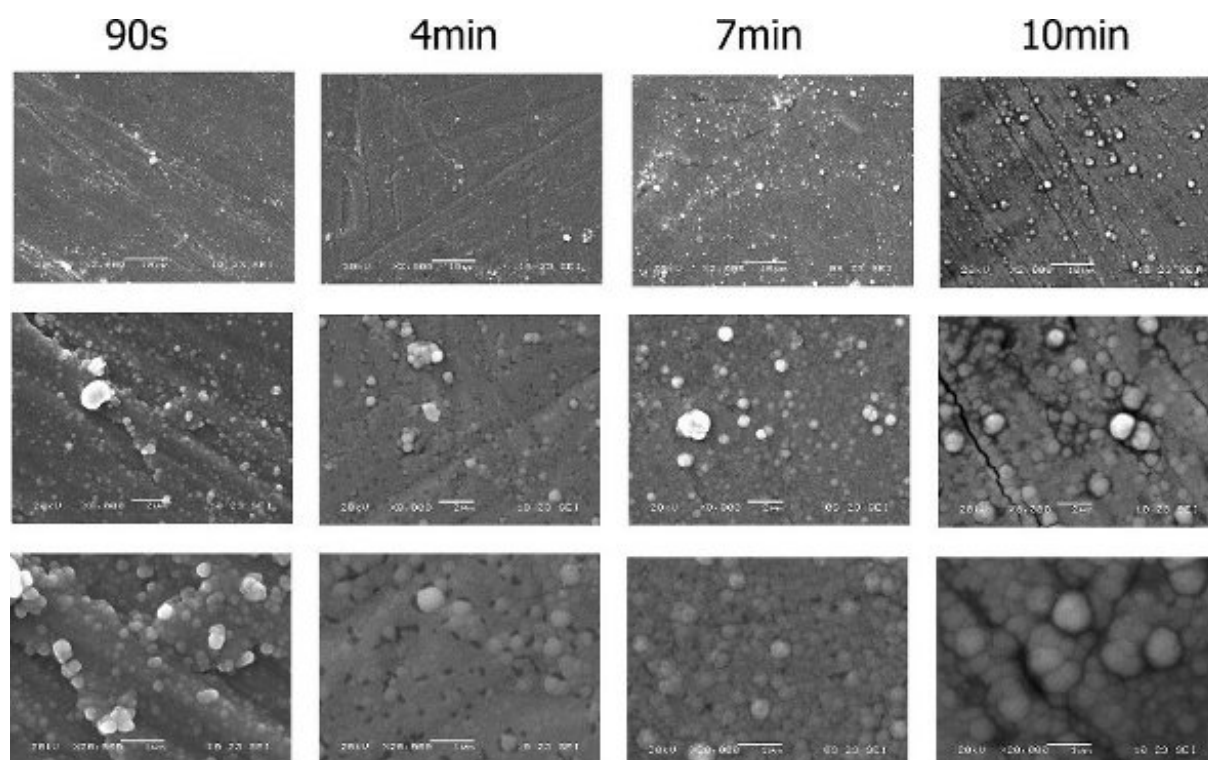
Fig. 7.29: Morphology of the deposit after 90s to 10 minutes of the deposition process on 2205 duplex stainless steel.

7.2.4.2   Influence of the substrate nature on the deposition rate.

The evolution of the Ni content was measured on the surface by EDX. As was said in section 7.2.2.3, it does not represent the effective surface of the sample but the average composition of the top $1\mu m$ of the coating. It can thus only be used to give qualitative indications about the formation of a continuous coating and a qualitative image of the deposition rate.

As the stainless steels already contain nickel (approx. 5wt% for 2205 duplex and 10 wt% for AISI 304), the EDX measured were corrected to take into account the nickel contained in the substrate.

The correction applied was the following:

- The weight ratio between iron and nickel was calculated from the nominal composition. It was found that the weight of iron was 6.9 times the weight of nickel in the AISI 304 and 11.9 times for the 2205 duplex.

- From this, the atomic ratios were calculated and found to be quite close to the previous ratios (the molar weights of iron and nickel being in the same range): 7.2 for AISI 304 and 12.5 for 2205 steel.

- The amount of nickel present in the steel was subtracted from the measured value to obtain the amount of nickel deposited. The initial values and results of the calculation are shown in table 7.7.

Plating time (s)	Measured Ni content (at.%)		Measured Fe content(at.%)		calculated Ni content(at.%)	
	AISI 304	2205 duplex SS	AISI 304	2205 duplex SS	AISI 304	2205 duplex SS
5	10.7	7.43	67.83	64.68	1.32	2.25
15	7.41	13.77	62.92	60.91	8.71	8.90
30	21.58	14.18	59.22	60.1	13.39	9.37
60	34.86	22.79	48.43	54.21	28.17	18.45
90	39.78	29.27	45.38	49.23	3.51	25.33
240	66.46	62.56	24.5	24.94	63.07	60.56
420	86.12	75.9	10.02	16.12	84.73	74.61
600	92.35	88.96	5.67	7.38	91.57	88.37

Tab. 7.7: Unprocessed and corrected Ni content detected on stainless steel after immersion in the electroless plating bath for various times.
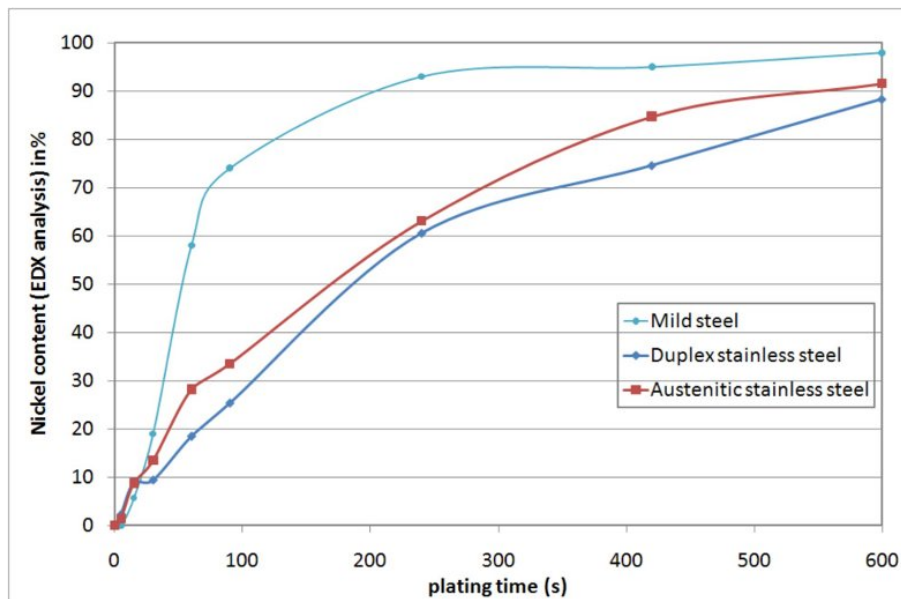
Fig. 7.30: EDX analysis carried out on various ferrous samples, during the first stages of the plating process.

The evolution of the nickel linked to the deposit on St 37, AISI 304 and Duplex steel is shown in figure 7.30. Those results confirm the SEM observation made on the coating: while nickel is deposited earlier and in a slightly greater amount on stainless steel than on carbon steel up to 15 seconds into the deposition process, the deposition rate becomes then far slower on stainless steel and the amount of nickel detected after 10 minutes of plating is significantly lower on those substrates. The AISI 304 steel appears to be coated slightly quicker than the Duplex steel which reinforce the hypothesis than chromium may have a detrimental affect on the plating rate. While this hypothesis cannot be proven after

this experiment, it is widely supported by the work of bielinski et al. [28] that showed that chromium had a relatively good stabilizing effect on electroless deposition baths.

7.2.5   Conclusion.

Observation of the initiation of electroless nickel-boron deposits on substrates of varying nature and roughness led to several very interesting observations:

- On mild steel (St 37), the initiation of the deposit is nearly instantaneous: while the nickel deposit cannot be distinguished on SEM images, EDX and XPS analysis already detect it on the surface after 15 seconds. This is not surprising when keeping in mind that the redox reaction on the surface is very quick and that the diffusion of reactive is the rate-limiting step.

- On St 37 mild steel, a complete coverage of the sample surface can be observed by SEM very soon (after only 60 seconds of plating) and a continuous coating may be formed even sooner as a very thin layer of nickel can be seen under the deposited nodules after 90 s.

- Still on St 37 steel, the deposit formation begins by a 'lace-like' aggregation of nuclei that is soon replaced by a nodular growth. During those first stages, the deposited material is quite rough but its densification occurs after only 4 minutes, accompanied by a smoothing of the coating.

- On St 37 steel, the initiation mechanism is not a displacement reaction between iron and nickel but a catalytic oxidation of the reducer.

- The roughness of the substrate has a important influence on the initiation and early formation of the deposit: a rougher substrate appears to favor a quick initiation of the deposit, with a high density of nodules on the surface after very short (15 s) times but to impede the later growth of the coating that is quicker on smoother substrates.

- The nature of the substrate has also a tremendous influence on the initiation and propagation of the deposition, not unlike the roughness: the formation of nickel nodules begins earlier on austenitic (304) and duplex (2205) stainless steels but the spread of deposit on the while surface is far slower on them than on St 37 steel and they present a far smaller growth rate for times higher than 30 seconds.

There are still lots of questions left unanswered about the initiation of electroless nickel-boron deposits but the present results constitute a good beginning for the complete understanding of this phenomenon.

7.3 Growth of electroless nickel-boron on mild steel.

The growth of electroless nickel-boron is usually studied by the growth rate (measured by microscopy and/or by the weight gain of the sample). There is not a lot of information about how it influences the morphology of the samples. In the present section, the growth of the deposit and the effect of the substrate roughness on the growth of deposits will be examined in the case of an unreplenished bath. An interesting accompanying study could be carried out on a continuously replenished bath to discriminate the eventual effects of reactive depletion. However, it is not possible to implement continuous replenishment at the lab scale.

7.3.1 Deposit growth in an unreplenished bath.

In this section, we will observe the deposit just after we cease to do it in the section about initiation. The evolution of the deposit between 90 seconds and 60 minutes of plating will be examined by different techniques.

7.3.1.1 Morphology of the deposits at different stages of their growth.

After an immersion of 90 seconds, the surface of the samples is completely covered but the deposit layer is not homogeneous: it is constituted of nodules separated by valleys and grooves (see figures 7.31a and 7.32a). After 4 minutes, however, the surface appears more homogeneous and regular, which is confirmed by the cross section observation. The size of the nodules is similar after 90 seconds and 4 minutes and is in the range of 200-500 nm.

After 7 minutes (see figure 7.31c), some smaller nodules can be observed on the surface of the sample but the average size stays close to 500 nm. On cross section, the transition between the nodules (observables on figures 7.32a and b) and the columnar morphology happens between 4 and 7 minutes of deposition (see figure 7.32c).

10 minutes into the plating process, the surface morphology of the coating is completely changed: the size of the cells (nodules or columns) observed is consequently smaller and does not exceed 200 nm (figure 7.31d). On cross sections, it is now clear that the transition between the nodular and columnar growth is finished.

There are no important modifications of the coating morphology between 10 and 30 minutes of plating: the columnization process continues and evidence of a subdivision of the columns (that could be caused by secondary nucleation) can be observed (figure 7.32e), as well as leveling of the coating surface but some of the intercolumnar interstices are still very important.

At the end of the deposition process, the size of the 'cells' observed on the surface is not modified but they are more difficult to distinguish because of the surface leveling (figure 7.31f). The deposit is fully densified and it appears to be constituted of several layers of columns, as if formed by alternating germination and growth phases.
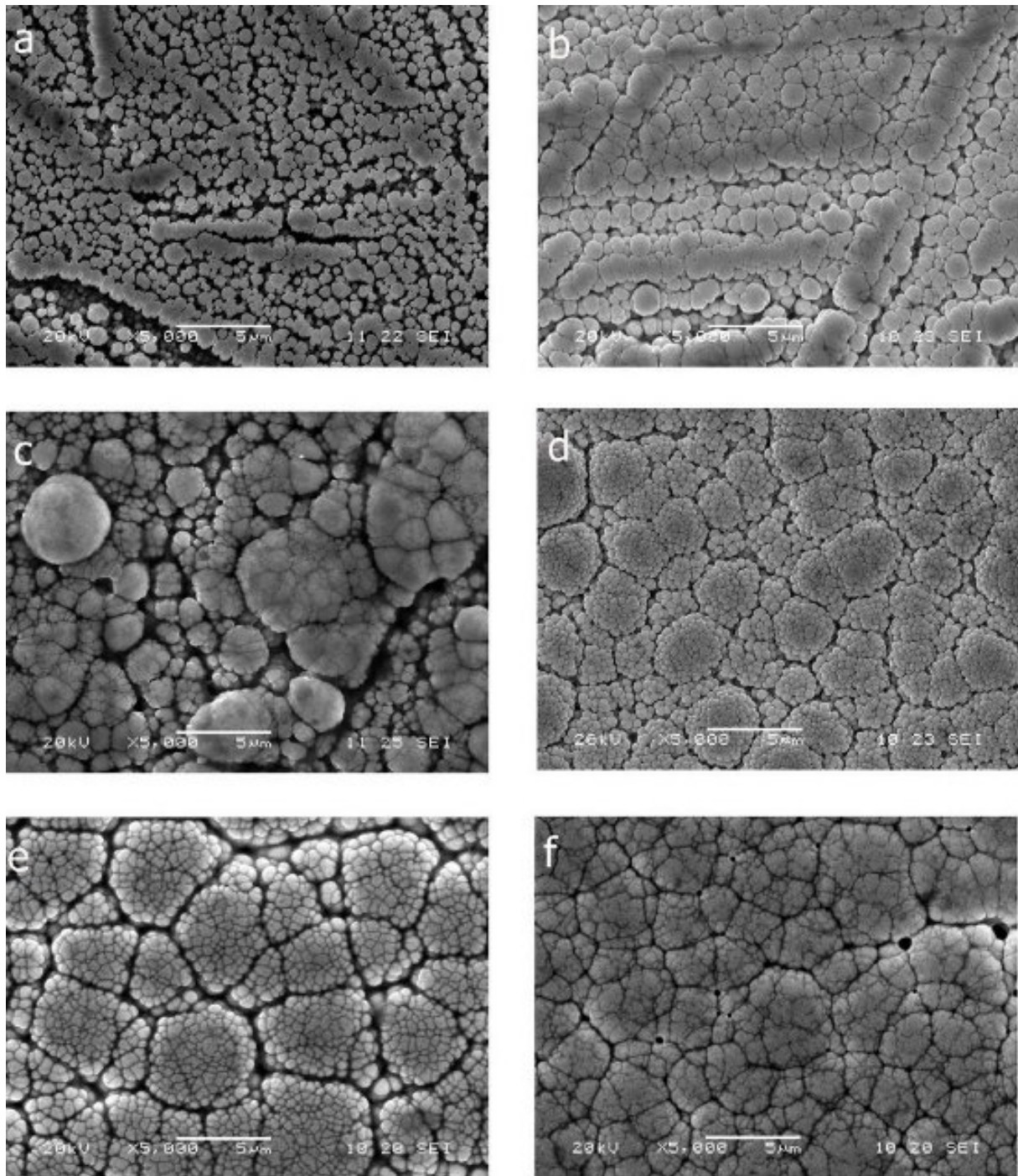
Fig. 7.31: SEM observation of the surface of samples immersed in the plating bath for
a) 90s; b) 4min; c) 7min; d) 10 min; e) 30min; f)60 min.
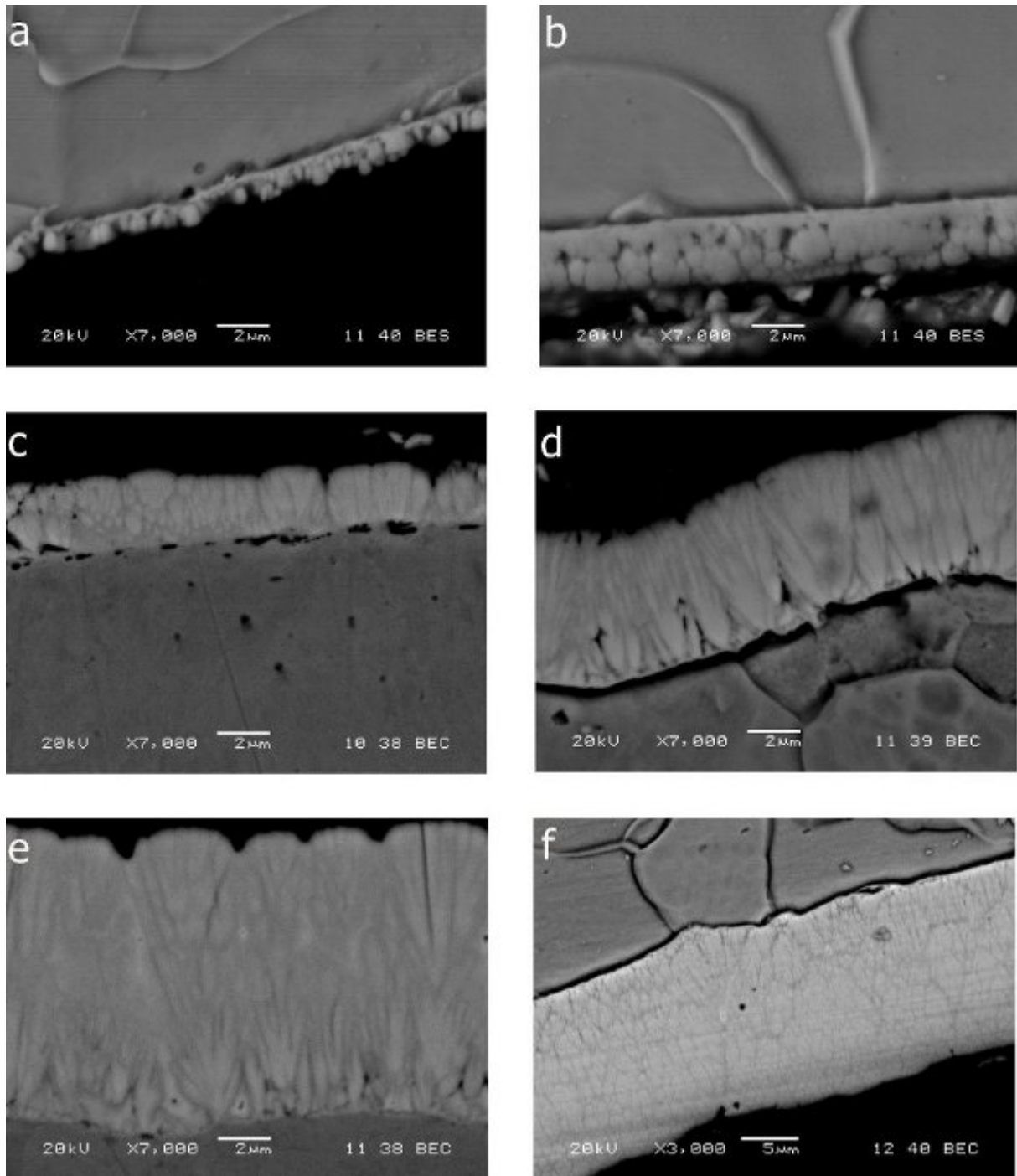
Fig. 7.32: SEM observation of the cross section of samples immersed in the plating bath for
a) 90s; b) 4min; c) 7min; d) 10min; e) 30 min; f) 60min.

7.3.1.2   Growth rate.

For this experiment, the thickness of the deposits was measured on SEM micrographs. The growth rate was then derived from the thickness. The instantaneous growth rate is the rate calculated between two consecutive thickness measurement while the growth rate is the average rate up to the point of calculation.

The growth of electroless nickel can be divided in several stage:

- During the very first stage, the thickness increases very quickly (the instantaneous growth rate exceeds 40 $\mu m/min$). However, as the thickness was measured by SEM, this rate cannot be linked to reactive consumption or to the amount of nickel deposited because the coating is very porous at this stage (see figures 7.32a and b). This stage lasts for the 4 first minutes of plating, approximatively.

- After this stage of high growth rate with an important porosity comes a step of consolidation: after 7 minutes, the thickness curve shows an inflection that is matched by a minimum of both the average and the instantaneous growth rate (see figure 7.33). This does not signify that no deposition is taking place during this time because observation of figure 7.32c shows that the coating is fully densified after 7 minutes of deposition. As a consequence, when microscopy is used as a mean to evaluate the thickness, the values measured in the first stages of deposition are higher than what would have been obtained from weighing. The apparent plateau in the thickness observed between 4 and 7 minutes is thus a manifestation of the densification of the coating. The apparent thickness increases very slightly during this time but the amount of nickel deposited is non negligible.
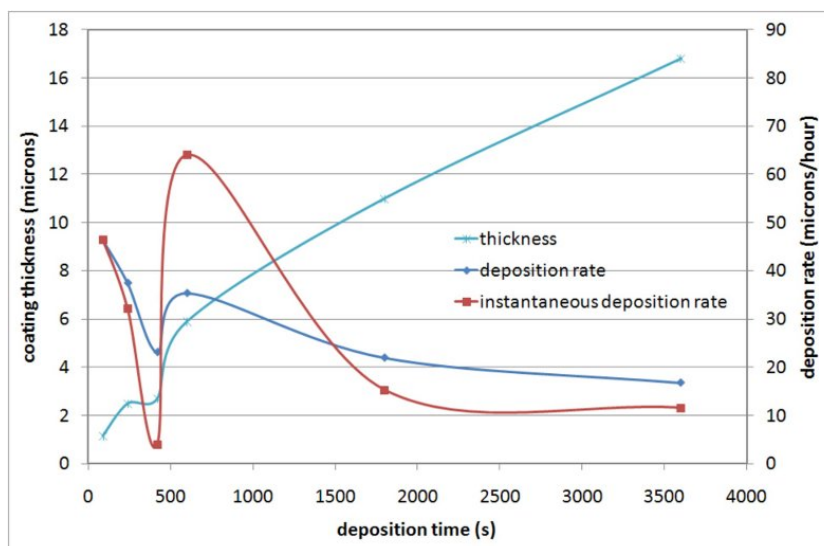
Fig. 7.33: Evolution of the thickness and growth rate during the deposition process.

- Just after this plateau, there is a new peak in the instantaneous deposition rate while the thickness recovers from the delay due to the densification.

- After 10 minutes of plating, the growth or the coating is nearly linear and there is a stabilization of the growth rate that reaches 18 $\mu m/min$ in average and 11 $\mu m/min$ in 'instantaneous' rate after one hour of plating.

7.3.1.3 Evolution of the boron content across the deposit.

The profile composition of the coating was measured by Glow-discharge Optical Emission Spectroscopy (GD-OES). The nickel and boron content of the coating is relatively stable across the whole deposit, as can be seen on figure 7.34. Calibration of the apparatus for nickel, boron, lead and other elements allowed to obtain a quantitative analysis of the coating. The boron content is close to 6 wt.% over the whole deposit. The lead content of the coating and its evolution will be discussed in section 7.3.1.4.
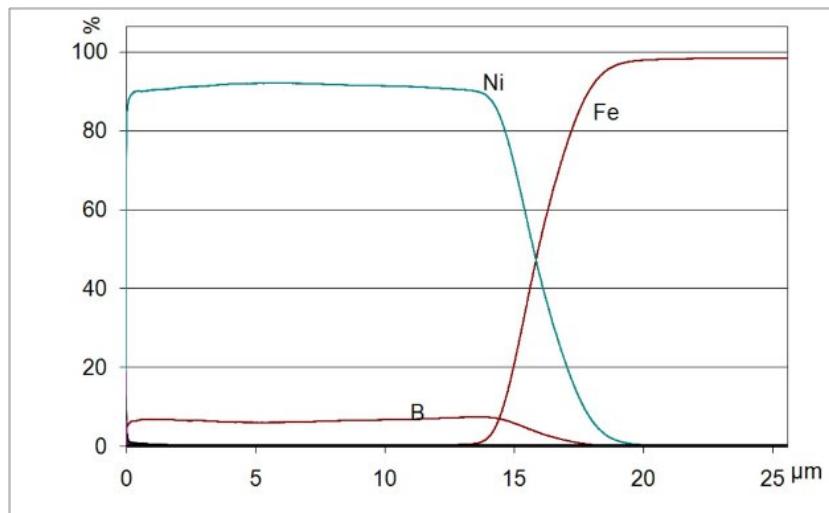
Fig. 7.34: Evolution of the composition across the deposit.

Those results indicate that the deposition process is reliable because it produces coatings with an homogeneous composition. They also mean that the diminution of reactive concentration during the deposition does not influence very strongly the composition of the coating. This is very interesting because important variations of the composition of deposit during the deposition process have been reported [56].

7.3.1.4 Evolution of the lead concentration and its influence on deposition rate and deposit morphology.

The lead content of the deposit is a lot smaller than the boron content and stays in the range 0.25-0.45% at all times. However, the evolution of this content is more noticeable than the evolution of the boron content and its influence on the coating's morphology can be studied. To do this, the results of a GD-OES cross section analysis of the sample, in which the lead content was up scaled for ligibility, were superposed to a SEM cross section image of the coating.

The observation of the lead content's influence on the morphology is not easy and certain considerations must be kept in mind:

- The GD-OES method is quantitative if the apparatus is calibrated (which is the case). However, in some cases, the different constituents of the sample may not be sputtered at the same speed exactly, which can induce errors in the composition. Moreover, the conversion between sputtering time and depth, which is made by measuring the size of the sputtered crater, is influenced by the nature of the sputtered matter and thus by the composition. It is thus difficult to realize this conversion precisely when a coating/substrate system is analyzed, due to the dual nature of the material.

- While both the SEM and GD-OES analysis were carried out on the same sample, they were performed on different areas of the sample as both techniques are destructive. It is thus possible that there are slight differences in the morphology and/or composition of both areas.
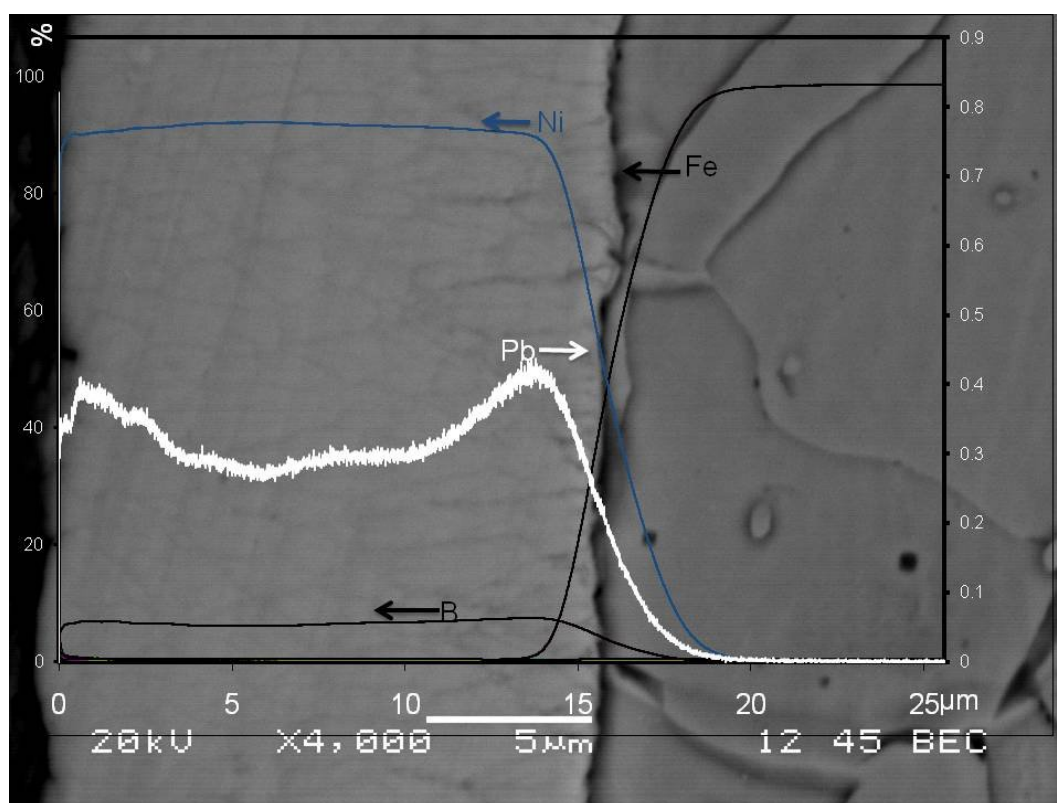
Fig. 7.35: Comparison of the composition and morphology across the deposit.

The observation of figure 7.35 shows that the lead content is close to 0.45 wt.% at the substrate/coating interface then decreases quickly down to 0.3% in the first 2-3 μm of the coating. The content stays then low (0.25-0.3 wt.%) for the next 10 μm of the deposit before going up in near the surface (at the end of the deposition process). The lowest lead concentration of the coating can be matched with the stage of quick growth observed

after 7 minutes of deposition, while the high concentration detected in the coating that is first deposited can be linked with the plateau observed in the deposition rate described in section 7.3.1.2. In view of this, an explanation of the plateau phenomenon that was observed can be given: During the first 90 to 250 seconds of deposition, the deposition rate is high but the material that is deposited is not very dense and possess thus a very high specific surface. At this moment, an important amount of lead is adsorbed on this surface and slows signicatively the deposition process until the majority of the cavities formed by the initial deposit are filled. The growth continues then at a more controlled rate because the process enters a steady state. The decrease of the deposition rate at the end of the deposition process can likewise be linked to the higher lead content observed near the surface of the coating.

Comparison of the lead content and morphology shows that the lower lead content observed in the center of the coating coincides with the wider columns, while the columns appear to be smaller at the very beginning and the very end of the process (which was already observed on figure 7.31), when the lead content is higher.

7.3.1.5   Evolution of instantaneous composition of the deposit measured by XPS.

The iron content, that is probably linked to a surface pollution, was subtracted to allow interpretation of the XPS analysis. Those results are presented in table 7.8 for the atomic composition and figure 7.36 for the weight content. At the very beginning of the plating process (after 15 s), the main deposited element is nickel (close to 84 at.% or 95 wt.%), the boron content is close to 16 at.% and the lead content is lower than 0.5 at.%.

Deposition time (s)	15	30	60	90	240	600	3600
Ni (at.%)	83.08	80.71	72.22	57.38	54.86	60.87	57.65
B (at.%)	16.50	18.69	27.78	42.62	43.55	37.49	40.49
Pb (at.%)	0.42	0.60	0	0	1.60	1.63	1.86

Tab. 7.8: Evolution of the surface composition (by XPS analysis) during the first stages of deposition.

The nickel content measured on the surface decreases quickly during the deposition process and stabilizes around 60 at.% after only 90s. The boron content increases to reach nearly 40 at.% at the same time. The evolution of the lead content appears more complex: lead represents 0.5 at.% of the surface at the beginning, it is then detected as traces for some time (up to an immersion of 240 s), and it constitutes finaly 1.5 at% of the surface content. This evolution is very similar to what is observed in GDOES (see section 7.3.1.4). The detection of an higher amount of lead in the bulk of the coating by GDOES compared to XPS could be due to a levelling effect of the GDOES technique: as the deposit grows in a columnar manner, there are horizontal composition inhomogeneities between the center of a column (deposited earlier) and its periphery (deposited
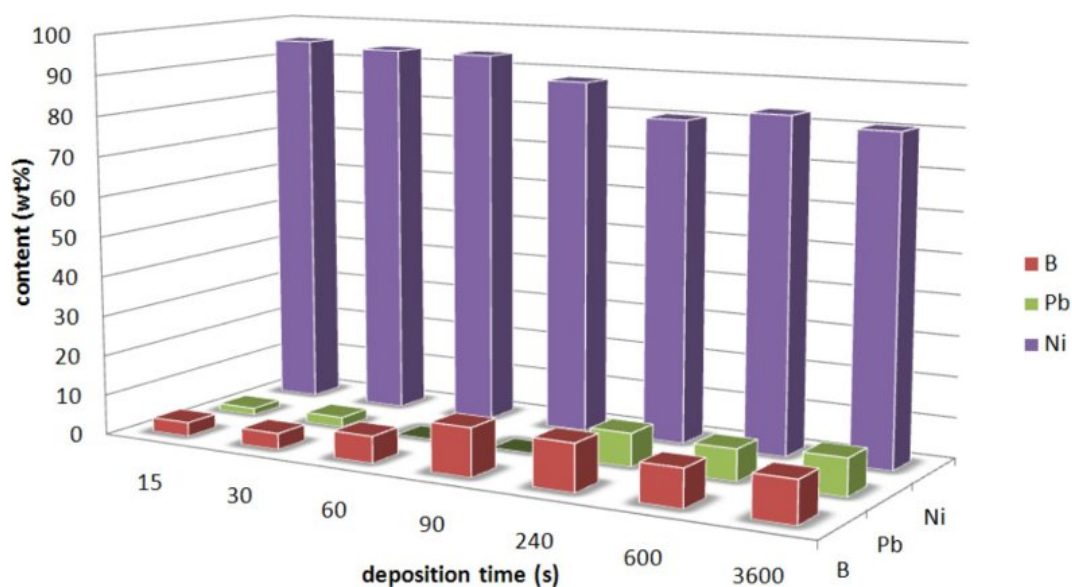
Fig. 7.36: Surface composition of electroless nickel-boron deposits measured by XPS (wt.%).

later). XPS analyses the exposed surface of the deposit and thus deposit formed at the same time. However GDOES analyses a straigth surface formed by sputtering, over a large area (several mm^2), which means that material formed over a larger span of time are analyzed.

The variation in the composition of the instantaneous deposit can be linked to variation of the deposit morphology: the deposition of a material with a lower lead content corresponds with the larger nodules observed and the increase of the lead content can be linked to the decrease of columns size.

It is difficult to link the evolution of the boron content of the instantaneously deposited coating with the morphology as this variation happens at the very beginning of the process, when it is not yet possible to observe cross sections of the deposit. However, the observation of a thin continuous layer of nickel under the nodular structure could be linked to the formation of a low-boron alloy at the very beginning of the process (see figure 7.13a, page 104).

7.3.1.6   Effect of substrate roughness on the growth of the deposit.

The roughness of the substrate has a non negligible effect on the first stages of the deposition process, as was shown in section 7.2.3. It is thus possible that this parameter still influences the deposit in later stages of the plating. The objective of this section is to identify the eventual effects induced by a modification of the substrate roughness on the coating. The surface preparations used for this study are the same as in section 7.2.3 and were presented in table 7.4.

The parameters on which the influence of the substrate roughness will be studied are the growth rate, the morphology and the roughness of the deposit.

7.3.1.6.1 Effect on the growth rate.

The growth rate was measured from thickness values obtained by SEM observation. The results are shown on figures 7.37, 7.38 and 7.39.
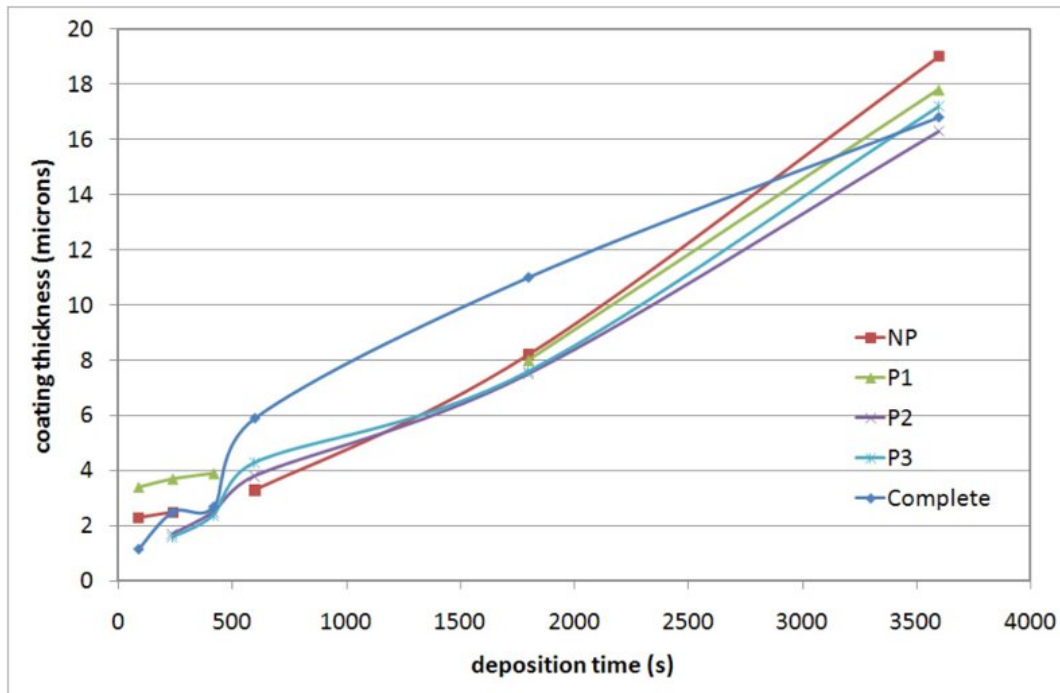
Fig. 7.37: Influence of the substrate roughness on the thickness of the deposit.
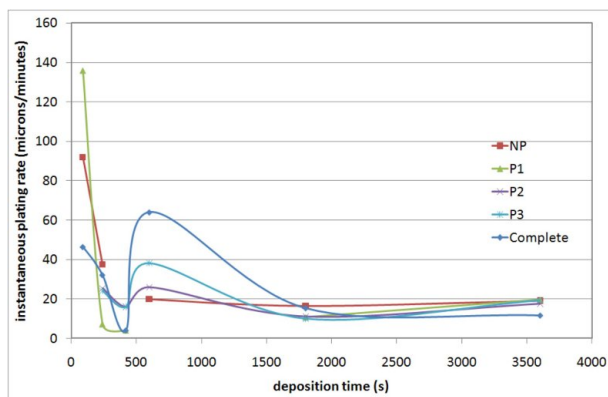
Fig. 7.38: Influence of the substrate roughness on the instantaneous growth rate of electroless deposits.
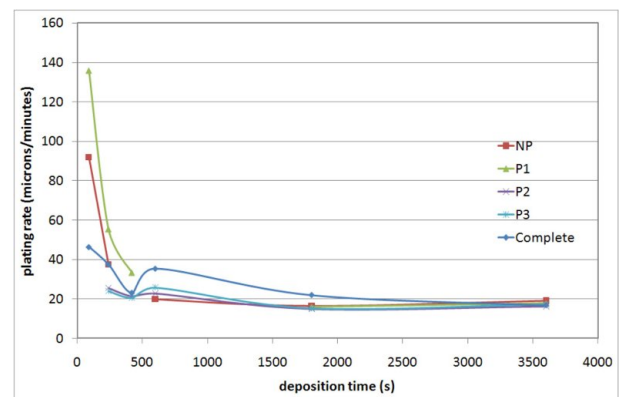
Fig. 7.39: Influence of the substrate roughness on the average growth rate of electroless deposits.

At the beginning of the plating process, the coating thickness is more important on the rougher substrate, which confirms the results obtained for the deposit initiation in section 7.2.3. However, at later stages of the deposition, the difference is less marked and all samples end with a thickness between 16 and 20 μm after one hour of plating but the rougher sample appear to be still thicker than the others.

The instantaneous plating rate shows a similar evolution for all samples, with a very high initial value followed by a minimum around 4 to 7 minutes, then a new increase followed by a stabilization at a lower value (10 to 20 $\mu m/min$ in all cases). The average plating rate follows a similar but less marked tendency.

It is remarkable that the deposit grows slower on the sample having been submitted to the complete surface preparation process than on the other samples at the beginning of the process but is thicker than on every other sample after 10 to 30 minutes of plating. This comportment may be related to the hypothesis we made about the lead content in section 7.3.1.4: as this surface is initially very smooth, the deposit grows quite slowly during the first stages of the process and the specific surface obtained is less important than on other samples. The time needed to fill the cavities between the nodules and the amount of lead adsorbed on the surface are thus smaller and the deposit can grow quicker in the next stage of the process.

7.3.1.6.2   Effect on the morphology of the deposit: SEM observation of Ni-B deposits.
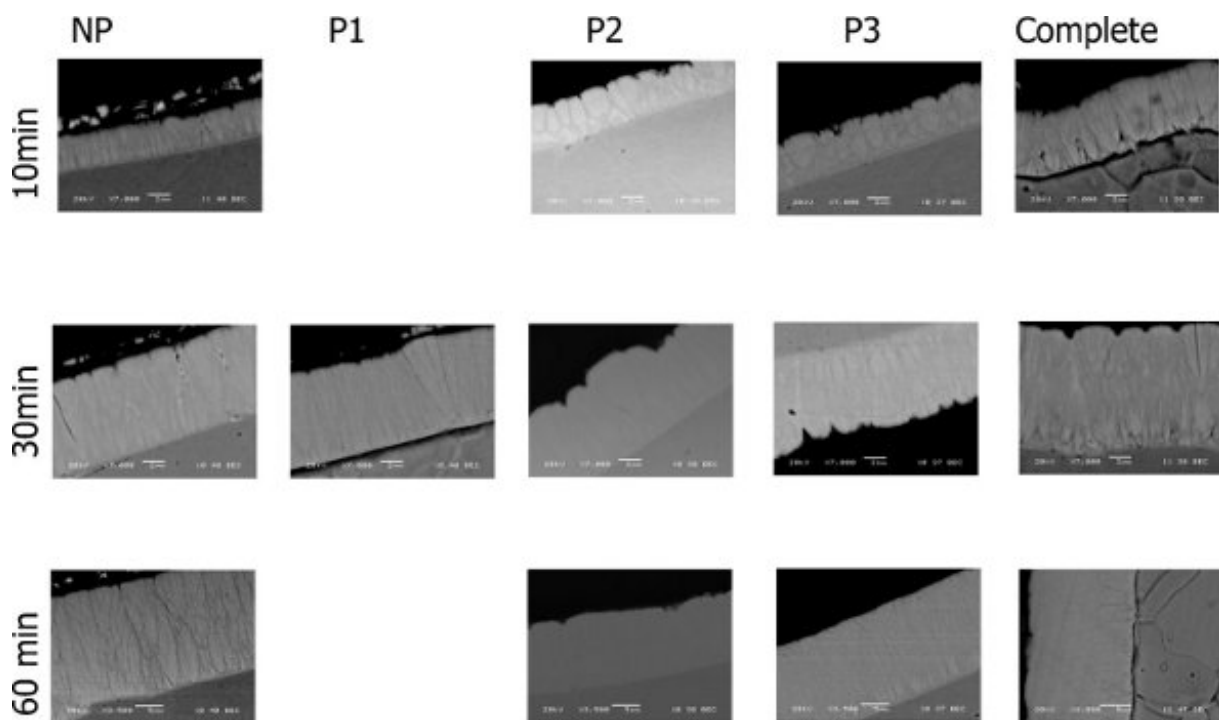
Fig. 7.40: Influence of the substrate roughness on the morphology of the deposit: cross section observation.

As shown on figure 7.20, in section 7.2.3.1, the surface aspect of electroless nickel-boron deposits is not much influenced by the substrate roughness. In this section, we will thus focus our attention on cross sections of the samples, presented in figure 7.40.

The morphology of cross sections of the electroless coatings deposited on substrate with different roughness is similar in all cases, with a 'fan-like' disposition of the columns at the bottom and parallel columns at the top of the coating.

7.3.1.6.3   Effect on the roughness of the deposit.

The electroless nickel-boron coating preserves very well the geometry of the substrate. It is thus expected that the roughness will be slightly smoothed but otherwise preserved. The results presented on figure 7.41 confirm this expectation: after one hour of electroless plating, the order of coating roughness is the same as the initial order of substrate roughness (the rougher coating corresponds to the rougher substrate) except for the non polished substrate, that is slightly smoother than the P1 substrate while the NP coating is rougher than the P1 coating.
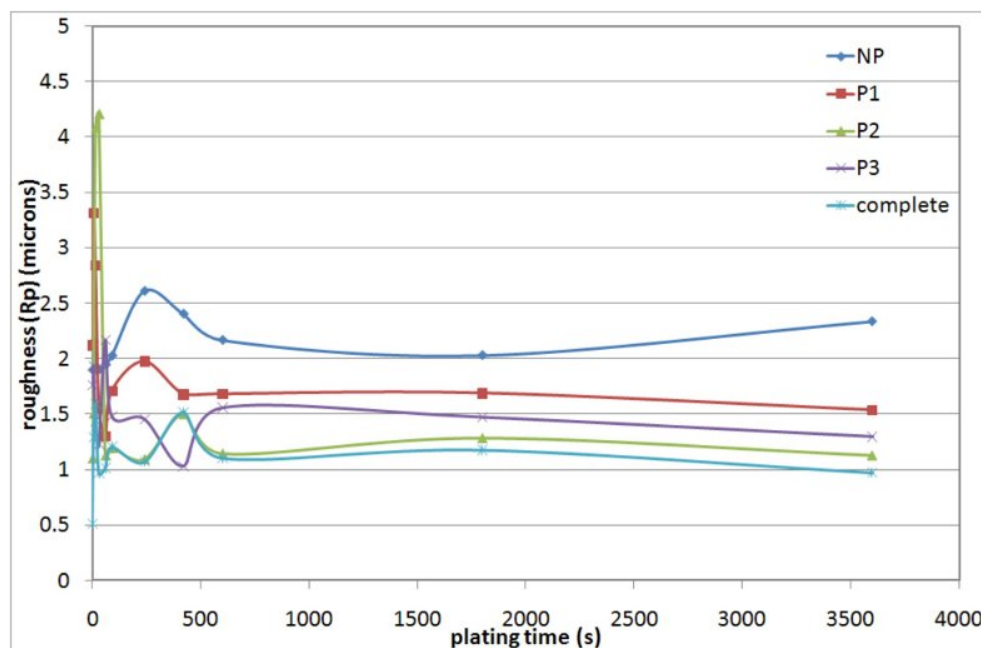
Fig. 7.41: Influence of the substrate roughness on the morphology of the deposit: cross section observation.

The magnitude of the substrate roughness is globally conserved after the deposition process (see table 7.9), except for the substrate that has been submitted to the complete surface treatment, on which the roughness increases slightly. However, this modification is not inevitably due to the plating process: the chemical etching carried out on the substrate just before plating may be the origin of this increasing roughness.

Sample	initial $R_a(\mu m)$	initial $R_p(\mu m)$	final $R_a(\mu m)$	final $R_p(\mu m)$
NP	0.674±0.111	1.896±0.502	0.684±0.146	2.336±0.446
P1	0.559±0.144	2.122±0.467	0.424±0.061	1.537±0.381
P2	0.294±0.084	1.103±0.515	0.300± 0.058	1.129± 0.329
P3	0.476±0.120	1.759±0.596	0.422± 0.104	1.297± 0.355
Complete	0.184±0.0640	0.510±0.329	0.434±0.145	0.971 ± 0.240

Tab. 7.9: Initial and final (after one hour of plating) roughness of samples submitted to electroless nickel-boron coating.

7.3.1.7   Conclusion.

The observation of the growth of electroless nickel-boron deposits led us to observe a phenomenon that is not dissimilar to the findings of Clerc [54] about the formation of strata in the deposit: we observe, after the formation of nodules on the substrate, an homogenization and densification of the structure leading to the well known columns. After this, a refinement of the columns size is observed, still early (4 to 10 min) in the plating process, followed by a progressive leveling.

The deposition rate, in terms of thickness, confirms this: the deposit first knows a quick growth but stays porous. The thickness increases then very slowly while the coating is consolidated and densified. After this, the deposition rate is higher during the end of the plating, as the growth happen more regularly. This means that following the deposition rate only by a measure of the weight of the deposit or of their thickness could lead to very different results during the first 7 to 10 minutes of the deposition.

The nickel and boron content are overall very stable in the whole deposit, excepts at the very beginning where a lower boron concentration is measured by XPS. The lead content variations can be linked to the coating microstructure: the columns are larger when the lead content is lower and the refinement of the columnar structure appears to be closely linked to a non negligible increase of the lead content of the coating.

Overall, the roughness of the substrate is conserved by the electroless plating process but it influences the growth rate that is higher at the beginning on rough parts but is in average better on smoother samples.

7.4 Conclusion.

In this chapter, several aspects of the initiation and formation of the deposit were discussed and the influence of parameters such as substrate roughness and composition was observed. Several noteworthy observations were made.

First, we observed the near instantaneous character of the initiation of the deposition process and the nature of the initiation mechanism.

Secondly, the ambiguous effect of rougher substrates and of the use of stainless steel on the deposit formation was determined: they favor a quicker initiation of the process but the deposit spreads (and grows) then slower.

Thirdly, the morphology of the deposit, with thicker nodules at the interfaces and smaller columns near the top was observed and could be linked with the evolution of the lead content of the deposit, the lead-rich zone corresponding with the finer structure.

Finally, the very good conservation of the substrate shape could be shown by the preservation of the roughness of the substrate after one hour of deposition.

There are however still phenomena that could not be observed or explained such as the effect of continuous replenishment on the deposit formation, the reason for the lead content variations, the preferred phase for initiation of the deposit on Duplex steel.

8. CHARACTERIZATION OF NICKEL-BORON DEPOSITS IN THEIR AS DEPOSITED STATE.

8.1   introduction.

As electroless nickel-boron coatings are studied with an industrial application in mind, it is very important to get the most detailled knowledge of their properties. The present chapter aims to describe those properties in the case of coating in their initial as-deposited state. The influence of heat treatments on the coatings will be assessed separately in chapter 9.

Before describing the properties measured on the samples, the preparation procedure of the samples will be briefly introduced. Then, the chemistry of the deposits will be examined by diverse techniques, in order to get information on the average composition of the samples but also on the evolution of this composition inside the deposit. It is important that the chemistry of the deposits is studied first because it was shown in part I that it influences greatly the other properties.

The next set of properties that will be examined are the structure related properties that include the global aspect of the coating, its morphology (as observed by SEM) and its structure. A particular emphasis will be put on the structural characterization of the coating by Transmission Electronic Microscopy (TEM).

After that, the focus will be set on the properties that are the most interesting for industrial application, which are the mechanical properties and the wear and corrosion resistances. The study of mechanical properties will focus on hardness as it is the most relevant for the usual applications of electroless nickel and the wear resistance will be determined by abrasive wear tests. The corrosion resistance will be mostly studied by electrochemical methods and the influence of wear on the corrosion resistance will also be discussed.

8.2   Samples preparation.

The samples studied in this chapter were in most cases immersed in the deposition bath (loaded with approximatively 25 cm^2/l) for one hour without replenishment and their thickness typically reached 15 μm. However, some tests needed thicker or thinner deposits that were obtained respectively by the way of bath replenishment and shorter immersion time.

The shapes and size of the samples were always one of the following:

- Cylinders with an approximate diameter of 25 mm and a thickness of 10 mm were plated in the 800 ml cell. They were used for chemical, structural and mechanical testing.

- Square sheet coupons (10 * 10 cm; thickness: 1 mm) were coated in the bigger cell and were used for all tests except the abrasion wear test. They were mainly used for electrochemical evaluation of the corrosion resistance.

- Disc sheet coupons (diameter: 10 cm; thickness: 1 mm) were coated in the bigger cell and were used for wear testing and electrochemical evaluation of the corrosion resistance.

All the samples observed in the present chapter were deposited either on St 37 steel or on aluminum alloy (pre-treated with a nickel-phosphorous underlayer), following the surface preparation procedure described in section 5.2.

8.3   Global and local composition of the deposits.

The knowledge of the coatings chemistry is important because their properties are strongly influenced by the composition. To obtain the global composition of the deposits, samples were dissolved in aqua regia (1/3 nitric acid - 2/3 hydrochloric acid) and the solution was analyzed by ICP. The composition of our samples is, on average, 6 wt.% Boron, approximatively 1 wt.% lead, the balance being nickel (93 wt.%).
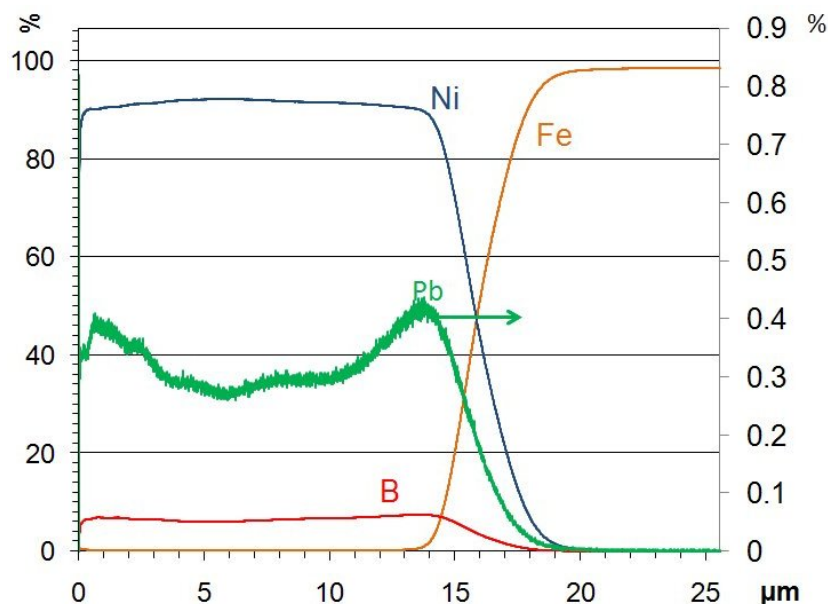
Fig. 8.1: Quantitative GDOES analysis of nickel-boron deposit on steel.

The evolution of the chemistry of the nickel-boron across the deposit was studied by Glow Discharge Optical Electron Spectroscopy (GDOES), which is described in section

??. This technique is usually only qualitative but it is possible to obtain quantitative results by careful calibration of the optical signal for each element. The GDOES experiments were carried out on steel and aluminum substrates in 2 different labs. Only one set of results, measured on steel are truly quantitative (see figure 8.1); the others are shown for reproducibility.

A sample synthesized in the 8 liters cells, on St-37 steel was analyzed by quantitative GDOES. As can be seen on figure 8.1, the boron content of the deposits is very stable across the coating and is close to 6 wt.%, which confirms the results of the ICP analysis. The lead content, however, appears to be lower in GDOES analysis, in the range of 0.5 wt.%. It is also not as stable as the boron content, with an higher value at the interface and near the external surface of the coating.

Figure 8.2 shows results of a non-quantitative GDOES analysis made on a steel substrate coated in the 800ml cell. The scale of the figure cannot be compared with the quantitative analysis but it is obvious that the measured intensities evolve in a similar manner than on figure 8.1. The stability of the boron content of the deposit and the evolution of the lead content are thus reproducible for our bath, even when used in a different deposition cell.
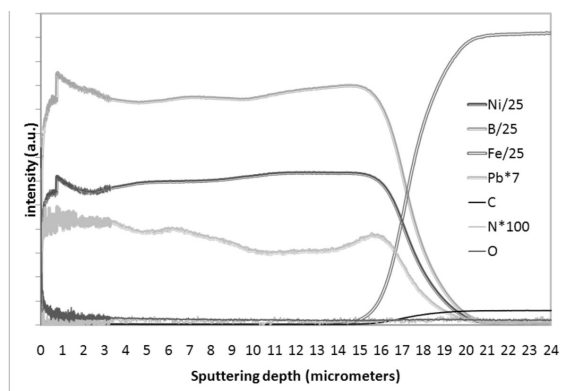
Fig. 8.2: Qualitative GDOES analysis of nickel-boron deposit on steel.
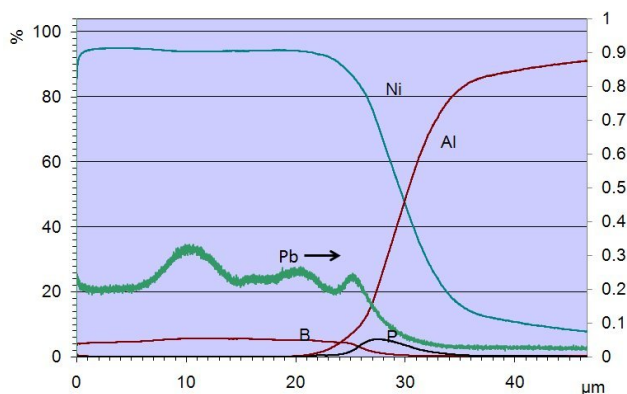
Fig. 8.3: Qualitative GDOES analysis of nickel-boron deposit on aluminum.

Figure 8.3 was obtained by the analysis of a sample deposited on aluminum. The phosphorous detected at the interface shows the presence of the protective NiP underlayer. The boron content is still stable across the coating on this deposit but the lead content presents more important variations, while having a similar trend: there is a maximal lead content at the interface and surface of the sample.

The stability of the boron content observed on our samples is an important feature because those samples were obtained without bath replenishment. It could thus be expected that, as the sodium borohydride is consumed, the amount of boron incorporated into the deposit decreases. However it appears it is not the case for the bath chemistry we use. The boron content appears to be more influenced (as far as we know) by the bath

load (as was shown in section 6.3.3.2.2.4) than by the plating time.

The influence of bath replenishment on the local composition of the samples was also investigated by GDOES. The samples used for this were left 1.5 hour in the bath with a replenishment after 0.5 hour. As can be seen on figure 8.4, there is no brutal chemistry modification linked to the replenishment process. However, the boron content of the coating is slightly higher in the first 10 μm (near the interface) than in the rest of the coating. The sharp decrease observed in the top five μm (near the surface) happens at the same time than a sharp decrease of the nickel signal and increase of the lead and iron signals. It is thus very probable that this is linked to the proximity of the surface and to an eventual superficial pollution rather than to an effective modification of the deposit chemistry. Once more, the progressive diminution of the boron content that could be expected is not observed.
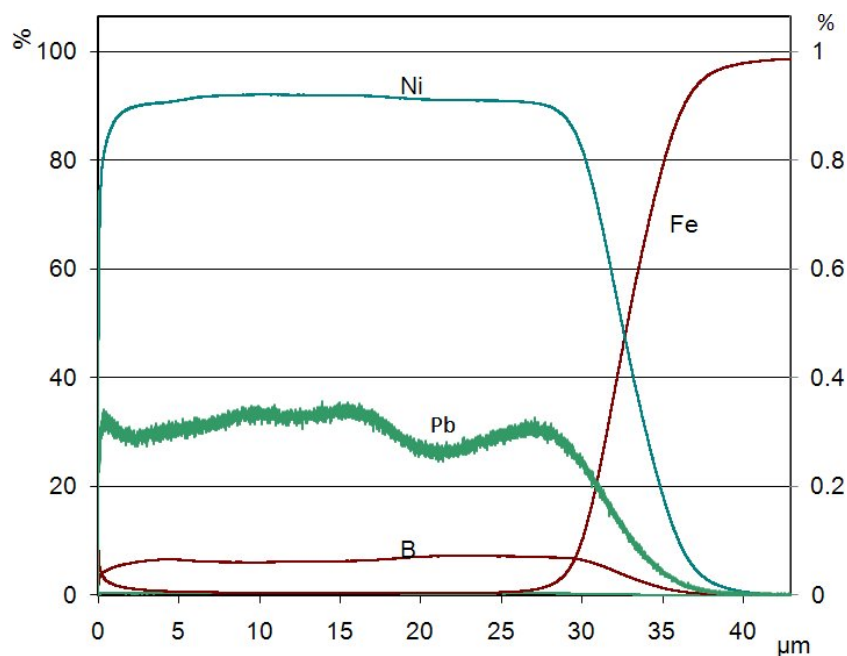
Fig. 8.4: Quantitative GDOES analysis of nickel-boron deposit, with bath replenishment, on steel.

The lead content in the sample with replenishment evolves in a way similar to coatings made with reactive addition for the first 15 μm of the coating (before the addition). After this, it increases slightly up to a plateau before decreasing once more towards the surface. It is possible that it re-increases near the surface but as this corresponds with the increase of the iron signal, this evolution could be a measuring artifact.

8.4   Aspect, morphology and structure of as-deposited electroless nickel-boron.

In this section, the morphological and structural properties of the coatings will be discussed. First, the coating will be examined visually and by SEM to obtain information about its aspect, texture and microstructure. Then, the results of X-ray diffraction (XRD) analysis will be presented. The last part of this section will be dedicated to Transmission Electron Microscopy (and electron diffraction) observation of the as-deposited coatings and to discussion of their crystalline state.

8.4.1   Optical and SEM observation of the aspect, texture and morphology of electroless nickel-boron deposits.

The NiB coatings are smooth and semi-bright as can be seen on figures 8.5, 8.6 and 5.5 (page 64). Their aspect is homogeneous, which is important as well for aesthetic reasons than for practical reasons: inhomogeneities in the surface aspect of electroless nickel-boron coatings are mostly the manifestation of structural and morphological inhomogeneities that are detrimental to the deposit properties. SEM observation of the surface of our electroless deposits confirmed that they possess the typical cauliflower-like texture (figure 8.7).
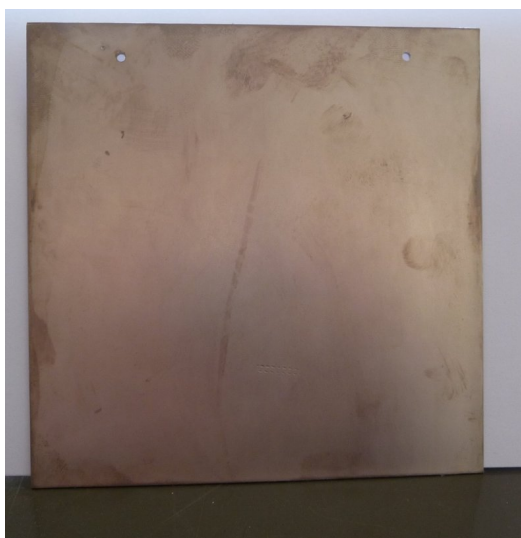
Fig. 8.5: Aspect of nickel-boron coated steel.

Fig. 8.6: Aspect of NiB coated steel.

Cross section examination of the coating can give more information than superficial observation: it allows observation of the growth morphology of the coating, as well as the influence of substrate and bath replenishment. Figures 8.8 and 8.9 present nickel-boron deposits synthesized on steel, without bath replenishment. The columnar growth of the deposit can be seen very clearly on figure 8.8, as well as the undulating surface that generates the cauliflower-like structure. The different strata that constitutes the coating are better seen on figure 8.9.
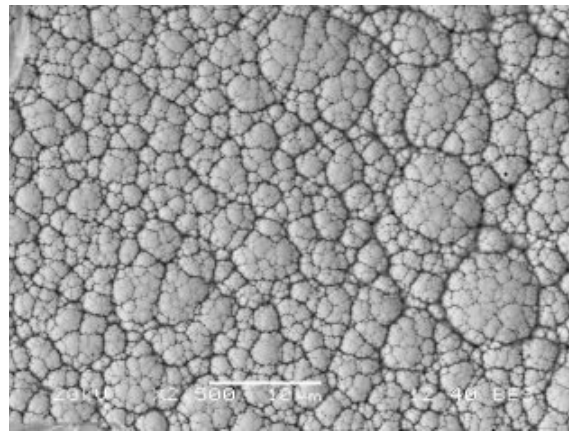
Fig. 8.7: SEM micrograph of the surface texture of electroless nickel-boron.
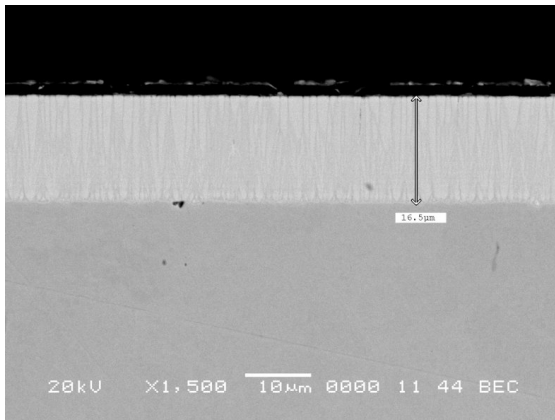
Fig. 8.8: Electroless nickel-boron on steel (SEM - cross section).
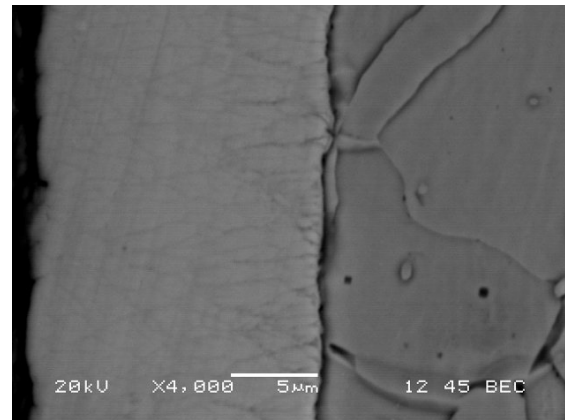
Fig. 8.9: Electroless nickel-boron on steel (SEM - cross section).

Bath replenishment influences the morphology of the coating and can be detected by SEM observation of cross sections. In the case of punctual replenishment, the addition of reactive in the bath causes a new episode of high density germination. This appears on the micrography as if a second coating was deposited on top of the first, with a very clear demarcation line, as can be seen on figure 8.10. Both layers of the coating are similar in the evolution of their morphology with bigger columns at the bottom and a refining of the apparent morphology near the top.

The growth of electroless nickel-boron on aluminum samples is similar as on steel (see figure 8.11. However, it must be noted that the nickel-boron is not deposited directly on the aluminum but on a nickel-phosphorous underlayer that can be seen on the figure. The consequences of bath replenishment are identical on this kind of samples than on steel substrates.
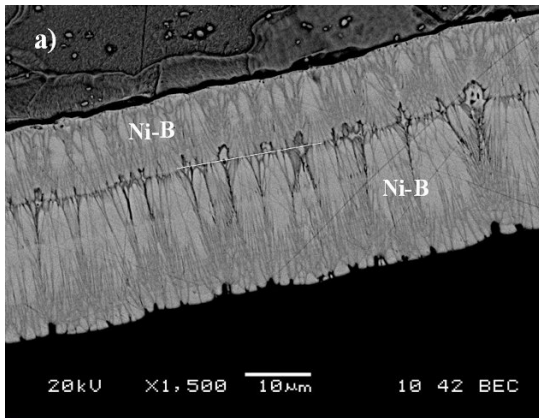
Fig. 8.10: Electroless nickel-boron on steel, with punctual replenishment (SEM - cross section).
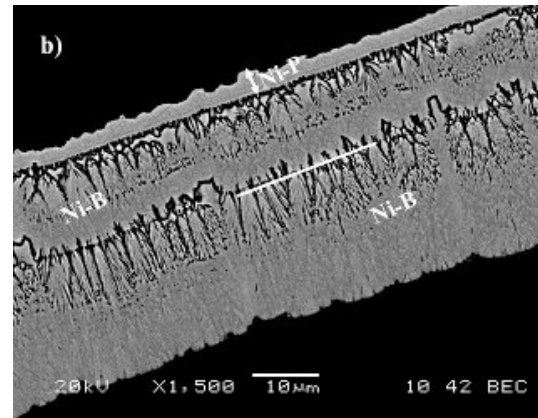
Fig. 8.11: Electroless nickel-boron on aluminum, with punctual replenishment (SEM - cross section).

8.4.2   Structural analysis of electroless nickel-boron by X-ray diffraction (XRD).

X-ray diffraction was used to assess the structure of electroless nickel-boron deposits (using Cu $K\alpha$ radiation ($\lambda = 1,54\dot{A}$). As can be seen on figure 8.12, the patterns obtained on steel and aluminum are very similar, which shows that the structure of the deposit is not influenced by the substrate.
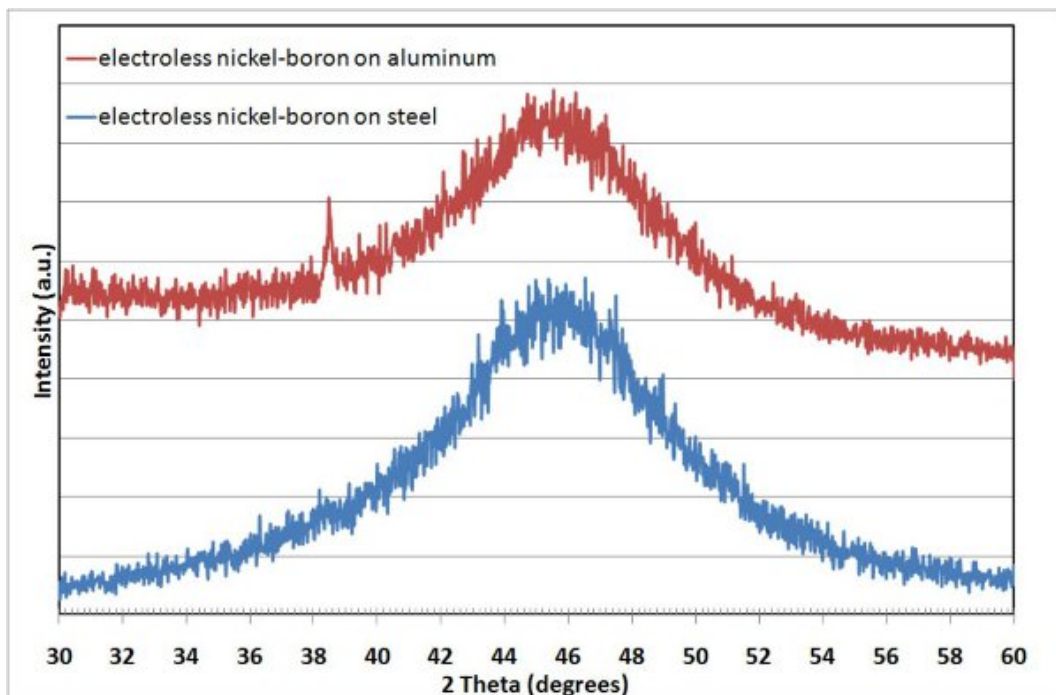
Fig. 8.12: X-ray diffraction patterns for untreated NiB deposited onto steel and aluminum.

The patterns present no sharp well defined peaks, except for the one at $38.7\,°$ on the coated aluminum which is due to the substrate. The very important mound centered

around $45\,^{\circ}$ shows that nickel is present in an amorphous or nanocrystalline form and cannot be macrocrystalline. However, it is not possible from the simple observation of those patterns to affirm that the sample is either amorphous or nanocrystalline. The discussion of the crystallinity of the sample is the object of section 8.4.2.1.

8.4.2.1 Grain size measurement from X-ray diffraction data.
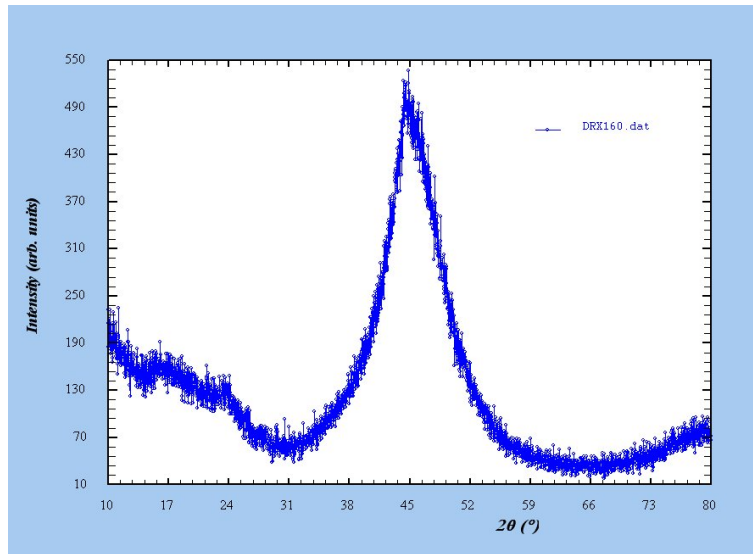
Fig. 8.13: X-ray diffraction patterns for untreated NiB deposited onto steel.

To determine the grain size from XRD data, new patterns were recorded, as shown in figure 8.13. The FullProf program was then used to determine the grain size, from the full width at half maximum, following Scherrer's equation (eq. 8.1) [141], where L is the average grain size, K = 0.94, λ is the X-ray source wavelength, θ is the diffraction angle and $(\delta 2\theta)^S$ is the full width at half maximum of the peak.

$$(\delta 2\theta)^S = \frac{K\ \lambda}{L\ cos\theta} \tag{8.1}$$

This calculation lead to an average grain size of 1 nm. This means that while the material is not amorphous, the size of crystallites is excessively small, which could suggest a fully amorphous state.

8.4.3 Morphological and structural examination of electroless nickel-boron by Transmission Electron Microscopy (TEM) and Electron Diffraction.

While there are some papers about TEM observation of electroless nickel-boron deposits, most of them are carried out on peeled off deposits [31, 33, 59, 60]. The observation

is thus always carried out on sections perpendicular to the growth direction, which is a real problem because the formation mechanism of electroless nickel coatings makes them very anisotropic. The usual observation are thus not able to give any reliable information about the evolution of structure in the coating.

There are few techniques that allow to obtain sections parallel to the growth direction of electroless coatings: as the samples are metallic and are often deposited on metallic substrates, it is very difficult to cut them with the usual tools of TEM preparation because they are too hard to be prepared with the procedures adapted to polymers and too ductile to be cut like glass or ceramic samples without important modification of their structure.

Preparation of thin sections by focused ion beam (FIB) ensures that the structure of the sample will be left unmodified during the process and allows preparation of thin sections out of metallic samples.
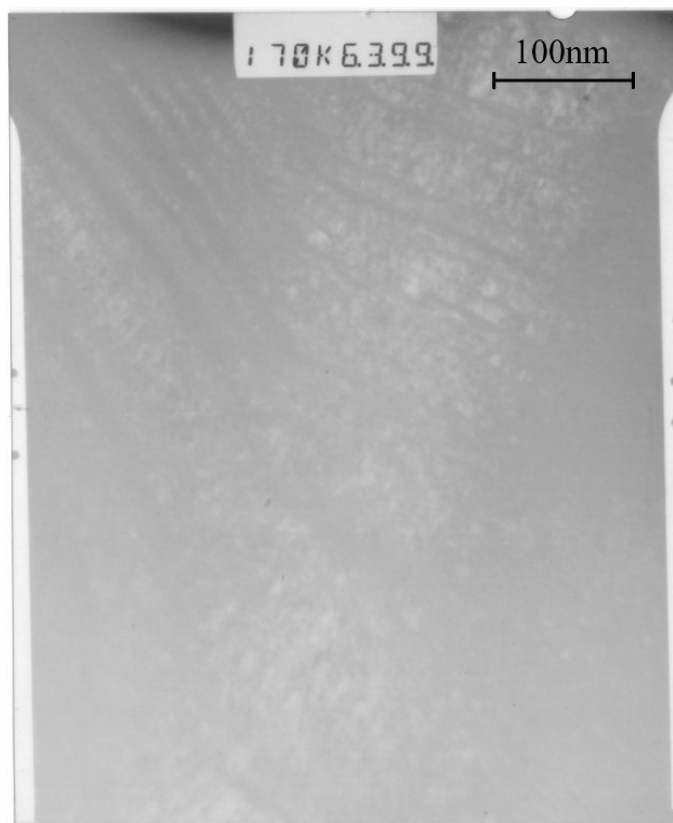
Fig. 8.14: TEM image of an as-deposited electroless nickel-boron deposit.

The observation of thin sections of our samples shows that they cannot be considered as fully amorphous. Very small grains are observable everywhere in the sample (see figures 8.14, 8.15 and 8.16), contrary to observations made on peeled off coatings by Sankara Narayanan et al.[31].
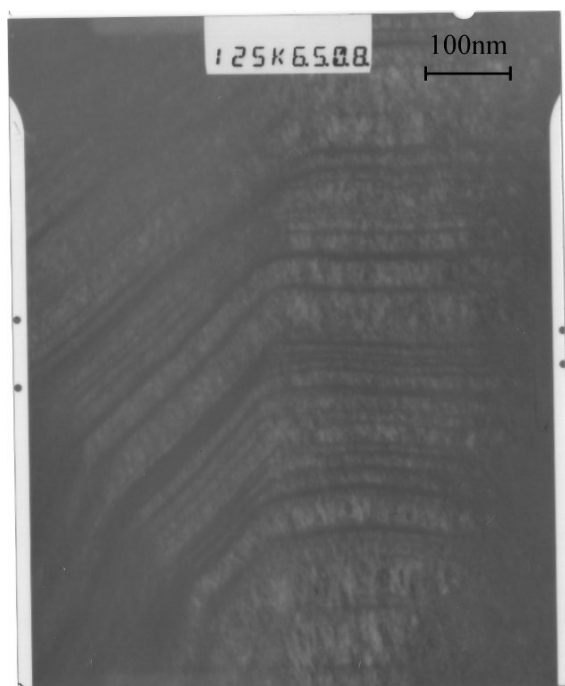
Fig. 8.15: TEM image of an as-deposited electroless nickel-boron deposit.
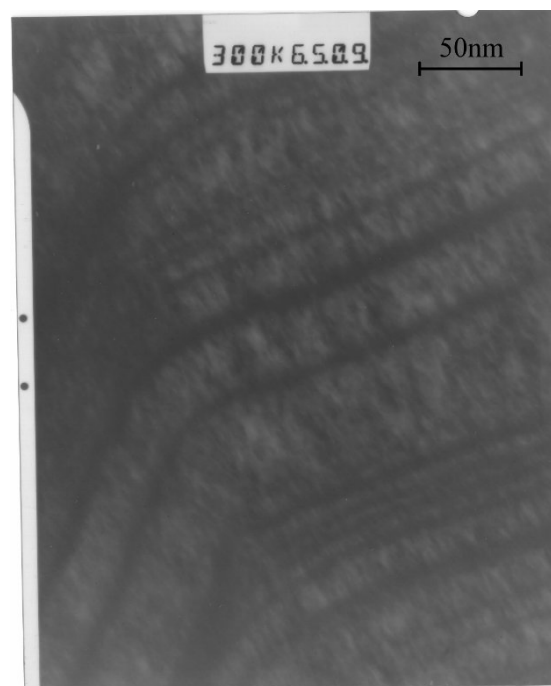
Fig. 8.16: TEM image of an as-deposited electroless nickel-boron deposit.

The grains appear to follow the profile of the sample surface in a wave-like pattern (see figures 8.14 and 8.15), and the delimitation of the columns that are observed by SEM are faintly visible. The successive layers that form this pattern are obviously reminiscent of the laminated microstructure observed in electroless nickel-phosphorous deposits [2], but on a much smaller scale, each strata being, in the case of electroless nickel-boron, formed of a number of smaller grains.

It is very likely that those layers are linked to variations of the deposit composition (and mainly of lead concentration) but it was not possible, at the present stage of research, to prove this.

Electron diffraction patterns of the electroless nickel-boron deposits (see figures 8.17, 8.18) confirm that they are not amorphous as two faint but well defined diffraction rings are observed.

The inter-reticular distances can be obtained from the electron diffraction patterns using equation 8.2 [142–144].

$$D \cdot d = \lambda \cdot L = \text{Constant} \tag{8.2}$$

Where D is the distance between the refracted and transmitted rays, λ is the wavelenght (calculated from the excitation energy), L is the camera length of the microscope and d is the inter-reticular distance.
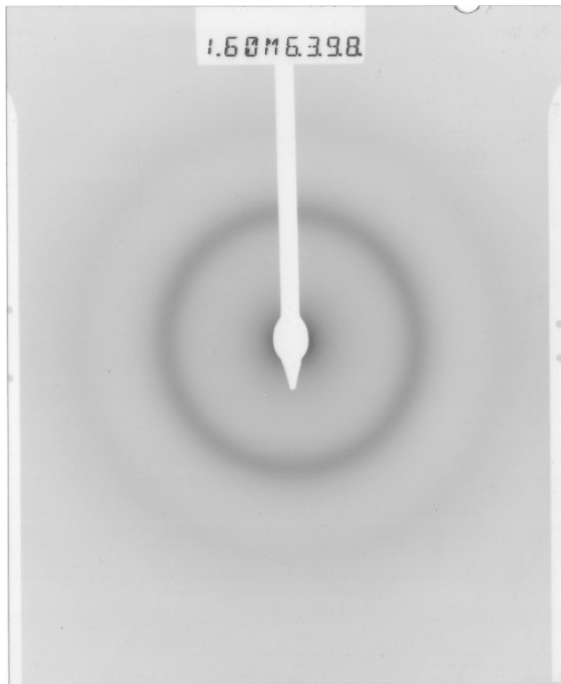
Fig. 8.17: Electron diffraction pattern of as-
deposited electroless nickel-boron.
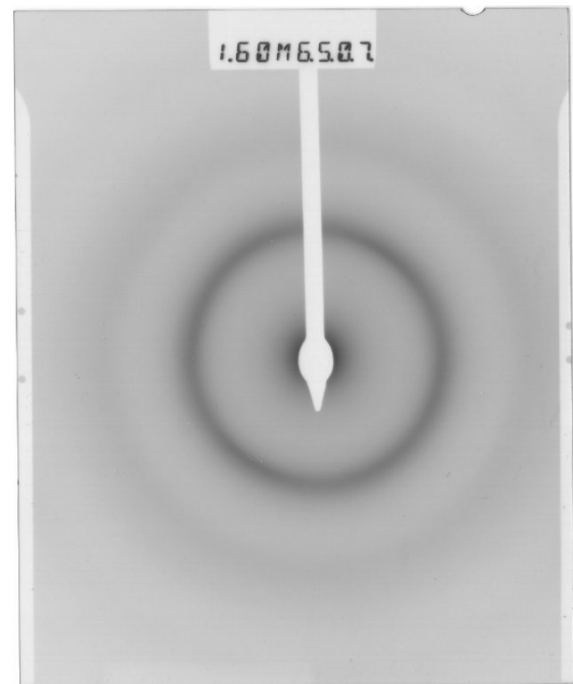
Fig. 8.18: Electron diffraction pattern of as-
deposited electroless nickel-boron.

It was possible to obtain values of d for the 2 diffraction rings observed on figures 8.17 and 8.18. They are presented in table 8.1. They correspond, in both cases to strong reflexions of the FCC Nickel phase. It was thus possible, as it is a cubic phase, to determine the cell parameter of the phase from d and Miller's indices of the diffracting planes. This parameter was found to match relatively closely the ideal value for FCC Nickel: 3.5238 Å, which confirms that the structure of the nanocrystallites is similar to that of nickel.

Ring	D (cm)	d (Å)	h	k	l	a (Å)
Fig 8.17, interior	1.95	2.05	1	1	1	3.557
Fig 8.17, exterior	3.17	1.26	2	2	0	3.563
Fig 8.18, interior	1.94	2.06	1	1	1	3.571
Fig 8.18, exterior	3.18	1.25	2	2	0	3.551

Tab. 8.1: inter-reticular distances calculated from electron diffraction patterns.

8.5   Mechanical properties of as-deposited coatings.

Mechanical resistance of electroless deposits is of crucial importance for most of their applications. This resistance is assessed by the mechanical properties of the coating, one of the most important being the hardness. In this section, the results of hardness measurement carried out on as-deposited coatings will be discussed. In order to get as much information as possible, 3 hardness testing techniques were used:

- Vickers microindentation was used on the surface of the sample,

- Knoop microindentation was carried out on cross sections,

- Instrumented nanoindentation with a Berkovitch indenter was also used on polished cross sections. This technique allowed to obtain further information on the mechanical properties of the coating firstly as it gives access to Young's modulus of the material and finally because the size of the indents allows to study the evolution of hardness across the coating.

Measurement technique	Hardness Value
Knoop (cross section; 25g)	891 ± 35 hk$_{25}$
Knoop (cross section; 50g)	834 ± 20 hk$_{50}$
Vickers (surface; 100g)	854 ± 40 hv$_{100}$
Berkovitch nanoindentation (cross section; $4000\mu N$)	925 ± 70

Tab. 8.2: Hardness of as-deposited electroless nickel-boron deposits.

As shown in table 8.2, the hardness of the electroless nickel-boron coatings is high even in their as-deposited state. It is far higher than the hardness of electroless nickel-phosphorous and is even higher than the usual values given for electroless nickel boron (650 to 750 hv$_{100}$) in section 2.4.2, page 37. It is probable that this difference is due to the nanocrystalline state of the deposits, as nanocrystalline materials are reputed for having better properties than in their coarse grained state [63]. The values obtained by the different techniques are not equal but they are in the same range. The average Young's Modulus obtained from the nanoindentation data is 190.1 ± 9.8 GPa.

The nanoindentation profile (see figure 8.19) shows that the hardness is relatively stable across the deposit, with a slightly higher value in the center of the deposit. However this difference is not very high and stays well in the range of experimental dispersion for that technique. It may thus not be really significant.
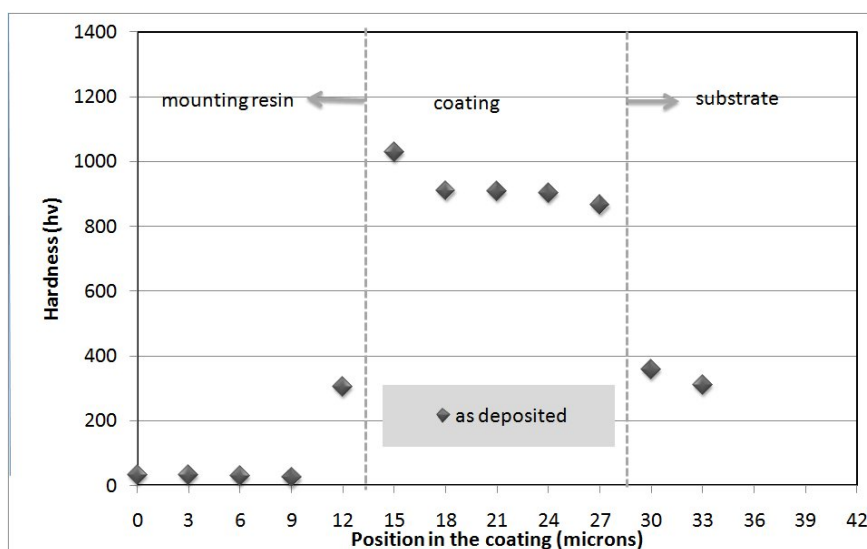
Fig. 8.19: Hardness profile of as-deposited electroless nickel-boron on steel (by nanoindentation).

8.6   Tribological properties of the coatings.

As the mechanical properties, the tribological properties of electroless nickel-boron coatings play a great role in their industrial applications: many electroless nickel coated parts are used for wear applications. In this section, the roughness and wear resistance on electroless coatings will be discussed.

The roughness is important because it conditions the in-use contact area of the plated parts as well as the retention of lubricants.

The wear resistance (in this particular case, the abrasive wear resistance) gives very useful information about the service life of the coated part.

The scratch resistance of the coating will also be studied because it brings information about the damage modes of the coated system and the adhesion of the coating.

8.6.1   Roughness of electroless nickel-boron coatings.

The roughness of as-deposited electroless nickel boron coatings has already been discussed. In section 7.3.1.6.3 (see table 7.9), the influence of the surface state of the substrate on the roughness of the final part has been discussed. It appears than the magnitude of the substrate roughness is conserved in the final value and that smoother substrates lead to smoother plated systems. The electroless coating allows thus to keep quite precisely the shape and state of the parts that are covered.

However, a tribological study of the roughness cannot be limited to the evolution of simple geometrical parameters such as R_a. More roughness parameters, measured on steel substrates with varying surface state (see table 7.4 page 109 for a description of the surface states) are thus shown in table 8.3.

	NP	P1	P2	P3	complete
Ra (μm)	0.76 ± 0.18	0.45 ± 0.07	0.34 ± 0.11	0.42 ± 0.10	0.43 ± 0.05
Rq (μm)	0.96 ± 0.23	0.57 ± 0.08	0.44 ± 0.16	0.54 ± 0.13	0.52 ± 0.06
Rz (μm)	4.70 ± 1.15	2.96 ± 0.31	2.41 ± 0.90	2.67 ± 0.63	2.22 ± 0.23
Rp (μm)	2.62 ± 0.88	1.62 ± 0.24	1.38 ± 0.64	1.30 ± 0.35	0.97 ± 0.09
Rv (μm)	2.08 ± 0.32	1.34 ± 0.08	1.03 ± 0.26	1.38 ± 0.30	1.25 ± 0.14
Rt (μm)	6.46 ± 2.02	3.98 ± 0.78	3.66 ± 2.07	3.55 ± 0.97	3.51 ± 0.55
Rsk	0.31 ± 0.30	0.33 ± 0.21	0.36 ± 0.43	-0.09 ± 0.22	-0.35 ±0.07
Rku	3.20 ± 0.59	3.30 ± 0.27	3.78 ± 0.72	3.37 ± 0.58	2.47 ± 0.06

Tab. 8.3: Roughness parameters of as-deposited electroless nickel-boron deposits.

As can be seen in table 8.3 and on figure 8.20, Ra and Rq are of the order of 0.5-1 μm while the maximum peak to valley distance (Rz) is higher and reaches nearly 5 μm on non-polished substrates. The peak height (Rp) and valley depth (Rv) are always of the same order. Figure 8.21 shows that the skewness (Rsk) is slightly positive for the less polished substrates and slightly negative for the more polished ones. The kurtosis (Rku) has a similar comportment than the skewness and decreases when the substrates are more polished. It is higher than 3 for all substrates excepted the smoothest.
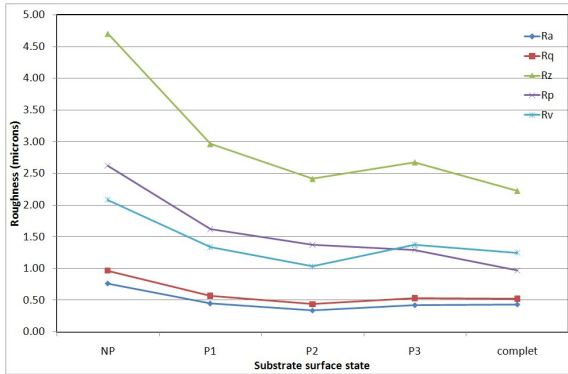
Fig. 8.20: Evolution of roughness parameters with the surface state of the substrate.
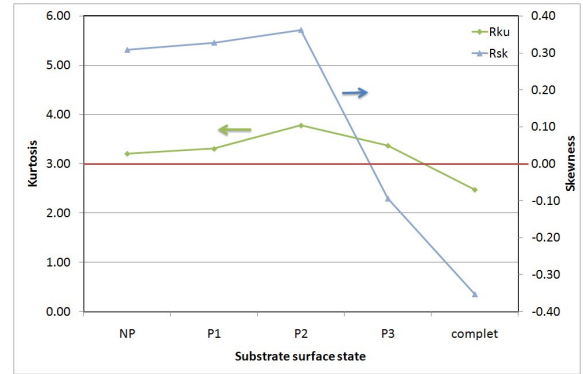
Fig. 8.21: Evolution of roughness parameters (Skewness and Kurtosis) with the surface state of the substrate.

From this, we can say that, on substrates with a not very good surface state, there are slightly more peaks than valleys on the surface and that the peaks are relatively close packed and steep. However, on the smoother substrate, the negative skewness is in good accord with the cauliflower-like texture of the electroless nickel-boron deposits. Nevertheless, the low Ra, Rq and Rt observed for all samples suggest that the coatings are well adapted for wear applications even if the substrate is not smooth enough to guaranties negative skewness and low kurtosis (which are important parameters for wear application).
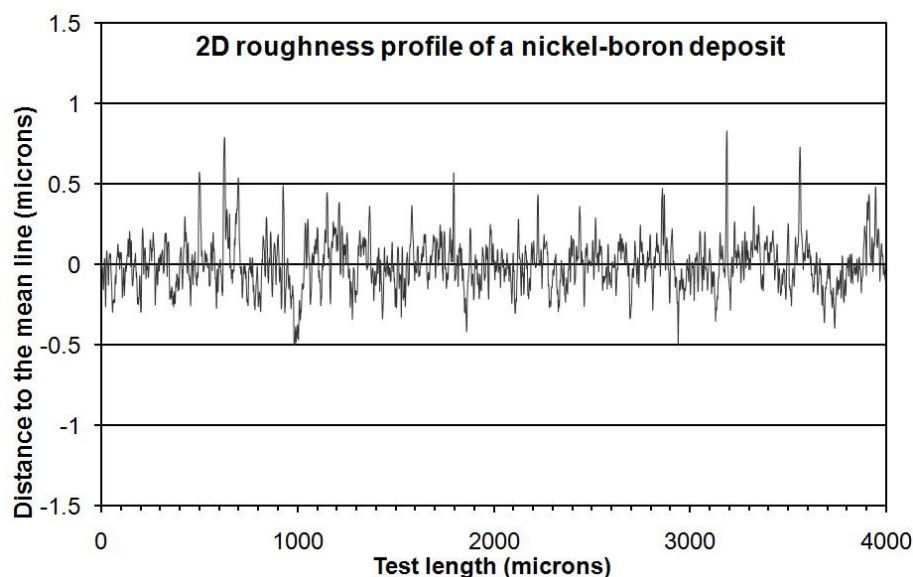
Fig. 8.22: Roughness profile of an electroless nickel-boron deposit.

Observation of the profile measured on an electroless coating (figure 8.22) indicates that the high kurtosis and positive skewness may be due to the presence of a few sharp peaks on a profile that otherwise should have the roughness properties of a cauliflower-like surface (negative skewness and low kurtosis). It is this probable that even the coating with the less encouraging results will have a good in-use comportment.

8.6.2   *Roughness of electroless coatings deposited on aluminum.*

The whole roughness study was carried out on steel as, on this substrate, there is no need for a protective intermediate layer between substrate and coating. However, as some of this work concerns electroless deposits on aluminum substrates, it is useful to study the surface state obtained in this case and to compare it with what is obtained on steel.

To this effect, roughness measurements were carried out on first on steel and aluminum substrates ground up to the same point (grade 1200 SiC paper), prior to the chemical steps of the surface preparation and the roughness of both substrate was in a similar range (R_a of 0.156 ± 0.046 μm for steel and of 0.181 ± 0.026 μm for aluminum), meaning that the final roughness of the coated system will depend mainly on the subsequent steps (etching, zincating and NiP and NiB coating) of the process.

The roughness obtained on the steel substrate was higher than on aluminum, as shown in table 8.4. This can be explained by the smoothing effect of the protective NiP layer deposited on the aluminum substrate to avoid its corrosion during the immersion in the alkaline NiB plating bath.

Sample	Ra (μm)	Rq (μm)	Rz (μm)
coated steel (Ni-B coating)	0.898±0.063	1.143±0.089	6.318±0.967
coated aluminium (Ni-P/Ni-B coating)	0.455±0.101	0.601±0.170	3.464±0.845

Tab. 8.4: Roughness parameters of as-deposited electroless nickel-boron deposits on steel and aluminum.

8.6.3   Wear resistance of the coatings.

The abrasive wear resistance of the coatings was evaluated by the Taber test, using CS-17 wheels that are particularly harsh. As such, the Taber Wear Index (TWI) obtained are higher than the usual values obtained for electroless coatings that were tested using softer CS-10 wheels. The operating conditions for the wear tests were :

- load: 1000g;

- speed: 72 rpm;

- number of cycles: 10 X 1000 cycles, weighting every 1000 cycles;

- wheels refacing: every 1000 cycles, alternatively with emery paper and 'wheel refacer'.

Fig. 8.23: Aspect of a sample after Taber testing.

The aspect of a sample after Taber testing is shown on figure 8.23. Figure 8.24 presents the weight loss measured on 5 different samples (deposited on steel) during the Taber abrasion tests and shows that the experiment is really reproducible. The Taber Wear Index obtained at the end of the test is 24.2 ± 0.476, which is a good value for a TWI using CS-17 wheels. It appears thus that the coating will present a good resistance to abrasive wear.
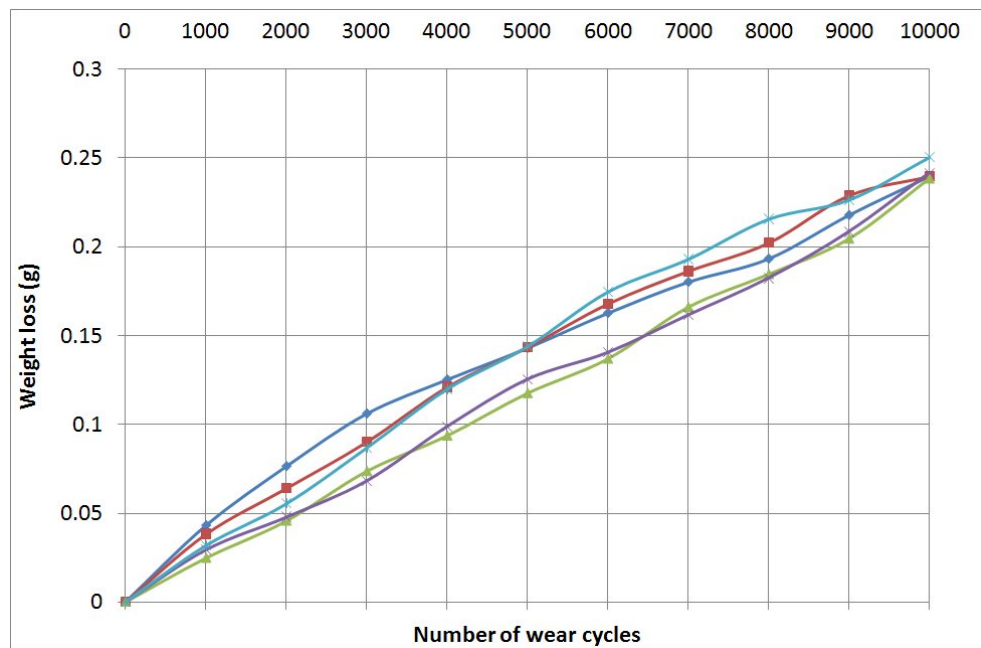
Fig. 8.24: Evolution of weight loss during Taber Wear test on electroless nickel-boron coating
on steel - reproducibility of the experiment.

While abrasive wear should by definition be independent of the substrate nature, it
was interesting to verify this assumption for coated steel and aluminum. These results
are presented on figure 8.25 and it is clear that the Taber resistance of both coatings is
similar, with a TWI of 27 for the steel-based system and 28 for the aluminum-based one.
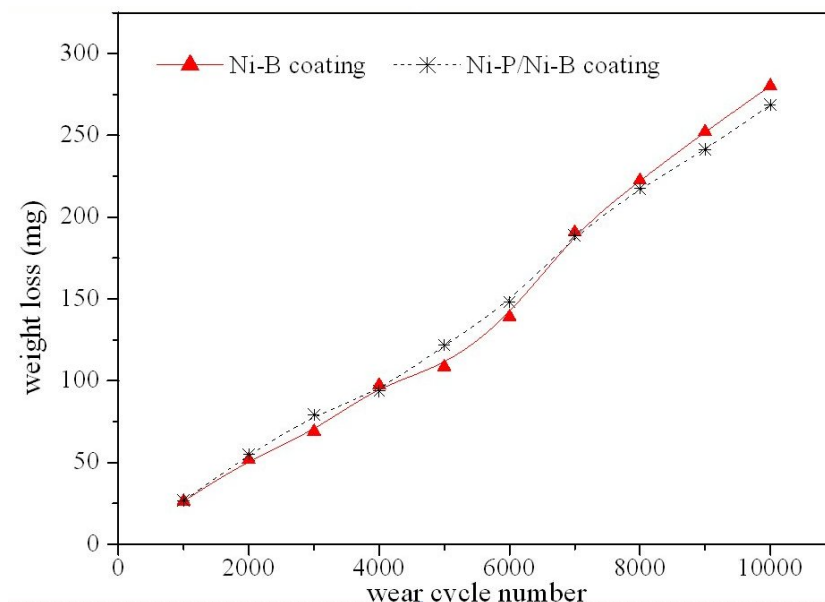
Fig. 8.25: Evolution of weight loss during Taber Wear test on electroless nickel-boron coating
on steel and aluminum substrate.
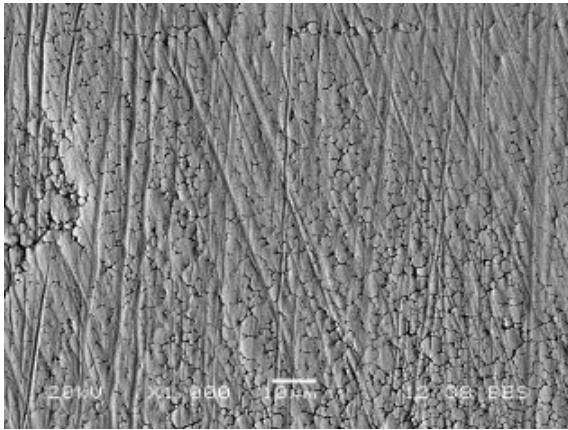
Fig. 8.26: Cross section of an electroless nickel-boron coating after Taber abrasion test.
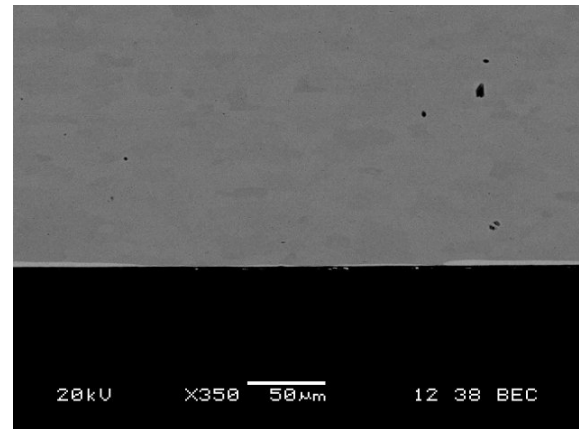
Fig. 8.27: Surface of an electroless nickel-boron coating after Taber abrasion test.

Even if the Taber Wear Index is useful to characterize the resistance of a coating, there is other information that can be obtained from the Taber abrasion test. Surface and cross section SEM images of the abraded area of electroless nickel-boron coatings are shown on figure 8.26 and 8.27. The surface image shows that there is some deposit left on the substrate, as the boundaries of the columns that form the cauliflower-like texture are visible under the scratches. However, observation of the deposit's cross section shows that the coating has been nearly completely removed during the abrasion test (figure 8.27). This is confirmed by observation of the depth profile of the abraded area (obtained by 3D roughness measurement): the depth of the worn path reaches 4 μm (which is the limit for this kind of measurements) very quickly at the edge of the tested area (see figure 8.28).
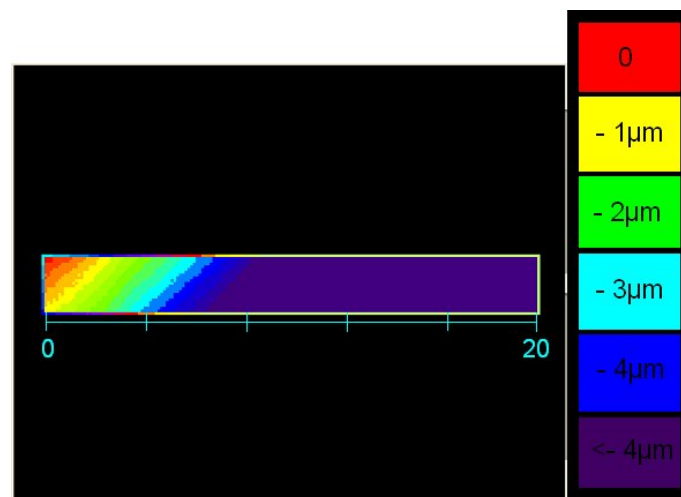
Fig. 8.28: Depth profile of the abraded area of an electroless nickel-boron deposit.

8.6.4   Scratch resistance of the coatings.

Scratch tests provide insightful information about the in-use comportment of materials and coatings. To assess the comportment of electroless nickel-boron, they were performed on $15\mu m$ thick samples synthesized on aluminum alloy for the observation of global damage and on thinner ($\approx 6\mu m$) samples synthesized on mild steel for the investigation of the coating adhesion. The tests were carried out using a continuously increasing load (up to 25N) and the acoustic emission and friction coefficient were monitored during the experiment. The residual scratches were observed either by optical microscopy or SEM.

Firstly, the scratch resistance of 15 μm thick coatings on aluminum substrate was assessed with a maximal load of 25N. During this experiment, no critical load was detected, even at the highest values, as can be seen in figures 8.29 and 8.30. The coating only suffered elastic and plastic deformation, as well as some microcracks on the edge of the scratches that are typical of metallic comportment of the sample. The friction coefficient increased linearly with the normal load and no acoustic emission was recorded. The nickel-boron coatings show thus a good scratch resistance. The fact that there isn't any damage except plastic deformation in the coatings during scratch test is probably due to the important plastic recovery of the coating and substrate: the penetration depth at maximal load of the scratch stylus is always close to 20 μm while the residual penetration depth is only 10 μm (less than the coating thickness).

(a)untreated sample

Fig. 8.29: Residual scratch on electroless nickel-boron coated aluminum (maximal load: 25N).

Fig. 8.30: Residual scratch on electroless nickel-boron coated aluminum (maximal load: 25N) - end of the scratch.

In order to detect a critical load, thinner coatings (close to 6 μm) deposited on steel were tested under the same experimental conditions. It was then possible to determine

values for the critical load, from the friction coefficient variation and SEM observation. Both values are in good agreement, close to 21 N, as shown in table 8.5.

Critical load	
from friction coefficient	from SEM observation
21.8N	21N

Tab. 8.5: Critical load (adhesive) of electroless nickel-boron coatings.

The detection of the critical load by the variation of the friction coefficient was possible because there is an increase from 0.3 up to 0.45 when it is reached.

The observation of the residual crack (see figure 8.31) allowed identification of the damage modes of the coating: longitudinal cracking on the edge of the coating appeared first, then forward chevron cracks. The first adhesive failure was discontinuous ductile perforation of the coating. This shows that the coating has a metallic, ductile comportment at all stages of the testing and allows, combined with the good abrasion and roughness results, to predict a good comportment in wear applications. Moreover, the type of failure that was observed (ductile perforation) indicates that the adhesion of the coating to the substrate is very good.
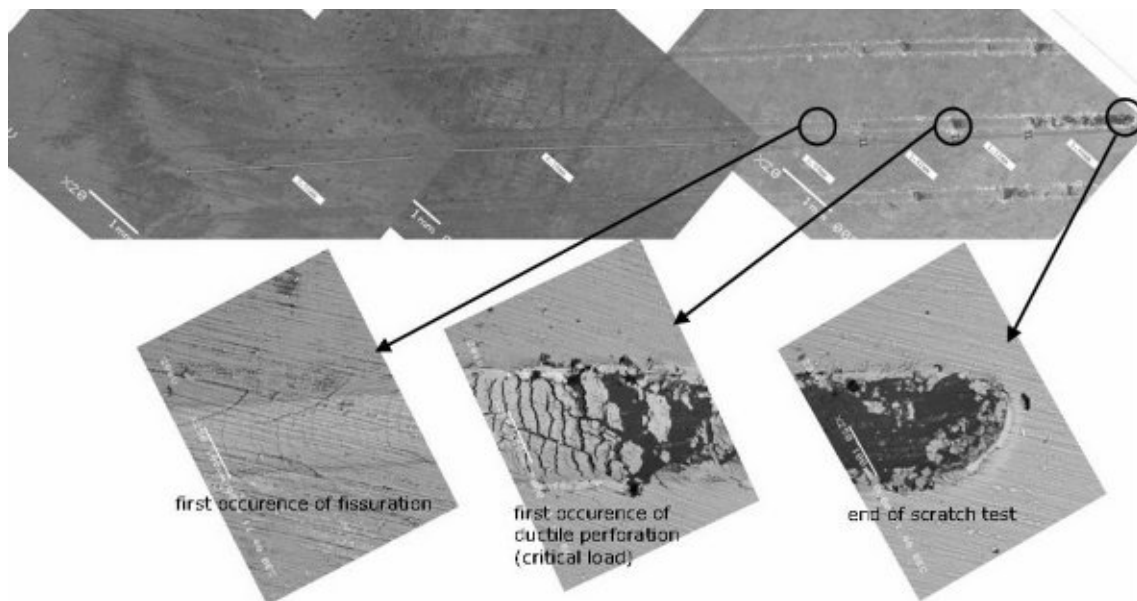
Fig. 8.31: Residual scratch on electroless nickel-boron coated aluminum (maximal load: 25N).

8.6.5   Conclusions.

The tribological properties of the coating were investigated by three different methods: roughness measurement, abrasive wear testing and scratch testing. All of those tests rendered a similar response: the electroless nickel-boron coatings are good candidates for

wear applications, because they are smooth and their surface texture is favorable to sliding, their Taber Wear Index is low, their comportment during scratch testing is ductile and they have a good adhesion with the substrate.

8.7   Corrosion resistance of as-deposited electroless nickel-boron.

As electroless nickel coatings were first developed for corrosion application, their electrochemical properties and corrosion resistance must be studied with great attention.

In the present section, the coatings will be submitted to a battery of electrochemical tests that are designed to predict the corrosion resistance of the coating.

There are many factors influencing the corrosion resistance of materials. For this reason, this study will cover several coated systems. First of all, the properties of nickel-boron coated steel will be measured, as this system is the simplest. Then those results will be compared to nickel-boron coated aluminum, which is a more complex system as there is a nickel-phosphorous underlayer. Finally, as the electroless coatings are intended to be used in wear applications, the effect of wear on their corrosion resistance will be observed.

8.7.1   Investigation of the corrosion resistance of electroless nickel-boron by electrochemical tests.

Electrochemical methods for the evaluation of the corrosion resistance of materials were developed to predict their performance. They are in many cases less destructive and quicker than the traditional exposure methods and they allow access to information about the corrosion mechanisms. In this section, two electrochemical methods will be used:

- Potentiodynamic polarization curves were recorded on the samples. For this, the electrode potential varied from -600 to +250 mV against the reference electrode, at a rate of 10 mV.min^{-1}. In all cases, the sample was immersed in the solution 15 minutes before the test in order to stabilize the open circuit potential.

- Electrochemical Impedance Spectroscopy (EIS) measurements were carried out in the frequency range 10^5 - 10^{-2} Hz with a sinusoidal signal perturbation of 5 mV and 50 data points taken per interval.

All of the electrochemical tests were carried out with a Parstat 2273 potentiostat frequency response analyzer (FRA), in 0.1 M NaCl, at room temperature with a conventional three-electrode cell. The electrodes used for the tests were :

- Working electrode : electroless nickel-boron specimen.

- Counter electrode: platinum grid.

- Reference electrode: Ag - AgCl/KCl (saturated) (offset potential against normal hydrogen electrode: 0.197V)

The analyzed surface was normalized by masking with silicone (exposed area : 1 cm^2). In order to minimize external interference, the electrochemical cell was placed in a Faraday cage.

8.7.1.1 Corrosion resistance of electroless nickel-boron plated steel.

Among the system that were investigated during this study, steel coated with electroless nickel-boron is the simplest: the use of a protective nickel-phosphorous layer to avoid degradation of the aluminum substrate during the plating brings a far more complicated system and modifies its properties in a non negligible manner. To be sure that only the protective characteristics of the nickel-boron coating are investigated, it is thus better to begin with the coated steel.

In this section, the corrosion resistance of this system will be observed from different point of view. First, the potentiodynamic polarization curve and EIS results will be discussed. Then, examination of the surface of the tested samples by SEM will be presented.

8.7.1.1.1 Potentiodynamic polarisation.

Potentiodynamic polarization curve measured on uncoated and NiB coated steel are shown on figure 8.32. From this, it is evident that the nickel-boron coating brings a significant rise of the corrosion resistance of the steel, as the comportment of the coated sample is much nobler than the substrate.
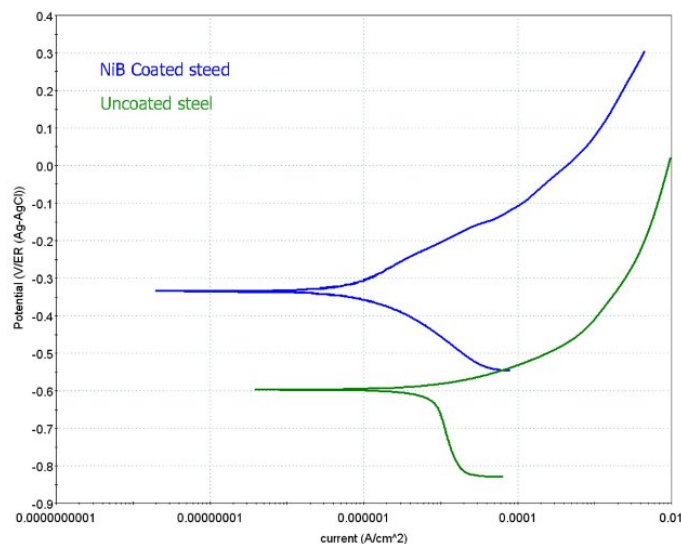
Fig. 8.32: Potentiodynamic polarization curve of electroless nickel-boron coated steel.

The cathodic reaction shown by the polarization curve is the reduction of dissolved oxygen and it is not apparently modified by the coating. Only the anodic part of the curve is linked with corrosion and it is favorably influenced by the electroless nickel-boron

deposit. The corrosion current and potential were calculated by Tafel approximation for both the uncoated substrate and the nickel-boron coating. They are shown in table 8.6.

Sample type	Corrosion current (μA)	Corrosion potential (mV vs. Ag/AgCl)
Uncoated steel	2.34	-595.25
NiB coated steel	0.09	-335.05

Tab. 8.6: Corrosion current and potential of electroless nickel-boron.

To allow comparison of those results, figures 8.33 and 8.34 present potentiodynamic polarization curves recorded on NiP in a similar medium (3.5% NaCl). While the reference electrodes used in this study are not the same as ours, the difference in offset against normal hydrogen electrode is small enough that the results can be qualitatively compared. It is clear that the corrosion potential of the electroless nickel-boron coating is as good as the noblest of the nickel-phosphorous coatings presented in both figures.
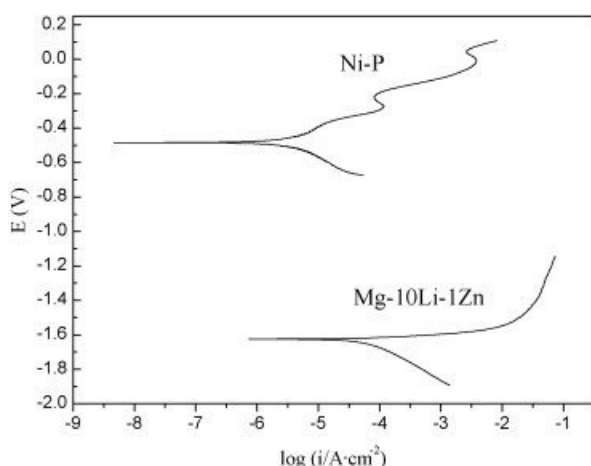
Fig. 8.33: Potentiodynamic polarization curve on electroless nickel-phosphorous coating [145]. Potential against saturated calomel electrode (offset potential against NHE: 0.240V).
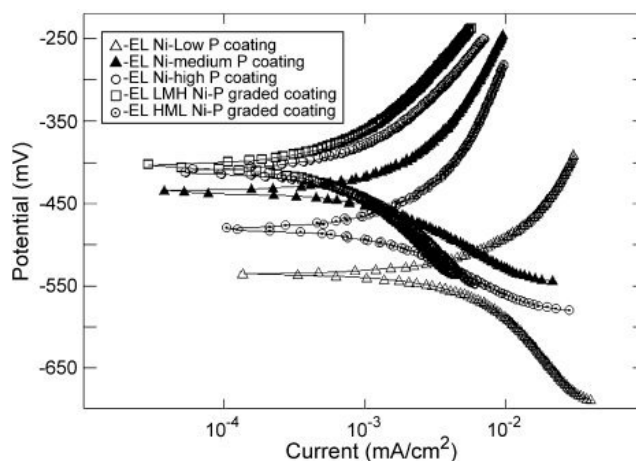
Fig. 8.34: Potentiodynamic polarization curve on electroless nickel-phosphorous coating [146]. Potential against saturated calomel electrode (offset potential against NHE: 0.240V).

8.7.1.1.2   *Electrochemical Impedance Spectroscopy.*

Electrochemical impedance spectroscopy was used to evaluate the resistance of the coating and its evolution with exposition to 0.1 M NaCl. The results are shown on figures

8.35 (Bode phase diagram) and 8.36 (Bode modulus diagram).
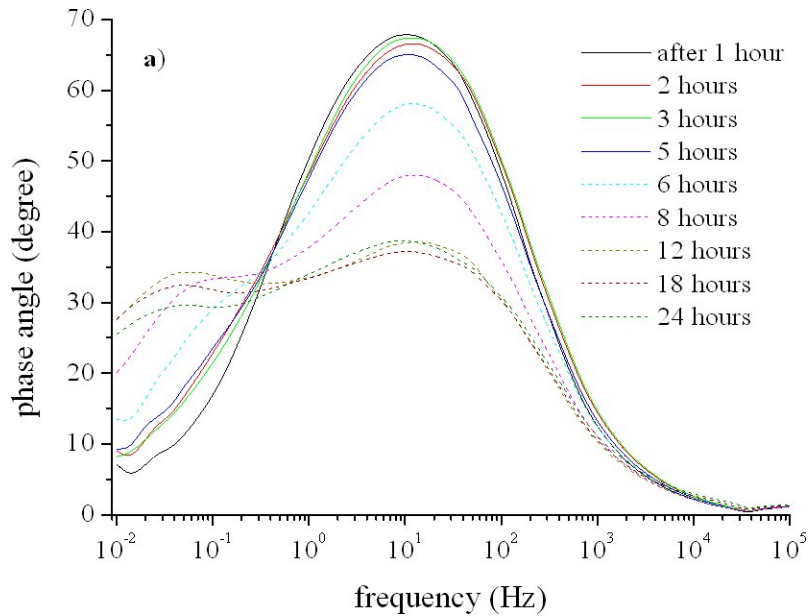
Fig. 8.35: Electrochemical impedance spectroscopy curves of electroless nickel-boron coated steel (Bode phase diagram).
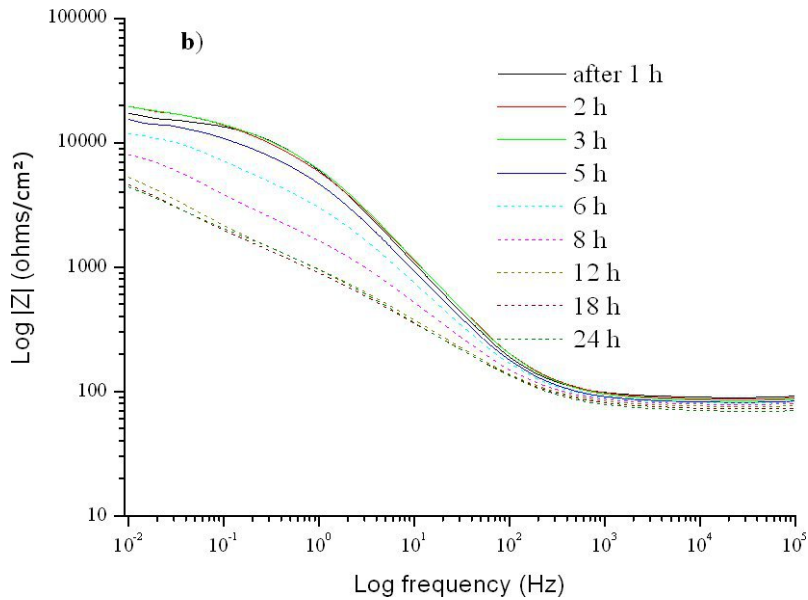
Fig. 8.36: Electrochemical impedance spectroscopy curves of electroless nickel-boron coated steel(Bode modulus diagram).

Initially, there is a single inflection point in the Bode phase diagram (figure 8.35), which indicates a process involving a single time constant that corresponds to a charge transfer resistance. The Bode modulus diagram (figure 8.36) confirms this, from which it is possible to obtain approximation of the solution resistance (91 $\Omega.cm^2$), the modulus at

low frequency ($1.7 * 10^4$ $\Omega.cm^2$) and the double layer capacitance ($1.49 * 10^{-5}$ F/cm^2). This indicates a good comportment of the coating that is nearly unmodified during the first 5 hours of exposition to the sodium chloride solution. This comportment can be represented by the equivalent circuit shown in figure 8.37, whose typical Bode diagrams constitute figure 8.38. Those results appear to be in good adequation with the findings of Contreras et al [98] (see figure 3.12, page 50).
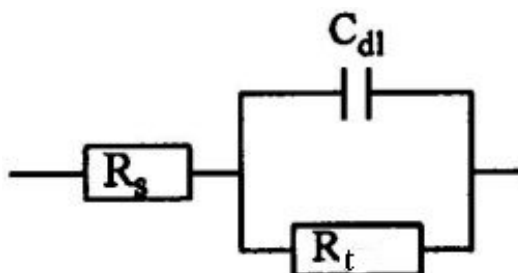
Fig. 8.37: Equivalent circuit for the fresh electroless coating comportment in impedance spectroscopy [147].
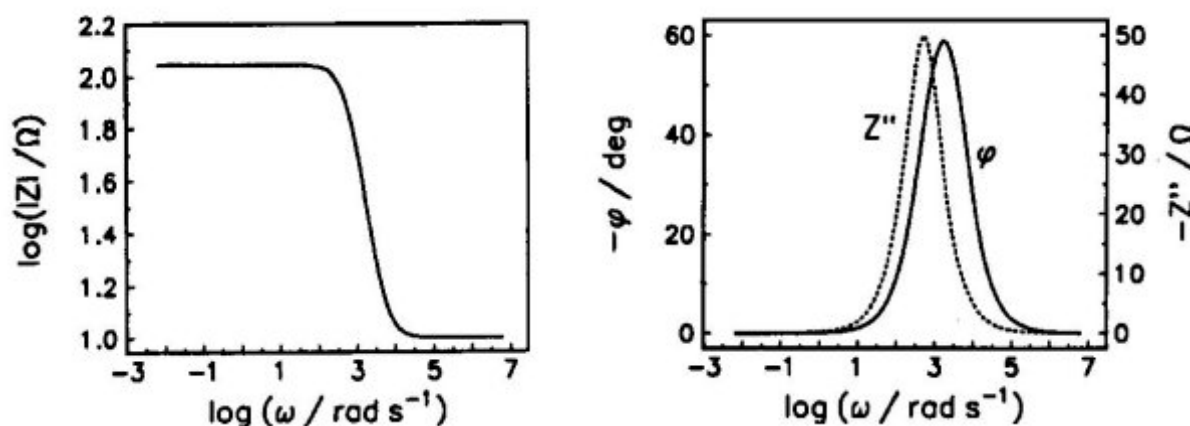
Fig. 8.38: Typical Bode diagrams for circuit shown in figure 8.37[147].

After an immersion of 6 hours in NaCl, the comportment of the coating starts changing and a second time constant appears (there are two loops at low and high frequencies in the Bode phase diagram (figure 8.35)). The modulus at low frequency is also significantly decreased ($5 * 10^3$ $\Omega.cm^2$ after 12 hours, figure 8.36), which indicates a lowering of the corrosion resistance. The response of the coating appears to be stabilized after a 12 hours long immersion in NaCl. The final response can be represented by the equivalent circuit shown in figure 8.39: the high frequency response is linked to the double layer capacitance and charge transfer resistance of the coating, while the low frequency response is due to the charge transfer resistance and double layer capacitance of the substrate. This means that some corrosion paths (or pores) are present in the coating and that some of the substrate is exposed to the electrolyte.
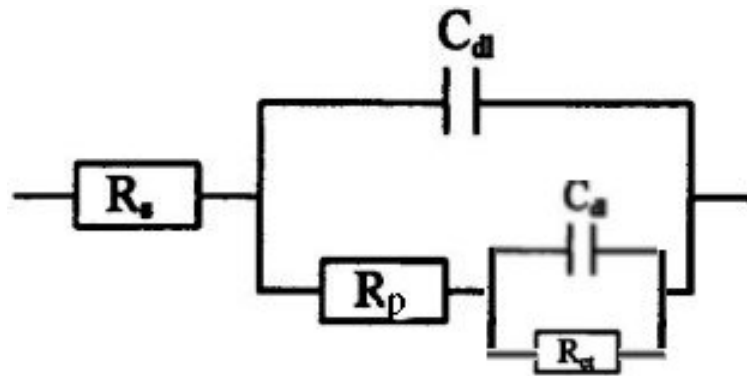
Fig. 8.39: Equivalent circuit for the electroless coating comportment in impedance spectroscopy after immersion in NaCl for 12 or more hours [147].

Those results were compared with published data for electroless nickel-phosphorous and nickel-boron coatings for validation. The impedance response recorded on fresh coatings is very similar (and even somewhat better) to what is found for electroless nickel-phosphorous (figure 8.40). An equivalent circuit similar to the one presented on figure 8.37 was proposed for those coatings by Sankara Narayanan et al. [146].
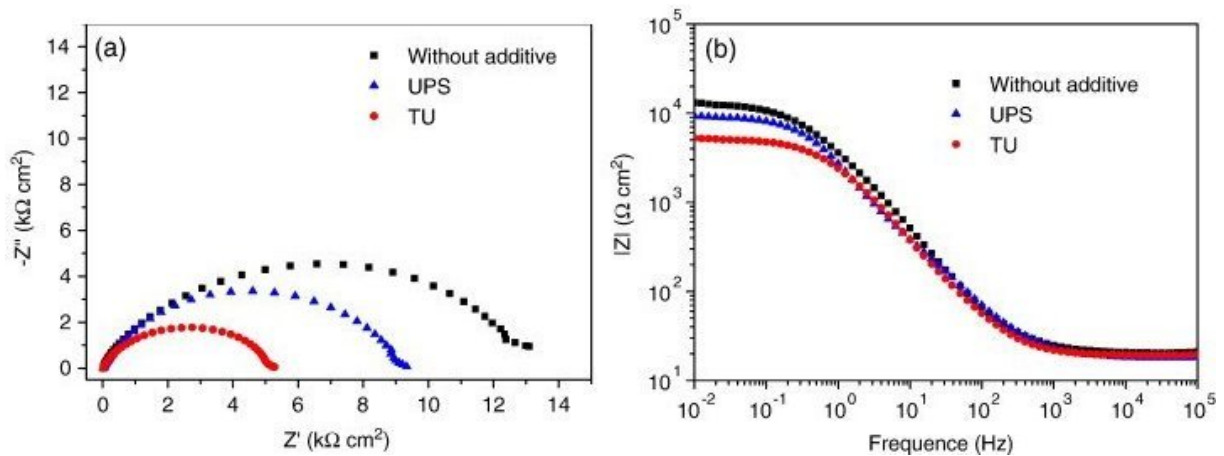
Fig. 8.40: EIS data for Electroless nickel-phosphorous coatings in 3.5 wt.% NaCl solution at their respective open circuit potentials. [148].

8.7.1.1.3   SEM observation of tested areas and corrosion mechanisms.

An electrochemical study of the corrosion of electroless nickel-boron coatings would not be complete without observation of the surfaces after the electrochemical tests: the corrosion mechanisms can be better understood if the damage inflicted during the test is carefully observed, for example by SEM.

During potentiodyamic polarization tests, the samples are submitted to conditions that lead to corrosion. As such, it is inevitable that some damage occurs. The observation of this damage brings interesting information about the corrosion processes taking place on the sample. Figure 8.41 shows the surface aspect of an electroless nickel-boron sample (untreated, on steel) after the polarization test. Spots are visible on the surface of the sample. The presence of chloride ions in the testing solution may at first suggest pitting as an explanation for the presence of those spots. However, the electroless nickel-boron coating shows no evidence of passive behaviour and as such, its polarization curve (see figure 8.32) does not indicate pitting episodes. Another explanation was thus searched for the presence of the spots.
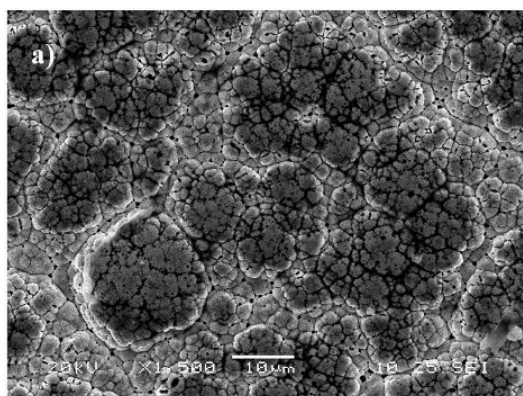
Fig. 8.41: Electroless coating after potentiodynamic polarization test.

Similar spots were observed on nickel-phosphorous coatings by Crobu et al. [149] in NaCl solution and they report observation of this phenomenon in other media as well. They attribute those to composition heterogeneities of the coating inducing galvanic coupling between areas with differing phosphorous content or to the influence of the bath stabilizer. The hypothesis of Crobu [149] could be extended to electroless nickel-boron deposits but further investigation is needed to ascertain this.

While EIS is less destructive than potentiodynamic polarization (the experiment is carried out very close to the open circuit potential), the long immersion in the (0.1 M) NaCl solution needed to study the aging of the coatings causes an attack of the grains and columns boundaries and, as was shown by the apparition of a second time constant during the EIS tests, diffusion occurs inside the coating, which decreases the corrosion resistance. The extent of the damage caused by this long immersion can be seen on figure 8.42. After 24 hours of exposure to NaCl, the surface is mainly undamaged (figure 8.42a).

However, after 21 days, numerous black spots are apparent on the surface of the samples (that is then reminiscent of the surface obtained after potentiodynamic polarization) but there is no apparent pitting.
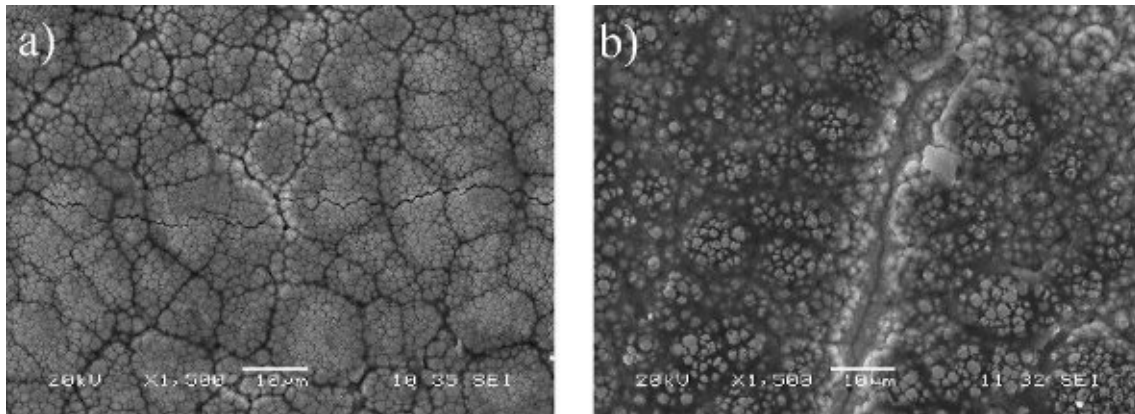
Fig. 8.42: Electroless coating after immersion in NaCl solution for
(a) 24h and (b) 21 days.

Combination of immersion in NaCl (0.1 M) solution and subsequent polarization test causes more damage to the coating, as shown on figure 8.43: the superficial structure of the coating is strongly modified and intercolumnar corrosion is evident. This particular corrosion is due to the lesser density of the intercolumnar boundaries as well as their differences of composition with the rest of the coating. However, cross sections observation of 30 μm thick coatings after this treatments showed that the corrosion does not reach the substrate (see figure 8.44), indicating that the coating keeps some of its protective properties.
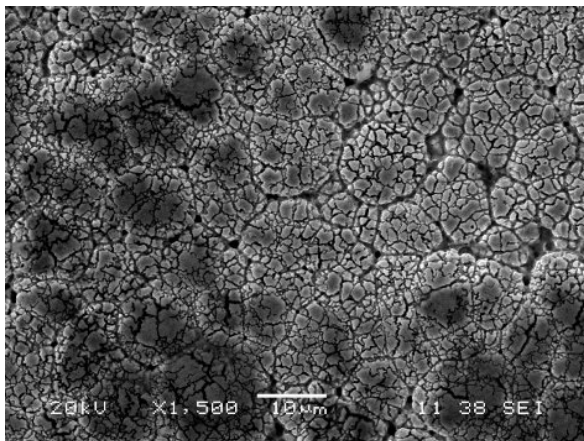
Fig. 8.43: NiB coating after immersion in NaCl solution for 19h and potentiodynamic polarization.
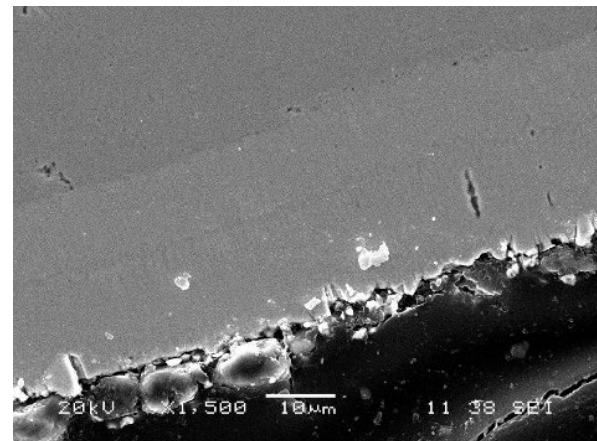
Fig. 8.44: Cross section of NiB coating after immersion in NaCl for 19h and potentiodynamic polarization.

8.7.1.2   Comparison of the corrosion resistance of electroless nickel boron deposited on steel and on aluminium.

Now that the electrochemical properties of the simpler substrate-coating system (steel coated with nickel-boron, or Steel/NiB) have been investigated, more complex systems, such as aluminium coated with NiP and NiB (Al/NiP/NiB), can be evaluated and compared with the coated steel. In this section, the potentiodynamic polarization and electrochemical impedance spectroscopy results obtained on the Al/NiP/NiB system will be described and discussed.

8.7.1.2.1   Potentiodynamic polarisation.

As can be seen on figure 8.45, the polarization curve of the Al/NiP/NiB system is shifted to nobler potential than the Steel/NiB. The calculated corrosion current and potential (see table 8.7) appear to support this: there is a significant decrease of the corrosion potential on the Al/NiP/NiB, even if the corrosion current is slightly higher on this system. In view of this, one can predict a better corrosion resistance for the aluminum-based system. The reason for this better comportment cannot be directly attributed to the presence of the nickel-phosphorous underlayer, as nickel-boron is a barrier coating. However, it has an indirect effect on the corrosion properties: the Al/NiP/NiB system is, after similar mechanical surface preparation, smoother than the Steel/NiB system (as was shown in section 8.6.2) and can thus have a better corrosion resistance, as observed by Cheong [150] for NiP coatings. SEM observation of the coating revealed the presence of black spots similar to those that were observed on the NiB coated steel (see section 8.7.1.1.3).
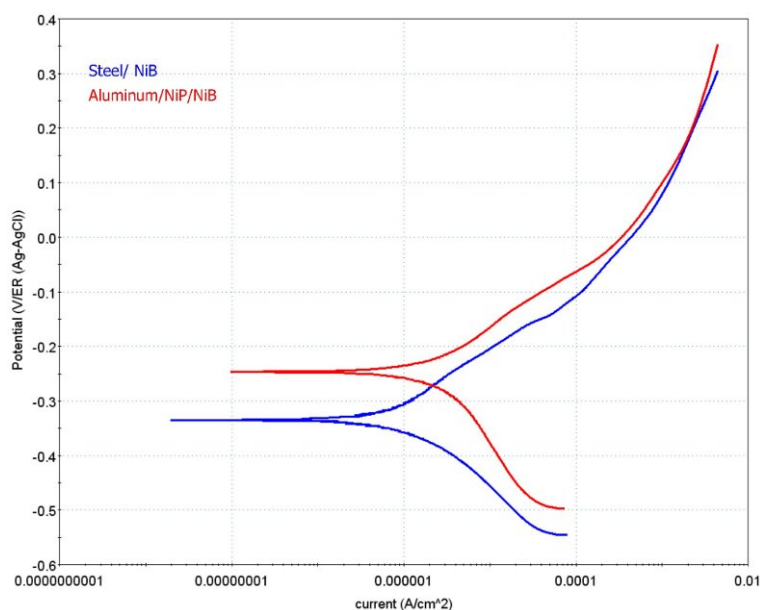
Fig. 8.45: Potentiodynamic polarization curve of the Steel/NiB and Al/NiP/NiB systems.

Sample type	Corrosion current (μA)	Corrosion potential (mV vs. Ag/AgCl)
NiB coated steel	0.09	-335.05
NiP/NiB coated aluminum	0.217	-245.14

Tab. 8.7: Corrosion current and potential of Steel/NiB and Aluminum/NiP/NiB systems.

8.7.1.2.2 Electrochemical impedance spectroscopy.

The comportment of the steel and aluminum-based systems during EIS tests are quite similar, as shown on figure 8.46 (and thus the equivalent circuit shown on figure 8.37 can also be applied to this system) but the low frequency modulus of the Al/NiP/NiB system is higher than on steel. This confirms that its corrosion comportment is expected to be better than on steel. Measure of the low frequency modulus(table 8.8) confirms this it is higher on Al/NiP/NiB than on steel/NiB. The double layer capacitance was also calculated and it is in the order of $4 * 10^{-6}$ F/cm^2.
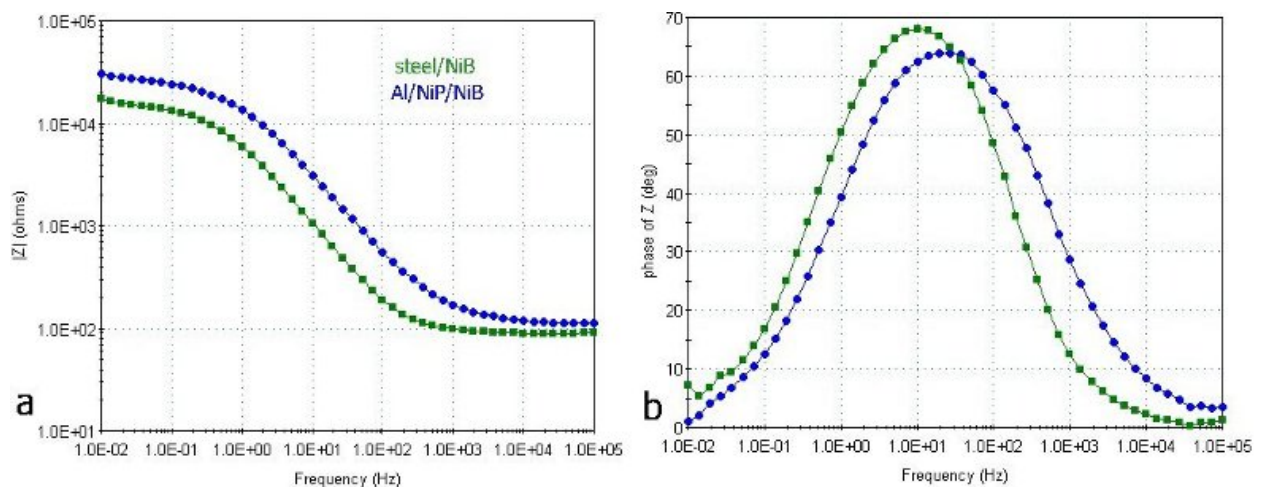
Fig. 8.46: Electrochemical impedance spectroscopy curves of the Steel/NiB and Aluminum/NiP/NiB systems:
Bode Modulus plot (a) and Bode phase plot (b).

Coating	Rs (Ω.cm^2)	Low frequency modulus (0.01Hz) (Ω.cm^2)
Steel/Ni-B as-deposited	91	17160
Al/NiP/Ni-B as-deposited	112	30138

Tab. 8.8: Solution resistance and low frequency modulus obtained on NiB coated systems in the as-deposited state.

As on steel, the aging of the system was studied. As shown on figure 8.47, after an exposure of 48 hours to the NaCl solution, the Al/NiP/NiB does not present a second time constant. However, the low frequencies modulus is lower ($1 * 10^{-4}$ $\Omega.cm^2$) and the phase angle peak has shifted to lower frequencies. This system presents thus a better resistance to aging in NaCl than the NiB coated steel. This may be a consequence of the presence of the NiP underlayer.
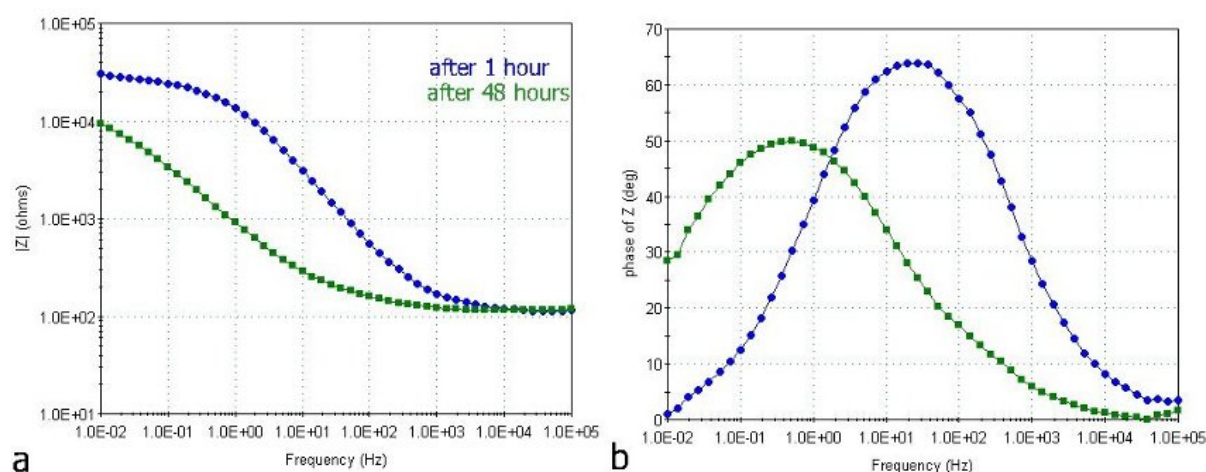
Fig. 8.47: Electrochemical impedance spectroscopy curves of Aluminum/NiP/NiB systems: Bode Modulus plot (a) and Bode phase plot (b).

8.7.1.3   Effect of wear on the corrosion resistance of electroless nickel-boron coatings.

As electroless coatings can be used in erosion-corrosion situation, the knowledge of the corrosion resistance of worn coatings is important. To obtain this information, the coatings were first submitted to a Taber abrasion test and then to the electrochemical tests for the evaluation of the corrosion resistance. In this section, the results obtained on the steel/NiB and Al/NiP/NiB systems will be presented and discussed.

8.7.1.3.1   Potentiodynamic polarisation.

To evaluate the influence of wear on the corrosion resistance of electroless nickel-boron coatings, potentiodynamic polarization tests were carried out on as-deposited and worn electroless nickel-boron coatings. To do this, very small electrochemical cells (1 cm^2) were carefully glued on the worn zone of the samples with silicon to avoid contact between the electrolyte and unworn zone. The experimental set-up used for the electrochemical testing of worn coatings is presented in appendix A.8.

First, the effect of wear on the corrosion properties of nickel-boron coated steel was studied. The worn areas show a lower corrosion potential than the unworn coating (see figure 8.48 and table 8.9). However, its properties are still far better than the uncoated steel. The coatings keeps thus some of its protective properties even after it has been worn by abrasion and its thickness has been greatly reduced.

Similar tests have been carried out on coated aluminum. Once more, the corrosion resistance of the abraded zones of the samples is lower than that of the unworn coating
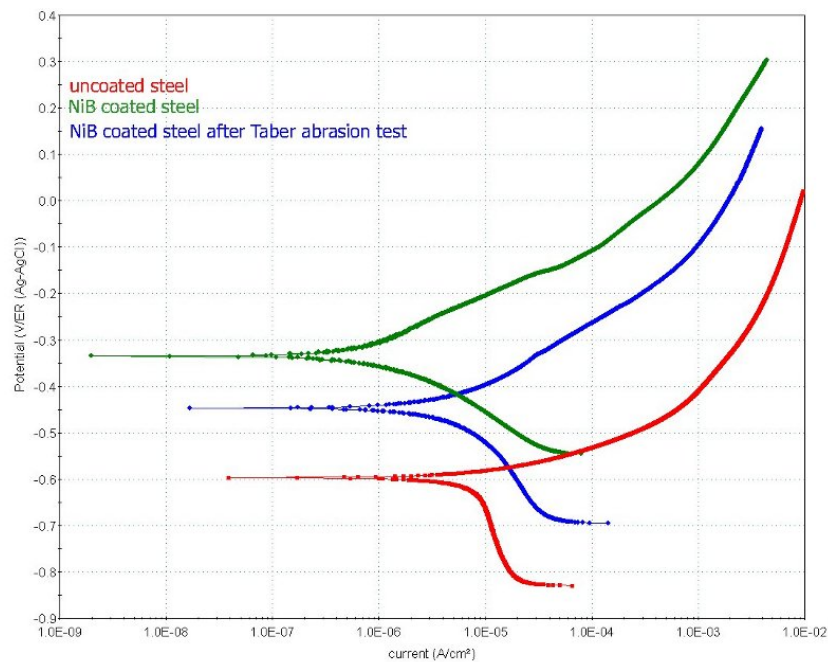
Fig. 8.48: Potentiodynamic polarization curve of NiB coated steel after abrasion.

(see figure 8.49 and table 8.9). However, this decrease is less marked than in the case of coated steel and the corrosion potential of worn Al/NiP/NiB is still higher than on unworn steel. This confirms the better properties already observed for the aluminum-based system (see section 8.7.1.2). SEM examination of the worn areas of the coating after the potentiodynamic polarization testing shows evidence of intercolumnar corrosion, which is not surprising knowing the structure and growth mechanism of the coating. However, the black spots that were observed on the unworn coating (see section 8.7.1.1.3) are present in a smaller number, as shown on figure 8.50.

Sample type	Corrosion current (μA)	Corrosion potential (mV vs. Ag/AgCl)
Uncoated steel	2.34	-595.25
NiB coated steel	0.09	-335.05
NiB coated steel after abrasion	0.69	-447.34
Al/NiP/NiB	0.217	-245.14
Al/NiP/NiB after abrasion	0.69	-284.1

Tab. 8.9: Corrosion current and potential of electroless nickel-boron on steel after abrasion.
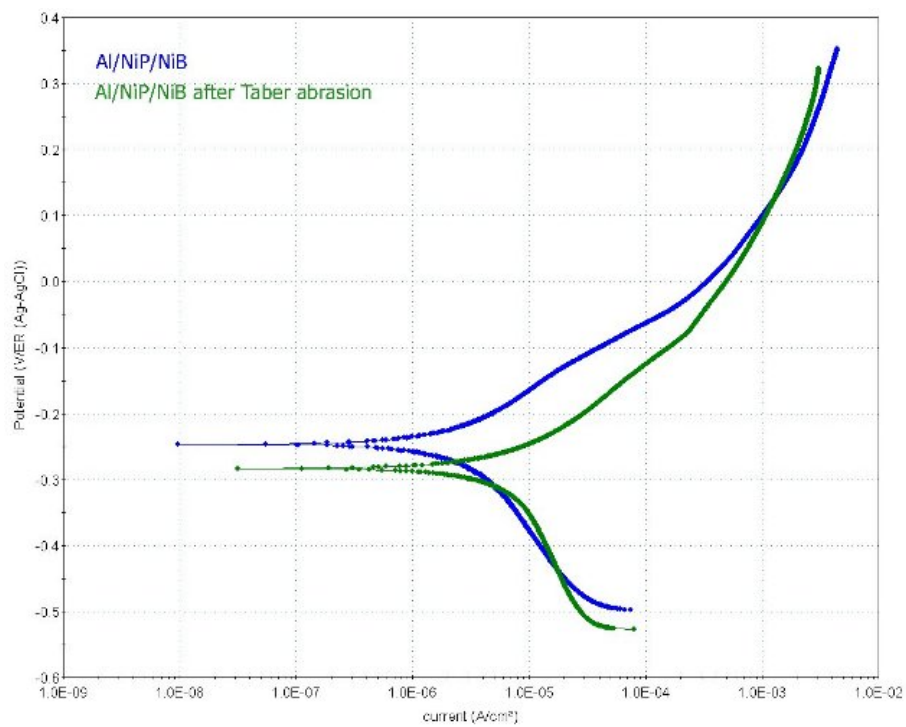
Fig. 8.49: Potentiodynamic polarization curve of NiP/NiB coated aluminum after abrasion.
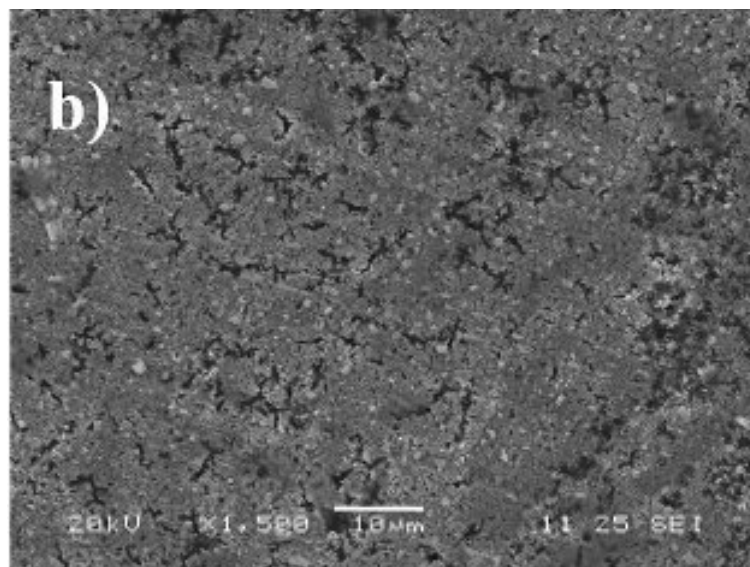
Fig. 8.50: Electroless coating on aluminum after Taber abrasion test and subsequent potentio-dynamic polarization.

8.7.1.3.2 Electrochemical impedance spectroscopy.

To complete the evaluation of the corrosion properties of the coatings by potentiodynamic polarization, electrochemical impedance spectroscopy was used once more, first on steel/NiB then on Al/NiP/NiB. On steel, the EIS results show a degradation of the corrosion resistance after the Taber abrasion test (figures 8.51 and 8.52, just as was observed by polarization: the modulus lowers at low frequencies and a second time constant appears. When the abraded zone is exposed to NaCl, the degradation continues. Observation of the Nyquist diagram (8.52 shows a constant decrease of the capacitive loop and thus a degradation of the coatings protective properties. This was confirmed by measuring the modulus at low frequency of the coating (table 8.10) which decreases from 17000 to 10000 $\Omega.cm^2$.
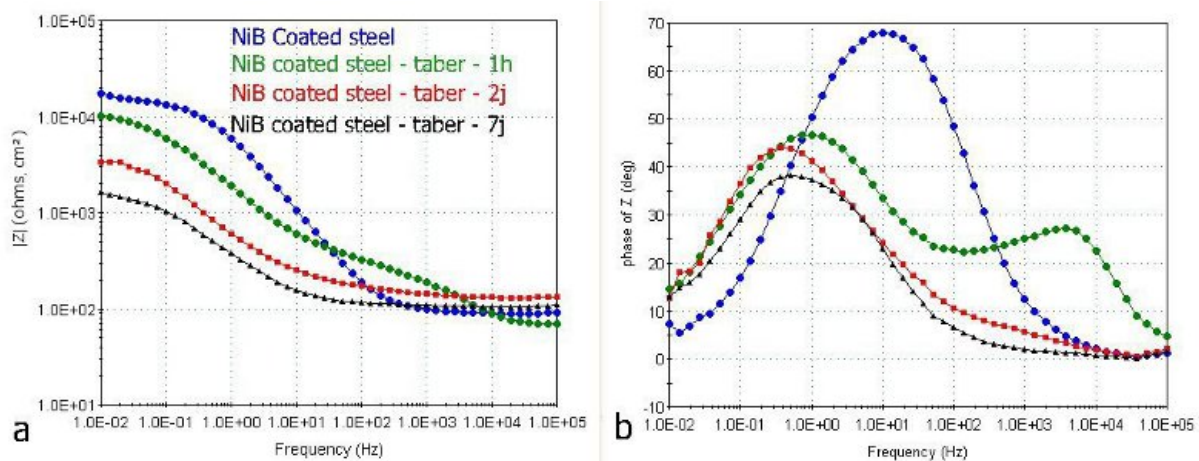
Fig. 8.51: Electrochemical impedance spectroscopy curves of NiB coated steel after Taber abrasion test: Bode Modulus plot (a) and Bode phase plot (b).
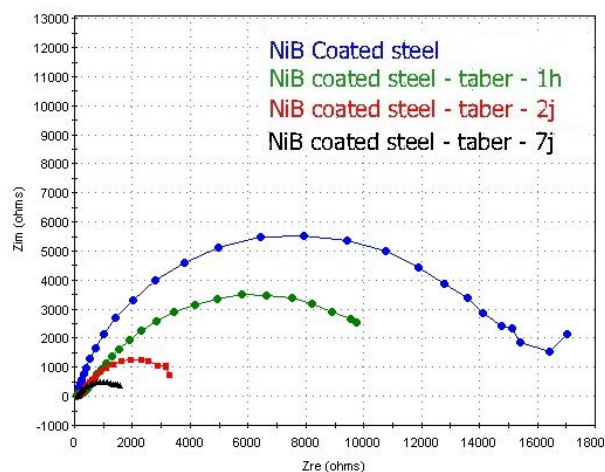
Fig. 8.52: Electrochemical impedance spectroscopy curves of NiB coated steel after Taber abrasion test: Nyquist plot.

As can be seen on the EIS results (figures 8.53 and 8.54), the abrasion affects the Al/NiP/NiB system by decreasing the corrosion resistance, just like on steel/NiB but the modifications appears to be slightly different as it implies only one time constant. The solution resistance and modulus at low frequency were measured for the coating before and after abrasion (table 8.10)and they confirm the decrease of corrosion resistance after abrasion. The abraded coating on aluminum has a charge transfer resistance similar to what is obtained on abraded steel. That shows that the corrosion resistance of Al/NiP/NiB is much more affected by abrasion than steel/NiB, because the first has a better R_{ct} before abrasion. Aging of the abraded area in NaCl (0.1 M) induces a further reduction of the corrosion resistance (figures 8.53 and 8.54), just like for the steel/NiB system.

Coating	Rs ($\Omega.cm^2$)	Low frequency modulus (0.01Hz)($\Omega.cm^2$)
Steel/Ni-B as-deposited	91	17160
Steel/Ni-B abraded	70	10135
Al/NiP/Ni-B as-deposited	112	30138
Al/NiP/Ni-B abraded	126	10740

Tab. 8.10: Corrosion current and potential of electroless nickel-boron on steel after abrasion.
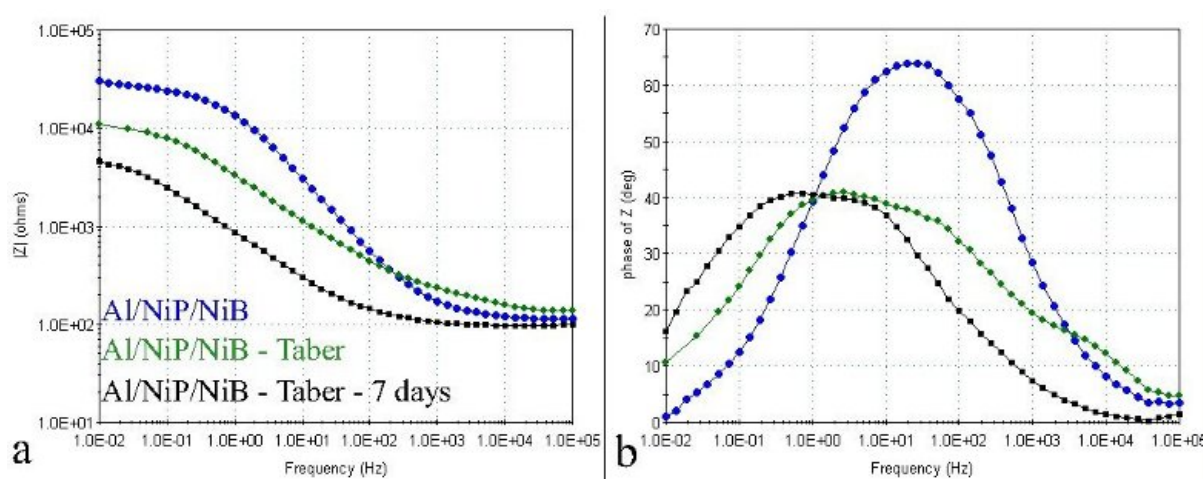
Fig. 8.53: Electrochemical impedance spectroscopy curves of NiB coated aluminum after Taber abrasion test: Bode Modulus plot (a) and Bode phase plot (b).
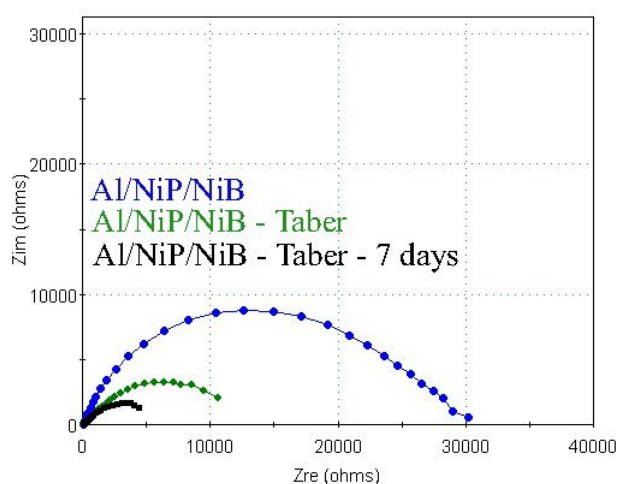
Fig. 8.54: Electrochemical impedance spectroscopy curves of NiB coated aluminum after Taber abrasion test: Nyquist plot.

8.7.2   Conclusions.

In the present section, different investigation methods were used to study the corrosion resistance of electroless nickel-boron coatings deposited either on steel or on aluminum (with an NiP underlayer). Electrochemical techniques showed that NiB, in its as-deposited state, improves the corrosion resistance of steel and that the properties obtained with an aluminum substrate and NiP underlayer were even better. Comparison with electroless nickel-phosphorous coatings showed that the NiB coatings have an as good, if not better, corrosion resistance.

Aging of the coating in NaCl (0.1M) solution for more than 5 hours induced a decrease of the corrosion resistance of both the coated steel and aluminum. Abrasion of the coating had a similar effect. However, the protective properties were not completely lost after abrasion and/or aging.

8.8   Conclusions.

The object of this chapter was the characterization of electroless nickel-boron coatings in their as-deposited state. To obtain this, several properties were investigated by various techniques. First, the chemical characterization of the deposits allowed to obtain their average composition (93 wt.% Ni, 6 wt.% B and nearly 1 wt.% Pb) and showed that the boron was homogeneously reparted across the deposit.

The morphological study allowed of course to observed the expected cauliflower-like surface texture and columnar morphology but it also showed the effect of bath replenishment that induces a secondary germination of the deposit.

The structural study, carried out by X-ray Diffraction and Transmission Electron Microscope (assisted by Focussed Ion Beam), allowed to prove the nanocrystalline character of the coating and to measure the size of the nanocrystallites, wich was found to be 1nm on average. This constitutes a breakthrough for electroless nickel-boron characterization because TEM structural studies of electroless coatings are usually performed on peeled-off coatings and do not take into account the very important anisotropy caused by the formation mechanism of the coatings, but also because most authors consider them as amorphous (which obviously is not correct for the coatings studied in this work).

Observation of the mechanical properties of the coating confirmed that they possess a very high hardness but it also brought new information. First, the hardness was found to be homogeneous across the coating. Then, the low roughness of the coating (and the lowering observed on aluminum substrate when compared to steel) suggested a good comportment in wear application. This was confirmed by the scratch test resistance (which was very good, even on thin coatings) and by the low Taber Wear Index obtained with very harsh abrasive wheels. In other words, all the mechanical properties of the coating point towards a good comportment in mechanical applications including wear resistance.

Finally, the corrosion properties of the coatings was better than expected, with a resistance similar to, if not better than, the best electroless nickel-phosphorous coatings. The effect of aging and wear was, expectedly, a lowering of the corrosion resistance but it was never completely lost, which is encouraging.

9. CHARACTERIZATION OF NICKEL-BORON DEPOSITS AFTER HEAT TREATMENT.

9.1 introduction.

While electroless nickel-boron deposits already present very good mechanical properties in their as-deposited state, those can be enhanced interestingly by a well chosen heat treatment. In the present chapter, the modifications brought by those treatments on all the properties that were studied in chapter 8 will be discussed.

After a section describing the heat treatments applied to the deposits and the reason for their choice, the chemistry of the coatings will first be briefly examined, then a longer section will be dedicated to the structural and morphological changes induced by heat treating of electroless nickel-boron. After that, the mechanical and tribological properties of the treated coatings will be examined and the last section of this chapter will focus on their corrosion resistance.

9.2 Samples preparation and heat treatments.

The samples used for this study were synthesized following the same procedures and requirement as for the study of the as-deposited coatings, which can be found in section 8.2.

Those samples were then submitted to different heat treatments, according to their substrate: the samples deposited on iron were treated during one hour at 400℃ under an argon-based atmosphere (95% Ar - 5% H_2), at ambient pressure. This treatment is chosen to induce a complete 'crystallization' of the coating, that is an optimum coarsening of the grains leading to the best mechanical properties. The samples deposited on aluminum alloys however, could not be treated at this elevated temperature because it would be detrimental to the mechanical resistance of the substrate. They were submitted to a treatment developed by Dr Delaunois [7]: four hours at 180℃ under an argon-based atmosphere (95% Ar - 5% H_2), at ambient pressure.

9.3   Global and local composition of the deposits after heat treatment.

The global composition of the coatings is of course not modified by the heat treatments as they are carried out in a non-reactive atmosphere, containing enough hydrogen to avoid superficial oxidation of the samples. This composition is thus similar to what was measured on as-deposited coatings: on average, 6 wt.% Boron, approximatively 1 wt.% lead, the balance being nickel (93 wt.%).

The profile repartition of elements in the coating was studied by GDOES on heat treated coatings. Figure 9.1 presents a profile measured on a sample deposited on aluminum and submitted to an heat treatment at 180℃. Apart for the higher thickness (this sample was synthesized using bath replenishment during the deposition), the profile is similar to the one presented in section 8.3, on figure 8.3. This means that the repartition of elements in the coating is not modified by this heat treatment. Moreover, there is no evidence of diffusion at the substrate/coating interface (the residual nickel measured in the substrate is an artifact of the measuring technique: a similar experiment carried out by EDX to confirm that result showed that, in fact, no nickel was present in the aluminum substrate and a similar phenomenon had already been observed on as-deposited samples).
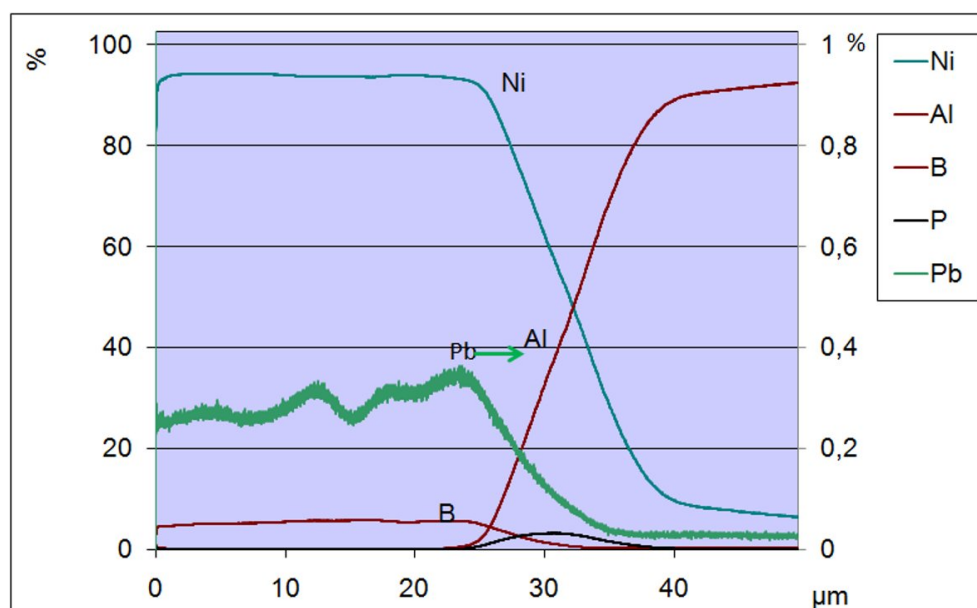
Fig. 9.1: GDOES profile of nickel-boron coated aluminum after heat treatment at 180℃ during 4 hours.

In the same way, the profiles measured on electroless deposits on steel substrates, after an heat treatment at 400℃, were also similar to their as-deposited counterparts, without (see figure 9.2) and with (see figure 9.3) bath replenishment during the deposition process.
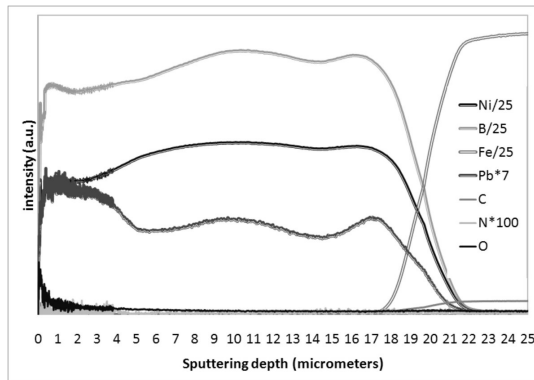
Fig. 9.2: GDOES profile of NiB coated steel after heat treatment at 400℃ during 1 hour.
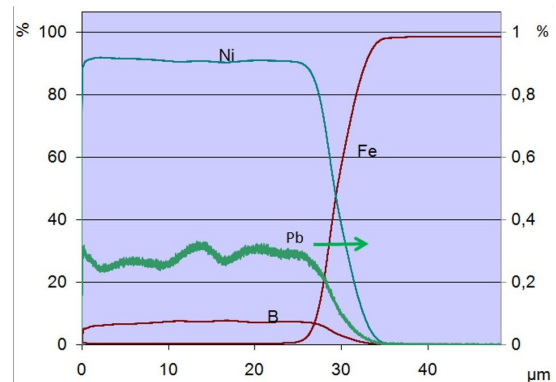
Fig. 9.3: GDOES profile of a thicker NiB deposit on steel after heat treatment at 400℃ during 1 hour.

9.4 Structure of heat treated electroless nickel-boron.

While the aspect and morphology of the coating were discussed for as-deposited samples, it is not useful to include a specific section about those properties in the present one as the heat treatments do not modify them in any sensible way: the typical columnar morphology is well kept after heat treatment, as is the cauliflower-like surface texture and the semi-bright aspect of the deposit. However, contrary to the chemistry, morphology and aspect of the coating, its structure is very much influenced by heat treatments, as their objective is to obtain an optimally crystallized state. This property will thus be discussed at length in the present section.

First, the structural modifications, as observed by X-ray diffraction will be discussed. In that section, both results obtained a posteriori on heat treated coatings as well as data obtained from in situ high temperature X-ray diffraction will be used to assess the crystalline state of the coating. Then, a section will be dedicated to TEM images and electron diffraction patterns obtained on heat treated samples to confirm the conclusions of the XRD analysis. Finally, Differential Scanning Calorimetry will be used to observe if some phase transition that are not observed by the other methods happens and to determine the onset temperature of the various transformations in continuous heating.

9.4.1 Effects of heat treatment on the structure of electroless nickel-boron (measured by X-ray diffraction).

To observe the structure of heat treated deposits, X-ray diffraction patterns were obtained from 3 samples, on aluminum substrates: an untreated sample, a sample treated at 180℃ for 4 hours and a sample treated at 400℃ for 1 hour, as shown on figure 9.4.

The choice of an aluminum substrate for this test was made to avoid interferences between the reflexions of the substrate and of the coating (some iron peaks are very close to the main nickel and Ni_3B peaks). As the electroless deposits are not very thick, the

measures were carried out using by Grazing Incidence X-ray Diffraction, using a copper source ($\lambda_{k_\alpha} = 1.54\dot{A}$).
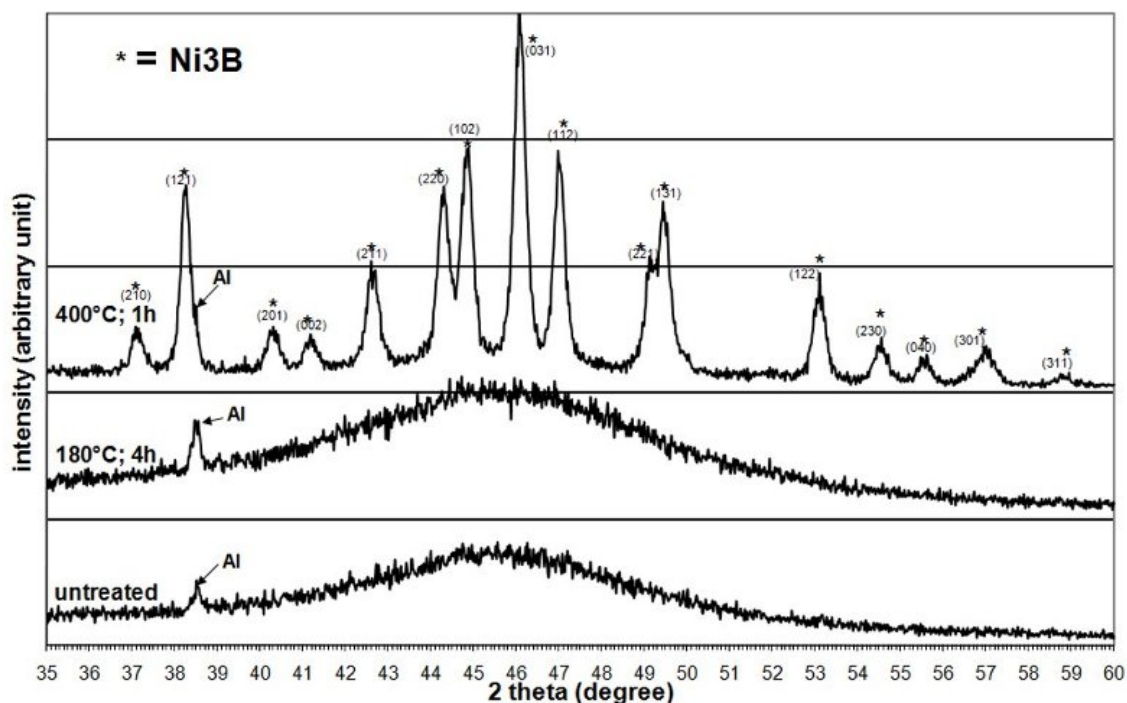
Fig. 9.4: X-ray diffraction patterns of electroless nickel-boron deposits after heat treatment.

After heat treatment up to 180℃, the X-ray diffraction pattern is only slightly modified and stays very similar to the untreated coating: the main peak is still very broad and keeps a low maximum intensity. This means that the structure is kept unmodified, except maybe for a slight grain size growth. However, after heat treatment at 400℃, the diffraction pattern is very different: the very broad peak centered around the main Ni (face centered cubic, fcc) reflexion disappears and is replaced by numerous peaks, all of whom can be easily indexed as they correspond to various Ni_3B reflexions. There are no other phases detected by this technique. Those peaks are very sharp and narrow, which indicates that the grain size is not in the nanometric range any more.

In other words, before heat treatment and after heat treatment at 180℃, the electroless nickel-boron deposits are constituted of a nanocrystalline phase that has the fcc structure of nickel while, after an heat treatment at 400℃, it is constituted of (relatively) coarse grained nickel boride (Ni_3B) phase. It is not surprising that only this phase is detected as the average composition of the deposits (around 6 wt.% B, see section 8.3) is very close to the nominal composition of the Ni_3B phase (see figure 2.6, page 28). However, as this boride is a line compound, it would not have been surprising to observe other phases, such as Ni and Ni_2B.

To complete the information obtained from heat treated coatings, high temperature in situ X-ray diffraction was carried out. In this case, as we chose to investigate an higher

range of temperature (up to 600℃), the experiment was carried out with a steel substrate, even if it brings a risk of substrate interferences. Those tests were carried out in a $\Theta - \Theta$ Bruker D8Advance diffractometer (see figure 9.5) equipped with a copper source $(\lambda_{k_\alpha} = 1.54\mathring{A})$. This spectrometer is fitted with an heating system (by radiations) and with a pumping system that allows testing under vacuum and/or controlled atmosphere. The sample placed on a ceramic sample holder (in alumina, that was used to avoid creep deformation of the metallic sample during heating) that is put on two cooled pegs. The radiative heating system comes around the sample during the experiment. To limit the effects of sample expansion (due to heating) on the x-ray diffraction results, Göbel mirrors are used to obtain parallel incoming beams.
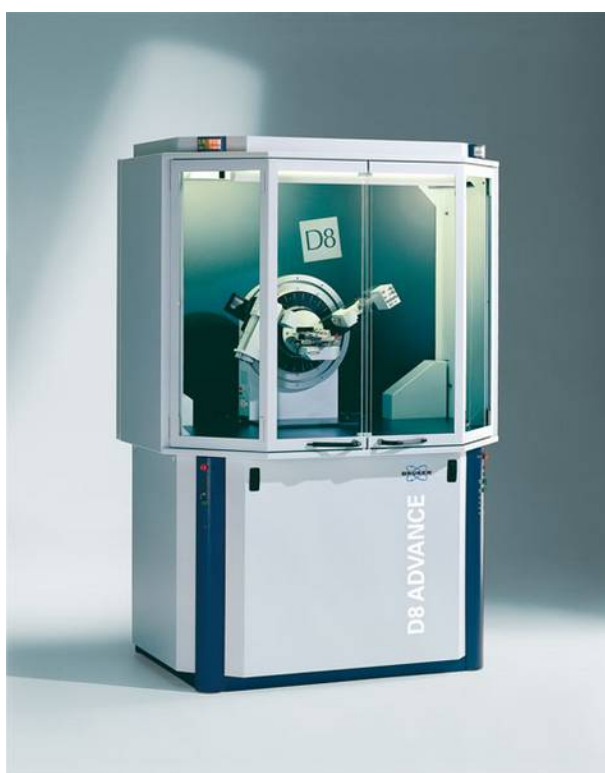
Fig. 9.5: High temperature x-ray diffractometer [151].

During this experiment, a single sample was heated progressively and the X-ray pattern was recorder for several preset temperatures. To keep each measuring step short and thus avoid grain growth, the angle range was kept as narrow as possible (from 40 to 50°), it was however chosen so that there is a good number of peaks for the expected phases (Ni, Ni_3B, Ni_2B) in the interval. The sample was maintained for 10 minutes at each temperature to attain thermal equilibrium before recording the diffractogramm.

The high temperature x-ray diffraction patterns are shown on figure 9.6. The small peak observable at all temperatures close to 43.7° corresponds to the corundum phase (Al_2O_3) of the sample supporting device that is slightly bigger than the sample. At low temperatures (up to 250℃), the diffraction pattern is left nearly unchanged and no new

phase appears (see figure 9.6). Ni$_3$B peaks are discernible from 300℃ and the pattern is then unmodified up to 450℃. At higher temperatures, the peaks become sharper and some of them are deformed, which suggests that another phase (probably Ni$_2$B) may appear in small quantities. The temperature increase is also accompanied by a slight shift of the peaks towards smaller angles that is a direct consequence of the sample expansion (an thus of the increase of the cell parameter).
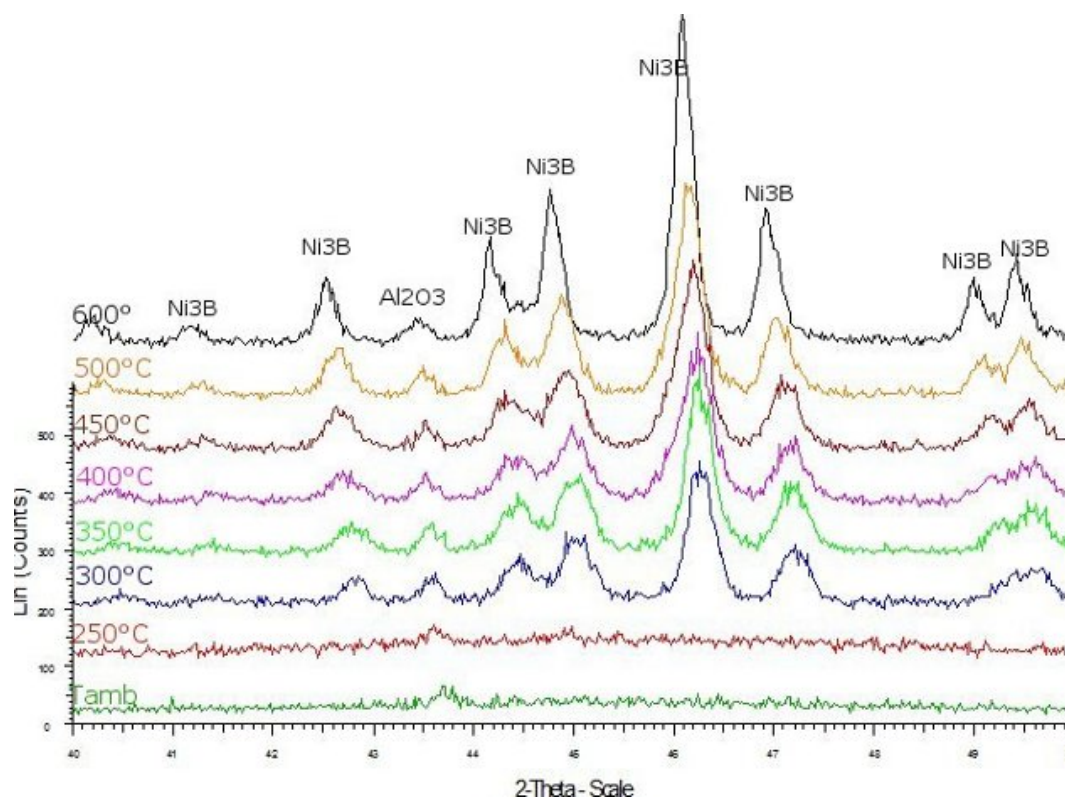
Fig. 9.6: In situ high temperature x-ray diffraction patterns of electroless nickel-boron on steel.

9.4.2   Structural analysis of heat treated electroless nickel-boron deposits by transmission electron microscopy.

TEM observation of coatings heat treated at 400℃ show the very important structural modification induced by the treatment. Where only very small crystallite could be faintly seen, bigger, well defined, crystallites can now be observed (figures 9.7, 9.8 and 9.9), their size reaching 50 nm. The heat treated coating keeps thus a nanocrystalline structure.

The layered organization observed on as-deposited coatings can still be observed after the heat treatment (figures 9.8, 9.9 and 9.10) but its manifestation is somewhat different: the crystallites forming the successive layer are better defined and the layer themselves appear broader than before the heat treatment. This supports the hypothesis that this layering effect is caused by chemical heterogeneity, the broadening effect being linked with
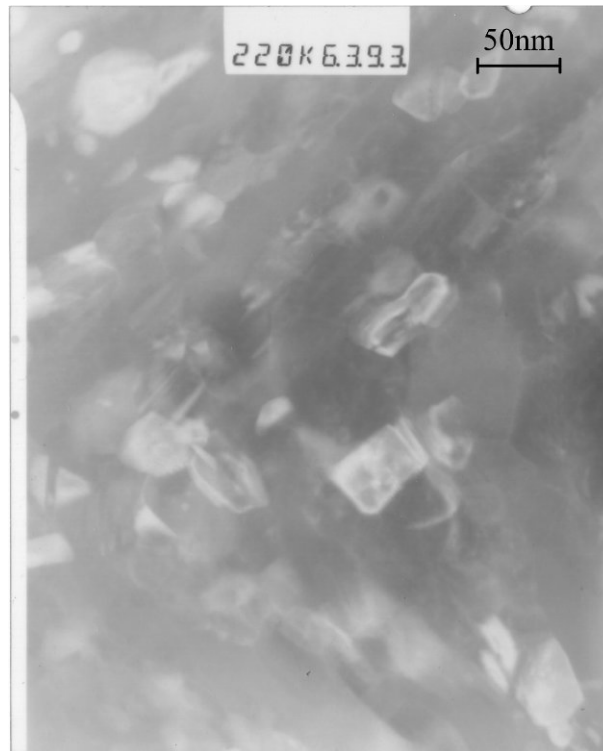
Fig. 9.7: TEM image of an electroless nickel-boron deposit treated at 400℃.
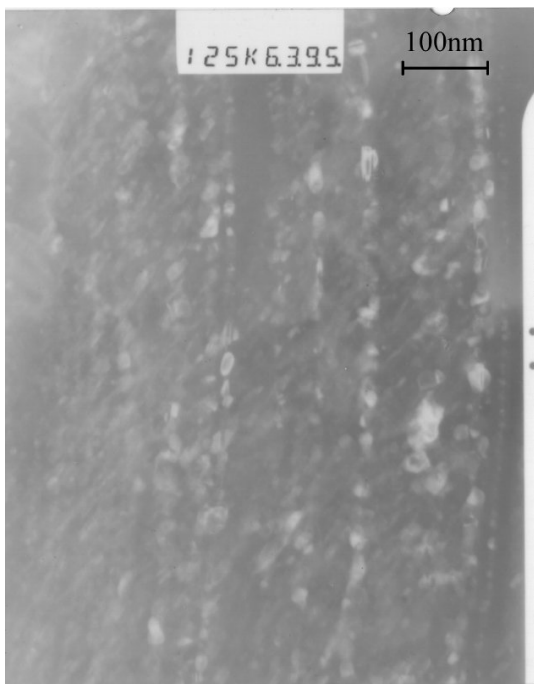
Fig. 9.8: TEM image of an electroless nickel-boron deposit treated at 400℃.
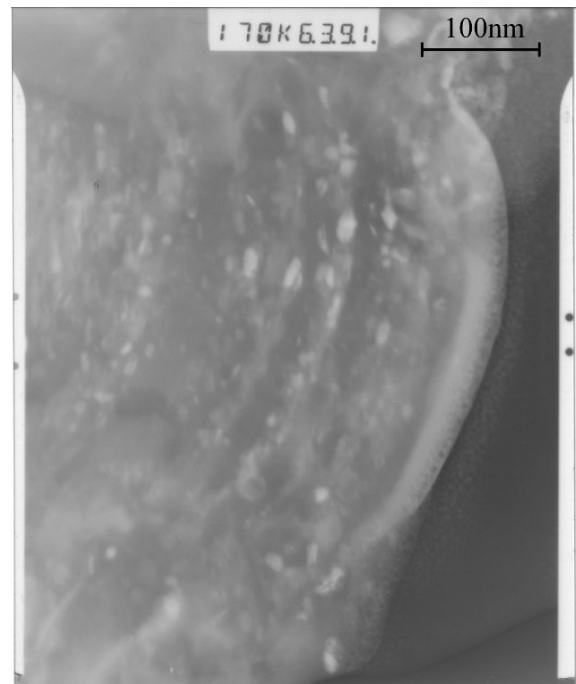
Fig. 9.9: TEM image of an electroless nickel-boron deposit treated at 400℃.
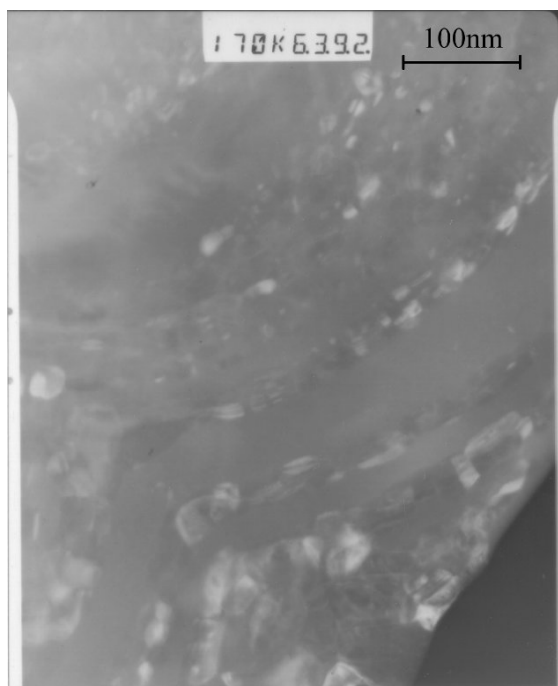
Fig. 9.10: TEM image of an electroless nickel-boron deposit treated at 400℃.
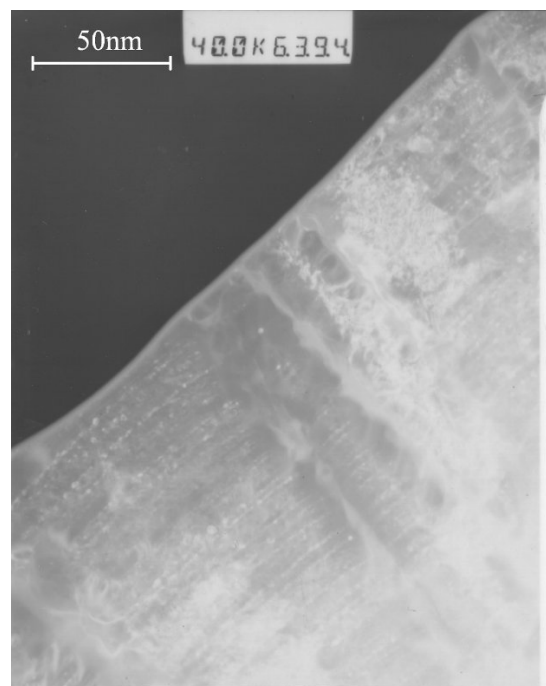
Fig. 9.11: TEM image of an electroless nickel-boron deposit treated at 400℃.

diffusion during the heat treatment.

The columnar morphology of the coatings is still perceptible by TEM observation after heat treatment: while it is difficult to observe a whole column at high magnification, it was possible at 40 000 times (figure 9.11). On this figure, several columns can be seen and it appears that the junction between those is less crystallized than the other areas of the coating. A similar junction can be observed on the bottom left part of figure 9.10 but no amorphous zone can be easily detected at this junction. It is thus possible than the lighter zones of figure 9.11 are due to differences in the foil thickness or density.

Electron diffraction patterns of the heat treated coating (figures 9.12 and 9.13) show that the coating is much more crystallized than in the as-deposited state, the dotted pattern typical of a polycrystalline state with few grains encompassed in the diffracting area. From the X-ray diffraction data (9.4), the structure of the deposit must be Ni_3B, however, the complex structure of this phase (orthorhombic (Fe_3C type, Pnma) with 12 nickel and four boron atoms per unit cell [115]) implies that a great number of plans are diffracting, which makes the indexation of the diffraction patterns very difficult and it was not possible to confirm this from the electron diffraction patterns.
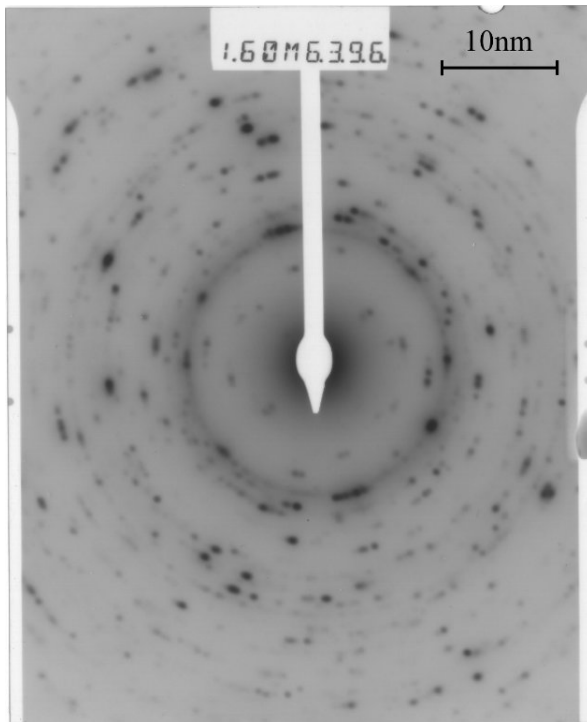
Fig. 9.12: TEM image of an electroless nickel-boron deposit treated at 400℃.
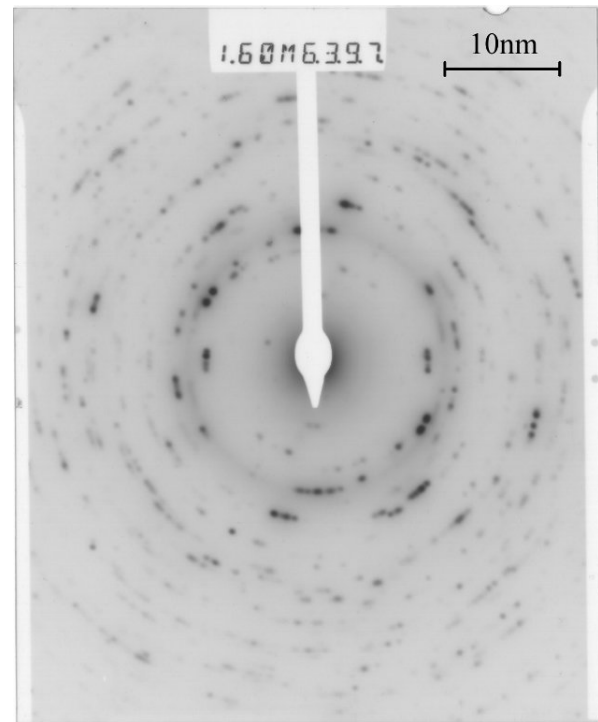
Fig. 9.13: TEM image of an electroless nickel-boron deposit treated at 400℃.

9.5 Mechanical properties of heat treated coatings.

As heat treatment induces a very important modification of the structural state of electroless nickel-boron deposits, it is expected that this will be accompanied by an important modification of the mechanical properties: the hardness of the coating increases during the heat treatment and reaches its optimum after one hour at 400℃(see section 3.3).

As the influence of heat treatments on the mechanical properties of electroless nickel-boron coatings was extensively studied by Dr Delaunois [7], we will not discuss the optimization of heat treatment time and temperature. However, the hardness obtained after our chosen heat treatments (4 hours at 180℃ and 1 hour at 400℃) will be studied by the same methods as the hardness of as-deposited coatings: Vickers and Knoop microindentations, on surface and cross sections respectively, and Berkovitch nanoindentation. More information about those testing methods can be found in section 8.5.

As shown in table 9.1, heat treating at 180℃ does lead to a sensible but not important increase of the deposit hardness, that is always in the range of a hundred hardness points. This slight increase has already been observed by Dr Delaunois [7, 32] and must be a consequence of the slight grain growth cause by the heat treatment. Heat treatment at 400℃, on the other hand, brings a more important increase of the hardness that reaches 1300 hv_{100} when measured on the surface. It was not possible to measure the Knoop hardness under a load of 50 grams after heat treatment at 400℃ because the coating

is then slightly less ductile than without heat treatment and cracking occurs during the indentation process, as can be seen on figure 9.14.

Measurement technique	as-deposited	180℃; 4h	400℃; 1h
Knoop (cross section; 25g)	891 ± 35 hk$_{25}$	981 ± 45 hk$_{25}$	1229 ± 160 hk$_{25}$
Knoop (cross section; 50g)	834 ± 20 hk$_{50}$	927 ± 30 hk$_{50}$	
Vickers (surface; 100g)	854 ± 40 hv$_{100}$	1014 ± 40 hv$_{100}$	1302 ± 40 hv$_{100}$
Berkovitch nanoindentation (cross section; $4000 \mu N$)	925 ± 70	1140 ± 75	1408 ± 120

Tab. 9.1: Hardness of heat treated electroless nickel-boron deposits.
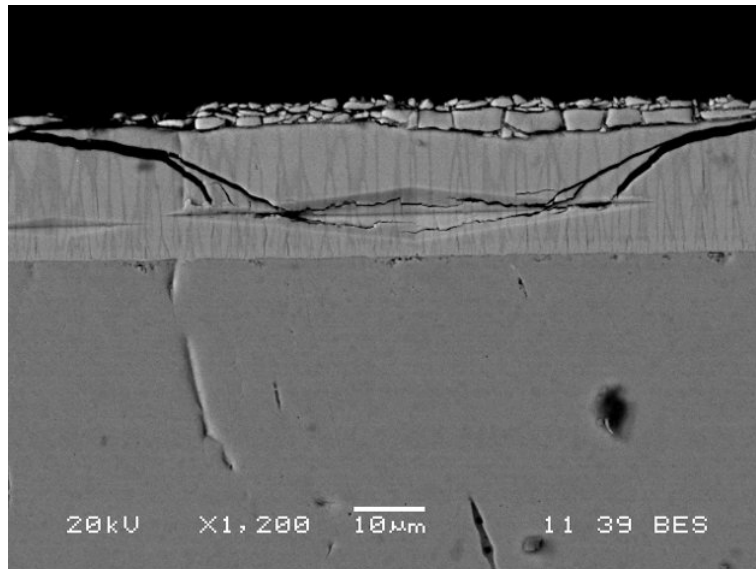
Fig. 9.14: SEM image of cracking induced by Knoop hardness testing of electroless nickel-boron.

According to most sources [2, 22, 31, 33, 39, 42, 114], the increase of the hardness of the deposit is due to the creation of grain boundaries in the originally amorphous material and can thus be linked to the Hall-Petch effect. However, as we have shown that the structural modification occurring in electroless nickel-boron coatings during heat treatment is not crystallization of an amorphous phase but transformation of a nanocrystalline nickel structure into a coarser grained nickel-boride phase, this explanation cannot be applied any more.

Effectively, the Hall-Petch effect must play an important role in explaining the high hardness of heat treated nickel-boron coatings, as is proven by the decrease of the mechanical properties when high temperature or longer times are used, and thus when grain coalescence occurs. But while this effect can explain the later decrease of the hardness, it is not sufficient to explain completely the increase observed when the optimal treatment is applied. It is probable that a non negligible part of the hardness increase is due to the

phase transformation between the face centered cubic nickel structure, which is rather soft and the orthorhombic nickel boride phase, which is similar to cementite (Fe_3C): in the same way that cementite is harder than ferrite and austenite, the nickel boride phase must be intrinsically harder than the metallic nickel phase.
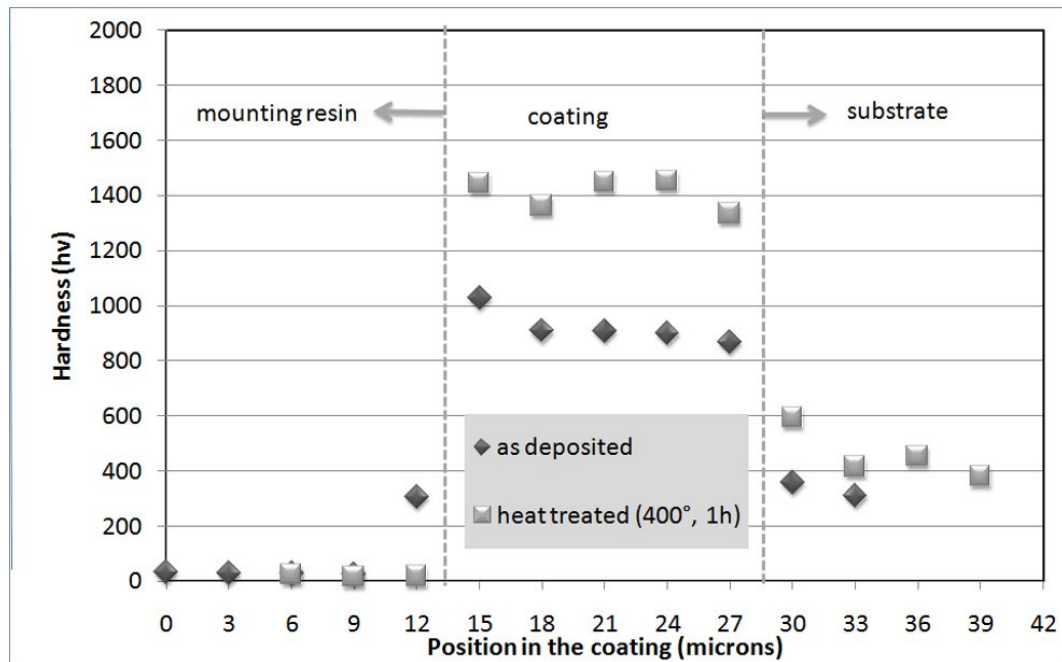
Fig. 9.15: Hardness profile of as-deposited electroless nickel-boron on steel after heat treatment (by nanoindentation).

To assess if the heat treatment modifies the repartition of the hardness across the coating, nanoindentation profiles were performed on samples that were treated at 400℃ (figure 9.15). As before, the hardness stays stable and homogeneous in the whole deposit. This is not surprising as the chemical repartition is not modified and the temperature homogeneity is easily obtained on coatings as thin as 15 to 30 μm.

9.6 Tribological properties of the heat treated coatings.

As the hardness of the coating is improved by heat treatment, so must be the tribological properties. However, while the increase of abrasive wear resistance can easily be deducted from the hardening, the same cannot be done for the roughness and scratch resistance of the coating. In the present section, those three parameters will be examined successively to assess if the heat treatment really improves them, beginning with the roughness and then going on with the abrasion and scratch resistance.

9.6.1   Roughness of heat treated electroless nickel-boron coatings.

In section 8.6.1, the roughness of electroless nickel-boron coatings was completely described and was found to be low on smooth substrates and good for wear applications. The object of the present section is not to repeat this analysis for heat treated coatings but to identify the influence of heat treatment on the various roughness parameters. For this, samples of two different thicknesses (15 and 6 μm) were submitted to heat treatments at 180 and 400℃. The roughness of those samples was then measured and the evolution of several parameters was followed.

As can be seen in table 9.2, the use of an heat treatment decreases all of the followed parameters and the decrease is more important after a treatment at an higher temperature. Heat treatments will thus surely improve the wear resistance of the coatings.

	15 μm			6 μm		
	untreated	180℃; 4h	400℃; 1h	untreated	180℃; 4h	400℃; 1h
Ra	0.125±0.017	0.127±0.006	0.101±0.014	0.159±0.028	0.105±0.019	0.098±0.011
Rq	0.170±0.03	0.167±0.012	0.135±0.022	0.215±0.044	0.143±0.03	0.131±0.023
Rz	1.193±0.251	1.069±0.19	0.941±0.219	1.48±0.412	1.086±0.367	0.855±0.230
Rp	0.712±0.234	0.619±0.177	0.537±0.194	0.76±0.234	0.704±0.333	0.528±0.207
Rv	0.481±0.071	0.499±0.053	0.405±0.069	0.719±0.268	0.382±0.131	0.326±0.059
Rt	1.693±0.403	1.425±0.133	1.391±0.301	2.291±0.935	1.869±0.499	1.328±0.669

Tab. 9.2: Roughness parameters of as-deposited and heat treated NiB deposits.

9.6.2   Wear resistance of the heat treated coatings.

To confirm if the decrease of the coatings roughness in accompanied by a real improvement of the wear resistance, Taber Abrasion Tests were carried out on treated coatings using the test conditions described in section 8.6.3. Samples deposited on aluminum and steel were tested separately as they were submitted to different heat treatment: the first were treated at 180℃ and the last at 400℃.

Treatment	TWI
As deposited	28.5 ± 3.5
180℃; 4h	24±2.2
400℃; 1h	13±1.5

Tab. 9.3: Taber Wear Index of as-deposited and heat treated electroless nickel-boron deposits.

Heat treating nickel-boron coated aluminum at 180℃ modifies the abrasive wear resistance (see figure 9.16 and table 9.3): the TWI decreases from 28.5 to 24. This slight modification is in good agreement with the small hardness increase observed in section 9.5 for this treatment.
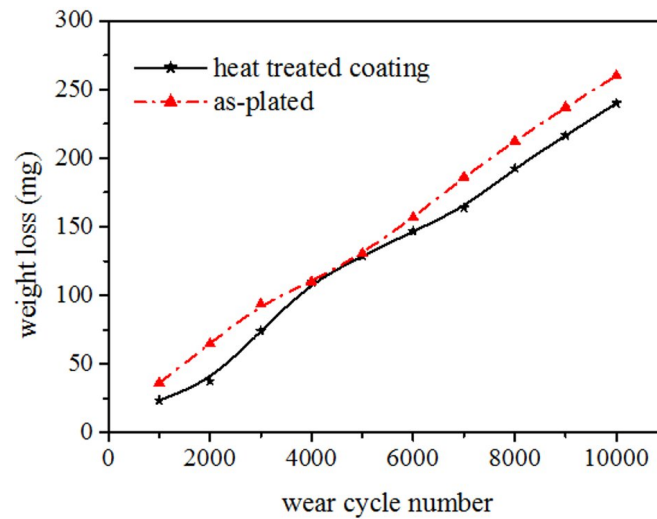
Fig. 9.16: Evolution of weight loss during Taber Wear test on electroless nickel-boron coating on aluminium with and without heat treatment.
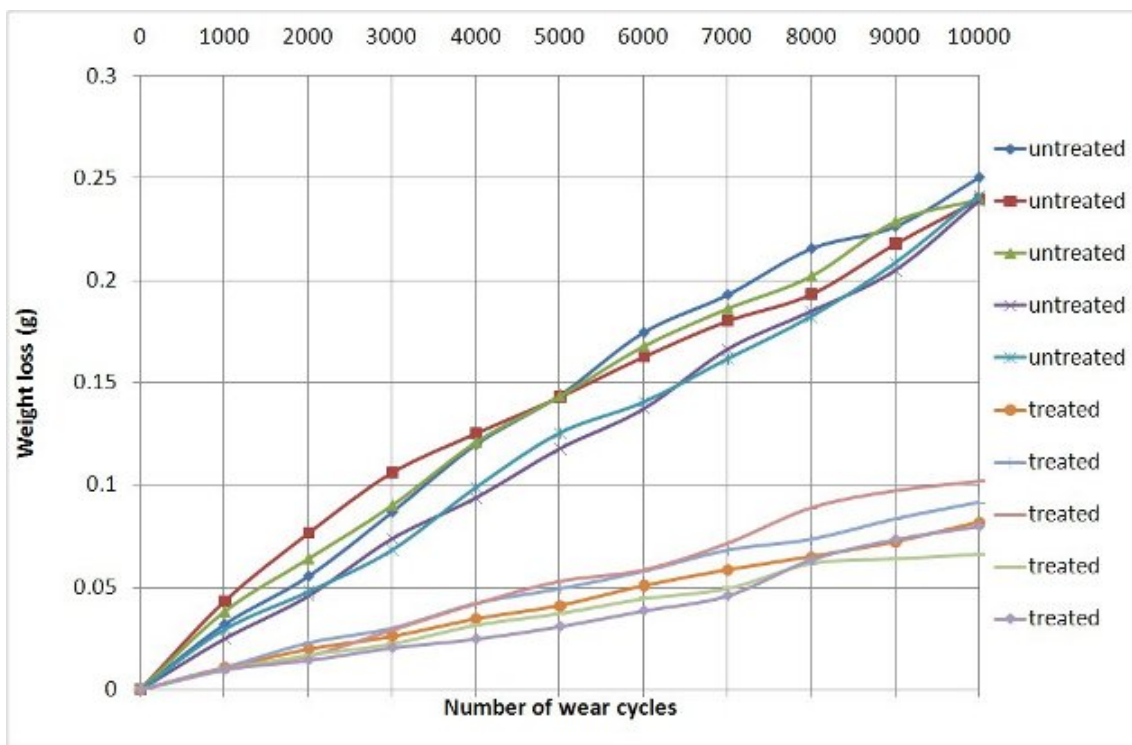
Fig. 9.17: Evolution of weight loss during Taber Wear test on electroless nickel-boron coating on steel with and without heat treatment.

On the other hand, heat treatments carried out on coated steel induced an important decrease of the TWI, which is halved (see figure 9.17 and table 9.3). Once again, this evolution matches the evolution of hardness and can be explained likewise by the crystallization of the nickel-boride phase. Moreover the decrease of the TWI also agrees with the evolution of the coating's roughness. From this, it can be easily deducted that heat treating the nickel-boron deposits will improve their wear resistance.

Like on untreated coatings, the study of wear resistance of the heat treated coatings was not limited to the determination of the TWI. On steel coated samples, for which the difference with untreated coatings is more marked, SEM examination of the abraded zone was carried out, as well as determination of the depth profile.

As can be seen on figure 9.18, the amount of removed coating is far smaller on heat treated samples, as the substrate is never bared after the wear tests. The thickness of the remaining coating is quite important and would still guarantee a good protection. Likewise, superficial observation of the abraded area (figure 9.19) shows that the cauliflower-like texture is still distinguishable under the scratches that are fewer and less marked than on the untreated coating (see figure 8.26, page 153).
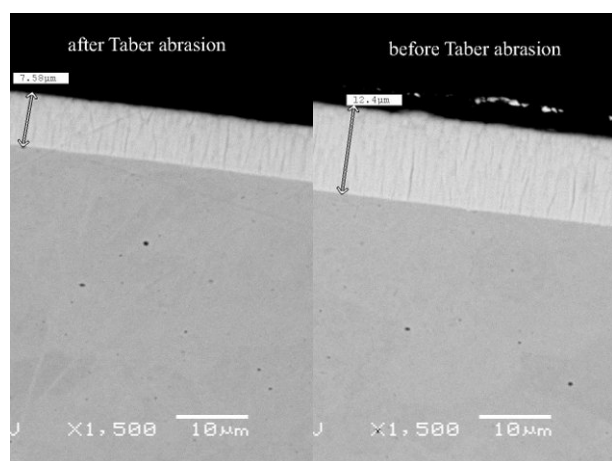
Fig. 9.18: Cross section of heat treated electroless nickel-boron coating before and after Taber abrasion test.
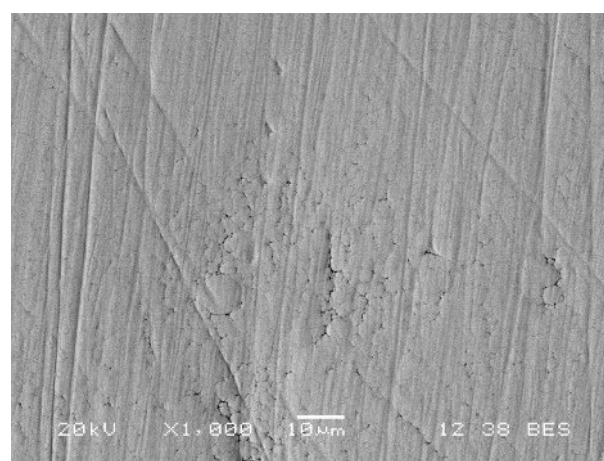
Fig. 9.19: Surface of an heat treated electroless nickel-boron deposit after Taber abrasion test.

The depth profile of the abraded zone (figure 9.20) is quite different from what was observed on untreated coatings (see figure 8.28, page 153): while the edges of the abraded area of the untreated sample present a steep profile, the depth of the racetrack increases slowly from the edge to the center after the heat treatment. This phenomenon is important in terms of wear resistance as it means that the area affected by the wear is smaller after the heat treatment.
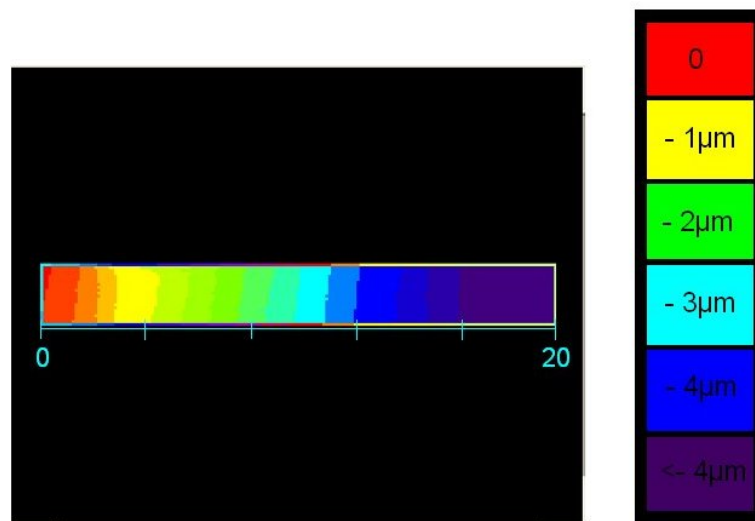
Fig. 9.20: Depth profile of the abraded zone on an heat treated electroless nickel-boron deposit.

9.6.3 Scratch resistance of the heat treated coatings.

To complete the results of the roughness and wear tests, scratch tests were performed on coatings heat treated at 180℃ and 400℃. Those tests were carried out using similar conditions that on untreated coatings (see section 8.6.4), on samples with a 15 μm coating deposited on aluminum substrate, in order to observe the global damage.

Fig. 9.21: Scratch test on a electroless nickel-boron coating after heat treatment at 180℃.

Figure 9.21 shows the residual scratch on a sample heat treated at 180℃. It was not possible to detect an adhesive critical load from this experiment, just as on the untreated coating. Only elastic and plastic deformation as well as some microcracks at the edge of the scratches that are typical of metallic comportment of the sample were observed. Once again, the system proved a very important elastic recovery as the residual scratch depth amounts only to 50% of the penetration during the test.

On samples treated at an higher temperature (400℃), the damage is similar than on the other ones, but more marked: plastic deformation, as well as cracks on the edge and bottom of the scratches can be observed (figure 9.22).
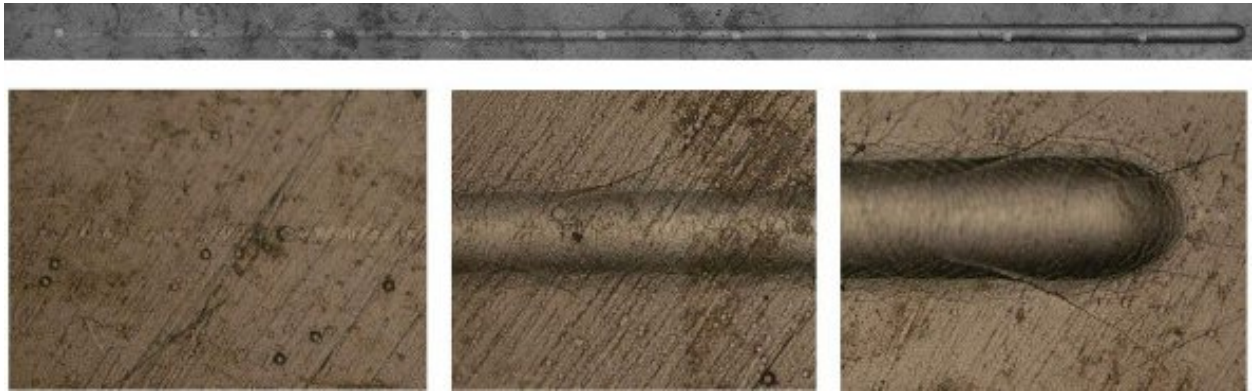
Fig. 9.22: Scratch test on a electroless nickel-boron coating after heat treatment at 400℃.

As it was not possible to determine the critical load of the samples (and thus the adherence of the coating), a similar experiment was carried out on 6 μm thick samples deposited on steel and treated at 180℃. The critical load was measured from the friction coefficient variations and from SEM observation. It was, in both cases, close to 13.5N which, while lower than on untreated coatings, is still very good (see table 9.4). The detection of the critical load by the variation of the friction coefficient was possible because there is a increase from 0.3 up to 0.45 when it is reached.

Critical load	
from friction coefficient	from SEM observation
13.3N	13.7N

Tab. 9.4: Critical load (adhesive) of electroless nickel-boron coatings after heat treatment at 180℃.

Observation of the residual scratch (figure 9.23) showed that the adhesive failure was reached by discontinuous, then continuous ductile perforation, which indicated a metallic, ductile comportment at all stages of the testing, and a very good adhesion to the substrate, and allows, combined with the good abrasion and roughness results, to predict a good comportment in wear applications. It was not possible, from this, to determine if the lowering of the critical load is caused by the heat treatment or if it is due to a slightly thinner coating, as this parameter has a strong influence on this value. To obtain more conclusive results, scratch tests with an higher final load (in similar conditions to the tests made by Dr Delaunois [7]) are required but it was not possible, for technical reason to carry them out at the present time.
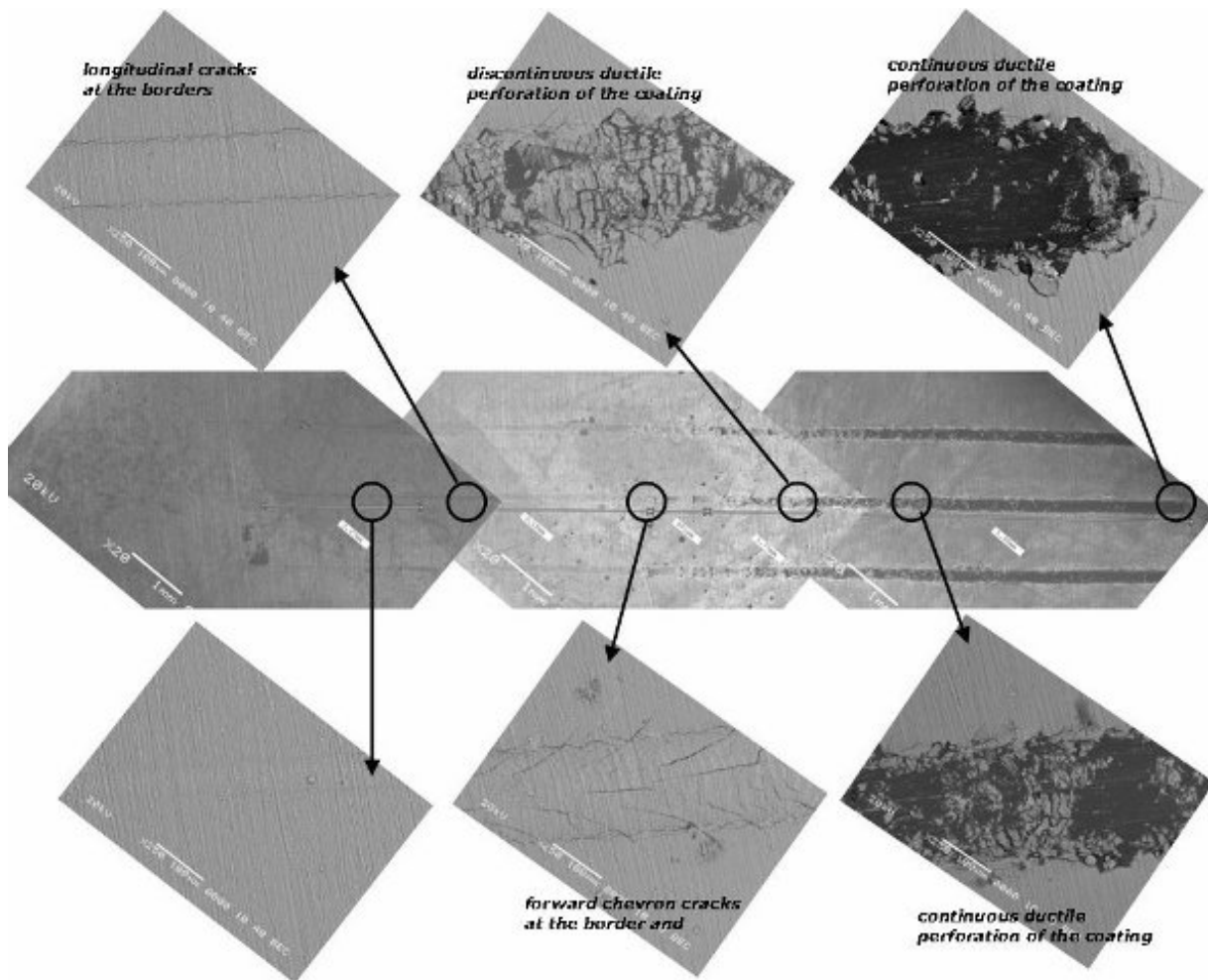
Fig. 9.23: Scratch test on a 6 μm electroless nickel-boron coating after heat treatment at 180℃.

9.6.4   Conclusions.

Heat treating electroless nickel-boron appears to be favorable to the wear resistance: the treated coatings are smoother and their Taber Wear Index is improved, even after a treatment at only 180℃. However, it is clear that treating at 400℃ is much more interesting as far as the wear resistance of the coatings is concerned. Only scratch testing did not conclude with a definite improvement after heat treatment but the results were already remarkable on as-deposited coatings and it was not possible to discern any significant modification.

9.7   Corrosion resistance of heat treated electroless nickel-boron.

While the use of heat treatment on electroless nickel-boron coatings are always reported to have a beneficial effect on their mechanical properties, the same cannot be said about their corrosion properties: as was said in section 3.4, most authors find a lowering of the corrosion resistance after heat treatment [31, 39, 98]. They usually attribute this to the creation of grain boundaries in a coating in which they were initially absent, because they consider the electroless nickel-boron coatings as amorphous. However, as we have shown (see section 8.4.2) that the coatings we study are not amorphous, this theory cannot be used in the present case.

It is thus very interesting to study the corrosion resistance of the heat treated coating, firstly to see if the comportment observed by other authors is still observed on initially nanocrystalline coatings and secondly to propose a mechanism to explain the modification of the corrosion resistance of our coatings.

In this section, the corrosion resistance of the coatings will be studied in a similar way than in the case of as-deposited coatings.

9.7.1   Investigation of the corrosion resistance of heat treated electroless nickel-boron by electrochemical tests.

The electrochemical methods that were applied to study the corrosion resistance of as-deposited samples were also used to characterize the heat treated coatings and the experimental conditions were kept identical to allow easy comparison of the test results. Those conditions are:

- For the potentiodynamic polarization : electrode potential varying from -600 to +250 mV against the reference electrode, at a rate of 10 mV.min^{-1}; immersion of the sample in the solution 15 minutes prior to the test to stabilize the open circuit potential.

- For the Electrochemical Impedance Spectroscopy (EIS): the frequency range 10^5 - 10^{-2} Hz with a sinusoidal signal perturbation of 5 mV and 50 data points taken per interval.

All of the electrochemical tests were carried out in 0.1 M NaCl, at room temperature, on a normalized surface (exposed area : 1 cm^2) obtained by silicone masking, with a conventional three-electrode cell constituted as follow:

- Working electrode : electroless nickel-boron specimen.

- Counter electrode: platinum grid.

- Reference electrode: Ag - AgCl/KCl (saturated) (offset potential against NHE: 0.197V)

9.7.1.1 Corrosion resistance of electroless nickel-boron plated steel after heat treatment.

Still following the same approach than on as-deposited coatings, we will first examine the corrosion resistance of the simplest system: electroless nickel-boron coated steel (Steel/NiB), after heat treatment (1 hour at 400℃). This will allow us to identify the influence of heat treatment on the nickel-boron deposit without interference from the NiP underlayer. Moreover heat treating at 400℃ modifies more the coatings properties than heat treating at 180 ℃, and thus it is more likely that any change in corrosion properties will be easier to observe on coatings treated at higher temperature. The potentiodynamic polarization will be discussed first, then the EIS data.

9.7.1.1.1 Potentiodynamic polarisation.

As can be seen on figure 9.24 and table 9.5, the corrosion potential of the heat treated coating is higher than in the as-deposited state, which implies a better corrosion resistance. This is contradictory with the finding of several authors [31, 39, 98]. However, as they consider that the loss of corrosion resistance in electroless nickel-boron alloys during heat treatment is due to the creation of grain boundaries, which can only be happening if the coating is completely amorphous in the as-deposited state, it is possible that any improvement we observe is due to the decrease of the grain boundaries density during the recrystallization of the nanocrystalline coating. It is also possible that the improvement we observe is linked to a decrease of the intercolumnar corrosion, that is preponderant in the as-deposited state. To identify the actual mechanisms, EIS tests and observation of the tested coatings are indispensable.
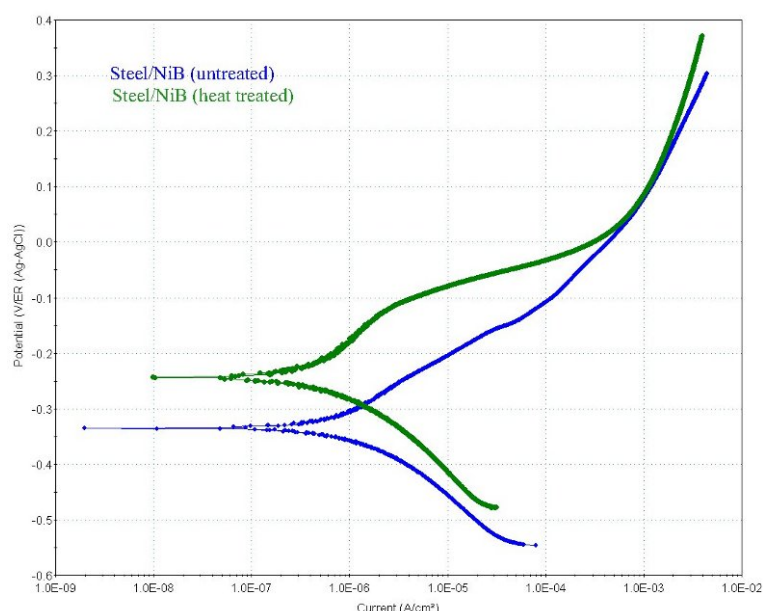
Fig. 9.24: Potentiodynamic polarization curves on untreated and heat treated nickel-boron on steel.

Sample type	Corrosion current (μA)	Corrosion potential (mV vs. Ag/AgCl)
Uncoated steel	2.34	-595.25
NiB coated steel	0.09	-335.05
NiB coated steel after heat treatment at 400 ℃	0.178	-240.67

Tab. 9.5: Corrosion current and potential of electroless nickel-boron.

9.7.1.1.2   Electrochemical Impedance Spectroscopy.
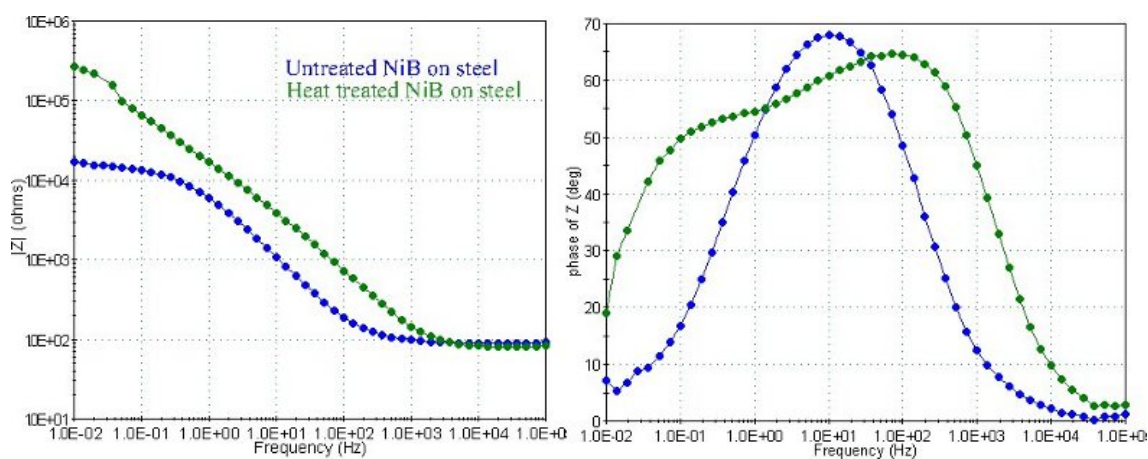
Fig. 9.25: Electrochemical impedance spectroscopy curves of NiB coated steel after heat treatment: Bode Modulus plot (a) and Bode phase plot (b).
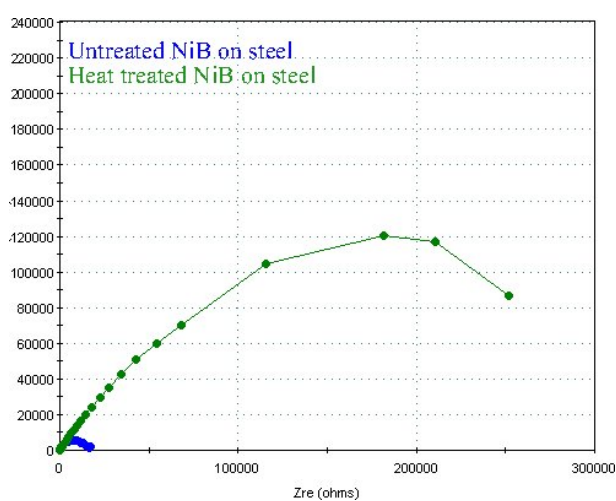
Fig. 9.26: Electrochemical impedance spectroscopy curves of NiB coated steel after heat treatment: Nyquist plot.

EIS data obtained on heat treated coatings (figures 9.25 and 9.26) confirm that their corrosion properties are better than on as-deposited coatings: the modulus at low frequency is much higher (over 100 $k\Omega/cm^2$) and the size of the loop in the Nyquist plot (figure 9.26) is much bigger. However, the Bode phase diagram is difficult to interpret: it looks like two time constants intervene in the corrosion phenomena, while only one is detected on the module plot. One explanation of this could be the presence of porosities that do not reach the substrate. The diffusion can thus be seen on the Bode phase diagram while the modulus plot stays unchanged.
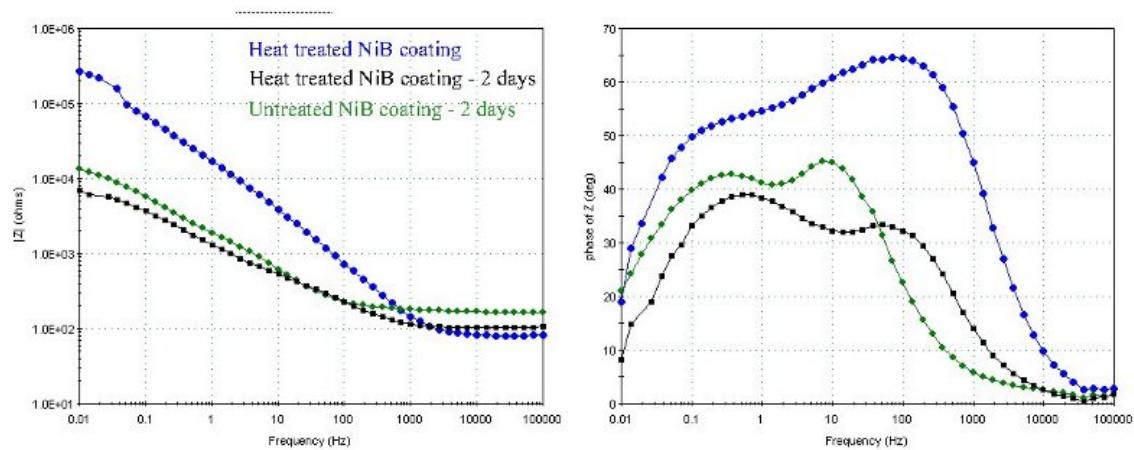
Fig. 9.27: Electrochemical impedance spectroscopy curves of NiB coated steel after heat treatment and aging in NaCl for 2 days: Bode Modulus plot (a) and Bode phase plot (b).
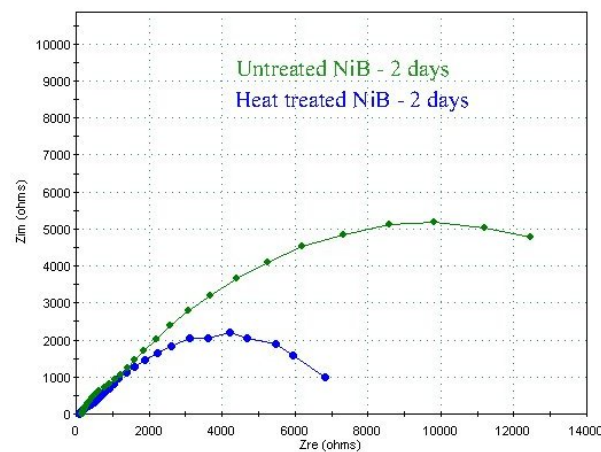
Fig. 9.28: Electrochemical impedance spectroscopy curves of NiB coated steel after heat treatment and aging in NaCl for 2 days: Nyquist plot.

Aging of the coating in NaCl for 2 days induces a decrease of the corrosion resistance similar to what was observed on untreated samples (see figures 9.27 and 9.28). The resistance of the aged heat treated coating appears to be slightly lower than the untreated

coating, as its modulus at low frequency and the size of the loop in the Nyquist plot are smaller.

9.7.1.2   Corrosion resistance of electroless nickel-boron on aluminum after heat treatment at low temperature.

The corrosion resistance of the Al/NiP/NiB system is better in the as deposited state than that of the steel/NiB system. Heat treatment leading to complete crystallization were shown to improve the corrosion resistance of the coating. It is thus interesting to observe if the low temperature heat treatment (at 180℃, for 4 hours) has also an influence on the corrosion resistance properties of the coatings and how this influence is manifested. In this section, electrochemical methods will thus be applied to the determination of the corrosion resistance of the Al/NiP/NiB system after heat treatment.

9.7.1.2.1   Potentiodynamic polarisation.

Figure 9.29 shows that heat treatment at 180℃ for 4 hours improves the properties of the electroless coating: the corrosion potential, which was already good, increases from -245 to -206 mV (Vs Ag/AgCl) and is significantly higher than on the heat treated Steel/NiB system (see table 9.6).
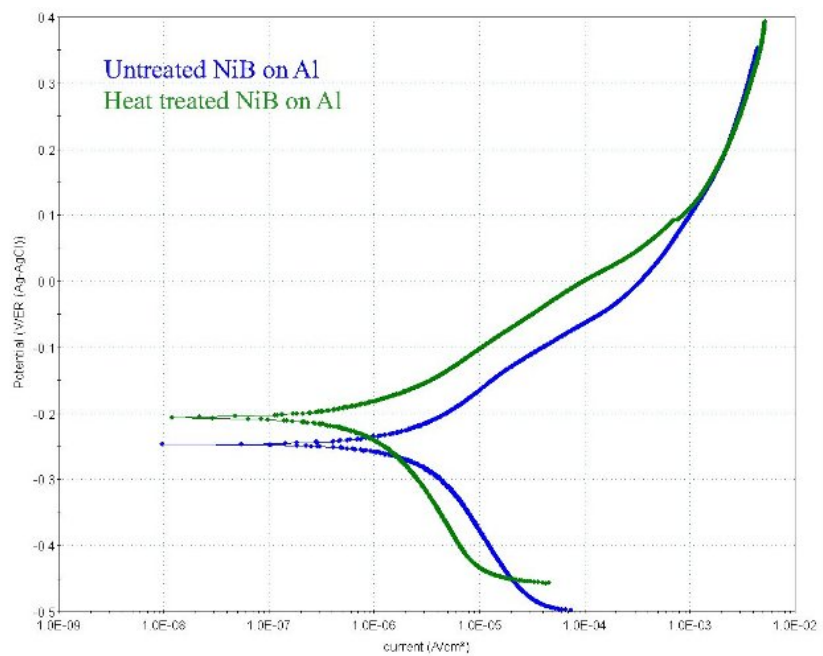
Fig. 9.29: Potentiodynamic polarization curves on untreated and heat treated nickel-boron on aluminum.

As the structure of the coating is not modified by the low temperature treatment, the modification of the corrosion properties cannot be attributed to crystallization. However,

as we have seen previously that the corrosion occurred mainly between the columns, it is probable that the improvement observed is caused by a slight densification of the coating that decreases the sensibility to corrosion of the intercolumnar zones.

Sample type	Corrosion current (μA)	Corrosion potential (mV vs. Ag/AgCl)
Al/NiP/NiB	0.217	-245.14
Al/NiP/NiB HT at 180 ℃	0.1958	-206.41
Steel/NiB -HT at 400 ℃	0.178	-240.67

Tab. 9.6: Corrosion current and potential of electroless nickel-boron.

9.7.1.2.2 Electrochemical impedance spectroscopy.

EIS data confirm the improvement of the corrosion resistance of the Al/NiP/NiB system brought by the heat treatment: after aging for 2 days in NaCl 0.1M, the modulus a low frequency is higher than it was in the case of a fresh untreated coating and only one time constant can be observed (figure 9.30). The size of the loop in the Nyquist diagram is also bigger in the case of heat treated and aged coatings than for fresh untreated ones (figure 9.31). As aged heat treated coatings have a better resistance than new untreated coatings, it appears that heat treatment at lower temperature modifies in a different, and better, way the corrosion properties of the coatings.
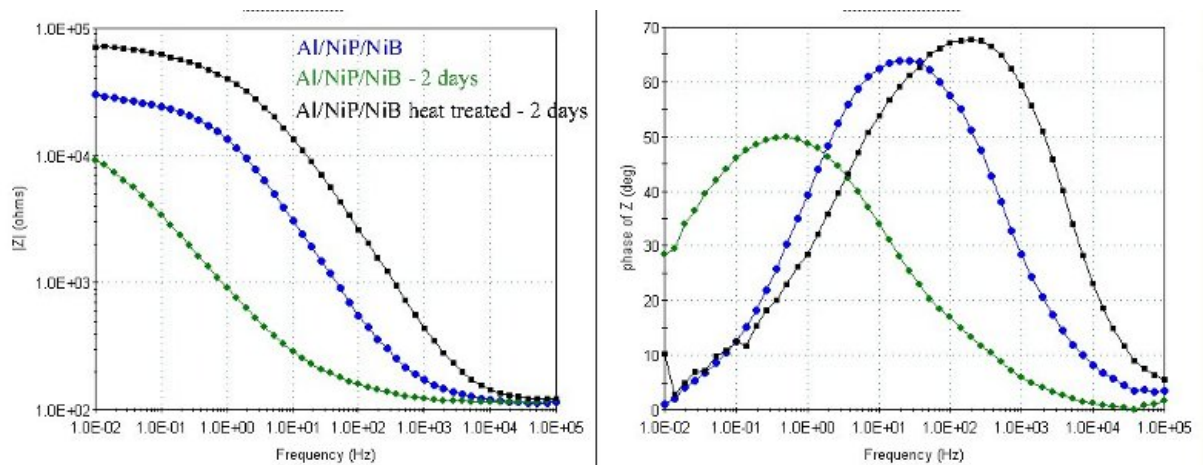
Fig. 9.30: Electrochemical impedance spectroscopy curves of NiP/NiB coated aluminum after heat treatment and aging in NaCl for 2 days: Bode Modulus plot (a) and Bode phase plot (b).
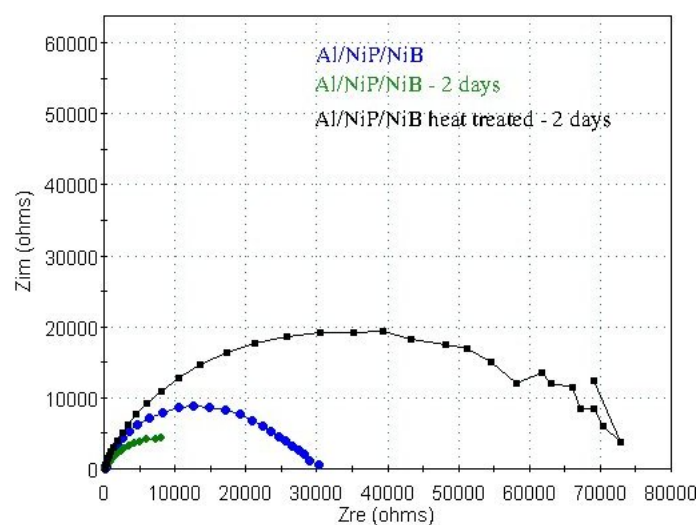
Fig. 9.31: Electrochemical impedance spectroscopy curves of NiP/NiB coated aluminum after heat treatment and aging in NaCl for 2 days: Nyquist plot.

9.7.1.3   Effect of wear on the corrosion resistance of electroless nickel-boron coatings.

The corrosion resistance of electroless nickel is significantly increased by heat treatment and decreased by abrasive wear. It is thus interesting to get information of the combined effect of those two parameters. This will be the object of the present section. Once more, the Steel/NiB system will be examined first, then the Al/NiP/NiB. However, this study will be limited to potentiodynamic polarization.

On steel, while the corrosion potential of heat treated coatings is lowered after abrasive wear, its stays higher than on unworn untreated coatings (see figure 9.32). On aluminum however, the potential of heat treated and abraded coatings is similar to untreated abraded coatings (see figure 9.33). The corrosion potential of worn heat treated coatings is similar for both systems (table 9.7). This is not surprising because the higher corrosion resistance of the Al/NiP/NiB system after heat treatment is accompanied by a lower hardness (compared with the coating treated at 400℃) and thus by a more important weight loss during the abrasion phase. The worn Al/NiP/NiB system is thus far thinner than the worn steel/NiB and the similar corrosion potential indicates thus an higher corrosion resistance of the coating deposited on aluminum.
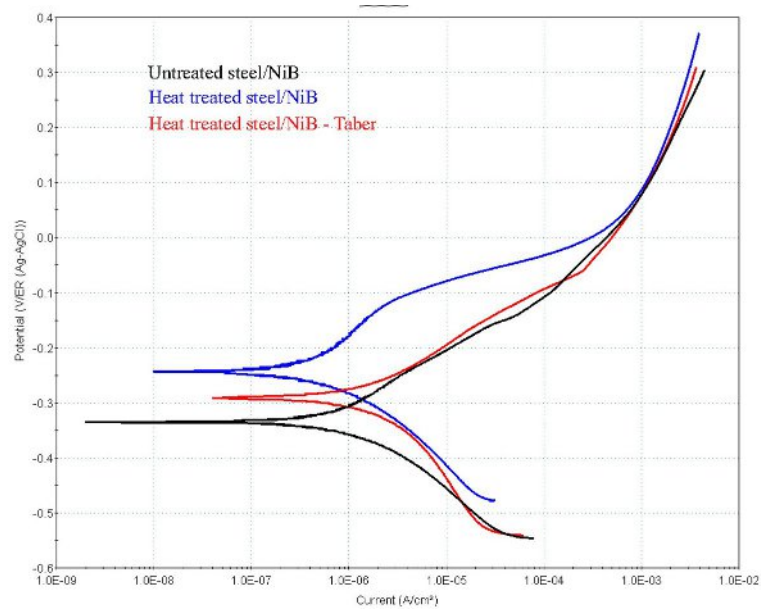
Fig. 9.32: Potentiodynamic polarization curves on heat treated nickel-boron on steel after Taber abrasion.
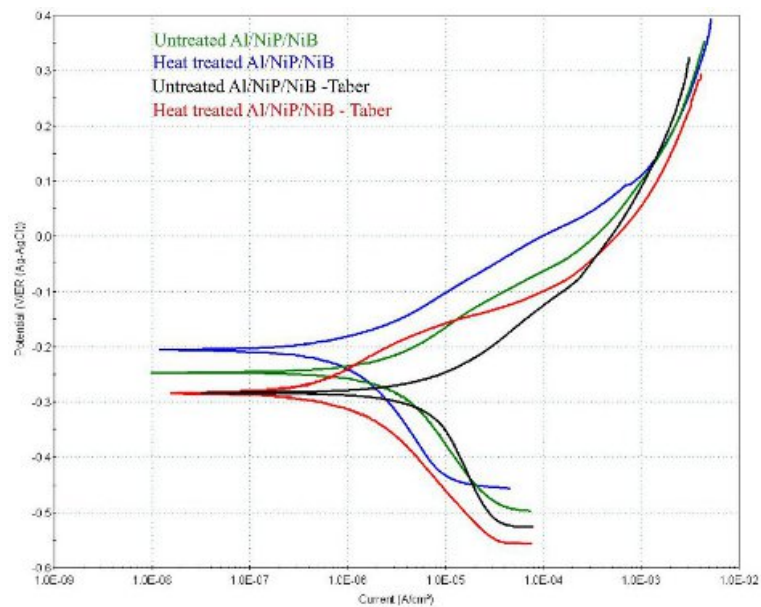
Fig. 9.33: Potentiodynamic polarization curves on heat treated nickel-boron on aluminum after Taber abrasion.

Sample type	Corrosion current (μA)	Corrosion potential (mV vs. Ag/AgCl)
Steel/NiB	0.09	-335.05
Steel/NiB -HT at 400 ℃	0.178	-240.67
Steel/NiB -HT at 400 ℃- Taber	0.7476	-297.56
Al/NiP/NiB	0.217	-245.14
Al/NiP/NiB HT at 180 ℃	0.1958	-206.41
Al/NiP/NiB HT at 180 ℃-Taber	0.2909	-285.53

Tab. 9.7: Corrosion current and potential of electroless nickel-boron.

9.7.2   Conclusions.

Contrary to most published results, we found an improvement of the corrosion resistance of the coatings after heat treatment at 180 or 400℃. This improvement can be explained by crystallization (which induces a diminution of the sensible grain boundary zones) but it is more likely that densification effects are involved in this phenomenon as an increase of the corrosion potential was observed on coatings treated at low temperature.

Aging of heat treated coating influenced the corrosion resistance in very dissimilar ways: while aged heat treated steel/NiB systems have a low corrosion resistance (just like the aged untreated coatings on this substrate), Al/NiP/NiB system keep a better comportment than fresh untreated coatings after 48h exposure in NaCl 0.1M.

Wear also influenced differently the heat treated steel/NiB and Al/NiP/NiB systems: on steel, the corrosion potential of worn heat treated coatings is higher than that of untreated unworn samples while on aluminum, worn coatings present similar corrosion potential with and without heat treatment. This can be easily explained by the effect of heat treatment on the hardness and wear resistance of the coating: while the weight loss registered on heat treated Al/NiP/NiB is similar to what is lost on untreated coatings (leading to similar corrosion resistance), the coating heat treated at 400℃ is far more wear resistant and the residual thickness is more important, which leads to a better corrosion resistance.

9.8   Conclusions: overall influence of heat treating on the properties of electroless nickel-boron coatings.

In the present chapter, several aspects of the influence heat treatments have on electroless nickel-boron coatings were examined. The treatments applied to the coatings were studied to either obtain the best mechanical properties of the coatings (treatment at 400℃ for 1 hour) or to improve the coating's properties without losing the mechanical resistance of the aluminum substrate (treatment at 180℃ for 4 hours).

First, the chemistry of the coating was not modified by any of the treatments and there was no interdiffusion between the coating and the substrate.

The structure of the deposits, however, was not left unmodified: while heating at 180℃ does not induce crystallization, this is not the case for treatments at higher temperatures (over 250℃). The coatings deposited on steel are thus constituted, after annealing, of Nickel boride Ni_3B which has a structure similar to cementite (Fe_3C). The grain size of this structure, while still in the nanometric range, is far bigger than on untreated coatings.

The hardness of the coatings was also modified, in a similar way to their structure: a small increase is observed for the low temperature treatment but heating at 400℃ brings the hardness in the 1200 hv_{100} range. This increase is due to the combination of a the formation of a harder phase (Ni_3B) and of an optimal grain size.

The tribological properties of the coating are also positively influenced: they are smoother and have a better Taber Wear Index after heat treatment while their scratch test resistance stays very good.

Finally, the corrosion resistance of electroless nickel-boron was also improved after heat treatment, which is in contradiction with other published results. This is probably due to a densification of the deposit during the treatment as this effect is already observed on coatings treated at 180℃ that decreases the sensibility to intercolumnar corrosion.

CONCLUSION.

This second part of the manuscript was entirely dedicated to experimental aspects and results. Its objective were multiple and each chapter was focused on one particular aspect of the experimental work.

The first point of focus was the description of the experimental setup and of its evolution during the project: the chemistry and operating conditions of the bath were described, as were the surface preparation procedures for the various substrates. An important part of that chapter discussed the evolution from a 800ml cell, allowing to plate only one very small sample at a time, to a 8 liter cell accommodating up to three 200 cm^2 samples at the same time.

The second point of focus was naturally linked to the first: with the increase of the bath volume, the problem of reactive and time wastes due to the elimination of all baths after a single use became unavoidable. Thus, even if the bath chemistry was not initially a focus of the research, an non negligible amount of work was carried out to get practical understanding of the reactive consumption during the plating process. This study was then used to determine how and when the replenishment process had to be implemented. Apart from allowing an important decrease of practical plating time (by suppressing most of the pre-heating needed to use one-shot baths) and cost, this study was very informative about the deposition mechanisms as some kinetic aspects of reactive consumption have been identified.

It was only natural, after examining bath operations, to turn ourselves to the study of the initiation and then to the growth of the deposit on the substrate. This part of the work allowed us to emphasize important features of the influence of surface roughness and (to a smaller extent) chemistry on the formation of electroless nickel-boron coatings on steel: the initiation of the deposition is nearly instantaneous and is favored by a rougher substrate; on steel, the initiation mechanism is catalytic oxidation of sodium borohydride and not a displacement reaction; the growth of the deposit is quicker on smoother substrates; the local morphology of the coating is linked to the local lead content.

However, while lots of information could be obtained from this study, there are still many unexplained phenomena like the effect of continuous replenishment on the deposit formation, the reason for the lead content variations, the eventual preferential initiation of deposit on a particular phase on Duplex and/or on high carbon steel.

The last two chapter of this experimental part of the work are dedicated to the description of the properties of the deposits before and after heat treatment. Lots of known properties of electroless nickel-boron coatings were confirmed during this study, like their

columnar structure, cauliflower-like surface texture and high hardness. However, that was not the complete extent of the work done as new information were gathered:

- Bath replenishment affects the morphology of the samples by inducing a secondary germination.

- Advanced structural study by TEM and X-ray diffraction allowed to identify the nanocrystalline nature of the as-deposited coatings and to calculate the grain size in the as-deposited state (close to 1nm). The nanocrystalline state of heat treated samples was also observed.

- Evaluation of the hardness via nanoindentation allowed to check the homogeneity of this property across the deposit for as-deposited as well as heat treated samples.

- The wear properties of the coatings were investigated. While they are already good in the as-deposited state, they are much improved by the application of an heat treatment. The same can be said about the roughness of the plated parts. However, it was possible to ascertain the influence of heat treatment on scratch test resistance as results obtained for both states of the coating are really similar.

- The corrosion resistance of the coatings was found to be as good, if not better than electroless nickel-phosphorous and to be favorably influenced by heat treatment, contrary to usual belief in the electroless nickel community. The mechanisms leading to this improvement of the properties, however are not fully identified yet.

While this experimental part of the work brought answers to lots of questions about the comportment of electroless nickel-boron coatings, during the plating and in use, it brought still more questions about the fundamental mechanisms involved in the described comportments. In the near future, more work will be carried out to define those fundamental mechanisms, using the new knowledge that was gained about electroless nickel-boron.

Part III

MODELING OF THE STRUCTURAL STATE OF ELECTROLESS NICKEL-BORON AND OF ITS MODIFICATION BY HEAT TREATMENTS.

INTRODUCTION.

The first two parts of this work were dedicated, for the first, to theoretical and background studies about electroless nickel-boron and, for the second, to experimental work carried out on synthesis and characterization of those coatings. This last part however will be dedicated to a completely different aspect of this study: modeling of the structure of the coatings and of its modifications during heat treatment.

The interest of this part lies in gaining a better understanding of the structural properties of the material by an analytical description of their comportment. In its most advanced state, this modeling would allow predictive description of the coating's structure from the sole knowledge of its composition and thermal history. Knowing the very strong dependence of the coatings' most useful properties to their structural state, the implementation of an effective structural prediction model would then lead to fine tuning the composition and heat treatment to the final application of the coating.

The implementation of such a complete model is of course a very ambitious goal that cannot be attained in the course of a single research project. However, it is already possible to set the path for the future and to determine the first steps that will have to be taken to complete this objective. For some parts of the model, it is even possible to already give practical results at the present time. In this part the approach of an analytical model for structural prediction of electroless nickel-boron deposits will be carried out in multiple steps.

The first chapter of this part will be an introductory chapter: the problem will be presented, as well as possible ways to solve it. The approach chosen for the modeling will then be introduced, in a very synthetic way.

The second chapter will be focused on the prediction of the grain size in as-deposited coatings from the coating's composition. In that chapter, the background and the actual model we used will be described. Our completed model will then be compared with experimental results for validation.

After this, a background chapter will be dedicated to the preparation of the most complicated part of the model: the prediction of the coating's 'crystallization temperature'. In this chapter the main equations leading to the establishment of such a model will be expressed, but we will not try to offer any numerical values or to solve them further than what is needed to understand the model.

The fourth chapter of this part will be dedicated to the ground work for the preparation of the model implementation. In this, most equations will be developed in order to isolate the data needed to solve them. The data will also be reviewed in order to determine which of them can be found in published work and which will have to be determined experimentally.

Finally, a small chapter will be dedicated to the experimental work that will be used not for the determination of the missing data but for the validation of the model. In this, examples of crystallization temperature determination will be presented.

10. PRESENTATION OF THE PROBLEM, BACKGROUND AND APPROACH CHOSEN FOR THE MODELING.

10.1   General presentation of the problem.

Most electroless nickel coatings are submitted to an heat treatment that allow enhancement of their mechanical properties by crystallization of the coating. At the present time, the treatment conditions are usually standardized (400℃, 1 hour) and used regardless of the deposit composition. Moreover, those conditions were initially determined experimentally, either by determination of the crystallization temperature of the coating or by an trial and error method for the optimization of the hardness.

While this approach has given good results, using a more rigorous method, including pre-determination of the crystallization temperature and of the structural state of heat treated deposits could bring more information and allow fine tuning of the heat treatment in regards to the chemistry of the coating and the desired properties. This will be very useful for alloy design for example where the fine tuning of heat treatment using modeling will allow avoiding expensive experimental work for the synthesis and testing of materials.

In a first step towards global modeling of structural modifications during heat treatment, determination of the crystallization temperature was chosen because it is a parameter that is widely used and that do not require extensive experimental testing to obtain, which will ease the validation of the model.

There are two possible ways to determine the crystallization temperature: either working with isothermal conditions and determining if the crystallization happens (in a reasonable time frame) or not, or working in anisothermal conditions (with a fixed heating rate) and recording the temperature of the onset of the transformation.

10.2   Different approaches for the modeling of heat treatment comportment of materials, choice of a method for modeling and justification.

A lot of the modeling work carried out in the materials science field concerns the variation of materials structure and properties with the temperature. It is so much studied because the thermal history of matter has a tremendous influence on its comportment: when heated or cooled, the material can undergo, for example, phase transformations, grain growth, mechanical properties variations, diffusion, sensitization to some corrosion processes, dry oxidation, etc.

The most used structural modeling in material science is the modeling of phase diagrams, usually in the CALPHAD (CALculation of PHAse Diagrams) formalism. In this approach, thermodynamical equilibrium data are used to determine the stability boundaries of the different phases in a material in regard to pressure, temperature and chemistry (A review of this kind of methods was written by Kattner [152]). While those diagrams are really useful in lots and lots of applications, they are not very well adapted to our case as, in their more current form, they only apply to equilibrium systems, which our nanocrystalline-nearly amorphous coating is not.

Another well used tool for structural study is thermal history diagrams, such as Time - Temperature - Transformation (TTT) and Time - Cooling/Heating Rate - Transformation (T-CR/HR-T) diagrams. While they are usually determined experimentally (because they are often applied to very complicated chemistry), it is possible to calculate them on the base of a kinetic approach, described in the framework of the Avrami formalism (or one of its derivatives, such as the Kolmogorov, Johnson and Mehl and Avrami model (KJMA)) and allows to obtain very precious information about the crystallization and even the microstructure after treatment of the material. A very complete review about that kind of modeling has been written by Clavaguera-Mora et al [153].

Thermal history diagrams can offer very important and useful information about phase transformations in the coatings, such as the onset point of phase transformation and the transformed fraction for a defined set of conditions. However, they are used for materials with a known and homogeneous initial state, which is not the case of nanocrystalline electroless nickel-boron coatings for which the grain size (or grain boundary fraction) is a parameter that has to be taken into account. Moreover, there is no evident link between them and DSC data, so we decided not to use them.

The last approach we found was a model proposed by Jiaqiang et al [86] for the crystallization temperature of amorphous electroless nickel-phosphorous. It constitutes an interesting answer to our problem as it describes the phenomenon observed by DSC. Moreover, it is quite convenient for us as it uses thermodynamic properties of the material and includes few kinetics data.

10.3   Brief description of the chosen model.

The methodology used for modeling is adapted from Jiaqiang et al. [86] and, as we said before, describes the phenomenon observed by DSC: during the calorimetric experiment, heat consumption and/or release caused by transformations in the material (phase transformations, Curie point, ...) are recorded. The events inducing those heat variations can be described by thermodynamic relations, which are at the basis of the model.

They described the crystallization of electroless coatings using 2 different mechanisms that coexist:

- Assuming there are pre-existing nuclei or grains, those must grow following a classical kinetic parabolic law, that expresses the relation between the grain size and the temperature.

- For an event to begin to register in DSC, thermodynamic equilibrium must be reached, and thus the variation of Gibbs' Free Energy of the system must be null. Using this, it is possible to obtain an expression linking grain size and temperature.

As the phenomenon that is observed is a grain growth at thermodynamical equilibrium, both mechanisms must be used conjointly. This means that, when the two expressions of the grain size as a function of temperature are put together, the solution of the problem is the temperature for which a similar grain size is obtained from both equations.

For practical use of this modeling method, a first, preliminary step, must be taken: the size of the pre-existing grains or nuclei must be calculated, first because it constitutes the initial state of the material, and secondly because it is needed in further calculations.

The basis of the three modules of the model is described hereunder.

10.3.1 Modeling of the grain size of as-deposited electroless nickel-boron.

The determination of the grain size in the as-deposited material is the first step of the model. It is based on the work of several authors about the structure of nanocrystalline materials.

According to Phillpot et al [68], nanostructured materials are constituted of nano-sized grains, with the same structure and properties than perfect crystals, embedded in a cement-like phase that is heavily disordered and holds the grains together and has a more or less uniform width. This particularity of the 'boundary phase' has thus been used, assuming that the grains have the shape of spheres (see figure 10.1), to estimate the grain boundaries fraction (x_i) of the material as:

$$x_1 = \frac{d^3 - (d - \delta)^3}{d^3} \tag{10.1}$$

where δ is the average thickness of the grain boundaries and d is the average grain diameter.

In the course of their experimental work on electrodeposited nickel-phosphorous alloys, Farber et al [81] and of Hentschel et al [80] showed that the phosphorous is not homogeneously distributed in the material but segregates to a large extent in the grain boundaries. Measures by atom-probe field-ion microscopy (APFIM) and tomographic atom-probe (TAP) allowed them to determine that the concentrations of phosphorous in the grains and grain boundaries were not dependent on the average material composition.
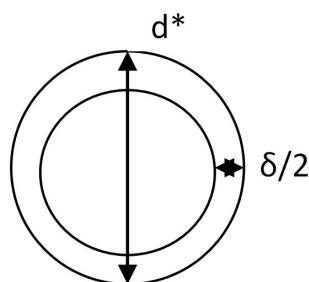
Fig. 10.1: Schematic representation of a grain (and its grain boundary) in a nanocrystalline material.

From this discovery, using the constant width property of the boundaries and the knowledge of the average phosphorous concentration of the coating, they used a simple mass balance to determine the grain boundary fraction:

$$C_0 = x_i \cdot C_{gb} + (1 - x_i) \cdot C_g \tag{10.2}$$

where C_0 is the average P concentration in the material, C_{gb} and C_g are the P concentrations respectively in the grain boundaries and in the grains.

Combining equations 10.1 and 10.2, they proposed a model that allows to calculate the average grain diameter of the material and that we will use and develop in chapter 11.

$$d = \frac{\delta}{1 - \sqrt[3]{\dfrac{C_0 - C_{gb}}{C_g - C_{gb}}}} \tag{10.3}$$

10.3.2   *Determination of the crystallization temperature of electroless nickel-boron.*

While both parts of this module have to be used concurrently to obtain a value, there are easier understood if they are kept separate. The first part that will be described is the diffusion based law, then the expression of thermodynamic equilibrium.

10.3.2.1   *Diffusion-based law.*

The diffusion-based law used to determine the first expression of the grain size dependence on the temperature is quite straightforward. It is obtained from the isothermal grain growth law:

$$d^2 = d^{*2} + 8 \cdot \xi \cdot D \cdot t \tag{10.4}$$

where d is the grain size, d* the initial grain size (obtained from equation 10.3), ξ is a function of the chemistry of the material, D is the diffusion coefficient and t is the time.

The temperature dependence comes from D, which is obtained from :

$$D = D_0 \cdot exp(\frac{-Q}{RT}) \qquad (10.5)$$

with D_0 the diffusion constant, Q the activation energy of diffusion, T the temperature, and R the gas constant.

Equation 10.4 cannot be used directly for anisothermal calculation but if the continuous heating is considered as a succession of very short isothermal steps, it is easily modified to suit our means [86] (this will be described in section 13.2).

10.3.2.2 Thermodynamic-based law.

As Jiaqiang [86] used, for the establishment of his model, the assumption that the electroless deposit is amorphous, this assumption will also be used in the present section, because this allows important simplification of the relations and leads to a more straightforward form. However this assumption will not be kept for further developments.

During heating of electroless nickel-boron alloys, phase transformations and grain growth occur. Those transformations can be expressed as follow:

$$
\begin{aligned}
\text{Initial state} \quad &\rightarrow \quad \text{final state} \\
\text{Amorphous Ni-B} \quad &\rightarrow \quad \text{Ni nanocrystallites} + \text{ Ni compounds} + \text{ interfaces}
\end{aligned}
\qquad (10.6)
$$

The Gibbs free energy of this transformation can thus be expressed as :

$$\Delta G(T) \; = \; (1 - x_i)\, \Delta G_f^c(T) \; + \; x_i \Delta G_f^i(T) - \Delta G_f^a(T) \qquad (10.7)$$

where $\Delta G_f^c(T)$, $\Delta G_f^i(T)$ and $\Delta G_f^a(T)$ are the Gibbs free energy for formation of, respectively, the crystallites, interfaces and amorphous phase and x_i is the volume fraction of interfaces (which is related to the grain size by equation 10.1).

At equilibrium, $\Delta G(T)$ in equation 10.7 is null. It is thus possible to express the volume fraction of interfaces as a function of the Gibbs free energy for formation of the different phases, which are all functions of the temperature. From this, using equation 10.1, the grain size can be expressed as a function of the temperature, which is the second module needed to make the model work.

As we will not be using all of Jiaqiang assumptions, further developments of this part of the model will not be described in the present section.

11. GRAIN-SIZE MODELING IN AS-DEPOSITED NICKEL-BORON: DATA COLLECTION, MODEL IMPLEMENTATION AND VALIDATION.

11.1 Introduction.

Now that the method for the modeling has been presented, the different modules will be examined separately and developed for calculation. As the initial grain size is necessary for both other parts of the model and as it was actually possible to obtain numerical results for this module, it will be studied first.

As this module is based on relatively simple equations, those do not need to be further developed. We will thus begin by a review of the equations presented in section 10.3.1, a listing of the various data needed for the calculations and the strategies chosen to obtain or approximate the data that are not directly available.

After this, a short section will be dedicated to the actual calculations and to the modeling results.

The last section of this chapter will be focused on model validation: the collection of experimental data and their comparison to our model will be discussed.

11.2 Model presentation, data and data collection.

11.2.1 Modeling equations and data listing.

The following equation, on which the determination of the grain size is based, has already been described in section 10.3.1 (eq 10.3).

$$d = \frac{\delta}{1 - \sqrt[3]{\dfrac{C_0 - C_{gb}}{C_g - C_{gb}}}}$$

This equation needs relatively few parameters:

- δ, the grain boundary thickness, which is a constant parameter.

- C_b, the boron content of the crystallites, which is a constant parameter.

- C_{gb}, the boron content of the grain boundaries, which is a constant parameter.

- C_0, the average boron content of the material, which is the variable of the model.

The process involved in the determination of the three constant parameters is the object of the next section.

11.2.2 Data collection and calculation.

Only three constant parameters need to be determined before the implementation of the model. However, none of them are easily available. Moreover, their determination is not an easy process.

11.2.2.1 Grain boundaries thickness.

The thickness of the grain boundaries area is supposed to be a near constant in nanocrystalline materials [68]. However, as this thickness, and the size of the grains, are very small, it is not possible to measure them by classical analysis methods such as SEM and TEM.

It was thus not possible for us to obtain direct experimental measurement of this value for electroless nickel-boron deposits. However, two studies were realized on nickel-phosphorous by Farber [81] and Hentschel [80], in which the structure of the deposit was observed by more sophisticated methods such as Tomographic Atom Probe (TAP) and Atom Probe Field-Ion Microscopy (APFIM). Using those local techniques, they were able to evaluate the thickness of this grain boundaries as 0.5-1 nm by TAP [81] and 0.8 ± 0.1 nm by APFIM [80].

As we did not dispose of this kind of analytical techniques for this project, we had to settle for approximation of the data we need. However, knowing that boron and phosphorous have similar segregation properties (see section 2.2.3 in part I) and that electroless NiB and NiP have similar structural features, we can reasonably assume that the grain boundary thickness would be similar in Ni-B alloys than in Ni-P and use the value of 0.8 nm.

11.2.2.2 Boron concentration in the crystallites.

The determination of the boron content of the crystallites is also a very delicate operation because they are very small (close to 1nm in the as-deposited state for our electroless nickel-boron coatings, see section 8.4.2.1 in part II) and would thus require the use of very localized techniques that are not easily available to us. Moreover, the quantitative analysis of boron in a nickel matrix by X-ray fluorescence, atomic contrast in electron microscopy and EDX is not very reliable because of re-absorption effects. We are thus left in a similar predicament than with the boundary thickness as far as this value is concerned.

Once again, the only available values come from the work of Hentschel and Farber and have been obtained for nickel-phosphorous. Hentschel measured, by selected area atom-probe analysis, at the center of the grains, a phosphorous content of 1.4 at.% that indicates that the nickel nanocrystallites are supersaturated in phosphorous [80]. Farber

however, obtained, by tomographic atom-probe a value of 1 at.% or less for the phosphorous content of the interior of the grains [81].

Still assuming a similar segregation state for nickel-phosphorous and nickel-boron, we decided to use a value of 1 at.% in the grain as boron content for our calculations.

11.2.2.3   Boron concentration in the grain boundaries.

The determination of the boron content of the grain boundaries, however, cannot be derived from the values obtained on nickel-phosphorous: while it is possible to assume that the boundary thickness and supersaturation are similar to what is obtained on nickel-phosphorous, it is less reasonable to do the same for the grain boundary composition. This value was thus calculated from other data, as follow:

- The density of the nickel boron can be calculated from a balance of the densities of the nanocrystallites and boundaries:

$$\rho_0 \;=\; \rho_g \;\cdot\; Vf_g \;+\; \rho_{gb} \;\cdot\; Vf_{gb} \tag{11.1}$$

  where ρ_0 is the average density of the material, ρ_g and ρ_{gb} the densities of the grains and grain boundaries and Vf_g and Vf_{gb} the volume fractions of the grains and grain boundaries.

- It is possible to link the density of the material to its composition (boron content) by an analytical or empirical law.

- The volume fraction of electroless nickel-boron has been measured, for various compositions, by X-ray diffraction, by Kumar et al. [60].

Thus, it is possible, after calculation of the average density of the coating and the density of the grains, to use the volume fractions to calculate the density of the grain boundaries. The boron content is then calculated using the law that links content and density.

11.2.2.3.1   Variation of density with boron content.

The density of electroless nickel-boron decreases when the boron content increases, as was said in section 2.3.1 of part I. It is possible to calculate a theoretical law expressing this dependence using the following assumptions:

- The nickel boron alloy consists of a (fictitious) interstitial solid solution of boron in nickel (in reality, the solubility of boron in nickel is very low) and possesses the face centered cubic structure typical of pure nickel.

- The interstitial sites of each unit cell are either completely void of boron or completely filled.

- The density decreases linearly when the boron content increases.

Firstly, the type of interstitial sites occupied by the boron alloy in the fcc nickel structure must be determined from the atomic radii (see table 11.1). For atoms to be able to occupy the tetraedric sites, the ratio between the atomic radii of the solute and the solvent must be less than 0.225 (and 0.414 for the octaedric sites). The ratio between boron and nickel is 0.62, which shows that, theoretically, this element cannot form interstitial solid solution in nickel (which is confirmed by the very low solubility of boron in nickel). However, for our fictitious solid solution, we will assume that boron occupies the octaedric sites and dilates the nickel fcc lattice as presented in figure 11.1.

	Nickel	Boron
structure	fcc	
cell parameter (Å)	3.52	
atomic radius (Å)	1.24	0.77
atomic weight (awu)	58.69	10.81

Tab. 11.1: Structural parameter of nickel and boron.
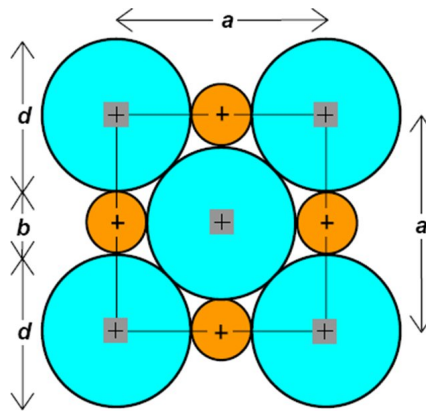
Fig. 11.1: Position of boron in the octaedric sites of a fcc nickel structure.

The lattice parameter of a unit cell whose octaedric site are all occupied by boron atoms ($\tilde{a}$) is $2 \cdot (r_{Ni} + r_B) = 4.024$ Å(see figure 11.1). The saturated unit cell, with a boron atom in each of the octaedric sites, contains 4 nickel atoms and 4 boron atoms (50 at.% B).

The density of a fictitious nickel lattice saturated with interstitial boron atoms can thus be calculated from the geometric representation

$$
\begin{aligned}
\text{density} &= \frac{\text{unit cell mass}}{\text{unit cell volume}} \\
&= \frac{(4 \cdot M_{Ni} + 4 \cdot M_B)/N_A}{\tilde{a}^3} \\
&= \frac{\dfrac{4 \cdot 58.69 + 4 \cdot 10.81}{6,02 \cdot 10^{23}}}{(4.024 \cdot 10^{-10})^3} \\
&= 7.11
\end{aligned}
\tag{11.2}
$$

The density of any nickel-boron alloy is then obtained from a balance between pure nickel and the saturated fictitious interstitial solution with 50 at.% B, as follow:

$$
\text{density} = 8.94 - (C_0 \cdot \frac{1.83}{50})
\tag{11.3}
$$

To check the validity of this expression, experimental data where obtained from published results [154] and compared with the calculated values, as shown in table 11.2 and figure 11.2. The experimental and theoretical values are very close together which means that the assumptions used for this model are sound and that the model can be used without introducing an important error.
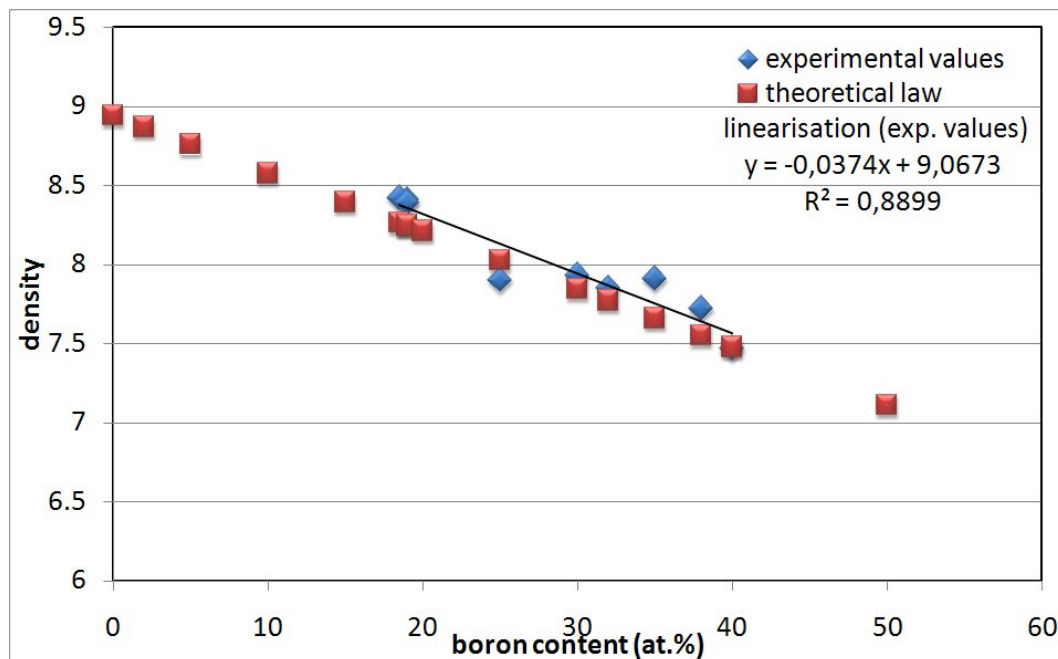
Fig. 11.2: Comparison of calculated and experimental values of the density of Ni-B alloys.

at.% B	wt.% B	experimental density	calculated density
19	4.14	8.41	8.24
19	4.14	8.39	8.24
18,5	4.01	8.42	8.26
25	5.78	7.9	8.03
30	7.32	7.93	7.84
32	7.98	7.85	7.77
35	9.02	7.91	7.66
38	10.14	7.72	7.55
40	10.94	7.47	7.48

Tab. 11.2: Comparison of calculated and experimental values of the density of Ni-B alloys.

11.2.2.3.2 *Volume fraction of interfaces for various boron contents.*

The interfaces (or grain boundaries) in nanocrystalline materials can represent an important part of the volume. They influence thus the X-ray diffraction patterns obtained from the material and it is possible, with the adequate analytical tool, to separate the peaks caused by the crystallized fraction (grains) and by the disordered grain boundaries.

However, as the nickel-boron alloys we synthesize have a near constant and very high boron content, it was not possible to use them for this calculation and we had to, once more, borrow results from other research groups. In 1994, Kumar et al. [60] have published a study about the deconvolution of diffraction patterns of electroless boron with various boron content. In this work published at a time when nanocrystalline materials were not as well known than now, they considered that the alloys was constituted of a mix of amorphous phase and crystallized nickel. They calculated the ratio between the peak areas relative to both phases (I_c/I_a), which can be, using the current knowledge about nanostructured materials, interpreted as the ratio between the volume fraction of crystallites and grain boundaries. We could thus obtain two values for the volume fraction of interface of alloys with a known composition. They are presented in table 11.3.

wt.%B	I_a/I_c	volume fraction of crystallites	volume fraction of boundaries
3.85	7	12.5	87.5
4.32	25	3.84	96.15

Tab. 11.3: Volume fraction of grain boundaries in Ni-B with varying B content [60].

11.2.2.3.3   Determination of the boron content of grain boundaries.

    The determination of the boron content of the grain boundaries was made from the volume fraction data of table 11.3, using equation 11.1 for the density balance and equation 11.3 to determine the density of the various phases. The results of these calculation are shown in table 11.4.

    The boron content of the grain boundaries calculated for both alloys is similar, which confirms the hypothesis of a value independent on the average content of the alloy. To simplify the calculation, we decided to round the value of the atomic boron content of the grain boundaries at 20 at.%. This value, while larger than the 14 at.% P that were measured for Ni-P by Henstchel [80] and Farber [81], is not overly large. Moreover it coincides with the boron content determined by Gaevskaya et al [71] as the lower limit of X-ray amorphous alloys.

wt.%B in alloy	at.%B in alloy	volume fraction of boundaries	at.%B in boundaries
3.85	17.86	87.5	20.26
4.32	19.69	96.15	20.43

Tab. 11.4: Boron content of the grain boundaries of alloys with varying boron content.

11.3   Model implementation and results.
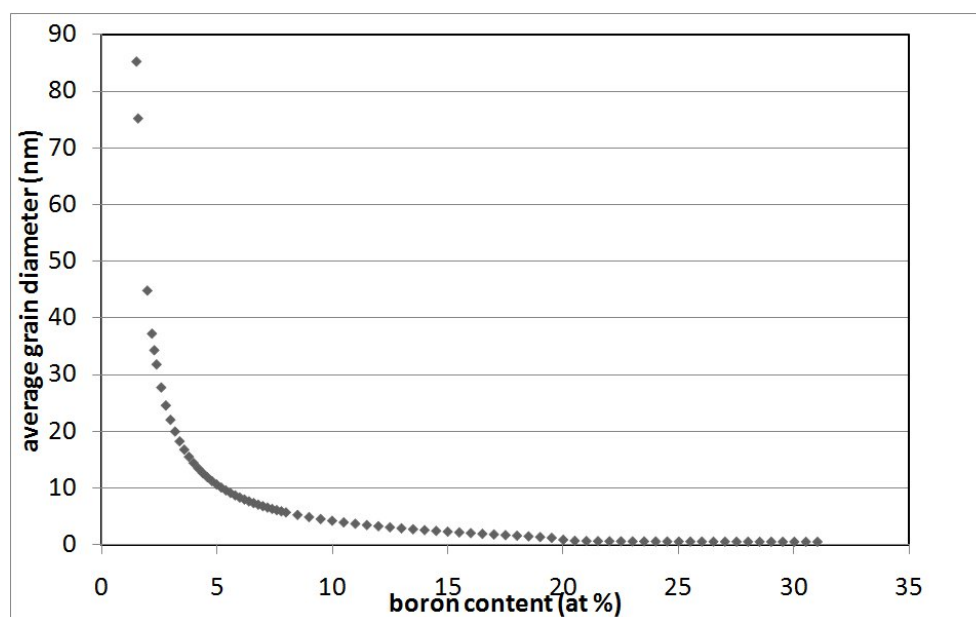
Fig. 11.3: Evolution of grain size with boron content in electroless nickel-boron.

As the equation used for this model is quite simple (equation 10.3), it can be implemented using a single excel sheet. The results are presented on figure 11.3. The grain size decreases quickly when the boron content of the material increases and reaches 1 nm for a boron content close to 5 at.%.

11.4 Collection of experimental results and model validation.

In section 8.4.2.1 of part II, the grain size of electroless boron with a boron content close to 5 wt.% was measured. However, as we have not the means to synthesize electroless nickel-boron deposits in a wide range of composition, we had to recourse to published results to validate the model for lower boron content. In 1996, Gaevskaya et al [71] published a study in which they measured grain sizes for electrodeposited nickel-boron with various boron content. Those results, as well as ours, are presented in table 11.5. As can be seen on figure 11.4, the model is in good adequation with the experimental results.
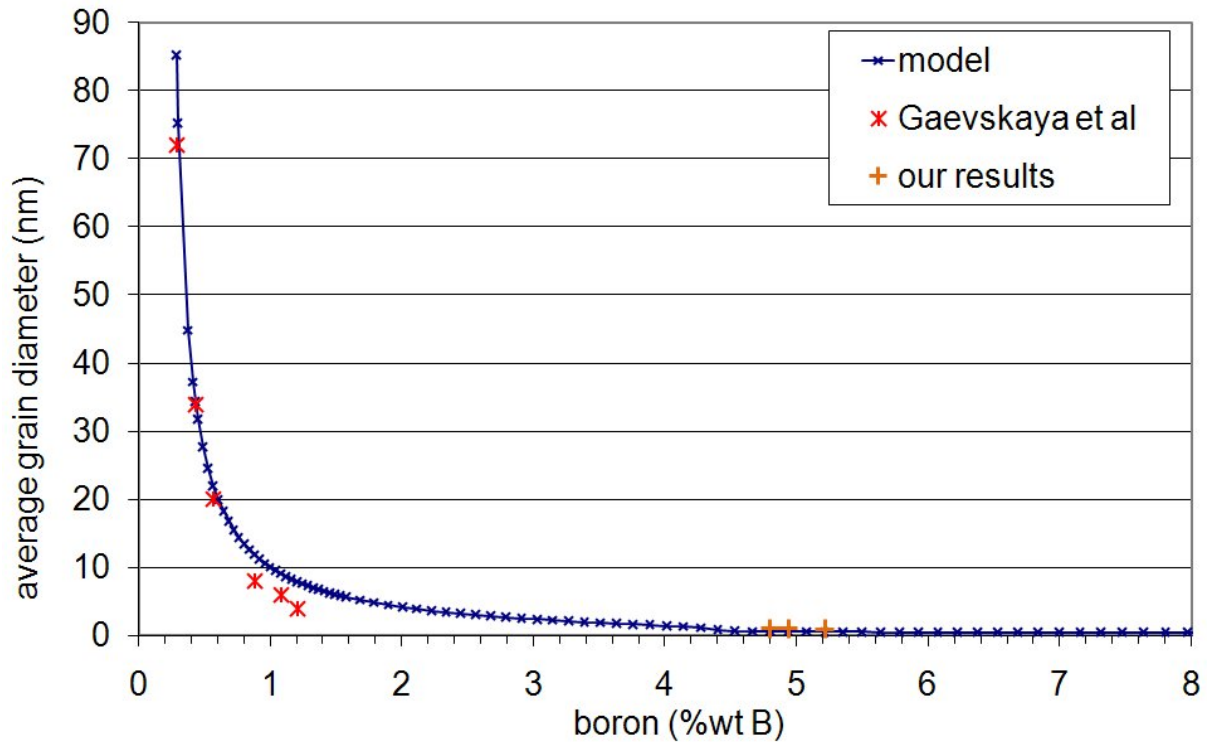
Fig. 11.4: Evolution of grain size with boron content in electroless nickel-boron, comparison of model and experimental results.

at.%B in alloy	grain diameter (nm)
Gaevskaya et al.	
1,53	72
2,3	34
3	20
4,6	8
5,6	6
6,2	4
Our results	
21,5	0,955
22	0,959
23	0,927

Tab. 11.5: Measured grain size in nickel-boron alloys with variable boron content.

11.5   Conclusions.

In this chapter, the equations allowing to calculate the average grain size of electroless nickel-boron deposits in their as-deposited state have been presented and the parameters needed for the model have been determined either from experimental results or from theoretical calculation. The results of the model have then been compared to experimental results and the model has been validated.

12. MODELING OF THE CRYSTALLIZATION TEMPERATURE OF ELECTROLESS NICKEL-BORON: THEORETICAL BACKGROUND.

12.1 Introduction.

The modeling procedure we chose is based on a model proposed for initially amorphous materials. It is thus useful, before modifying it to take into account the different initial structure, to present the model as proposed by Jiaqiang et al [86]. This is the object of the present chapter.

First, the expression of the Gibbs free energy variation for the crystallization of an amorphous material will be presented and developed. The equilibrium condition will then be used to isolate the grain size in the expression.

12.2 Expression of Gibbs free energy variation for the crystallization of an amorphous material.

As was said in section 10.3.2.2 (page 211), it is possible to describe the crystallization of an amorphous material as a chemical reaction (see equation 10.7) and to calculate the Gibbs free energy associated to this transformation, according to the following equation (equation 10.7) [86].

$$\Delta G(T) \,=\, (1 - x_i)\,\Delta G_f^c(T) \,+\, x_i \Delta G_f^i(T) - \Delta G_f^a(T)$$

In this equation, $\Delta G_f^c(T)$, $\Delta G_f^i(T)$ and $\Delta G_f^a(T)$ are the Gibbs free energy for formation of, respectively, the crystallites, interfaces and amorphous phase and x_i is is the volume fraction of interfaces.

Equation 10.7 can be modified to show the Gibbs free energy difference between the different phases instead of their Gibbs free energy of formation:

$$
\begin{aligned}
\Delta G(T) \;&=\; (\Delta G_f^c(T) - \Delta G_f^a(T)) - x_i \cdot (\Delta G_f^c(T) \,-\, \Delta G_f^i(T)) \\
&=\; \Delta G^a(T) - x_i \cdot \Delta G^i(T)
\end{aligned}
\tag{12.1}
$$

Where $\Delta G^a(T)$ is the Gibbs free energy difference between the amorphous and crystalline phase and $\Delta G^i(T)$ is the Gibbs free energy difference between the interfaces and the crystalline phase. Those parameters can then be calculated from thermodynamical data.

12.2.1 Gibbs free energy of formation of the crystallized fraction.

In the completely crystallized state, nickel-boron alloys (in the range of composition that can be obtained by electroless deposition) can be constituted of Ni, Ni_2B, Ni_3B and Ni_4B_3 phases. However, as most coatings contain less than 6 wt% B, it is possible to restrain the range of phases to Ni and Ni_3B.

The Gibbs free energy of formation of the crystalline phases can be obtained by a weighted average of the energies of formation of the phases that are formed:

$$\Delta G_f^c(T) \ = \ y_{Ni} \cdot \Delta G_f^{Ni}(T) \ + \ (1 - y_{Ni}) \cdot \Delta G_f^{Ni_3B}(T) \tag{12.2}$$

where y_{Ni} is the the fraction of Ni in the crystallized phases, $\Delta G_f^{Ni}(T)$ is the formation free energy of crystalline nickel (and can be approximated by 0) and $\Delta G_f^{Ni_3B}(T)$ is the formation free energy of crystalline Ni_3B, that is calculated by:

$$\Delta G_f^{Ni_3B}(T) = \Delta G^{Ni_3B}(T) - 3\Delta G^{Ni}(T) - \Delta G^B(T) \tag{12.3}$$

In equation 12.3, $\Delta G^{Ni_3B}(T)$, $\Delta G^{Ni}(T)$ and $\Delta G^B(T)$ are the free energies of the 3 phases, that can be determined from thermodynamical data.

Under the assumption that only Ni and Ni_3B can be formed, y_{Ni} is calculated following:

$$
\begin{aligned}
C_0^B &= y_{Ni} \cdot C_{Ni}^B + (1 - y_{Ni}) \cdot C_{Ni_3B}^B \\
&= y_{Ni} \cdot (C_{Ni}^B - C_{Ni_3B}^B) + C_{Ni_3B}^B
\end{aligned}
$$

$$
\begin{aligned}
\Rightarrow y_{Ni} &= \frac{C_0^B - C_{Ni_3B}^B}{C_{Ni}^B - C_{Ni_3B}^B} \\
&= 1 - \frac{C_0^B}{C_{Ni_3B}^B}
\end{aligned} \tag{12.4}
$$

where C_0^B is the average atomic concentration of boron in the material and $C_{Ni_3B}^B$ is the concentration of boron in the nickel boride: 25 at.%.

Using equations 12.3, 12.4 and replacing $\Delta G_f^{Ni}(T)$ by its value, equation 12.2 can be simplified to :

$$\Delta G_f^c(T) \ = \ \frac{C_0^B}{25} \cdot (\Delta G^{Ni_3B}(T) - 3\Delta G^{Ni}(T) - \Delta G^B(T)) \tag{12.5}$$

12.2.2 Gibbs free energy difference between the amorphous and crystalline phase.

It is very difficult to obtain a free energy of formation for an amorphous phase. However, the difference between free energies of the amorphous and crystallized (coarse grained) states of a material is more easily calculated. This difference, $\Delta G^a(T) = \Delta G_f^a(T) - \Delta G_f^c(T)$ is calculated as follow:

$$\begin{aligned}
\Delta G^a(T) \quad &= \Delta H^a(T) && -T \cdot \Delta S^a(T) \\
&= \Delta H_m - \int_T^{T_m} \left[C_p^a(T) - C_p^c(T) \right] dT && -T \cdot \left[\Delta S_m - \int_T^{T_m} \left[C_p^a(T) - C_p^c(T) \right] dlnT \right]
\end{aligned}$$

(12.6)

where ΔH_m is the melting enthalpy, $\Delta S_m = \frac{\Delta H_m}{T_m}$ is the entropy of melting, T_m is the melting temperature, $C_p^a(T)$ and $C_p^c(T)$ are the heat capacities of the amorphous and crystalline phases respectively.

The heat capacity variation between amorphous and crystalline phases $\Delta C_p(T) = C_p^a(T) - C_p^c(T)$ has been the focus of several studies [155, 156], which have given way to various expressions for $\Delta C_p(T)$:

- The simplest (and also the first) was proposed by Turnbull [157]: $\Delta C_p = 0$;

- Jones and Chadwick [158] used : $\Delta C_p(T) = \Delta C_p(T_m)$;

- Thompson and Spaepen [159] proposed :$\Delta C_p(T) = \frac{\Delta H_m}{T_m}$;

- Battezatti and Garrone [160] recommend :$\Delta C_p(T) = 0.8 \cdot \frac{\Delta H_m}{T_m}$;

- Dubey and Ramachandrarao [161] proposed (based on the hole theory of liquids):
  $\Delta C_p(T) = \Delta C_p^m \left[\frac{2T^3 + 3T^2 \Delta T - \Delta T^3}{2T^3} \right]$;

Using Lu's comparison of results obtained with the various approximations of $\Delta C_p(T)$, we chose Thompson and Spaepaen's expression because it gives similar results to the more complicated ones without overcomplicating the calculations.

This lead to the following expression for the variation of Gibb's free energy between the amorphous and crystalline state :

$$\begin{aligned}
\Delta G^a(T) \quad &= \quad \Delta H_m - \int_T^{T_m} \Delta C_p dT - T \cdot \left[\Delta S_m - \int_T^{T_m} \Delta C_p dlnT \right] \\
&= \quad \Delta H_m - \int_T^{T_m} \frac{\Delta H_m}{T_m} dT - T \cdot \frac{\Delta H_m}{T_m} + T \cdot \int_T^{T_m} \frac{\Delta H_m}{T_m} dlnT \\
&= \quad \Delta H_m - (T_m - T)\frac{\Delta H_m}{T_m} - T\frac{\Delta H_m}{T_m} + T\frac{\Delta H_m}{T_m} \cdot ln\frac{T_m}{T} \\
&= \quad \Delta H_m \cdot \frac{T}{T_m} \cdot ln\frac{T_m}{T}
\end{aligned}$$

(12.7)

Equation 12.7 uses only the temperature (T), the melting temperature and enthalpy of metling (ΔH_m) to determine the free energy variation between the amorphous and crystalline (coarse grained) states.

12.2.3 Gibbs free energy of formation of the interfaces.

The determination of the thermodynamical properties of the grain boundaries in a nanocrystalline material must take into account the importance of those boundaries in the materials properties: nanocrystalline materials are considered to be made of a 'skeleton cluster of randomly oriented crystallites and a labyrinthine cluster containing highly disordered material (the grain boundaries)' [65]. The properties of the grain boundaries of such materials can be significantly different of the bulk properties: increase of specific heat, decrease of the bulk modulus, reduction of density, increase of the coefficient of linear thermal expansion,... [65, 162].

The highly disordered grain boundary phase on nanocrystalline (nc) metals can be described by a reduction of the number of nearest neighbors, expressed by an excess volume of the grain boundary (ΔV). This excess volume, which is the most significant parameter for the study of the thermodynamic properties of nc grain boundaries is expressed as:

$$\Delta V = \frac{V}{V_0} - 1 \tag{12.8}$$

where V_0 is the volume of the perfect crystal and V is the volume of the dilated crystal representing the grain boundary.

The dilated crystal used for calculation of nc grain boundaries has a perfect crystal structure but its nearest neighbor distance is increased (compared to the equilibrium atom-atom distance) in order to match the densities of the grain boundaries and the dilated crystal [65]. The calculation of the dilated crystal can then be carried out either using equation of state [86, 162] or a central force model in the quasi-harmonic Debye approximation [65, 86], or by a combination of the two [67]. The developments leading to this calculation will be discussed in section 13.4.

12.3 Expression of thermodynamical equilibrium and extraction of the grain size.

Gibbs' free energy variation during crystallization of an amorphous material (into a nanaocrystalline material) is expressed by equation 12.1, page 221. The crystallization temperature determination happens at thermodynamical equilibrium, which can be expressed by $\Delta G(T) = 0$. Using this, equation 12.1 can be modified (using equation 10.1, 209) to show the dependence of the grain size to the temperature.

$$x_i = \frac{d^3 - (d - \delta)^3}{d^3} \tag{10.1}$$

$$0 = (\Delta G_f^c(T) - \Delta G_f^a(T)) - x_i \cdot (\Delta G_f^c(T) - \Delta G_f^i(T))$$

$$x_i \cdot (\Delta G_f^c(T) - \Delta G_f^i(T)) = (\Delta G_f^c(T) - \Delta G_f^a(T))$$

$$x_i = \frac{(\Delta G_f^c(T) - \Delta G_f^a(T))}{(\Delta G_f^c(T) - \Delta G_f^i(T))}$$

$$\frac{d^3 - (d - \delta)^3}{d^3} = \frac{(\Delta G_f^c(T) - \Delta G_f^a(T))}{(\Delta G_f^c(T) - \Delta G_f^i(T))}$$

$$d^3 - (d - \delta)^3 = d^3 \cdot \frac{(\Delta G_f^c(T) - \Delta G_f^a(T))}{(\Delta G_f^c(T) - \Delta G_f^i(T))} \tag{12.9}$$

To calculate the equilibrium grain size, equation 12.9 must be solved as a function of temperature. For this, the temperature dependence of the various $\Delta G(T)$ must be previously determined. $\Delta G_f^c(T)$ has been described in section 12.2.1 and $\Delta G^a(T)$ in section 12.2.2. The free energy of the interfaces is obtained from the dilated crystal model, and will be developed in section 13.4.

13. MODELING OF THE CRYSTALLIZATION TEMPERATURE OF ELECTROLESS NICKEL-BORON: DATA COLLECTION, CALCULATIONS, PREPARATION OF THE IMPLEMENTATION, LIMITATIONS.

13.1   Introduction.

Now that the theoretical background for the modeling of the crystallization temperature has been set, a more in depth study of some of the various expressions and parameters needed will be carried out and strategies for the running of the model and for collection of the useful data will be described.

The first section of this chapter will be dedicated to the adaptation of the diffusion-based grain growth law for use in an anisothermal context. Then, the expression of the Gibbs' free energy variation will be modified to include the assumption that the material is already nanocrystalline in the initial state. The next section will be focused on the description of the calculations needed to obtain the Gibbs free energy of the grain boundaries using the dilated crystal model.

After this in depth exploration of the mode complex parts of the modeling, a flow sheet for the modeling procedure and recapitulatory equations will be presented, before the data actually needed for the modeling are listed and their values or strategies to obtain them are presented.

13.2   Anisothermal diffusion law for grain growth.

The usual diffusion-based law for grain growth in isothermal regimen is (equation 10.4):

$$d^2 = d^{*2} \, + \, 8 \cdot \xi \cdot D \cdot t$$

This equation can be modified for use in anisothermal conditions (continuous heating at constant heating rate) if the heating ramp is considered as a succession of very short isothermal steps (of duration Δt) between the initial temperature (T_0) and a given temperature T ($= T_0 + \beta \cdot \Delta T$, β being the heating rate). The anisothermal growth can thus be expressed as [86]:

$$d^2 \;=\; d^{*2} \;+\; \sum_{0}^{\frac{(T-T_0)}{\beta}} 8 \cdot \xi \cdot D_0 \cdot exp(-\frac{Q}{R(T_0 + i \cdot \beta \cdot T)})$$

$$d \;=\; d^* + 2 \cdot \sum_{0}^{\frac{(T-T_0)}{\beta}} \sqrt{2 \cdot \xi \cdot D_0 \cdot exp(-\frac{Q}{R(T_0 + i \cdot \beta \cdot T)})} \qquad (13.1)$$

where d is the grain diameter, d^* is the initial grain diameter, D_0 and Q are the diffusion constant and the activation energy of diffusion, R is the gas constant and i is the iteration number. ξ is a coefficient depending of the boron concentration, that is expressed in our case by:

$$\xi = 0.5. \left| 1 - \frac{C_0}{19} \right| \qquad (13.2)$$

In equation 13.2, C_0 is the atomic concentration of boron in the alloy. This expression was chosen in order to have a linear evolution of the function on either side of the eutectic point between Ni and Ni_3B (that is situated at 19 at.% B), where the function is null.

13.3 Modifications of the expression of Gibbs free energy variation during crystallization to take into account the nanocrystalline initial state.

As was said in section 10.3.2.2, the model developed by Jiaqiang [86] is based on the assumaption that the material is amorphous in the initial state. However, our experimental results (see section 8.4.2, page 142 in part II) have shown that as-desposited electroless nickel-boron coatings are constituted of nanocrystalline nickel. Moreover, this initial nanocrystalline state is in good agreement with the diffusion-based part of the model that needs an initial grain size to calculate the grain growth. For this reason, we chose to modify the thermodynamic part of the model to take into account the nanocrystalline nature of as-deposited electroless nickel-boron. The transformations observed in the material (see equation 10.7) can thus be expressed as:

$$\text{Initial state} \quad \rightarrow \quad \text{final state} \qquad (13.3)$$
$$\text{Ni nc} + \text{ interfaces} \quad \rightarrow \quad \text{Ni nc} + \text{ Ni compounds} + \text{ interfaces}$$
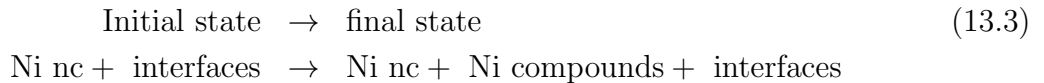
Equation 10.7 is thus modified and leads to :

$$\Delta G(T) \;=\; (1 - x_i)\, \Delta G_f^c(T) \;+\; x_i \Delta G_f^i(T) - \left[(1 - x_i^*)\Delta G_f^{c_i}(T) \;+\; x_i^* \Delta G_f^i(T) \right] \quad (13.4)$$

where x_i^* is the initial grain boundaries fraction, that can be calculated from the initial grain size.

The use of equation 13.4 needs a precise definition of the initial and final states of the material.

- In the final state, the crystalline part is constituted of Nickel and Nickel boride (Ni$_3$B) in proportions defined by equations 12.2 and 12.4.

- In the initial state, the crystalline part is considered to be constituted only of Ni, following the work of Hentschel [80] and Farber [81].

- In the initial state, the definition of the interfaces will be based on the work of Hentschel [80] and Farber [81]: as most of the boron appears to be located in the interfaces of the as-deposited material, with a boron content that we calculated as 20 wt.% (see section 11.2.2.3, page 214), it is not really realistic to use the cfc nickel structure as basis for the dilated crystal representing those interfaces. However, their composition being closer to that of Ni$_3$B (25 wt.% B), that structure can be used to describe the as-deposited interfaces.

- For the description of the interfaces in the final state, the assumption will be made that they are similar to the as-deposited interfaces, meaning they are based on the Ni$_3$B structure.

So, in the calculation of $\Delta G_f^{c_i}(T)$ (the Gibbs energy of formation of the crystalline phase in the initial state), only Ni must be computed as the Ni$_3$B phase is not supposed to be present in as-deposited NiB coatings. Equation 13.4 can thus be simplified (knowing $\Delta G_f^{c_i}(T) = \Delta G_f^{Ni}(T) = 0$) as follow:

$$\Delta G(T) \;=\; (1 - x_i)\,\Delta G_f^c(T) \;+\; x_i \Delta G_f^i(T) -\; x_i^* \Delta G_f^i(T) \tag{13.5}$$

Those modifications induce changes in the determination of the grain size dependence on the temperature and equation 12.9 (see section 12.3, page 224) becomes:

$$d^3 - (d - \delta)^3 = d^3 \cdot \frac{(\Delta G_f^c(T) -\; x_i^* \Delta G_f^i(T))}{(\Delta G_f^c(T) -\; \Delta G_f^i(T))} \tag{13.6}$$

Equation 13.6 does not require the calculation of the free energy variation between the amorphous and crystalline state. However, it needs an accurate determination of the Gibbs' free energy of the grain boundaries (interfaces) in both states. This calculation will be based int the assumption presented hereover that the interfaces are represented by a dilated crystal of nickel boride Ni$_3$B.

13.4 Towards determination of the Gibbs free energy of the interfaces [65, 67, 162].

As was said in section 12.2.3, determination the Gibbs free energy of the interfaces is based on a dilated crystal model where the interfaces are represented by a perfect crystal with an enhanced nearest-neighbor distance, in such a way that the densities of the interface and dilated crystal match. The calculation of the thermodynamic properties of the dilated crystal is based on either the equation of state [86, 162] or a central force model in the quasi-harmonic Debye approximation [65, 86], or on a combination of the two [67]. The developments presented hereunder are based on the mixed approach proposed by Song et al. [67].

The equation of state (EOS) can be expressed as a function of volume and temperature [162] that leads to the following expressions for the thermodynamic properties (as functions of the excess volume of the grain boundary):

$$\Delta H(V) = E(V) + PV \tag{13.7}$$

$$\Delta S(V) = C_v \cdot \gamma \cdot ln\frac{V}{V_0} \tag{13.8}$$

$$\Delta G(V,T) = \Delta H(V) + C_v \cdot \Delta T - T\left[\Delta S(V) + C_v \cdot ln\Delta T\right] \tag{13.9}$$

Equation 13.9 is obtained from equations 13.7 and 13.8, with the addition of the terms expressing the temperature dependence of the Gibbs free energy.

Some of the terms used in equations 13.7, 13.8 and 13.9 are quite explicit. Some others however need further description:

- V_0 is the atomic volume of the perfect crystal and V is the atomic volume of the dilated crystal;

- $\Delta T = T - T_R$, with T_R the reference temperature for the thermodynamic calculations;

- C_v is the specific-heat capacity at constant volume and can be calculated, using the quasi-harmonic Debye approximation, as follow:

$$C_v = 3R\left[12(\frac{T}{\theta})^3 \int_0^{\frac{\Theta}{T}} \frac{x^3}{e^x - 1}dx - \frac{3(\frac{\Theta}{T})}{e^{\frac{\Theta}{T}} - 1}\right] \tag{13.10}$$

where R is the gas constant and Θ the Debye temperature of the dilated crystal, which can be expressed, as a function of the excess volume, as:

$$\Theta(\Delta V) = \Theta_0\left\{2\,exp\left[-4\gamma_0\left((1 + \Delta V)^{1/3} - 1\right)\right] - exp\left[-2\gamma_0\left((1 + \Delta V)^{1/3} - 1\right)\right]\right\} \tag{13.11}$$

In equation 13.11, Θ_0 is the Debye temperature of the perfect crystal in the equilibrium state and γ_0 is the Grüneisen parameter of the perfect crystal in the equilibrium state ($\gamma = \frac{V}{C_v}(\frac{\delta P}{\delta T})_V$) [163].

- $E(V)$ is the binding energy of atoms at the nanograin boundaries. It can be expressed as:

$$E = E_0 \cdot E^*(a^*) \tag{13.12}$$

In equation 13.12, E_0 is the binding energy of atoms at the equilibrium state and $E^*(a^*)$ is an universal function [164] expressed as

$$E^*(a^*) = (-1 - a^* - 0.05a^{*3})e^{-a^*} \tag{13.13}$$

$$\text{with} \qquad a^* = \frac{r_b - r_0}{l} \tag{13.14}$$

in which r_0 and r_b are the interatomic distances respectively at equilibrium and in the dilated crystal representing the grain boundary and l is a scaling length characteristic of the metal.

- P is a negative pressure developped at the grain boundaries as a result of the diminution of the grain size. It can be expressed (as a function of atomic volume of the boundaries (V) and temperatures) as [165]:

$$P(V,T) = \frac{3B_0}{(V/V_0)^{2/3}}(1-(V/V_0)^{1/3})exp\left[\eta_0(1 - (V/V_0)^{1/3})\right] + \alpha_0 B_0(T - T_R) \tag{13.15}$$

where α_0 is the zero-pressure bulk expansion coefficient, B_0 is the bulk modulus at T_R and $\eta_0(= 3/2[(\delta B/\delta P)_{P=0} - 1])$ is a function of the derivative of the Bulk modulus (B) with respect to the pressure.

- γ is the Grüneisen parameter of the dilated crystal (representing the grain boundaries), expressed as [67]:

$$\gamma = -1 - \frac{V_b}{2}\left[\frac{\delta^2 P/\delta V_b^2 - 10P/9V_b^2}{\delta P/\delta V_b + 2P/3V_b}\right] \tag{13.16}$$

Using those expressions, it is possible to obtain a value of the Gibbs free energy of the interfaces in the nanocrystalline material. However, for this, numerical values of several parameters are needed. The way to obtain those values will be discussed in section 13.6. The Gibbs free energy of the interfaces can then be used in the thermodynamic part of the model.

13.5 Flow sheet and equations for the modeling of crystallization temperature.

Now that all of the expressions have been described, the modeling flow sheet can be constituted. It is quite simple if the calculations needed for the determination of the Gibbs free energy of grain boundaries are not developed, as shown on figure 13.1: determination of the initial grain size is a prerequisite for both parts of the model; the Gibbs free energy of the interfaces and crystallites must also be pre-calculated; both expressions of the grain size dependence on the temperature can then be written and compared to obtain the crystallization temperature.
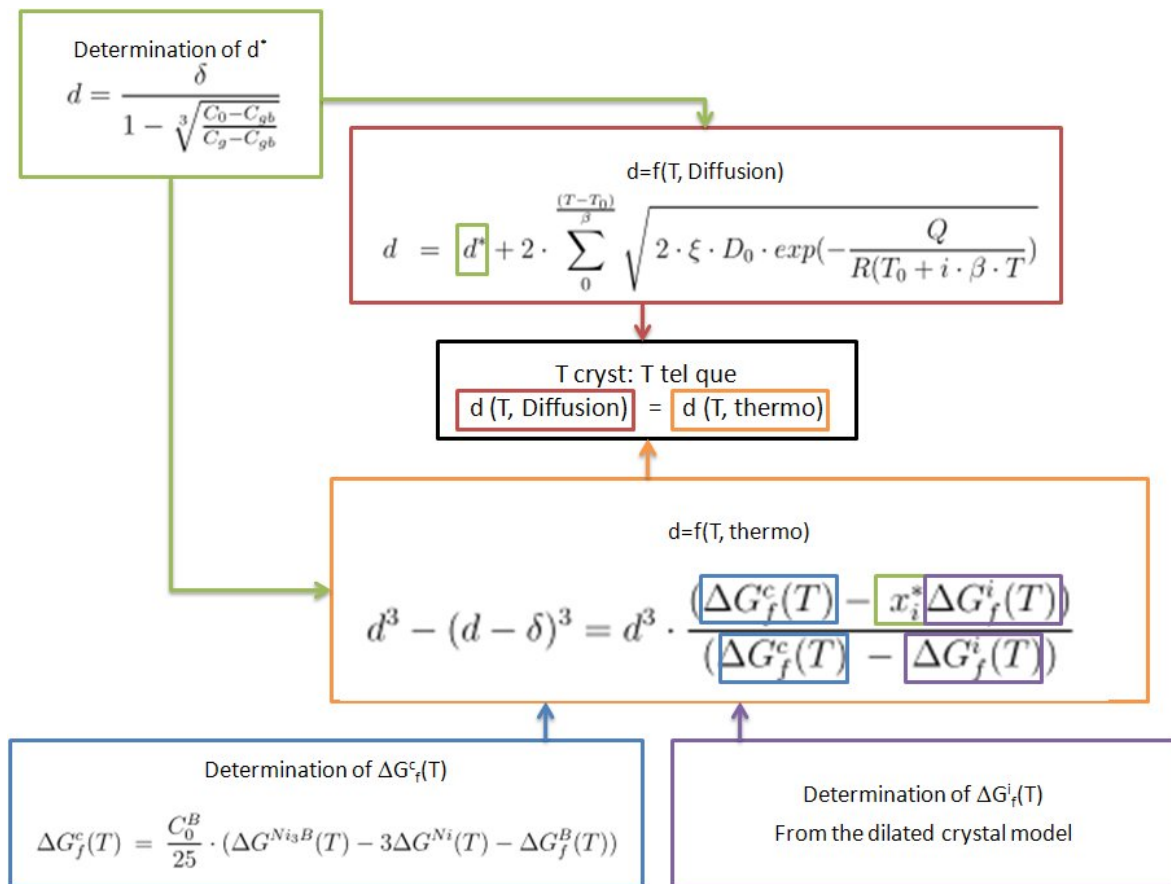
Fig. 13.1: flow sheet for the implementation of the modeling of crystallization temperature.

13.6   Data listing and strategies for their determination.

Several thermodynamical, chemical and other data are needed for the numerical calculation of the crystallization temperature. Some of them are readily available in tables or published experimental results. Others will need to be either measured or calculated. In this section, all the data needed for the modeling are listed, with the values that will be used, if they are available or, in they are not, with strategies to obtain numerical values.

First are the data needed for the diffusion-based part of the model:

- C_B is the composition of the alloy (variable parameter);

- d* is the initial crystallite size, that is calculated from equation 10.3, page 210;

- β is the heating rate(K/s), that is a variable parameter of the model;

- R is the gas constant (8.31 J mol^{-1}K^{-1});

- D_0 and Q are the diffusion constant and the activation energy of diffusion for boron in nickel: Q = 110 $\pm$ 2 kJ/mol and D_0 = 2,3.10^{-9} cm^2/s [166]

- T_0 is the initial temperature (variable parameter);

- T is the final temperature (variable parameter);

- Δt is the time increment (variable parameter);

The data needed for the thermodynamic-based part of the model are listed hereunder:

- C_B is the composition of the alloy (variable parameter);

- x_i^* is the initial grain boundary fraction, that can be determined from d* (using equation 10.3, page 210);

- $\Delta G^{Ni}(T)$ is the Gibbs free energy of nickel. It can be calculated from the thermodynamic data of the JANAF thermochemical tables [167]: the standard entropy of crystalline nickel at 298.15K is 29.87 $\pm$ 0.21 J K^{-1} mol^{-1}. The value of C_p° is given for various temperatures in the JANAF tables.

- $\Delta G^B(T)$ is the Gibbs free energy of boron that can also be calculated from the thermodynamic data of the JANAF thermochemical tables [167]: the standard entropy of crystalline boron at 298.15K is 5.83 $\pm$ 0.08 J K^{-1} mol^{-1}. The value of C_p° is given for various temperatures in the JANAF tables.

- $\Delta G^{Ni_3B}(T)$ is the Gibbs free energy of nickel boride. Contrary to pure nickel and boron, its properties are not listed in the JANAF thermochemical data tables. However, values can be found in a number of published papers:

– Yamamoto et al. [168] proposed the following expression for the Gibbs free energy of **formation** of Ni_3B :
$\Delta G_f^{Ni_3B}(T)(J \cdot mol^{-1}) = -124800 + 23.1 \cdot T(K) \pm 300$ in the temperature range 1198-1298K.

– Ushio et al. [169] proposed (for the Gibbs free energy of **formation** of Ni_3B)
$\Delta G_f^{Ni_3B}(T)(J \cdot mol^{-1}) = -132720 + 44.18 \cdot T(K) \pm 300$ in the temperature range 800- 1225K.

– Teppo et al. [170] provide values for the thermodynamic properties of **formation** of Ni_3B:
$\Delta H_f^{Ni_3B}(298K) = -30457.24 \ J \cdot mol^{-1}$,
$\Delta S_f^{Ni_3B}(298K) = -7.89166 \ J \cdot mol^{-1}K^{-1}$ and
$S°Ni_3B(298K)(15.92995 \ J \cdot mol^{-1}K^{-1})$.

– Moiseev et al. [171] give, apart from the enthalpy and entropy of Ni_3B, an expression for the temperature dependence of the specific heat:
$\Delta H^{Ni_3B}(298K) = -98920 \ J \cdot mol^{-1}$,
$S°Ni_3B(298K) = 62.86 \ J \cdot mol^{-1}K^{-1}$,
$C_p^{Ni_3B} = 87.50 + 28.64 \cdot 10^{-3} \cdot T - 22.04 \cdot 10^3 \cdot T^{-2}(J \cdot mol^{-1}K^{-1})$.

- δ is the thickness of the interfaces in the nanocrystalline material. It has already been discussed at lenghts in section 11.2.2.1, page 213 and the chosen value is 0.8nm.

- V_0 is the atomic volume of the perfect crystal. As all the grain boundaries will be assimilated to the Ni_3B phase (or obvious composition reason), the value for Ni_3B is needed. It can be obtained from the lattice parameters given by Teppo et al. [170]: Ni_3B has an orthorombic structure (similar to Fe_3C) with a = 0.5211 nm, b = 0.6617 nm and c = 0.4390 nm. Shein et al. [172] used first principle calculation to obtain V_0 for various compounds. They propose a value of 151.55 $Å^3$ for Ni_3B.

- V is the atomic volume of the dilated crystal. It is closely related to the excess volume. As it is difficult to evaluate either of those parameters, they will be considered as variables of the model.

- R is the gas constant (8.31 J mol^{-1}K^{-1});

- Θ_0 is the Debye temperature of the perfect crystal (Ni_3B) in the equilibrium state. Values of this parameter are given by Smolin et al. [173] for the average parameter: 244K. Finch et al. [174] detected anisotropy of the Debye temperature obtained from resistivity measurements and obtained values of 194 for the [100] plane, 312 for the [010] and 330 for the [001]. We will use Smolin's value.

- γ_0 is the Grüneisen parameter of the perfect crystal (Ni_3B) in the equilibrium state. It can be obtained from the following expression : $\gamma = \frac{V}{C_v}(\frac{\delta P}{\delta T})_V$ [163]. Bibliographic research has not lead to numerical data for this parameter yet.

- C_v is the constant volume heat capacity of Ni$_3$B. It can be evaluated, in first approximation, by the constant pressure heat capacity (C_p) that is calculated from Moiseev et al. [171]. However, for more accurate calculations, C_v can be calculated from thermodynamic data, as follow:

$$C_v = C_p + 9BV\alpha_L^2 T \qquad (13.17)$$

where α_L is the linear thermal expansion coefficient.

- α_0 is the zero-pressure bulk thermal expansion coefficient. It can be approximated by experimental values of the thermal expansion coefficient, such as those given by Smolin et al. [173]: $7.9 \ 10^{-6}$ K^{-1}, or by the values determined by Finch et al. [174], taking into account the anisotropy (see figure 13.2).
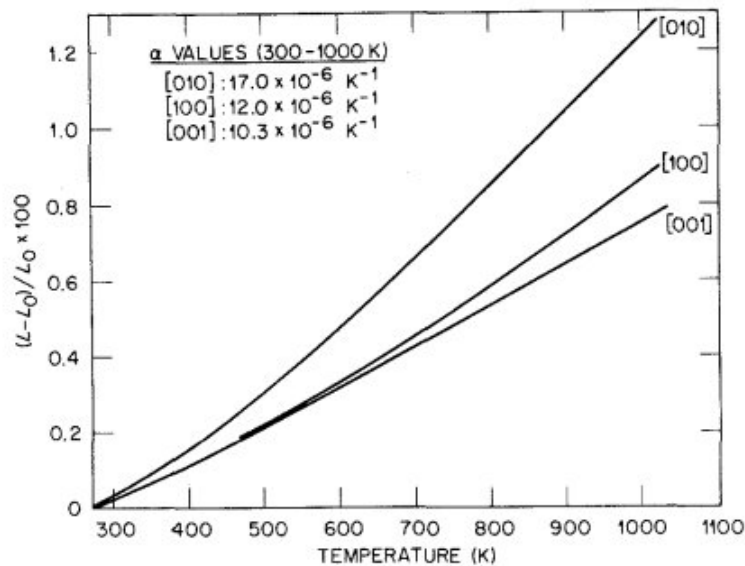
Fig. 13.2: Thermal expansion of Ni3B in the temperature range 300 to 1000 K for the [010], [100], and [001] directions [174].

- B_0 is the bulk modulus of Ni$_3$B that can be calculated from Young's modulus (E) and Poisson's ratio (ν) as follow:

$$B = \frac{E}{3(1-2\nu)} \qquad (13.18)$$

Values of those parameters could be found in the literature:

  - Smolin et al. [173] use a value of $16.7 \ 10^{10}$ N/m^2.
  - Fich et al [174], give values that take anisotropy into account:
    E[100] = 151 ; E[010] = 166 ; E[001] = 182 GPa
    $\nu_{32} = 0.249$; $\nu_{31} = 0.395$; $\nu_{21} = 0.404$

- E_0 is the binding energy of atoms at the equilibrium state in Ni_3B. It can be obtained from first priciples calculations or from XPS experimental measures.
  Deshpande et al. [175] obtained a value close to 3eV for the binding energy of atoms in Ni_3B.
  Other researchers measured the binding state of Ni and B in Ni_3B but they did not calculate the binding energy of the material [100, 176, 177].

13.7 Conclusion.

The equations and procedure needed for the modeling have now been all described and the data needed to run the numerical processing have been listed. It was possible to obtain values for most of them, but not all: the Grüneisen parameter of $Ni_3 B$, for example will be difficult to determine using the expression that was given hereover.

14. COLLECTION OF EXPERIMENTAL DATA FOR MODEL VALIDATION.

14.1   Introduction.

While the theoretical research, implementation and collection of data are the most important part of the modeling work, it would not be complete without validation from experimental data. The object of this chapter is not to enumerate experimental results intended for validation but it is to briefly present the experimental procedures that will be undertaken to obtain the pre-cited results and to list some published data that could be used to confirm our results.

14.2   Experimental procedures and example of obtained data.

The determination of the crystallization temperature of electroless coatings can be carried out by various techniques, such as dilatometry, differential scanning calorimetry and in-situ high temperature X-ray diffraction. For the present study, two techniques will be used conjointly: X-ray diffraction and differential scanning calorimetry (DSC).

DSC was chosen because it can be used with (very) small amounts of material, which is perfectly adapted to electroless coatings. Moreover, if the substrate is well chosen (and do not present phase transformations in the investigated temperature range), the coating need not be peeled off, which makes the experiment easier to prepare. However, DSC, used by itself, only allow to detect the temperature at which transformations are occurring, not the type of transformation that is happening. For this reason, the experiments will be completed by in situ high temperature X-ray diffraction to identify the transformations observed by DSC. X-ray diffraction could not be used by itself because the measures are not recorded during continuous heating of the material but during successive heating steps.

14.2.1   Example of high temperature X-ray diffraction results.

A coating with approximatively 5 wt.% B was submitted to high temperature X-ray diffraction, in the conditions that were described in section 9.4.1 of part II (see figure 9.6, page 178). However, as the focus of this experiment is to detect the crystallization temperature and not to identify the phases that are formed, the experiment was only carried out between 250 ℃ (the higher temperature where the pattern is unmodified) and 300 ℃(the lower temperature where a modified pattern was observed).

As can be seen on figure 14.1, the very first modification is observed after heating at 270 ℃ but it is not very important. The pattern recorded at 280 ℃ shows that the transformation is nearly completed already as heating at higher temperature does not induce important further modifications. This experiment allowed to approximate the crystallization temperature of the sample. It is close to 270 ℃. The DSC results can then be used to obtain more accurate data.
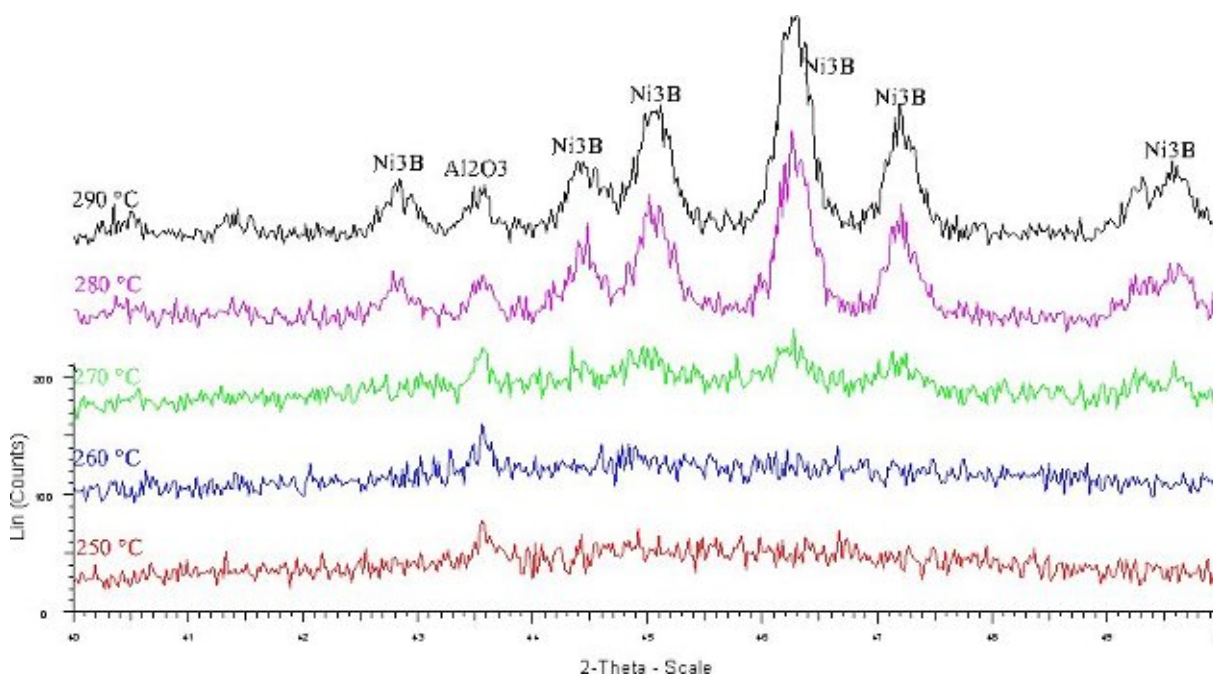
Fig. 14.1: High temperature X-ray diffraction patterns of electroless nickel-boron coating (250-290 ℃).

14.2.2 Use of differential scanning calorimetry for the determination of the crystallization temperature.

Differential scanning calorimetry was be used to complete and precise the results of high temperature X-ray diffraction: after the temperature range in which the formation of Ni_3B occurs had been roughly delimited, the precise temperature of the beginning of the transformation was be detected from the DSC trace. The experiment was carried out with an heating rate of 5 ℃/min. As this technique was only used to detect the onset temperature of the transformation, the experiments have been carried out on coated specimens (the substrate was not dissolved), without weighing of the sample.

As shown on figure 14.2, the onset temperature found for both tested coatings are very close. Values of 289℃ were obtained after extrapolation of the onset temperature for both samples (which have a boron content close to 5 wt%). It is not surprising that the crystallization temperature determined by DSC is slightly higher than the value from high temperature X-ray diffraction: the present experiment was carried out under continuous

heating while the conditions of the XRD experiment were close to isothermal heating and the settling time was rather long (10 minutes).
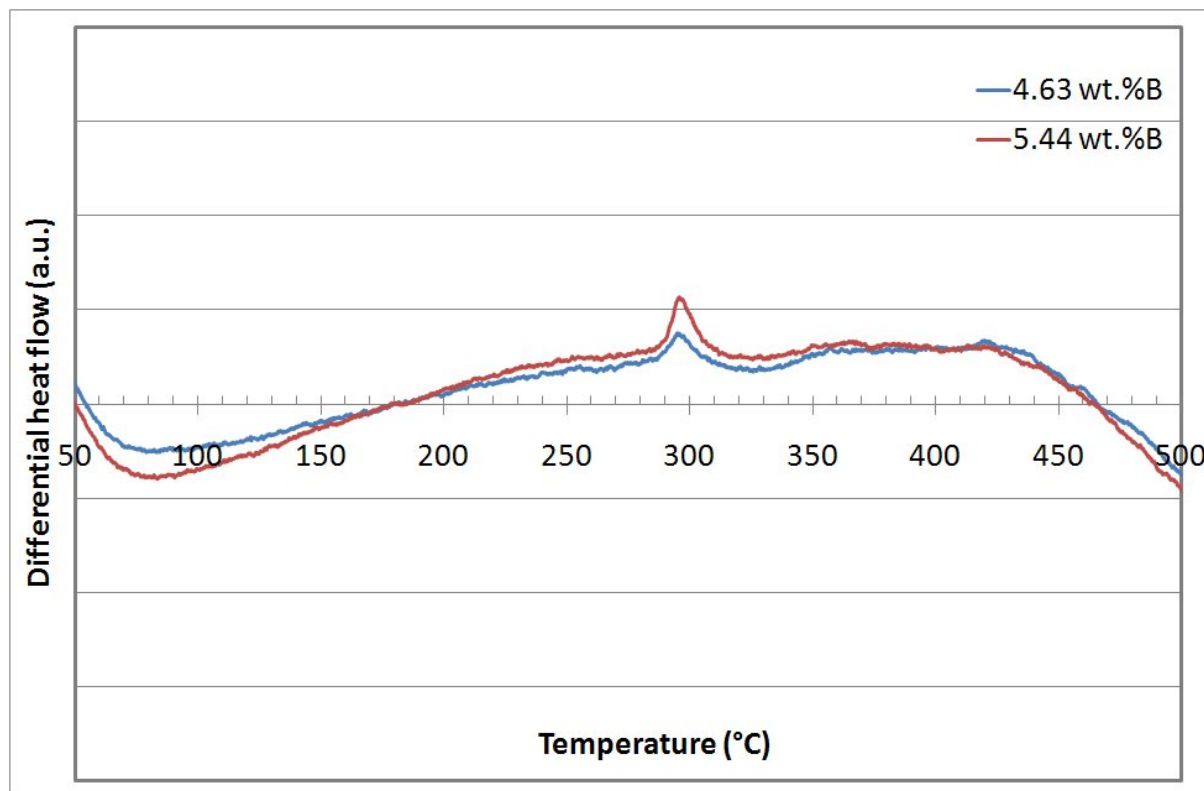
Fig. 14.2: DSC trace of electroless nickel-boron samples.

Comparison with published results was difficult because there are not a lot of published data for both the composition and heating rate we used. However, Lee et al. [70] found a similar value in the same conditions for a coating with slightly less boron than ours (see table 14.1).

14.3   Published data that can be used for model validation.

A number of authors have carried out DSC studies on electroless nickel-boron coatings, that could be useful for the validation of our model: at the present time, we are only able to synthesize electroless nickel-boron alloys with a boron content close to 5 wt.%. We are thus not able to obtain experimental data outside of this composition range yet. The use of published data proposed by other researcher will allow us to expend the composition range for the validation of the model and thus to increase its accuracy.

The published data we found are shown in table 14.1 and figure 14.3. Some of those published data were already presented in section 3.2 of part I (page 44).

Heating rate (℃/min)	B content (wt.%)	Crystallization temperature (℃)	Notes
Lee et al. [70]			
5	0.374	370	electrodeposited Ni-B
5	1.16	363	electrodeposited Ni-B
5	1.78	292	electrodeposited Ni-B
5	2.25	290	electrodeposited Ni-B
Gaevskaya et al. [71]			
10	1.16	348	electrodeposited Ni-B
10	2.45	336	electrodeposited Ni-B
10	3.88	318	electrodeposited Ni-B
10	7.31	415	electrodeposited Ni-B
Anik et al. [39]			
10	6	319.47	Stabilized with Tl compound
Contreras et al. [98]			
10	8.34	312.9	bath using sodium acetate
Li et al. [101]			
10	0.92	332.45	nanoparticules obtained by drippping
10	8.21	361.55	nanoparticules obtained by drippping
Baskaran et al. [40]			
20	1.2	299.64	Stabilized with Tl compound
20	2	301.16	Stabilized with Tl compound
20	2.6	298.53	Stabilized with Tl compound

Tab. 14.1: DSC results from various sources.

The crystallization temperatures obtained by DSC are generally higher than the predicted temperature we measured by X-ray diffraction. This is not surprising because, in the 'step-process' used in the last case, a settling time of 10 minutes is observed at each temperature before the measure, meaning that the transformation may be observed even when it is very slow.

Moreover, the data hereover were obtained by various groups on materials synthesized in different ways: some were electrodeposited [70, 71], some were electroless coatings with various stabilizing agents [39, 40, 98] and some were even obtained in powder form [101]. Those differences in the synthesis route may induce differences in crystallization temperature: for example, while it is possible to ignore the presence of lead into electroless coatings as it amounts generally to less than 1 wt.%, the same cannot be said about thallium stabilized coatings which can contain up to 6 wt.% Tl. The presence of such a large amount of an alloying element must modify strongly (but in a not yet known way) the phases stability in the material and thus the crystallization temperature. For this
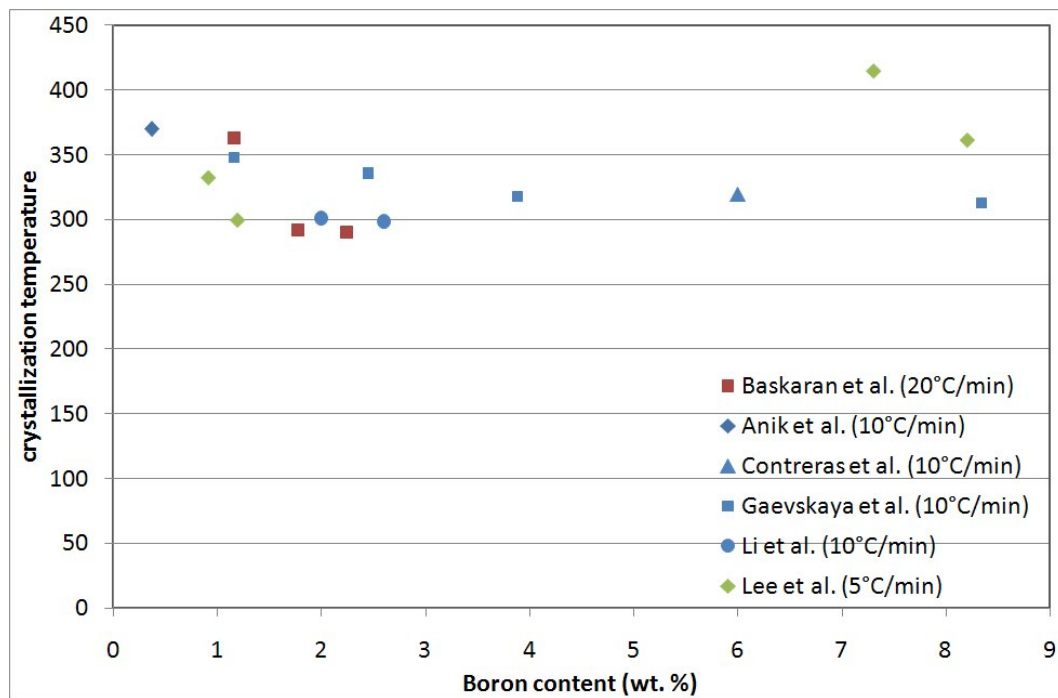
Fig. 14.3: DSC results from various sources [39, 40, 70, 71, 98, 101].

reason, while the results we found in published data cover a wide range of composition, it is indispensable to obtain other results (ideally from coatings that were all synthesized in very similar conditions) for the validation of the model.

CONCLUSION.

The modeling part of this work has multiple aims: first, the description, implementation and validation of a model allowing to predetermine grain size in electroless nickel-boron coatings from their composition; secondly, the creation of a predictive analytical model for the crystallization temperature of the pre-cited coatings.

The grain size modeling was based on geometric assumptions about the nanocrystalline nature of electroless coatings. It was possible to obtain a working model that has then been validated by our own experimental data as well as published values. This validation process is however not finished yet: for lack of data concerning electroless nickel-boron coatings, the published values that were used were obtained from electrodeposited coatings, which may have different properties. The next step will thus be to obtain data from a wider composition range of electroless nickel-boron deposits.

On the front of the crystallization temperature modeling, very important steps were made during this study: firstly, the theoretical bases were set (and, when needed, modified to suit our means) and the general equations of the model were established and put together in a flow sheet. Those equations were then developed in a way to show the ensemble of the data that are needed and numerical values of those data (or, if they were not available, ways to obtain them) were given. Finally, the experimental validation of the model was started.

The modeling of the crystallization temperature is however far from finished as some data are not yet available and will have to be either calculated or measured experimentally. Moreover, the practical implementation of the model calculation has yet to be carried out. Lastly, the published data that were found for the model validation will have to be supplemented by our own experimental results.

GENERAL CONCLUSION AND PERSPECTIVES.

GENERAL CONCLUSION AND PERSPECTIVES.

Electroless nickel-boron deposits have been used successfully for various industrial applications for some years now. One should thus expect that every aspect of their making, properties and comportment has been studied and understood by the plating community. Surprisingly, this is not the case and many phenomena occurring during their synthesis or their heat treatments, as well as the reasons for some of their properties, stay mysterious, even for people that have worked for many years with those materials.

This is not really surprising: the technique was introduced some years after a similar, but cheaper, process (electroless nickel-phosphorous) had been developed, and the plating community did not put great interest in the study of nickel-boron, often considering it as a sub-class of nickel-phosphorous plating. Nowadays, the majority of the research about electroless plating is still focused on the latter. Moreover, electroless processes are often studied in a purely applied point of view, keeping only in mind the need for an efficient and cost-limited deposition bath, leading to coatings whose properties are in adequation with their prospective applications. Knowing the delicate nature of the catalytic process and the diversity of bath compositions, this in itself can provide substance for years and years of research.

The aims of this work were not to add to the ever growing studies of bath compositions and the subsequent coatings properties: a reliable and efficient plating bath has been developed several years ago by Dr Delaunois and the properties of the synthesized coating are overall well known. We could then focus on the study of the formation of the coatings and their comportment during heat treatment, while ascertaining and completing the knowledge of their properties.

The study of reactive consumption during the plating, initially carried out in order to prepare bath replenishment, brought really interesting information about some mechanisms of the film formation, specifically about the rate limiting step of the process, which appears to be controlled by the diffusion of sodium borohydride towards the active surface. Surprisingly, knowing its very low concentration in the plating bath, diffusion did not play a role in the consumption of lead tungstate. It was also possible to prove adsorption of lead on the cell walls and to determine the amount of adsorbed lead. Another rather surprising piece of information allowed us to link the bath load to the composition of the deposited films.

The initial goal of the reactive consumption study was nevertheless attained and a semi-predetermined replenishment routine was implemented: the concentrations of reactive are checked each morning before heating of the bath to return to the nominal

composition and pre-calculated amounts are added regularly during plating operations. This routine, while rudimentary compared to industrial replenishment processes, was not too much time consuming (as our lab does not dispose of quick chemical analysis tools), proved satisfactory for our means and allowed the plating of 11 successive samples in a bath.

The second experimental study of this work was the observation of the initiation and growth of the coating during the plating. This was carried out ex-situ, by various techniques. The first noteworthy observation of this study is that the initiation of the deposit is nearly instantaneous, which is remarkable because the substrates were not subjected to catalytic activation. The effect of surface roughness on the speed of initiation and growth was also observed with great interest: a rougher substrate favors quick initiation of the deposit but leads to a slower spread of the coating.

During the observation of the coating formation, a link between the deposit morphology and the local lead content was established. However it was not actually possible to explain the reasons for the lead content fluctuations leading to that phenomenon.

The last part of the experimental study was the characterization of the coatings' properties and of the effect of heat treatments. The main chemical, structural and mechanical features of the coatings were investigated, as well as the wear and corrosion resistances of the deposits. The structural study, by XRD and TEM observations of cross sections, allowed to identify the nanocrystalline (and not, as often assumed, amorphous) nature of the as-deposited coatings and to determine an average grain size close to 1 nm. The good mechanical properties, scratch test resistance and wear resistance of as-deposited nickel boron were also shown, as well as its interesting corrosion resistance, that is similar to the best nickel-phosphorous coatings.

The modifications caused by heat treatments to the various properties of the coatings were also investigated. It was found that the heat treated coatings are more crystallized and the heat-treatment induced hardening and improvement of the wear resistance were confirmed. A better corrosion resistance was observed for heat treated coatings than for as-deposited ones, probably due to densification of the deposit during the heat treatment.

The very last part of the work was dedicated to the analytical modeling of the structural state of electroless nickel-boron deposits in the as-deposited state and after heat-treatment, with the aim to get a better understanding of the coating's comportment. It was possible, using geometric assumptions about the structure of nanocrystalline materials, to obtain a working model for the grain size in as-deposited electroless nickel-boron coatings, and to validate it with experimental results.

The other part of the modeling process however, is not as accomplished as the grain size predetermination: it is based on extensive thermodynamic calculations and some of the parameters, such as the Gruneisen parameter, are not readily available for nickel borides and will have to be calculated in order to run the model. The fundamental

relations and development of the modeling of crystallization temperature of electroless nickel-boron were however obtained and described, and preliminary data were collected for validation of this model.

While this project answered some really interesting questions about the formation and structure of electroless nickel-boron coatings, it was at the origin of a lot of new ones that arose during the course of our investigations. The reasons for the fluctuations of lead concentration across the coating, for one, are still mysterious, as are the phenomenon influencing the initiation speed on various substrates.

Many mechanisms of the formation and comportment of the coatings are also not yet identified and further study of those would be beneficial to the general knowledge of electroless processes. There is also a lot work still to be done as far as the understanding and modeling of heat treatments and crystallization of the coatings is concerned.

APPENDIX

A. APPARATUS AND CONDITIONS FOR COATING ANALYSIS.

A.1   X-ray diffraction.

X-ray diffraction was carried out in ambient conditions as well as at high temperature. The devices used for both experiments were different.

A.1.1   Room temperature X-ray diffraction.

The structure of the nickel-boron deposits was investigated by X-ray diffraction, with a Siemens D500 X-rays Θ Ű Θ apparatus using a copper source ($\lambda_{k\alpha} = 1.54\dot{A}$).

A.1.2   In situ high temperature X-ray diffraction.

Those tests were carried out in a Θ - Θ Bruker D8Advance diffractometer (see figure 9.5) equipped with a copper source ($\lambda_{k\alpha} = 1.54\dot{A}$). This spectrometer is fitted with an heating system (by radiations) and with a pumping system that allows testing under vacuum and/or controlled atmosphere. The sample is placed on a ceramic sample holder (in alumina, that was used to avoid creep deformation of the metallic sample during heating), that is put on two cooled pegs. The radiative heating system comes around the sample during the experiment. To limit the effects of sample expansion (due to heating) on the x-ray diffraction results, Göbel mirrors are used to obtain parallel incoming beams.

A.2   Scanning electron microscopy.

A Jeol JSM 5900 LV scanning electron microscopy (SEM) apparatus was used for the morphological characterization of the coatings, as well as for basic chemical analysis.

A.3   Microhardness testing.

The microhardness of the samples was measured with a LECO M-400-A hardness tester. A Vickers indenter was used to measure free surface hardness while a Knoop indenter was used to measure the hardness on polished cross-sections. Several loads (10, 25, 50, 100, 200, 500 g) were used and the holding time for the experiments was 15s.

A.4   Nanoindentation.

In a first phase, the nanoindentation tests were carried out using a MTS nano-indenter XP with a Berkovitch (tetrahedron shaped) indenter. The routine was a depth controlled indentation (300nm) of 5 columns with 10 indents each.

A second phase of testing was carried out using a Hysitron Inc. Triboindenter equipped with a scanning probe microscope. Those tests were carried out at a load of 4000μN.

A.5 Roughness testing.

Roughness measurements were carried out using a Zeiss 119 Surfcom 1400D-3DF apparatus, results analysis was carried out using the Zeiss brand software.

A.6 Glow discharge optical electron spectroscopy.

GDOES experiments were carried out using two separate Horiba-Jobin-Yvon apparatus. Qualitative analysis was carried out in the Horiba-Jobin-Yvon plant in Longjumeau (France) and quantitative analysis was carried out in the University of Udine (Italy).

A.7 X-ray photoelectron spectroscopy.

XPS analysis were carried out in a VG-ESCALAB 220iXL. The pressure in the chamber was typically 10^{-11} bar.

A.8 Experimental set up for the electrochemical tests.

As corrosions tests were carried out on the worn surface of samples submitted to Taber abrasion tests, the usual clamped devices could not be used: the surface is not perfectly plane and the watertightness of the device could not be guaranteed. Moreover, the worn zone is relatively small, which can cause problems with classical corrosion cell. For this reason, we used 'masking cells' in the form of a hollowed cylinder with a calibrated aperture on the top. The opening on the top has a surface of exactly 1 cm^2 and is placed on the interesting zone of the tested sample. The watertightness and fixation of the cell on the sample is ensured by silicone. Great care must be taken during the placement of the cell so that the sample surface is not contaminated by silicone and there is no possibility for cavernous corrosion at the sample-cell jointures.

A.9 Potentiodynamic polarization.

Corrosion behaviors were investigated using a Parstat 2273 potentiostat. The potentiodynamic polarization curves were measured in 0.1 M NaCl solution at room temperature in a three-electrode cell with an Ag, AgCl/KCl (sat'd) electrode as reference, a platinum grid as a counter electrode, the third electrode being the tested specimen. The coatings were masked so that only a 1 cm^2 area was exposed to the electrolyte. The anodic and cathodic polarization curves were measured by a dynamic potential scanning technique.The electrode potential was scanned from -600 to +250 mV at the rate of 10 mV min^{-1} after a settling time of 15 min to stabilize the open-circuit potential.

A.10   Electrochemical impedance spectroscopy.

Corrosion behaviors were investigated using a Parstat 2273 potentiostat. The potentiodynamic polarization curves were measured in 0.1 M NaCl solution at room temperature in a three-electrode cell with an Ag, AgCl/KCl (sat'd) electrode as reference, a platinum grid as a counter electrode, the third electrode being the tested specimen. The coatings were masked so that only a 1 cm^2 area was exposed to the electrolyte. EIS measurements were carried out in the frequency range 10^5 - 10^{-2} Hz, with a sinusoidal signal perturbation of 5 mV and 50 data points taken per interval. In order to minimize external interference on the system the electrochemical cell was placed in a Faraday cage.

A.11   Transmission electron microscopy.

A FEI Quanta 200 3D dual beam (combined SEM-FIB) apparatus was employed for the preparation of the thin sections. The TEM observation was carried out in a JEOL 2000FX electron microscope, operating at 200 kV.

A.12   Scratch testing.

Scratch tests were performed on selected samples using the continuous load increase method up to 30N with a load rate of 19.17N/min and an advance rate of 9.58mm/min, resulting in a scratch of 15mm. The tip was a diamond Rockwell C diamond stylus indenter with a radius of 200 μm. The instrument used was a Microphotonics Micro Scratch Tester (MST). After scratch test, the samples were examined by SEM.

A.13   Taber abrasion test.

The abrasion resistance of the coatings was determined using a Taber 5155 apparatus mounted with CS17 abrasive rubber wheels, under a weight of 1000 g at 72 rpm. The abrasive wheels were refaced every 1000 cycles, alternatively with SiC abrasive paper and with a wheel refacer apparatus (Taber brand).

A.14   Differential Scanning Calorimetry.

The onset point of the crystallization of the samples was investigated using a Setaram DSC-TG 92-16,18. The heating rate was set to 5 ℃/min. The experiments were carried out under argon flow.

LIST OF FIGURES

LIST OF TABLES

BIBLIOGRAPHY

[1] Bernard Etcheverry. *Adhérence, mécanique et tribologie des revêtements composites NiP – Talc multifonctionnels à empreinte écologique réduite.* PhD thesis, Institut National Polytechnique de Toulouse, 2006.

[2] Riedel A. *Electroless nickel plating.* Finishing Publication LTD., London, 1989.

[3] Brenner A. and G. E. Riddell. *J. Res. Nat Bur stand.*, 37:31–34, 1946.

[4] Bert J. Sherwood. Serendipity Produces a Radically New Plating Process: Electroless Nickel : Historical perspective on electroless nickel in its industrial infancy and the birth of one of the first job shops. *Metalfinishing*, 6:92–94, 2008.

[5] US Patent 2.461.661, 1945.

[6] Louis Lacourcelle. Nickelage chimique. volume M 1565 of *Techniques de l'ingénieur.* 1995.

[7] Fabienne Delaunois. *les dépôts chimiques de nickel-bore sur alliages d'aluminium.* PhD thesis, Faculté Polytechnique de Mons, 2002.

[8] F. Delaunois, J.P. Petitjean, M. Jacob-Dulière, and P. Liénard. Autocatalytic electroless nickel-boron plating on light alloys. *Surface and Coatings Technology*, 124: 201–209, 2000.

[9] I. Ohno. Electrochemistry of electroless plating. *Materials Science and Engineering*, A146:33–49, 1991.

[10] I. Ohno, O. Wakabayashi, and S. Haruyama. Anodic oxidation of reductants in electroless plating. *Journal of the electrochemical society*, 132:2323–2330, 1985.

[11] B. Veeraraghavan, H. Kim, and B. Popov. Optimization of electroless Ni–Zn–P deposition process:experimental study and mathematical modeling. *Electrochimica Acta*, 49:3143–3154, 2004.

[12] B. Thuillier. *Caractérisation structurale des contacts ohmiques réalisés à partir d'encres métalliques sur cellules photovoltaïques en sillicium multicristallin.* PhD thesis, Institut national des Sciences Appliquées de Lyon, 2001.

[13] D. Devilliers and M. Chemla. Cinétique électrochimique dans les systèmes inorganiques. volume COR 930 of *Techniques de l'ingénieur.* 1995.

[14] B Tremillon and G Durand. Électrochimie : lois régissant les processus. volume J 1604 of *Techniques de l'ingénieur.* 1995.

[15] Milan Paunovic. Electrochemical aspects of electroless nickel deposition. *Plating and Surface Finishing*, 70:62–66, 1983.

[16] Y.S. Huang, X.T. Zeng, I Annergen, and F.M. Liu. Development of electroless NiP-PTFE-SiC composite coating. *Surface and Coatings Technology*, 167:210–211, 2003.

[17] T.N. Khoperia. Investigation of the substrate activation mechanism and electroless NiP coating ductility and adhesion. *Microelectronic Engineering*, 69:391–398, 2003.

[18] Hiroshi Matsubara, Takehide Yonekawa, Yoshihiro Ishino, Nobuo Saito Hiroshi Nishiyama, and Yasunobu Inoue. Observation of initial deposition process of electroless nickel plating by quartz crystal microbalance method and microscopy. *Electrochimica Acta*, 47:4011–4018, 2002.

[19] Hiroshi Matsubara, Takehide Yonekawa, Yoshihiro Ishino, Nobuo Saito, Hiroshi Nishiyama, and Yasunobu Inoue. The observation of the nucleation and growth of electrolessly plated nickel deposited from different bath pH by TEM and QCM method. *Electrochimica Acta*, 52:402–407, 2006.

[20] Marlène Charbonnier, Maurice Romand, and Yves Goepfert. Ni direct electroless metallization of polymers by a new palladium-free process. *Surface and Coatings Technology*, 200:5028–5036, 2006.

[21] J.P. Elder and A. Hickling. Anodic behavior of the borohydride ion. *Transactions of the Faraday Society*, pages 1852–1864, 1962.

[22] D. W. Baudrand. Electroless nickel plating. In *Surface Engineering*, volume 5 of *ASM handbook online*. ASM international, 2002.

[23] C. Ricci. depôts autocatalytiques de nickel-bore sur acier inoxydable. Master's thesis, Faculté polytechnique de Mons, 1991.

[24] K. Hari Krishnan, S. John, K.N Srinivasan, J Praveen, M. Ganesan, and P.M. Kavimani. An overall aspect of electroless Ni-P depositions - a review article. *Metallurgical and materials transactions*, 37A:1917–1926, 2006.

[25] W.J. Cheong, Ben L. Luan, and David W. Shoesmith. The effects of stabilizers on the bath stability of electroless Ni deposition and the deposit. *Applied Surface Science*, 229:282–300, 2004.

[26] Y.S. Huang and F.Z. Cui. Effect of complexing agent on the morphology and microstructure of electroless deposited Ni–P alloy. *Surface and Coatings Technology*, in press, 2006.

[27] I. Baskaran, T.S.N. Sankara Narayanan, and A. Stephen. Effect of accelerators and stabilizers on the formation and characteristics of electroless Ni-P deposits. *Materials Chemistry and Physics*, 99:117–126, 2006.

[28] J. Bielinski, J. Krol, and A. Bielinska. Inorganic additives in the solution for electroless nickel-boron alloy deposition. *Bulletin of electrochemistry*, 6:828–831, 1990.

[29] James R. Henry. Electroless (autocatalytic) plating. *Metal Finishing.*, 104:354–365, 2006.

[30] Patrick Bottari, Franck Robin, and Ron Parkinson. Dépôts de nickel chimique: Obtention et propriétés. volume M 1566 of *Techniques de l'ingénieur*. 2004.

[31] T.S.N. Sankara Narayanan and S.K. Seshadri. Formation and characterization of borohydride reduced electroless nickel deposits. *Journal of Alloys and Compounds*, 365:197–205, 2004.

[32] F. Delaunois and P. Lienard. Heat treatments for electroless nickel-boron plating on aluminium alloys. *Surface and Coatings Technology*, 160:139–148, 2002.

[33] Shi Ziyuan, Wang Deqing, and Ding Zhimin. Surface strengthening of pure copper by Ni-B coating. *Applied Surface Science*, 221:32–68, 2004.

[34] C.T. Dervos, J. Novakovic, and P. Vassiliou. Vacuum heat treatment of electroless nickel-boron coatings. *Materials Letters*, 58:619–623, 2004.

[35] J.T. Winowlin Jappes, B. Ramamoorthy, and P. Kesavan Nair. A study on the influence of process parameters on efficiency and crystallinity of electroless Ni–P deposits. *Journal of Materials Processing Technology*, 169:308–313, 2005.

[36] B. Oraon, G. Majumdar, and B. Ghosh. Application of response surface method for predicting electroless nickel plating. *Materials and design*, 27:1035–1045, 2006.

[37] A. Srivastava, S. Mohan, V. Agarwala, and R.C. Agarwala. Factors influencing the deposition rate of Ni-B electroless films. *Z. Metallkunde*, 83:251–253, 1992.

[38] K.M. Gorbunova, M.V. Ivanov, and V.P. Moiseev. Electroless deposition of nickel-boron alloys: mechanism of process, structure, and some properties of deposits. *Journal of the Electrochemistry Society*, 120:613–618, 1973.

[39] Mustafa Anik, Erhan Körpe, and Esin Sen. Effect of coating bath composition on the properties of electroless nickel-boron films. *Surface and Coatings Technology*, 202:1718–1727, 2008.

[40] I. Baskaran, R. Sakthi Kumar, T.S.N. Sankara Narayanan, and A. Stephen. Formation of electroless Ni–B coatings using low temperature bath and evaluation of their characteristic properties. *Surface and Coatings Technology*, 200:6888–6894, 2006.

[41] B. Oraon, G. Majumdar, and B. Ghosh. Parametric optimization and prediction of electroless Ni - B deposition. *Materials and Design*, 28:2138 – 2147, 2007.

[42] B. Oraon, G. Majumdar, and B. Ghosh. Improving hardness of electroless Ni - B coatings using optimized deposition conditions and annealing. *Materials and Design*, 29:1412–1418, 2008.

[43] Véronique Vitry. Contribution à l'etude de la nitruration des dépôts autocatalytiques de nickel-bore. Master's thesis, Faculté polytechnique de Mons, 2007. Travail de fin d'étude pour le DEA en Sciences appliquées.

[44] Zongyuan Xiao, Wenjing Wang, Liyi Ye, Yong Sha, and Song Tu. Effect of Cd^{2+} as a stabilizer in the electroless nickel plating system. *Surface and Coatings Technology*, 202:5008–5011, 2008.

[45] Kalle Kantola. *Modelling, estimation and control of electroless nickel plating process of printed circuit board manufacturing.* PhD thesis, Helsinki University of Technology, 2006.

[46] Ray Taheri. *Evaluation of Electroless Nickel-Phosphorus (EN) Coatings.* PhD thesis, University of Saskatchewan, 2003.

[47] Wu Yating, Shen Bin, Lui Lei, and Hu Wenbin. Artificial neural network modelling of plating rate and phosphorus content in the coatings of electroless nickel plating. *Journal of Materials Processing Technology*, 205:207–213, 2008.

[48] Extending electroless nickel bath life using electrodialysis, 1998. U.S. Environmental Protection Agency Region 9 Pollution Prevention Program.

[49] B. Fisher. Avoid nickel plating losses – protect the environment and improve profitability. Nickel institute technical series No. 10 089.

[50] Helmut Horsthemke. Automatic system for endless operation of electroless nickel. *metal finishing*, 01:18–20, 2008.

[51] Susan M. Morgan and Cindy M. Lee. Metal and acid recovery options for the plating industry. *Resources, Conservation and Recycling*, 19:55–71, 1997.

[52] M. Tanaka, Y. Huang, T. Yahagi, M.K. Hossain, Y. Sato, and H. Narita. Solvent extraction recovery of nickel from spent electroless nickel plating baths by a mixer-settler extractor. *Separation and Purification Technology*, 62:97–102, 2008.

[53] Y. Huang and M. Tanaka. Analysis of continuous solvent extraction of nickel from spent electroless nickel plating baths by a mixer-settler. *Journal of Hazardous Materials*, 2008. in press.

[54] Marie-Aline Clerc. *Morphologie, propriétés tribologiques et rhéologiques des alliages nickel-bore amorphes obtenus par voie chimique.* PhD thesis, Université de Besançon, 1986.

[55] Y.W. Riddle and T.O. Bailer. Friction and wear reduction via an Ni-B electroless bath coating for metal alloys. *JOM*, april:40–45, 2005.

[56] Qun li Rao, Gang Bi, Qing hua Lu, Hao wei Wang, and Xiao lan Fan. Microstructure evolution of electroless Ni-B film during its depositing process. *Applied Surface Science*, 240:28–33, 2005.

[57] volume 3 : Alloy Phase Diagrams of *ASM handbook online*. ASM international, 2005.

[58] K. Krishnaveni, T.S.N. Sankara Narayanan, and S.K. Seshadri. Electroless nickel-boron coatings: preparation and evaluation of hardness and wear resistance. *Surface and Coatings Technology*, 190:115–121, 2005.

[59] Torhu Watanabe and Yoshimi Tanabe. The lattice images of amorphous-like Ni-B alloy films prepared by electroless plating method. *Transactions of the Japan Institute of Metals*, 24:396–404, 1983.

[60] P.S. Kumar and P.K Nair. X-ray diffraction studies on the relative proportion and decomposition of amorphous phase in electroless nickel-boron deposits. *Nanostructured Materials*, 5:183–198, 1994.

[61] H. Niederprum and H.G. Klein. *Metalloberflache*, 24:468–474, 1970.

[62] H. Gleiter. Progress in material science. *Nanocrystalline materials*, 33:223–315, 1989.

[63] M.A. Meyers, A. Mishra, and D.J. Benson. Mechanical properties of nanocrystalline materials. *Metalloberflache*, 51:427–556, 2006.

[64] K. Lu. Nanocrystalline metals crystallized from amorphous solids: Nanocrystallization, structures and properties. *Materials Science and Engineering*, R16:161–221, 1996.

[65] Michael Wagner. Structure and thermodynamic properties of nanocrystalline metals. *Physical review B*, 45:635–639, 1992.

[66] Q. Meng, N. Zhou, Y. Rong, S. Chen, and T.Y. Hsu. Size effect on the Fe nanocrystalline phase transformation. *Acta Materialia*, 50:4563–4570, 2002.

[67] Xiaoyan Song, Lingmei Li, and Jiuxing Zhang. Thermodynamic properties and phase stability of nanocrystalline metals. *Rare metals*, 25:582–586, 2006.

[68] S. R. Phillpot, D. Wolf, and H. Gleiter. A structural model for grain boundaries in nanocrystalline materials. *Scripta Metallurgica et Materialia*, 33(8):1245–1251, 1995.

[69] A. Cerezo, M. Abraham, P. Clifton, H. Lane, D.J. Larson, A.K. Petford-Long, M. Thuvander, P.J. Warren, and G.D.W. Smith. Three-dimensional atomic scale analysis of nanostructured materials. *Micron*, 32:731–739, 2001.

[70] K.H. Lee, D. Chang, and S.C. Kwon. Properties of electrodeposited nanocrystalline Ni.B alloy films. *Electrochimica Acta*, 50:4538–4543, 2005.

[71] T.V. Gaevskaya, I.G. Novotortseva, and L.S. Tsybulskaya. The effect of boron on the microstructure and properties of electrodeposited nickel films. *Metal finishing*, pages 100–103, 06 1996.

[72] S. Suzuki, M. Tanino, and Y. Waseda. Phosphorus and boron segregation at prior austenite grain boundaries in low-alloyed steel. *ISIJ International*, 42(6):676–678, 2002.

[73] M.K. Miller, J.A. Horton, W.D. Cao, and R.L. Kennedy. Characterization of the effects of boron and phosphorus additions to the nickel-based superalloy 718. *Journal de Physique*, 6:241–246, 1996.

[74] C. J. McMahon. The role of solute segregation in promoting the hardenability of steel. *Metallurgical and Materials Transactions A*, 11(3):531–535, 1980.

[75] K. Hono and D.E. Laughlin. Evidence of phosphorous segregation in grain boundaries in electroless-plated Co-P thin film. *Journal of Magnetism and Magnetic Materials*, 80(2-3):L137 – L141, 1989.

[76] M. Jahazi and J. J. Jonas. The non-equilibrium segregation of boron on original and moving austenite grain boundaries. *Materials Science and Engineering A*, 335 (1-2):49 – 61, 2002.

[77] P. Lejcek and A. Fraczkiewicz. Boron segregation in intermetallics: on the possible origins of a low-level intergranular segregation. *Intermetallics*, 11(10):1053 – 1063, 2003.

[78] P. Lejcek and O. Schneeweiss. Solute segregation at ordered grain boundaries. *Surface Science*, 487(1-3):210 – 222, 2001.

[79] Michael Kurban, U. Erb, and K.T. Aust. A grain boundary characterization study of boron segregation and carbide precipitation in alloy 304 austenitic stainless steel. *Scripta Materialia*, 54(6):1053 – 1058, 2006.

[80] Th. Hentschel, D. Isheim, R. Kirchheim, F. Muller, and H. Kreye. Nanocrystalline Ni-3.6 at% P and its transformation sequence studied by atom-probe field-ion microscopy. *Acta Materialia*, 48:933–941, 2000.

[81] B. Farber, E. Cadel, A. Menand, G. Schmitz, and R. Kirchheim. Phosphorus segregation in nanocrystalline Ni±3.6 at.% P alloy investigated with the tomographic atom probe (TAP). *Acta Materialia*, 48:789–796, 2000.

[82] Reiner Kirchheim. Grain coarsening inhibited by solute segregation. *Acta Materialia*, 50(2):413 – 419, 2002.

[83] J. Ghosh, S. Mazumdar, M. Das, S. Ghatak, and A.K. Basu. Microstructural characterization of amorphous and nanocrystalline boron nitride prepared by high-energy ball milling. *Materials Research Bulletin*, 43:1023–1031, 2008.

[84] S. K. Pradhan, T. Chakraborty, S. P. Sen Gupta, C. Suryanarayana, A. Prefer, and F. H. Froes. X-ray powder profile analyses on nanostructured niobium metal powders. *Nanostructured Materials*, 5(1):53 – 61, 1995.

[85] V. Uvarov and I. Popov. Metrological characterization of X-ray diffraction methods for determination of crystallite size in nano-scale materials. *Materials Characterization*, 58(10):883 – 891, 2007.

[86] Gao Jiaqiang, Wu Yating, Liu Lei, Shen Bin, and Hu Wenbin. Crystallization temperature of amorphous electroless nickel-phosphorus alloys. *Materials Letters*, 59:1665 – 1669, 2005.

[87] Jeong-Won Yoon, Ja-Myeong Koo, Jong-Woong Kim, Sang-Su Ha, Bo-In Noh, Chang-Yong Lee, Jong-Hyun Park, Chang-Chae Shur, and Seung-Boo Jung. Effect of boron content in electroless Ni-B layer on plating layer properties and soldering characteristics with Sn-Ag solder. *Journal of Alloys and Compounds*, 466(1-2):73 – 79, 2008.

[88] James F. Rohan and Gerald O'Riordan. Characterisation of the electroless nickel deposit as a barrier layer/under bump metallurgy on IC metallisation. *Microelectronic Engineering*, 65(1-2):77 – 85, 2003.

[89] M. O. Alam, Y. C. Chan, and K. C. Hung. Reliability study of the electroless Ni-P layer against solder alloy. *Microelectronics Reliability*, 42(7):1065 – 1073, 2002.

[90] Peng Sun, Cristina Andersson, Xicheng Wei, Zhaonian Cheng, Dongkai Shangguan, and Johan Liu. Intermetallic compound formation in Sn-Co-Cu, Sn-Ag-Cu and eutectic Sn-Cu solder joints on electroless Ni(P) immersion Au surface finish after reflow soldering. *Materials Science and Engineering: B*, 135(2):134 – 140, 2006.

[91] K. Chen, C. Liu, D.C. Whalley, D.A. Hutt, J.F. Li, and S.H. Mannan. A comparative study of the interfacial reaction between electroless Ni-P coatings and molten tin. *Acta Materialia*, 56(19):5668 – 5676, 2008.

[92] Aditya Kumar, Zhong Chen, S.G. Mhaisalkar, C.C. Wong, Poi Siong Teo, and Vaidhyanathan Kripesh. Effect of ni-p thickness on solid-state interfacial reactions between Sn-3.5Ag solder and electroless Ni-P metallization on cu substrate. *Thin Solid Films*, 504(1-2):410 – 415, 2006.

[93] Chwan-Ying Lee and Kwang-Lung Lin. Preparation of solder bumps incorporating electroless nickel-boron deposit and investigation on the interfacial interaction behaviour and wetting kinetics. *Journal of Materials Science: Materials in Electronics*, 8(6):377–383, 1997.

[94] Chwan-Ying Lee and Kwang-Lung Lin. Materials interaction in Pb—Sn/Ni—P/Al and Pb—Sn/Ni—B/Al solder bumps on chips. *Thin Solid Films*, 229(1):63 – 75, 1993.

[95] Eric W. Brooman. Wear behavior of environmentally acceptable alternatives to chromium coatings: Nickel-based candidates. *Metal Finishing*, pages 75–82, september 2004.

[96] T.S.N. Sankara Narayanan, K. Krishnaveni, and S.K. Seshadri. Electroless NiP/NiB duplex coatings: preparation and evaluation of microhardness, wear and corrosion resistance. *Materials Chemistry and Physics*, 82:771–779, 2003.

[97] J. Takadoum, J. C. Pivin, J. Chaumont, and C. Roque-Carmes. Friction and wear of amorphous Ni-B, Ni-P films obtained by ion implantation into nickel. *Journal of Materials Science*, 20:1480–1493, 1985.

[98] A. Contreras, C. León, O. Jimenez, E. Sosa, and R. Pérez. Electrochemical behavior and microstructural characterization of 1026 Ni–B coated steel. *Applied Surface Science*, 253:592–599, 2006.

[99] Y.W. Riddle and C.E. McComas. Advances in electroless nickel-boron coatings: Improvement of lubricity and wear resistance on surface of automotive components. In *Proceeding of the 2005 SAE world Congress*, 2005.

[100] Hui Li, Hexing Li, Wei-Lin Dai, Weijiang Wang, Zhigang Fang, and Jing-Fa Deng. XPS studies on surface electronic characteristics of Ni-B and Ni-P amorphous alloy and its correlation to their catalytic properties. *Applied Surface Science*, 152(1-2): 25 – 34, 1999.

[101] Hexing Li, Hui Li, Weilin Dai, and Minghua Qiao. Preparation of the Ni-B amorphous alloys with variable boron content and its correlation to the hydrogenation activity. *Applied Catalysis A: General*, 238(1):119 – 130, 2003.

[102] Tonglin Li, Weinong Zhang, Roy Zhenhu Lee, and Qixin Zhong. Nickel-boron alloy catalysts reduce the formation of trans fatty acids in hydrogenated soybean oil. *Food Chemistry*, 114(2):447 – 452, 2009.

[103] Jia-Huei Shen and Yu-Wen Chen. Catalytic properties of bimetallic NiCoB nanoalloy catalysts for hydrogenation of p-chloronitrobenzene. *Journal of Molecular Catalysis A: Chemical*, 273(1-2):265 – 276, 2007.

[104] Yanfeng Ma, Wei Li, Minghui Zhang, Ying Zhou, and Keyi Tao. Preparation and catalytic properties of amorphous alloys in hydrogenation of sulfolene. *Applied Catalysis A: General*, 243(2):215 – 223, 2003.

[105] Yin-Zu Chen, Biing-Jye Liaw, and Shu-Jen Chiang. Selective hydrogenation of citral over amorphous NiB and CoB nano-catalysts. *Applied Catalysis A: General*, 284 (1-2):97 – 104, 2005.

[106] Shao-Pai Lee and Yu-Wen Chen. Selective hydrogenation of furfural on Ni-P-B nanometals. In Sagrario Mendioroz Avelino Corma, Francisco V. Melo and José Luis G. Fierro, editors, *12th International Congress on Catalysis*, volume 130, Part 4 of *Studies in Surface Science and Catalysis*, pages 3483 – 3488. Elsevier, 2000.

[107] Jing Xu, Luwei Chen, Kong Fei Tan, Armando Borgna, and Mark Saeys. Effect of boron on the stability of Ni catalysts during steam methane reforming. *Journal of Catalysis*, 261(2):158 – 165, 2009.

[108] Jixiang Chen, Donghui Ci, Rijie Wang, and Jiyan Zhang. Hydrodechlorination of chlorobenzene over NiB/SiO$_2$ and NiP/SiO$_2$ amorphous catalysts after being partially crystallized: A consideration of electronic and geometrical factors. *Applied Surface Science*, 255(5, Part 2):3300 – 3309, 2008.

[109] Yasuaki Okamoto, Yuriko Nitta, Toshinobu Imanaka, and Shiichiro Teranishi. Surface state and catalytic activity and selectivity of nickel catalysts in hydrogenation reactions : III. electronic and catalytic properties of nickel catalysts. *Journal of Catalysis*, 64(2):397 – 404, 1980.

[110] Jamal Amer. *Développement de membranes métalliques de nickel déposées sur supports céramiques par electroless plating. Etude des propriétés particulières de permsélectivité à lŠhydrogène à hautes températures.* PhD thesis, Université Louis Pasteur, Strasbourg, France, 2008.

[111] K. Brunelli, M. Dabalà, F. Dughiero, and M. Magrini. Diffusion treatment of Ni-B coatings by induction heating to harden the surface of Ti-6Al-4V alloy. *Materials Chemistry and Physics*, 115(1):467 – 472, 2009.

[112] Hexing Li, Hui Li, Weilin Dai, and Minghua Qiao. Preparation of the Ni-B amorphous alloys with variable boron content and its correlation to the hydrogenation activity. *Applied Catalysis*, A238:119–130, 2003.

[113] M. A. Kostyanovskii, Yu. V. Prusov, N. V. Suvorov, N. M. Kulin, and V. N. Flerov. Effect of heat treatment on the structure of chemically deposited nickel with a low boron content. *Zashchita Metallov*, 27:317–320, 1991.

[114] W. Thomas Evans and M. Schlesinger. Effect of solution pH and heat-treatment on the properties of electroless nickel boron films. *Journal of the Electrochemical Society*, 141:78–83, 1994.

[115] G.F. Kayser and F.X. Kayser. Ni$_3$B: powder diffraction pattern and lattice parameters. *Journal of Alloys and Compounds*, 233:74–79, 1996.

[116] Ron Parkinson. Properties and applications of electroless nickel.

[117] Patrick Bottari, Franck Robin, and Ron Parkinson. Dépôts de nickel chimique: Applications. volume M 1567 of *Techniques de l'ingénieur*. 2004.

[118] Don Baudrand and Brad Durkin. Automotive applications of electroless nickel. *Metal Finishing*, pages 20–23, 05 1998.

[119] Jack McCaskie and Suzanne Redding. Successful automotive applications for electroless nickel. *Metal Finishing*, pages 25–27, 04 2008.

[120] G. Reinhardt. Electroless nickel applications in aircraft maintenance. Technical Report 820609, SAE, 02 1982. SAE Technical Paper.

[121] url: http://www.uctcoatings.com/. UCT Coatings website.

[122] Jeong-Won Yoon and Seung-Boo Jung. Effect of isothermal aging on the interfacial reactions between Sn–0.4Cu solder and Cu substrate with or without ENIGplating layer. *Surface and Coatings Technology*, 200:4440–4447, 2006.

[123] Y. Namba, T. Shimomura, A. Fushiki, A. Beaucamp, I. Inasaki, H. Kunieda, Y. Ogasaka, and K. Yamashita. Ultra-precision polishing of electroless nickel molding dies for shorter wavelength applications. *CIRP Annals - Manufacturing Technology*, 57(1):337 – 340, 2008.

[124] Vishal Saxena, R. Uma Rani, and A.K. Sharma. Studies on ultra high solar absorber black electroless nickel coatings on aluminum alloys for space application. *Surface and Coatings Technology*, 201(3-4):855 – 862, 2006.

[125] M. Redlich, A. Katz, L. Rapoport, H.D. Wagner, Y. Feldman, and R. Tenne. Improved orthodontic stainless steel wires coated with inorganic fullerene-like nanoparticles of WS_2 impregnated in electroless nickel-phosphorous film. *Dental Materials*, 24(12):1640 – 1646, 2008.

[126] Joël Alexis. *Substitution des traitements de surface des alliages d'aluminium à base de chrome hexavalent en solution: adhérence de revêtements d'alliages Zn–Ni*. PhD thesis, Institut National Polytechnique de Toulouse, 2000.

[127] Sung-Ki Lee, Jae-Ho Lee, and Young-Ho Kim. Nucleation and growth of zinc particles on an aluminium substrate in a zincate process. *Journal of electronic materials*, 36(9):1442 – 1447, 2007.

[128] Libo Li and Maozhong An. Electroless nickel-phosphorus plating on SiCp/Al composite from acid bath with nickel activation. *Journal of Alloys and Compounds*, 461 (1-2):85 – 91, 2008.

[129] Shreepad Karmalkar and V. Pradeep Kumar. Effects of nickel and palladium activation on the adhesion and I-V characteristics of as-plated electroless nickel deposits on polished crystalline silicon. *Journal of the Electrochemical Society*, 151(9):C554 – C 558, 2004.

[130] Himendra Jha, Tatsuya Kikuchi, Masatoshi Sakairi, and Hideaki Takahashi. Palladium nanoparticle seeded electroless metallization of Al/Al_2O_3 surfaces. *Materials Letters*, 63(16):1451 – 1454, 2009.

[131] A. Duhin, Y. Sverdlov, Y. Feldman, and Y. Shacham-Diamand. Electroless deposition of NiWB alloy on p- type si(1 0 0) for NiSi contact metallization. *Electrochimica Acta*, In Press, Corrected Proof:–, 2009.

[132] Libo Li, Maozhong An, and Gaohui Wu. Model of electroless Ni deposition on SiCp/Al composites and study of the interfacial interaction of coatings with substrate surface. *Applied Surface Science*, 252:959–965, 2005.

[133] T. Homma, M. Tanabe, K. Itakura, and T. Osaka. Tapping mode atomic force microscopy analysis of the growth process of electroless nickel-phosphorus films an nonconducting surfaces. *Journal of the electrochemical society*, 144(12):4123 – 4127, 1997.

[134] Zhenmin Liu and Wei Gao. The effect of substrate on the electroless nickel plating of Mg and Mg alloys. *Surface and coatings technology*, 200:3553–3560, 2006.

[135] Zhenmin Liu and Wei Gao. Electroless nickel plating on AZ91 Mg alloy substrate. *Surface and Coatings Technology*, 200(16-17):5087 – 5093, 2006.

[136] Rajan Ambat and W. Zhou. Electroless nickel-plating on AZ91D magnesium alloy: effect of substrate microstructure and plating parameters. *Surface and Coatings Technology*, 179(2-3):124 – 134, 2004.

[137] M. Anik and E. Körpe. Effect of alloy microstructure on electroless NiP deposition behavior on alloy AZ91. *Surface and Coatings Technology*, 201:4702–4710, 2007.

[138] Shuo Sun, Jianguo Liu, Chuanwei Yan, and Fuhui Wang. A novel process for electroless nickel plating on anodized magnesium alloy. *Applied Surface Science*, 254(16):5016 – 5022, 2008.

[139] Enam Khan, C. F. Oduoza, and T. Pearson. Surface characterization of zincated aluminium and selected alloys at the early stage of the autocatalytic electroless nickel immersion process. *Journal of Applied Electrochemistry*, 37:1375–1381, 2007.

[140] C.K. Lee. Corrosion and wear-corrosion resistance properties of electroless Ni-P coatings on GFRP composite in wind turbine blades. *Surface and Coatings Technology*, 202:4868–4874, 2008.

[141] Guinier A. *Theorie et technique de la radiocristallographie*. Dunod., Paris, 3rd edition, 1964.

[142] A.D. Romig. Analytical transmission electron microscopy. In *Materials Characterization*, volume 10 of *ASM handbook online*. ASM international, 1986.

[143] Miroslav Karlík and Bernard Jouffrey. Étude des métaux par microscopie électronique en transmission (MET). volume M 4134 of *Techniques de l'ingénieur*. 2008.

[144] Ray F. Egerton. *Physical Principles of Electron Microscopy An Introduction to TEM, SEM, and AEM*. CSpringer, New York, 2005.

[145] Hua Zhang, Shulan Wang, Guangchun Yao, and Zhongsheng Hua. Electroless Ni-P plating on Mg-10Li-1Zn alloy. *Journal of Alloys and Compounds*, 474(1-2):306 – 310, 2009.

[146] T.S.N. Sankara Narayanan, I. Baskaran, K. Krishnaveni, and S. Parthiban. Deposition of electroless Ni–P graded coatings and evaluation of their corrosion resistance. *Surface and Coatings Technology*, 200:3438–3445, 2006.

[147] Andrzej Lasia. *Electrochemical Impedance Spectroscopy and its Applications*, volume 32 of *Modern Aspects of Electrochemistry*, chapter 2, pages 143 – 248. Kluwer Academic, New York, 1999.

[148] Hai-Ping Liu, Ning Li, Si-Fu Bi, De-Yu Li, and Zhong-Li Zou. Effect of organic additives on the corrosion resistance properties of electroless nickel deposits. *Thin Solid Films*, 516(8):1883 – 1889, 2008.

[149] Maura Crobu, Andrea Scorciapino, Bernhard Elsener, and Antonella Rossi. The corrosion resistance of electroless deposited nano-crystalline Ni-P alloys. *Electrochimica Acta*, 53(8):3364 – 3370, 2008.

[150] Woo-Jae Cheong, Ben L. Luan, and David W. Shoesmith. Protective coating on Mg AZ91D alloy - the effect of electroless nickel (EN) bath stabilizers on corrosion behaviour of Ni-P deposit. *Corrosion Science*, 49(4):1777 – 1798, 2007.

[151] url: http://www.bruker-axs.de/thenewd8advance.html.

[152] Ursula R. Kattner. Thermodynamic modeling of multicomponent phase equilibria. *JOM*, 49(12):14 – 19, 1997.

[153] Maria Teresa Clavaguera-Mora, Narcis Clavaguera, Daniel Crespo, and Trinitat Pradell. Crystallisation kinetics and microstructure development in metallic systems. *Progress in Materials Science*, 47(6):559 – 619, 2002.

[154] J.E. Briggs and R. Hasegawa. Nickel-boron binary amorphous alloy. US Patent 4 338 131, 1982.

[155] K. Lu. interfacial structural characteristics and grain-size limits in nanocrystalline materials crystallized from amorphous solids. *Physical review B*, 51:18 – 27, 1995.

[156] M.T. Clavaguera-Mora. Glassy materials: thermodynamic and kinetic quantities. *Joural of alloys and compounds*, 220:197 – 205, 1995.

[157] D. Turnbull. Formation of crystal nuclei in liquid metals. *Joural of applied physics*, 21:1022 – 1028, 1950.

[158] D.R.H. Jones and G.A. Chadwick. An expression for the free energy of fusion in the homogeneous nucleation of solids from pure melts. *Philosophical magazine*, 24: 995 – 998, 1971.

[159] C.V. Thompson and F. Spaepen. On the approximation of the free energy change on crystallization. *acta metallurgica*, 27:1855 – 1859, 1979.

[160] Battezzatti L. On the approximation of the free-energy of undercooled glass-forming metallic melts. *Zeitschrift fur Metallkunde*, 75:305, 1984.

[161] K.S. Dubey and P. Ramachandrarao. On the free energy change accompanying crystallization of undercooled melts. *acta metallurgica*, 32(1):91 – 96, 1984.

[162] Hans J. Fecht. Intrinsic instability and entropy stabilization of grain boundaries. *physical review letters*, 65(5):610 – 613, 1990.

[163] A. Fernandez Guillermet. On the use of grüneisen parameters in the treatment of shock-wave data. *International Journal of Thermophysics*, 8(6):751 – 761, 1987.

[164] James H. Rose, John R. Smith, and John Ferrante. Universal features of bonding in metals. *Physical review B*, 28:1835 – 1845, 1983.

[165] Pascal Vinet, John R. Smith, John Ferrante, and James H. Rose. Temperature effects on the universal equation of state of solids. *Physical review B*, 35:1945 – 1953, 1987.

[166] M Hasaka, T Morimura, Y Uchiyama, S Kondo, T Watanabe, K Histsune, and T Furuse. Diffusion of copper, aluminum and boron in nickel. *Scripta Metallurgica et Materialia*, 29(7):959–962, 1993.

[167] M. W. Chase, C. A. Daives, J. R. Downey, D. J. Frurip, R. A. McDonald, and A. N. Syverud. JANAF thermochemical tables, third edition. *Journal of Physical and Chemical Reference Data*, 14, 1985. Supplement No. 1, 1856 pages.

[168] Hiroaki Yamamoto and Masao Morishita. Composition-partial oxygen pressure diagram for Ni-B-O system. *Journal of Alloys and Compounds*, 438(1-2):L1–L3, JUL 12 2007.

[169] R. Ushio and O. Ogawa. Activities of boron in the binary Ni-B and the ternary Co-Fe-B melts. *Metallurgical transactions B*, 22:47–52, 1991.

[170] O. Teppo and P. Taskinen. Thermodynamic assessment of Ni-B phase diagram. *Materials Science and technology*, 9:205 – 212, 1993.

[171] G.K. Moiseev, N.I. Ilyanyh, and T.V. Kulikova. Determination of thermodynamic properties of condensed phases of NiB, Ni_2B, Ni_3B and Ni_4B_3 by calculation methods. *Metally*, 1:28 – 33, 2005. in Russian.

[172] I.R. Shein, N.I. Medvedeva, and A.L. Ivanovskii. Electronic and structural properties of cementite-type M3X (M = Fe, Co, Ni; X = C or B) by first principles calculations. *Physica B*, 371:126 – 132, 2006.

[173] M. D. Smolin, V. G. Grebenkina, Yu. M. Goryachev, E. I. Shvartsman, , and L. I. Panov. Elastodynamic characteristics of boride phases of nickel. *Powder Metallurgy and Metal Ceramics*, 23(5):405 – 407 , 1984. Translated from Poroshkovaya Metallurgiya, No. 5(257), pp. 84 - 86, May, 1984.

[174] C. B. Finch, M. K. Ferber, W. A. Simpson Jr, and R. K. Williams. Anisotropy of thermal expansion, elasticity, and electrical resistivity in single- crystal trinickel boride, Ni_3B. *Journal of Materials Science Letters*, 3(12), 1984.

[175] Mrinalini Deshpande, D. G. Kanhere, and Ravindra Pandey. Structures, energetics, and magnetic properties of NinB clusters with n=1-8,12. *Physical review A*, 71(6), 2005.

[176] Hui Li, Hexing Li, and Jing-Fa Deng. The crystallization process of ultrafine Ni-B amorphous alloy. *Materials Letters*, 50:41–46, 2001.

[177] M. V. Ivanov, E. N. Lubnin, and A. B. Drovosekov. X-Ray Photoelectron Spectroscopy of Chemically Deposited Amorphous and Crystalline Ni-B Coatings. *Protection of Metals*, 39:133–141, 2003. Translated from Zashchita Metallov, Vol. 39, No. 2, 2003, pp. 155-163.